Ana Gallet Segarra

Robust Control of a Solid Oxide Fuel Cell for Combined Heat and Power Applications

Institut für Nichtlineare Mechanik der Universität Stuttgart

Robust Control of a Solid Oxide Fuel Cell for Combined Heat and Power Applications

Von der Fakultät Konstruktions-, Produktions- und Fahrzeugtechnik
der Universität Stuttgart
zur Erlangung der Würde einer Doktor-Ingenieurin (Dr.-Ing)
genehmigte Abhandlung

Vorgelegt von

Ingeniero Industrial Ana Gallet Segarra

aus Barcelona

Hauptberichter: Prof. Dr.-Ing. Arnold Kistner

Mitberichter: Prof. Dr.-Ing. François Lapicque

Tag der mündlichen Prüfung: 03.02.2017

Institut für Nichtlineare Mechanik der Universität Stuttgart

2017

Declaration of Authorship

I herewith formally declare that I have written the submitted dissertation independently. I did not use any outside support except for the quoted literature and other sources mentioned in the paper.

I clearly marked and separately listed all of the literature and all of the other sources which I employed when producing this academic work, either literally or in content.

Acknowledgements

The doctoral thesis is a long way full of joy, challenges and obstacles. I could probably not have reached the end without the support of all people who accompanied me during these years. I would like to thank all of them.

Firstly, I would like to express my gratitude to my doctoral supervisors, Prof. Arnold Kistner and Prof. Françoise Lapique, for their guidance and help. Thank you for sharing with me your expertise, for giving me constructive criticism and for supporting me whenever a problem arose.

I am grateful to Robert Bosch GmbH, company which made possible the contact to the best experts and provided all facilities and financial support during my doctoral program.

Maxime Carre, I cannot imagine a better advisor. I am thankful for the discussions, for your encouragement and your support in difficulties. Thank you for your time giving criticism and corrections and for the effort of understanding the smallest details. But above all for being such a good person. I would like to thank Pedro da Silva and Kai Weeber, for giving me the possibility of working full-time for my thesis. Thank you for providing me the chances of learning and development, for the sincere advice and for supporting me in the transition to the next career step. I am grateful to all co-workers of the SOFC project. The support at the laboratory, technical discussions and suggestions have been a key for my success. Furthermore, I would like to thank all colleagues of AEB. It has been a privilege to work every day in such a positive

working atmosphere surrounded by great scientists. Thank you to Tania for the confidence in me at the very beginning, and to Datong and Wolfgang, whose inspiring guidance opened the door to a Ph.D. I want to show my gratitude to all the other colleagues and bosses who supported me. I am thankful to the former Ph.D. students for including me as one of them and for sharing their experience during these years. To my Ph.D. fellow students, thank you for sharing with me all positive and negative moments. Without the discussions and advice in coffee breaks it would have been much harder. I am especially thankful to Steffi, for all discussions about Modelica and SOFC, for your corrections, for sharing the disappointment after *inconsistent initial conditions* and for the immense joy when the model finally worked.

I am thankful to all my friends, who endured my stress, absences and bad mood with patience. Thank you for being there whenever I needed you, for talking, taking a break or supporting me with energy and motivation for carrying on. To the friends far away, thank you for welcoming me every time with open arms, even if it has been months since the time before. To friends nearby, thank you for helping me to feel at home abroad. Especially to Marta, for over 10 years of going in parallel paths. I am grateful for your sense of humor, for your sincerity and for your advice.

Steffen, thank you for being always there. For not complaining while the writing marathons and for enduring my stress peaks with patience. For taking care of me and for making me laugh when I needed it. For adapting our plans to my uncertain calender, thank you. For your love. And for being so proud of me.

A la meva família, avis, tiets i cosins. Especialment a l'Aleix i els meus pares. Gràcies per donar-m'ho tot. Per buscar la millor escola i esplai, preguntar-me els resums, calmar-me quan calia i ensenyar-me a relativitzar. Per escoltar-me i aconsellar-me, i per esforçar-vos a entendre de què treballo exactament encara que us soni a xino. Per creure en mi i convencem que podia aconseguir el que volgués. Us estimo.

Thank you all. Without you it would not have been possible.

Contents

List of Figures

List of Tables

Nomenclature

Table 0.1 – Latin symbols.

variable	*unit*	*description*
A_{act}	m^2	active area
CP	$J \cdot K^{-1}$	heat capacity
$C_{abs,j}$	bar^{-1}	absorption constant of the specie j
$C_{eq,i}$	bar^2	equilibrium constant of the reaction i
$C_{ki,i}$	$mol \cdot bar^{0.5} \cdot g^{-1} \cdot s^{-1}$	kinetic constant of the reaction i
C_r	$mol \cdot s^{-1}$	conversion rate
cp	$J \cdot K^{-1} \cdot mol^{-1}$	molar heat capacity
c_j	$mol \cdot m^{-3}$	volumetric molar concentration
D	$m^2 \cdot s^{-1}$	diffusion coefficient
D_h	m	hydraulic diameter
FU	-	fuel utilization
g	$J \cdot mol^{-1}$	molar Gibb's free energy
Gr	-	Grashof number
HHV	$J \cdot mol^{-1}$	higher heating value
H	J	enthalpy
h	$J \cdot mol^{-1}$	molar enthalpy
h_{conv}	$W \cdot m^{-2} \cdot K^{-1}$	convection coefficient
h_{loss}	m	head losses
I	A	electrical current
j	$A \cdot m^{-2}$	current density

continued on next page...

Table 0.1 – Latin symbols (continued from previous page).

variable	*unit*	*description*
j_0	$A \cdot m^{-2}$	exchange current density
j_{lim}	$A \cdot m^{-2}$	limiting current density
L	m	length
LHV	$J \cdot mol^{-1}$	lower heating value
p	m	perimeter
l_{char}	m	characteristic length
$N_{c,j}$	-	number of carbon atoms of the molecule j
N_{cells}	-	amount of cells which form the stack
$\bar{N}_{e^-}$	-	mean amount of electrons released per molecule
$N_{e^-,j}$	-	electrons released per molecule of specie j
Nu	-	Nusselt number
n_{e^-}	—	number of transferred electrons
$\dot{n}$	$mol \cdot s^{-1}$	molar flow
$\bar{n}$	-	mean of carbon atoms per molecule of fuel
$\bar{n}_{alk}$	-	mean of carbon atoms per alkane molecule of fuel
n_j	-	carbon atoms per molecule of specie j
P	Pa	pressure
P_{el}	W	electrical power
Pr	—	Prandt number
p_j	$Pa \cdot Pa^{-1}$	partial pressure of the specie j
$\dot{Q}$	W	thermal power
Re	—	Reynolds number
R	Ω	ohmic resistance
r	-	recycle rate
s	$J \cdot K^{-1}$	entropy
T	K	temperature
U	V	voltage
U_{OC}	V	open circuit voltage

continued on next page...

Table 0.1 – Latin symbols (continued from previous page).

variable	*unit*	*description*
v	$m \cdot s^{-1}$	velocity
w	$W \cdot mol^{-1}$	molar work
$\dot{v}$	$m^3 \cdot s^{-1}$	volumetric flow
x_j	$mol \cdot mol^{-1}$	molar fraction of the specie j
x_{alk}	$mol \cdot mol^{-1}$	sum of the molar fractions of all the alkanes
W	J	work
z_k	—	minor hydraulic losses

Table 0.2 – Greek symbols.

variable	*unit*	*description*
γ	$A \cdot m^{-2}$	frequency factor
Δ_y		deviation of the variable y
δ	m	thickness
ϵ	$\% \cdot 100^{-1}$	relative error
ϵ_k	—	porosity of the material k
ζ_0	N	resisting force
η	—	efficiency
ϑ	V	overpotential
ϑ_{act}	V	activation overpotential
ϑ_{conc}	V	concentration overpotential
ϑ_{ohm}	V	ohmic overpotential
λ	$W \cdot m^{-1} \cdot K^{-1}$	thermal conductivity
λ_p	—	friction factor
μ	$Pa \cdot s^{-1}$	dynamic viscosity
ν_{ij}	-	stoichiometric coefficient of the reaction i for the specie j

continued on next page...

Table 0.2 – Greek symbols (continued from previous page).

variable	*unit*	*description*
ξ_i	$mol \cdot s^{-1}$	reaction rate of the reaction i
ρ	$kg \cdot m^{-3}$	density
σ	$S \cdot m^{-1}$	electrical conductivity
τ	$-$	tortuosity
Φ	$mol \cdot mol^{-1}$	oxygen to carbon ratio

Table 0.3 – Subscripts.

subscript	*description*
air	air
alk	alkane
cell	single cell
chem	chemical
comb	combustion
cond	condensate
cons	consumed
conv	convection
cool	cooling fluid
el	electrical
elech	electrochemical
exp	experimental
flu	fluid
flue	flue gas
for	forward reaction
fuel	fuel gas
hex	heat exchanger

continued on next page...

Table 0.3 – Subscripts (continued from previous page).

subscript	*description*
inert	inert gas
loss	losses
max	maximal value
min	minimal value
m	measurement point in the system
n	counter for the experimental/simulation runs
NG	natural gas
prov	provided
rev	reverse reaction
sat	saturation
sim	simulation
sol	solid
stoich	stoichiometric
th	thermal
tot	total
λ	conduction

Table 0.4 – Superscripts

superscript	*description*
0	standard conditions
an	anode
bu	burner
cal	calorimeter
calc	calculated value
cath	cathode

continued on next page...

Table 0.4 – Superscripts (continued from previous page).

superscript	*description*
cont	contact
corr	corrected
elect	electrolyte
ic	interconnect
in	inlet
inf	inferior limit
meas	measured value
NASA	variable calculated by applying the NASA Polynomials
out	outlet
pr	prereformer
prod	product
r	reversible
reac	reactant
real	real value
rec	recycle gas
ref	reference value
set	set point value
stack	stack
sup	superior limit
sys	system
theo	theoretical value

Table 0.5 – Abbreviations.

abbreviations	*description*
0D	0 dimensional

continued on next page...

Table 0.5 – Abbreviations (continued from previous page).

Abbreviations	*description*
1D	1 dimensional
1D+1D	quasi 2 dimensional
2D	2 dimensional
3D	3 dimensional
AFC	alkaline fuel cells
APU	auxiliary power unit
BoP	balance of plant
CHP	combined heat and power
CPOX	catalytic partial oxidation
EV	end value
FCS	fuel cell system
HE	heat exchanger
HHV	higher heating value
LHV	lower heating value
MCFC	molten carbonate fuel cell
MV	measured value
MPC	model predictive control
OSR	oxidative steam reforming
PAFC	phosphoric fuel cell
PEMFC	polymer electrolyte membrane fuel cell
PEN	positive-electrolyte-negative
PI	proportional integrator controller
SOFC	solid oxide fuel cell
LSM	lanthanum strontium manganite
RH	relative humidity
TPB	triple phase boundary
YSZ	yttria-stabilized zirconia

Constants

Table 0.6 – Constants.

constant	*value*	*unit*	*source*	*description*
$\Delta h^0_{vap,H_2O}$	40016	$J \cdot mol^{-1}$	[89]	water standard molar enthalpy of vaporization
D_0^{C-H}	413237.16	$J \cdot mol^{-1}$	[118]	bond-dissociation energy C—H boundary
D_0^{C-C}	345829.68	$J \cdot mol^{-1}$	[118]	bond-dissociation energy C—C boundary
$D_0^{O=O}$	497810.52	$J \cdot mol^{-1}$	[118]	bond-dissociation energy O=O boundary
$D_0^{C=O}$	803865.6	$J \cdot mol^{-1}$	[118]	bond-dissociation energy C=O boundary
D_0^{H-O}	463060.08	$J \cdot mol^{-1}$	[118]	bond-dissociation energy H—O boundary
F	96485.34	$C \cdot mol^{-1}$	-	Faraday constant
P_0	101300	Pa	-	standard pressure
T_0	298.15	K	-	standard temperature
R	8.314	$J \cdot mol^{-1} \cdot K^{-1}$	-	universal gas constant
A_{H_2O}	10.196	-	[130]	parameter for the Antoine equation
B_{H_2O}	1730.63	K^{-1}	[130]	parameter for the Antoine equation
C_{H_2O}	-39.724	K	[130]	parameter for the Antoine equation

Table 0.7 – Calorific values of NG components for the ideal gas [89].

component	*HHV in* $kJ \cdot mol^{-1}$	*LHV in* $kJ \cdot mol^{-1}$
methane	890.63	802.60

continued on next page...

Table 0.7 – Calorific values of NG components for the ideal gas [89] (continued from previous page).

component	*HHV in* $\mathrm{kJ} \cdot \mathrm{mol}^{-1}$	*LHV in* $\mathrm{kJ} \cdot \mathrm{mol}^{-1}$
ethane	1560.69	1428.64
propane	2219.17	2043.11
n-butane	2877.40	2657.32
n-pentane	3535.77	3271.67
n-hexane	4194.95	3886.84

Abstract

The reduction of energy consumption and CO_2 emissions is one of the main environmental issues in the present-day society. Distributed combined heat and power systems (CHP-systems) are one of the most promising technologies for the achievement of this goal. The reason is that the power is produced near to the site of consumption, minimizing the heat loss during transport. Additionally, the waste heat generated in the process (which in the case of centralized electricity production becomes generally lost) can be recovered for heating purposes or warm water supply. As a consequence, the total efficiency of the energy conversion process is increased, resulting in a reduction of the CO_2 emissions and energy costs. Solid oxide fuel cells (SOFC) are the CHP technology with the highest electrical efficiency, achieving values of up to 60 %. Additionally, they operate directly with natural gas, enabling their installation in most industrial, commercial and residential buildings without the necessity of additional infrastructure.

The natural gas consumed in Germany is a mixture of gases extracted from different sources, resulting in a gas composition which varies over time and site of consumption. The consequence is a fluctuation of the heating value of up to 30 %, which can not be easily measured nor predicted. The mentioned variation is a risk for SOFC systems, since their degradation and efficiency are very sensitive to changes in the gas composition. However, the current control strategies for SOFC systems are still calibrated to one type of natural gas and do not regard the mentioned fluctuations. For instance, the system studied in this work has been calibrated with methane, leading to optimal operating conditions for this type of gas. However, it has been estimated

that if it was operated with other gases, the evaluation criteria regarding the degradation (fuel utilization and oxygen to carbon ratio) would have achieved deviations up to 25 % from the set point.

The aim of this work is to solve this problem by developing alternative control strategies which take changes in the natural gas composition into account. The mean amount of carbon atoms per molecule of fuel is identified as the key property for this issue, since it can be related analytically to the degradation criteria of fuel utilization and oxygen to carbon ratio. Thus, if this property of the fuel is identified, the control parameters can be determined and the system can work under optimal conditions, enabling the desired lifetime and efficiency of the system. For this purpose, different detection strategies of the natural gas carbon content have been developed, by relating the non-measurable mean amount of carbon atoms per molecule to other measurable gas properties. The most relevant strategies are based on the measurement of the inlet natural gas calorific value (*calorific value strategy*), on the oxygen mass fraction of the exhaust gas (*oxygen strategy*) or on the humidity and carbon dioxide mass fraction of the exhaust gas (*humidity strategy*).

The mentioned strategies have been evaluated by using a complete system model developed in Modelica® language, which includes a stack, a fuel processor and an air processor. The models have been parameterized and validated with experimental data. The evaluation results show that the usage of the *humidity strategy* does not improve the results compared to the reference strategy, which is the control strategy of the system without any adaptation to the gas composition. However, by using the *oxygen strategy* the deviation of the evaluation criteria from their set point is reduced to a maximum of 5 % and by applying the *calorific value strategy* it decreases to a maximum of 5.5 %. The detection of the mean amount of carbon atoms per molecule is experimentally tested for the *humidity strategy* and for the *oxygen strategy*. In the first case the carbon content in the gas can be identified with a mean error of 2.5 % and a maximal error of 15 %, while in the second case its detection is not pos-

sible. Thereby, the behavior observed at the simulation results is confirmed by the experimental tests.

The next step is to test the successful strategies in real systems connected to the natural gas network, in order to evaluate their effect on efficiency and long-term robustness of the system.

Kurzfassung

Eines der wichtigsten ökologischen Ziele unserer heutigen Gesellschaft ist die Senkung des Energieverbrauchs und der CO_2-Emissionen. Kraft-Wärme-Kopplungs- Systeme (KWK-Systeme) sind eine der vielversprechendsten Technologien für die Erfüllung diesen Zwecks. Der Grund dafür ist, dass der Strom sehr nah von dem Verbrauchsort erzeugt wird, welches die Minimierung der Transportverluste ermöglicht. Außerdem geht, im Gegensatz zu zentralisierten Kraftwerken, die im Prozess entstandene Wärme nicht verloren. Sie wird rückgewonnen und für Heizungs- und Warmwassersysteme verwendet. Die Folge ist die Erhöhung des gesamten Wirkungsgrades des Energieumwandlungsprozesses, welches zu niedrigeren CO_2-Emissionen und Energiekosten führt. Festoxidbrennstoffzellen (SOFC) sind jene KWK-Technologie, die mit Werten von bis zu 60 % den höchsten elektrischen Wirkungsgrad erreichen können. Ein weiterer Vorteil ist, dass sie direkt mit Erdgas betrieben werden können. Dadurch können sie ohne weitere Infrastruktur in den meisten kommerziell und industriell genutzten Gebäude und Wohnhäuser installiert werden.

In Deutschland wird eine Mischung von Erdgasvarianten verbraucht, die von unterschiedlichen Quellen kommen. Dadurch entsteht eine Gaszusammensetzung, die über die Zeit schwankt und die abhängig vom Verbrauchsort ist. Die Folge ist eine Veränderung des Brennwerts von bis zu 30 %, die weder gemessen noch vorhergesagt werden kann. Diese Variation stellt ein Risiko für die SOFC-KWK-Systeme dar, denn ihre Alterung und ihr Wirkungsgrad sind sehr sensitive gegenüber der Änderung der Gaszusammensetzung. Trotzdem werden derzeit SOFC-KWK-Systeme

noch mit einer konkreten Erdgasvariante kalibriert und ohne Beachtung von Variationen der Erdgaszusammensetzung betrieben. Beispielhaft wurde das in dieser Arbeit betrachtete System mit Methan kalibriert, welches zu einem optimalem Ergebnis bei der Benutzung von Methan führt. Das Verhalten würde sich jedoch ändern, wenn das System mit anderen typischer Erdgasvarianten betrieben würde. Die Kriterien für die Detektion jener Arbeitsbedingungen, bei der Degradierung stattfindet, sind die Kraftstoffausnutzung und das Sauerstoff/Kohlenstoff-Verhältnis. Die Berechnungen zeigen, dass die oben genannten Evaluierungskriterien bei Verwendung anderer Erdgasvarianten bis zu 25 % vom Sollwert abweichen.

Ziel dieser Arbeit war die Entwicklung von Regelungskonzepten, die die Veränderung der Erdgaszusammensetzung einbeziehen, um das genannte Problem zu vermeiden. Die mittlere Menge von Kohlenstoffatomen pro Brennstoffmolekül wurde als entscheidende physikalische Eigenschaft für dieses Problemstellung festgestellt. Grund hierfür ist, dass der Zusammenhang zwischen dieser Größe und den Evaluierungskriterien analytisch beschrieben werden konnte. Somit können, wenn die genannte Eigenschaft des Gases identifiziert wird, die Regelparameter entsprechend angepasst werden. Der Vorteil ist ein KWK-System mit höherem Wirkungsgrad und längerer Lebensdauer. Für diesen Zweck wurden verschiedene Strategien entwickelt, um die Kohlenstoffmenge im Erdgas zu detektieren. Diese basieren auf der Identifikation von Zusammenhängen zwischen der mittleren Menge von Kohlenstoffatomen pro Brennstoffmolekül mit anderen messbaren Eigenschaften des Gases. Die wichtigsten Strategien basieren auf der Messung des Erdgasbrennwertes am Eingang des Systems (*Brennwertstrategie*), des Sauerstoffanteils im Abgas (*Sauerstoffstrategie*) oder der Feuchtigkeit und des Kohlenstoffdioxidanteil im Abgas (*Feuchtigkeitsstrategie*).

Die genannten Strategien wurden mit Simulationsmethoden bewertet. Dafür wurde ein Gesamtsystemmodel in Modelica® entwickelt, welches ein Stack, ein Brennstoffprozessor und ein Luftprozessor beinhaltet. Es wurde mit experimentellen Daten parametrisiert und validiert. Die Ergebnisse zeigen, dass die *Feuchtigkeitsstrategie* keine

Verbesserung gegenüber der Strategie ohne Einbeziehung der Gaszusammensetzung (*Referenzstrategie*) bringt. Im Gegensatz dazu, wird die Abweichung zwischen Soll- und Istwerten der beiden oben genannte Evaluierungskriterien zu einem maximalen Wert von 5 % reduziert. Die Anwendung von der *Brennwertstrategie* führt zu einer Abweichung von bis zu 5.5 %. Die Detektion der mittleren Menge von Kohlenstoffatomen pro Brennstoffmolekül wurde für die *Feuchtigkeitsstrategie* und die *Brennwertstrategie* experimentell untersucht. Bei Anwendung der *Feuchtigkeitsstrategie* konnte der Kohlenstoffgehalt des Gases mit einem mittleren Fehler von 2.5 % und einem maximalen Fehler von 15 % identifiziert werden. Beim Einsatz der *Brennwertstrategie* war die Identifikation nicht möglich. Dadurch wurde das in den Simulationsergebnissen beobachtete Verhalten durch die experimentellen Tests bestätigt.

Der nächste Schritt besteht darin, die erfolgreichen Strategien in realen Systemen, die mit dem Erdgasnetz verbunden sind, zu testen. Damit könnte die Auswirkung der Strategien auf die Effizienz und die Lebensdauer des Systems experimentell bewertet werden.

1 Introduction

In the last decades the emission of greenhouse gases, one of the principal reasons for the climate change, has become a main issue for the society. Several governments have reacted in consequence, approving laws and subscribing international agreements with the objective of reducing the emissions, for instance the Kyoto Protocol adopted in 1997 by 191 states [15]. The carbon dioxide is the gas resulting from human activity with the highest contribution to the greenhouse effect [101]. The most important source of CO_2 emissions is the energy supply, representing a 26 % of the total [123]. That is the reason why many of the measures applied in order to reduce the emissions are focused in the energetic sector. One option is the use of renewable energy sources, for example solar or wind energy, which are not based on fossil fuels. Although the contribution of these energy sources to the total energy consumption increases year by year, their capacity is limited. An alternative is the energy production by using fossil fuels, but improving upon the efficiency of the current process. It results in a lower amount of energy to cover the same demand, and consequently the CO_2 emissions are reduced. At the same time, the costs for the energy production can be reduced and the energetic independence increased, since a reduced amount of fossil fuels has to be acquired.

One of the possibilities is the decentralized energy production with combined heat systems and power or CHP systems, which can reduce the primary energy consumption and CO_2 emissions by about 25 % [37]. The reason is that, since the production and consumption take place at the same point, the transport losses are negligible and the waste heat can be recovered locally becoming then useful energy.

Several different technologies can be used for CHP systems, being one of the most efficient solid oxide fuel cells (SOFC). Another advantage is that, combined with a fuel preprocessing unit, they can operate with natural gas. Consequently, they can be incorporated to residential, commercial or industrial buildings without the need for additional distribution network, which would be the case if hydrogen was used as a fuel. However, a problem of the standard natural gas distribution network is that the gas composition of the delivered gas varies over time and from supply point to supply point, being neither actively controlled not measured. At the same time, the current CHP SOFC systems are calibrated for a fixed gas composition. Thus, they controllers are not designed to react against the disturbances resulting from the fluctuating gas composition, which can result in a decrease of the lifetime and/or the efficiency of the system.

The analysis of the referred natural gas fluctuations in Germany and its influence on the behavior of the combined heat and power fuel cell system is a principal aim of this work. Additionally, if this fact constitutes a risk regarding lifetime and/or efficiency, the development and test of a solution for the problem becomes the second objective.

This work is structured as follows. Firstly, an overview of the most important concepts related to fuel cells and combined heat and power systems is given, followed in *Chapter 3* by the analysis of the state of the art regarding solid oxide fuel cells simulation and control. Then, the description of the natural gas distribution system and the resulting variation of the gas composition is presented in *Chapter 4*, leading to the analysis of its effects on the CHP-SOFC system. In *Chapter 5* the model used for the later analysis is described, together with the procedure and results of the parameterization and validation. The development of the different control strategies is presented in *Chapter 6*, and the results of their simulation and experimental tests in *Chapter 7* and *Chapter 8* respectively. Finally, an overview and discussion about the procedure and the results terminate the work.

2 Fundamentals of solid oxide fuel cells for combined heat and power applications

2.1 Solid oxide fuel cells or SOFC

Physical principles, operation and application of fuel cells are described in detail in many engineering books. In this section an overview about the topic is given, focused on the fundamental concepts for the rest of this work. It is based on [29, 105, 112, 121, 145], sources to which the reader is referred for more detailed explanation.

2.1.1 Description and function of a simple fuel cell

A fuel cell is an electrochemical device which converts the chemical energy contained in a fuel and an oxidant (typically air) into electrical energy, producing water, heat and in some cases carbon dioxide as by-products. The active part of the fuel cell is constituted by an electrolyte and two electrodes, the cathode and the anode. Fig. 2.1 shows the structure and operation of a single fuel cell, in this case a proton exchange membrane fuel cell (PEMFC).

There are different types of fuel cells, but the general operation principle and the global electrochemical reaction if operating with hydrogen (Eq. 2.1) are common to all of them. The hydrogen is oxidized at the anode, releasing electrons, while at the cathode it the oxygen reduction takes place. The protons formed at the anode

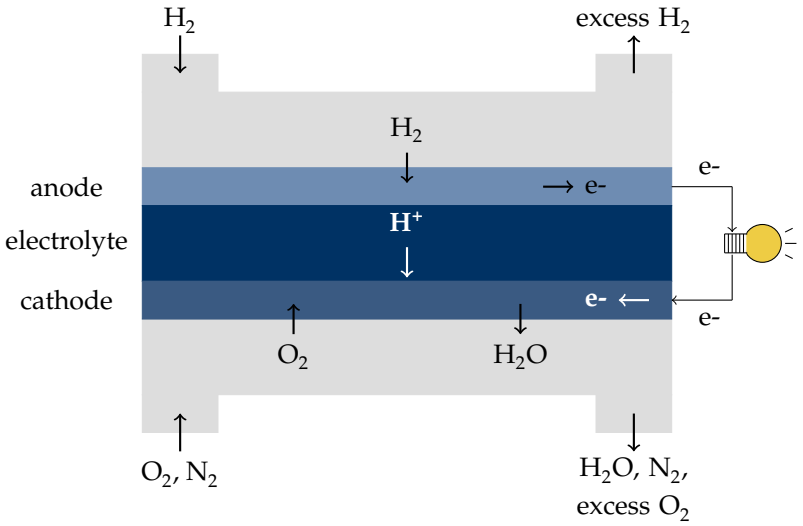

Figure 2.1 – Structure and species transport of a proton exchange membrane fuel cell (PEMFC), based on [1].

are transported through the electrolyte, which is impermeable to electrons. Consequently, electrons are forced to flow through an external circuit, resulting in the production of electricity.

$$H_2 + 0.5O_2 \rightarrow H_2O + P_{th} + P_{el} \tag{2.1}$$

The electrochemical half-reactions, which take place at the interface between the electrolyte and the electrodes, are different for each type of fuel cell. In case of a PEM fuel cell, the anode reaction is described by Eq. 2.2 and the cathode reaction by Eq. 2.3. PEM fuel cells are characterized by using H^+ as charge carrier and by the water production at the cathode.

$$H_2 \rightarrow 2H^+ + 2e^- \tag{2.2}$$

$$0.5O_2 + 2H^+ + 2e^- \rightarrow H_2O \tag{2.3}$$

The voltage generated by a single fuel cell is too low for most applications (below 1 V) [29]. For this reason, several cells are connected in series to each other forming stacks, which are then integrated in a system for stationary or mobile applications.

Fuel cells are similar to batteries, because both are electrochemical devices used for the direct generation of electricity. However, there is a significant difference between them: while the fuel cells function is exclusively the conversion of energy, by consuming the reactants which are continuously provided, batteries are used for the storage and the conversion of the reactants. This is the reason why the latter are consumed during the electricity production. On the contrary, fuel cells operate as long as they are fed with fuel and oxidant.

2.1.2 Fuel cell types and SOFC features

There are different types of fuel cell technology. Although all of them operate under the same physical principle, the use of different electrolytes results in different electrochemical reactions and technical characteristics. The main fuel cell types are the solid oxide fuel cells (SOFC), polymer electrolyte membrane fuel cells (PEMFC), alkaline fuel cells (AFC), phosphoric acid fuel cells (PAFC) and molten carbonate fuel cells (MCFC). In Tab. 2.1 the main characteristics of the different fuel cell technologies are presented, which lead to different advantages and disadvantages. This work is focused on SOFC, consequently only this type of fuel cell is described in detail. However, many of the referred concepts can be extended to the other technologies.

SOFC's use a ceramic electrolyte, usually yttria-stabilized zirconia (YSZ), which becomes O^{2-}-conducting at the SOFC operating temperatures. A material which is often used for the cathode is strontium-doped lanthanum manganite (LSM) with the anode formed by a mixture of nickel and YSZ, in both cases porous materials. The fact that all components are formed by solid materials results in a simpler structure and design [112].

The typical operation temperatures of SOFCs are between 600 °C and 1000 °C [29]. The main consequences are high efficiencies and tolerance against impurities compared with the other types of fuel cells. Furthermore, high temperatures lead to fast kinetics, which makes it possible the operation with non-noble catalysts, for instance nickel [121]. In addition, the alkanes can be internally reformed and the fuel cell provides highly valuable heat waste. However, high temperatures have disadvantages as well. These severe operating conditions are challenging for the materials and are the reason of several interconnect and sealing issues. Additionally, long start-up and shut-down procedures are required.

Due to these characteristics, SOFCs are mainly used for stationary applications (co-generation of heat and power at residential and non-residential buildings), for APUs (auxiliary power units) and for large transport (for instance large ships).

Solid oxide fuel cells can be encountered in different designs. The most important are the tubular and the planar SOFC. In the first case, the anode, electrolyte and cathode are build in concentric cylinders. Usually the cathode is to be found at the inner side, being thicker than the other layers in order to support the fuel cell mechanically [112]. This design has the advantage of simple sealing, but a high electrical resistance [139]. Planar SOFC are built from thin plates, similarly to the other fuel cells, for example the PEMFC presented in Fig. 2.1. In order to provide structural support, one of the layers is significantly thicker than the others, resulting in electrolyte-supported, cathode-supported or anode-supported fuel cells. Planar fuel cells have the advantage of a simpler design, achieving therefore lower investment costs.

Table 2.1 – Comparison between the main fuel cell technologies.

techno-logy	*electrolyte*	*operating temperature* [29]	*catalyst*	*charge carrier*	*electrical efficiency* [121]	*fuel*	*effect of CO presence*
SOFC	ceramic	600-1000 °C	non-noble metal	O^{2-}	50-60 %	H_2, CO, CH_4	fuel
PEMFC	polymeric membrane	80 °C	noble metal	H^+	40-50 %	H_2, methanol	poison
AFC	alkaline water solution	60-90 °C	non-noble metal	OH^-	50 %	H_2	poison
PAFC	liquid phosphoric acid	200 °C	non-noble metal	H^+	40 %	H_2	poison
MCFC	liquid molten carbonate salt	650 °C	non-noble metal	CO_3^{2-}	45-55 %	H_2, CO, CH_4	fuel

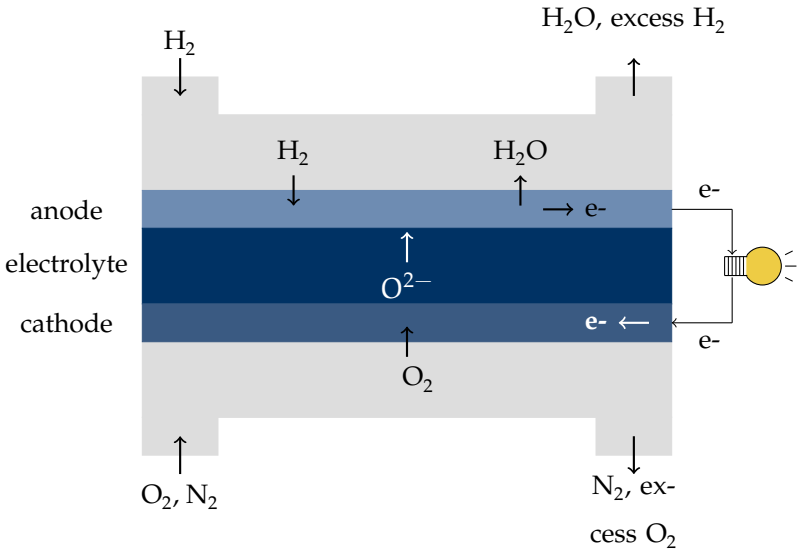

Figure 2.2 – Structure and species transport of a solid oxide fuel cell (SOFC) operating with hydrogen, based on [1].

2.1.3 Fuel cells operation and performance applied to a SOFC

In this section the operation and performance principles of a fuel cell is explained, by using as example a SOFC. Fig. 2.2 presents the structure of a SOFC operating with hydrogen and air and the species transport which take place during its operation.

The electrochemical half-reactions are described by Eq. 2.4 and 2.5. The oxygen is reduced at the cathode, acquiring two electrons. As explained in the previous section, in case of SOFC the charge carrier are the oxygen ions. They migrate through the electrolyte to the electrolyte-anode interface, where they react with the hydrogen molecules into water. In this process two electrons are released, which flow through the external circuit to the cathode, generating electricity.

$$0.5O_2 + 2e^- \rightarrow O^{2-} \tag{2.4}$$

$$H_2 + O^{2-} \rightarrow H_2O + 2e^- \tag{2.5}$$

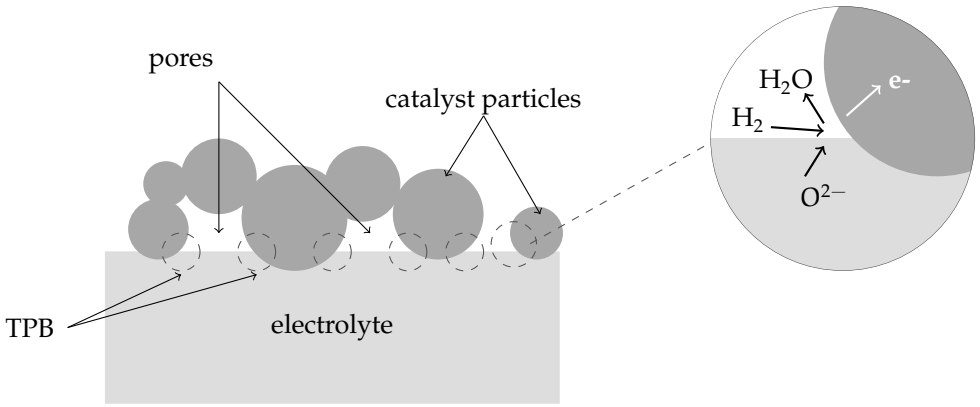

Figure 2.3 – Triple Phase Boundary, the area where the pores, electrolyte and catalyst particles converge (based on [52] and [121]).

The hydrogen oxidation implies three processes. First, the reactant molecules have to physically coincide simultaneously at the same site, the hydrogen diffusing through the anode bulk through the pores and the oxygen ions from the cathode through the electrolyte. Then, the reaction is activated by the catalyst (nickel). Finally, the created water molecule diffuses to the anode bulk and the released electrons flow through the nickel to the interconnect. Thus, the reaction can only take place if the pores, the electrolyte and the catalytic particles of the electrode are present at the same location. The area which fulfills this condition, shown in Fig. 2.3, is named the triple phase boundary or TPB [52]. The TPB is also necessary at the cathode-electrolyte interface so that the reduction of the oxygen can occur.

Since the electrochemical reactions involve released or consumed electrons, their reaction rate is related to the generated current. By applying Faraday's law, the reaction rate of the electrochemical reactions for a single fuel cell (ξ_{elech}) can be calculated by using Eq. 2.6.

$$\xi_{elech} = \frac{I}{n_{e^-} F} \tag{2.6}$$

n_{e^-} is the number of transferred electrons per mole of combustible (equal to 2 if re-

ferred to Eq. 2.4 and Eq. 2.5), I the produced current and F Faraday's constant.

The current generation of a fuel cell occurs, as seen previously, at the surface electrode-electrolyte. That is the reason why, in relation to fuel cells, it is more usual to talk about current per surface unit, named current density (j) and defined by Eq. 2.7. Additionally, it makes it possible to compare fuel cells of different sizes.

$$j = \frac{I}{A_{act}} \tag{2.7}$$

Together with the current density, the performance of a fuel cell is defined by the voltage between the cathode and the anode. Both properties are related by the polarization curve, which defines its electrochemical behavior. In the next paragraphs this topic is analyzed in detail.

The maximal electrical work achieved by a system is the electrical work produced under reversible conditions, that is to say, without generating losses. If it takes place under constant temperature and pressure, the maximal electrical work per mole of reactant is defined by the negative difference of the Gibb's free energy for the process (Eq. 2.8) [106]. The electrical work generated by the fuel cell can be defined as the work produced by moving the charge carried by the electrons through the cell potential U_{cell} (Eq. 2.9). By combining both definitions, the reversible cell potential under standard conditions, $U_{OC}^{r,0}$, can be defined (Eq. 2.10) [145].

$$w_{el} = -\Delta g^0 \tag{2.8}$$

$$w_{el} = U_{cell} n_{e^-} F \tag{2.9}$$

$$U_{OC}^{r,0} = -\frac{\Delta g^0}{n_{e^-} F} \tag{2.10}$$

$U_{OC}^{r,0}$ is also known as the reversible open circuit voltage, and it is the voltage difference when no current flows between both electrodes. It can be calculated as the difference between the standard potential of the cathode reaction (reduction) and of the anode reaction (oxidation) by Eq. 2.11 [105].

$$U_{cell}^{r,0} = U^{0,cath} - U^{0,an} \tag{2.11}$$

The U^0 values of the most common electrochemical half-reactions are tabulated, and can be found for example in [65]. However, these values are only valid for standard conditions and operating exclusively with pure components, in case of fuel cells H_2 at the anode side and O_2 at the cathode side. Variations in the operation conditions affect the reversible voltage in a different manner. For example, the higher the temperature the lower the voltage $U_{cell}^{r,0}$. In case of a H_2-O_2 fuel cell, the reversible voltage decreases 23 mV every 100 K temperature increase, which means a diminution of 166 mV in operations at 750 °C. On the contrary, the change in pressure has a minimal effect [121].

The free Gibb's energy change for the reduction-oxidation reaction defined by Eq. 2.12 (if two reactants and two products are involved, at any temperature and concentration), can be related to the standard Gibb's free energy by applying Eq. 2.13.

$$\text{(oxidation) } aA + bB \rightleftharpoons cC + dD \text{ (reduction)} \tag{2.12}$$

$$\Delta g = \Delta g^0 + RT \ln\left(\frac{a_C^c a_D^d}{a_A^a a_B^b}\right) \tag{2.13}$$

a_j is the activity of the species j, which under the assumption of ideal gases, valid in most SOFC systems, depends on the partial pressure of the species j (p_j) and the standard pressure P^0. It is defined by Eq. 2.14 [106].

$$a_j = \frac{p_j}{p^0} \tag{2.14}$$

By applying Eq. 2.10 for Δg and Δg^0 and replacing them at Eq. 2.13 the reversible voltage of a fuel for each temperature, pressure and concentration can be calculated. This equation is named the Nernst Equation, which for a SOFC operated with hydrogen is expressed by Eq. 2.15 [105].

$$U_{OC}^r = U_{Nernst} = U_{OC}^{r,0} - \frac{RT}{n_{e^-}F} \ln \left(\frac{\frac{p_{H_2O}}{p^0}}{\frac{p_{H_2}}{p^0} \left(\frac{p_{O_2}}{p^0} \right)^{1/2}} \right) \tag{2.15}$$

The actual cell voltage is always lower than the reversible voltage calculated by Eq. 2.15. Fig. 2.4 presents a typical polarization curve for a fuel cell compared to the reversible potential. It can be observed that the actual open circuit potential (U_{OC}) is lower than the theoretical, which is equal to U_{OC}^r. The reason is that under open circuit conditions it actually takes place a current exchange, caused by the internal currents and the species crossing through the electrolyte, since in reality is not completely impermeable against electrons [106]. Additionally, three different types of losses or overpotentials appear: the activation polarization (ϑ_{act}), the ohmic polarization (ϑ_{ohm}) and the concentration polarization (ϑ_{conc}). The fuel cell voltage $U_{cell} = f(j)$ can be calculated by subtracting the different voltage drops from the reversible voltage U_{OC}^r (Eq. 2.16).

$$U_{cell} = U_{OC}^r - \vartheta_{act} - \vartheta_{ohm} - \vartheta_{conc} \tag{2.16}$$

The activation losses are explained by the fact that the electrochemical half-reactions need to overcome an energy barrier, named activation energy, to actually occur. In particular, as long as the rate-limiting step (the elementary reaction with the lowest reaction rate) does not start, the electrode reaction cannot take place.

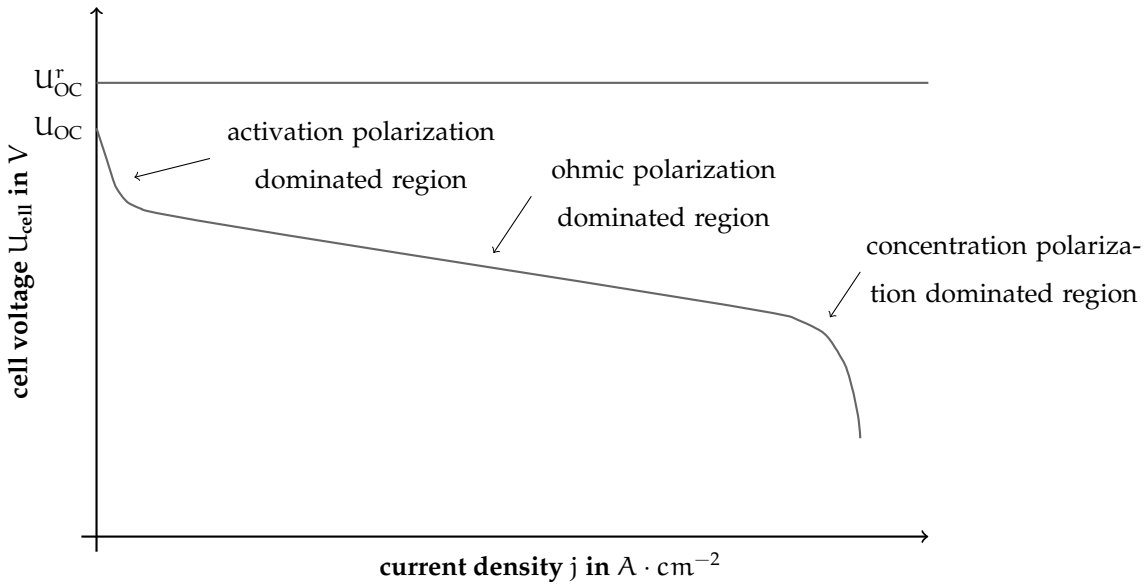

Figure 2.4 – Reversible cell voltage and typical cell voltage depending on the current density (based on [112] and [145]).

The reactions at one electrode can be generally described by Eq. 2.17, being Red and Ox the reducing and oxidant species respectively.

$$Red \rightleftharpoons Ox + n_{e^-} e^- \tag{2.17}$$

The elementary reaction happens in both directions at the same time, that is to say, that the reduction and the oxidation take place simultaneously at the electrode surface. In order to prevent from the confusion with the oxidation and reduction associated to the global electrochemical reaction in the fuel cell, they are named forward (Eq. 2.18) and reverse reaction (Eq. 2.19) [112].

$$Red \rightarrow Ox + n_{e^-} e^- \text{ , forward reaction} \tag{2.18}$$

$$Ox + n_{e^-} e^- \rightarrow Red, \text{ reverse reaction} \tag{2.19}$$

There is a current density associated to each reaction, j_{for} and j_{rev}, which depends on the energy barrier of each one. The energy level of the products state is lower than the reactants state. Thus, in principle the energy barrier in the reverse reaction is higher than in the forward reaction, and consequently the current flowing in the forward direction is higher. This causes a difference between the two current densities, which results in the net current density, defined by

$$j = j_{for} - j_{rev} \tag{2.20}$$

This difference of current densities is accompanied by a potential difference at the electrode-electrolyte interface, which is larger for higher current densities. At some point this potential rises enough to compensate the difference between the energy barriers for the forward and reverse reactions. It results in the achievement of the equilibrium state. At equilibrium, j_{for} and j_{rev} have the same value, which is named exchange current density (j_0). Thus, although there is a current exchanged in both directions, no net current is produced.

The way to change this undesired situation is to variate the electrical potential, which represents a change in the energy distribution of the system. The voltage drop (ϑ_{act}) results in a variation of the energy barriers of the forward and reverse reaction, so that the forward reaction is favored and a global current is produced. Thus, the current densities associated to each reaction can be written as function of the exchange current density and the applied potential as shown below in Eq. 2.21 and Eq. 2.22 [121].

$$j_{for} = j_0 exp\left(\frac{\alpha_1 F \vartheta_{act}}{RT}\right) \tag{2.21}$$

$$j_{rev} = j_0 exp\left(\frac{-\alpha_2 F \vartheta_{act}}{RT}\right) \tag{2.22}$$

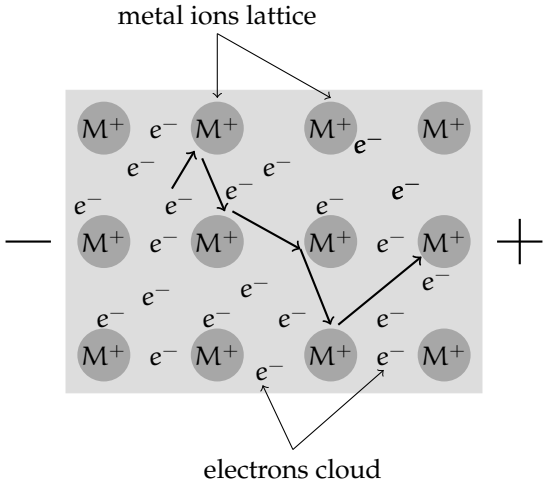

Figure 2.5 – Electrons transport through a metallic conductor (based on [121]).

α_1 and α_2 are the charge transfer coefficients, which indicate the influence of the overpotential to the energy activation barriers of the forward and reverse reactions respectively. By replacing Eq. 2.21 and 2.22 in Eq. 2.20 the Butler-Volmer equation (Eq. 2.23) is obtained [121]. It relates the current generated in an electrochemical reaction with the activation overpotential.

$$j = j_0 \left(exp\left(\frac{\alpha_1 F \vartheta_{act}}{RT}\right) - exp\left(\frac{-\alpha_2 F \vartheta_{act}}{RT}\right)\right) \tag{2.23}$$

Butler-Volmer equation is valid for both anode and cathode. This shows that the higher the produced current density, the more voltage has to be lost to overcome the activation energy barrier so that the cell voltage becomes lower.

The ohmic overpotential results from the losses caused by the charge transport through the different components of the fuel cell. It includes the resistance of the electrolyte to the ions flow (R_{ionic}), the resistance of the electrodes and the interconnect to the electrons transport ($R_{electronic}$) and the resistance caused by the contact layers (R_{cont}).

The electrical conductivity depends on the type of charge, the amount of charge carriers and on the mobility of these carriers in the conductor. The conduction mechanisms of the electrons and of the ions are utterly different. Metallic materials are

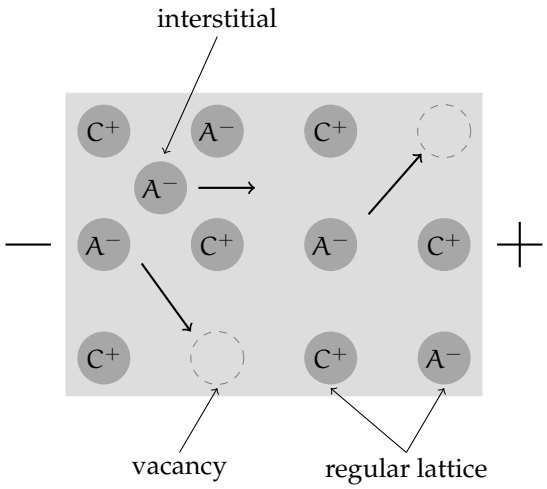

Figure 2.6 – Ions transport through a solid electrolyte (based on [121]).

constituted by positively charged metal ions surrounded by a cloud of delocalized electrons. The electrons are free to move and if an electric field is applied their transport takes place easily through the metallic conductor (Fig. 2.5). The transport of ions through a solid electrolyte does only take place as a result of the defects of crystal structure, such as vacancies (atoms which are missing in a lattice position) or interstitial (atoms which occupy a site in the lattice where they should not normally be present, Fig. 2.6). The ions flow is created by the displacement of these defects through the material, which happens significantly slower that the transport of electrons through the metal. The consequence is that the electrolyte is the component with the highest electrical resistivity.

The charge carriers have not only to be transported through a component, but also from a component to the other. For example, the oxygen ions are produced at the interface between the cathode and the electrolyte, and have to reach the electrolyte in order to migrate to the anode. The contact between two layers takes place usually in a small area, which results in resistance to the ions and electrons transport. This resistance is named contact resistance (R_{cont}). Furthermore, during the fuel cell operation resistive layers can be formed between the electrodes and the electrolyte by side oxidation mechanisms, specially at the cathode side, which causes an additional

contact resistance [104].

The voltage drop caused by the ohmic resistances, ϑ_{ohm}, is calculated by applying Ohm's law expressed in terms of current density:

$$\vartheta_{ohm} = jA_{act}\left(R_{ionic} + R_{electronic} + R_{cont}\right) \tag{2.24}$$

The resistance of each layer depends on its material and geometrical characteristics. In the case of planar fuel cells it is calculated by applying Eq. 2.25. A_{cross} is the external surface of the layer, perpendicular to the charge flow, l_{cond} the length of the charges path through the layer and σ the electrical conductivity of the material, which can be approximated by the thickness of the layer.

$$R = \frac{l_{cond}}{\sigma A_{cross}} \tag{2.25}$$

The concentration losses, ϑ_{conc} are consequence of the mass transport of the species from the bulk to the triple phase boundary, where the electrochemical half-reactions actually take place. The reactions result in the consumption of reactants and formation of the products, which are provided/delivered to the electrode-electrolyte contact surface by diffusion through the porous electrodes. Consequently, a concentration gradient appears between the flows at the bulk and the electrode-electrolyte interfaces. Thus, the concentration of the species at the TPB is lower than at the fuel/oxidant bulks (Fig.2.7), which results in a lower voltage compared to the reversible voltage, given by Eq. 2.15.

The concentration losses increase with stronger concentration gradients between the TPB and the bulk, which are proportional to the current production. The volume concentration of the species j at the TPB ($c_{j,TPB}$) can be calculated depending on the electrode thickness ($\delta^{an/cath}$) and on the diffusion coefficient (D) by applying Eq. 2.26 [121].

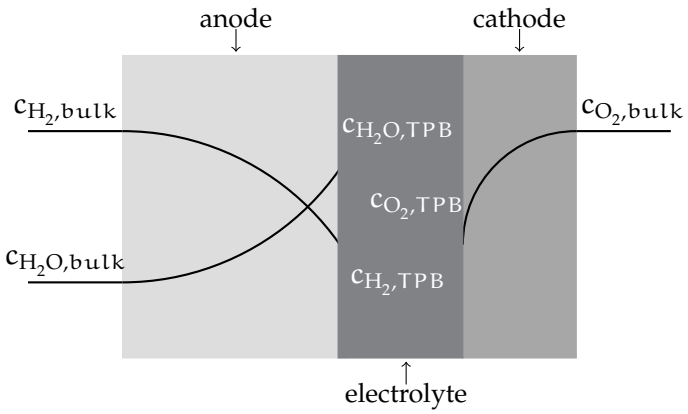

Figure 2.7 – Concentration gradients in an anode-supported fuel cell (based on [102]).

$$c_{j,TPB} = c_{j,bulk} - \frac{j\delta^{an/cath}}{n_{e^-}FD} \tag{2.26}$$

The concentration overpotential resulting from the sluggish diffusion of the species through the electrodes ($\vartheta_{conc}^{an/cath}$) can then be calculated as the difference between the reversible potential calculated with the concentrations at the bulk and the one calculated with the concentration at the TPB [121]:

$$\vartheta_{conc}^{an/cath} = U_{OC}^{r}(x_{j,bulk}) - U_{OC}^{r}(x_{j,TPB}) \tag{2.27}$$

Two diffusion mechanisms are involved in the species transport through the porous electrodes: the binary diffusion and the Knudsen diffusion. The binary diffusion predominates when the pore diameter is large compared to the diffusion path of the molecules. In this case, the molecules trend to collide to each other more often than against the pores walls. On the contrary, if the pores are smaller, the collisions are mainly between molecules and the porewalls and the dominating mechanism is the Knudsen diffusion. In case of fuel cells, both types of diffusion can take place [114].

If the concentration of a reactant at the TPB is zero, the electrochemical reaction cannot occur. It happens when the current increases up to the so called limiting current

density (j_{lim}), which can be calculated by imposing the condition of $x_{j,TPB} = 0$ in Eq. 2.26:

$$j_{lim} = x_{j,bulk} \frac{n_{e^-} F D}{\delta^{an/cath} RT} \tag{2.28}$$

The result is a voltage drop and a situation of a fuel starvation, which causes the fuel cell degradation.

A characteristic of SOFCs is that they cannot only operate with hydrogen, but carbon monoxide and methane can be used as fuels too. In case of CO, it can be directly oxidized at the anode by the electrochemical half-reaction given by Eq. 2.29. In this case, the cathode reaction is the same as in the SOFC operating with H_2 (Eq. 2.4), so that the global fuel cell reaction is expressed by Eq. 2.30.

$$CO + O^{2-} \rightarrow CO_2 + 2e^- \tag{2.29}$$

$$CO + 0.5O_2 \rightarrow CO_2 \tag{2.30}$$

The electrochemical behavior described for the operation with hydrogen can be extrapolated to the operation with carbon monoxide. Methane can also be directly oxidized. In this case the products of the methane oxidation can be H_2, H_2O and CO (Eq. 2.31 and Eq. 2.32). H_2 and CO can be further reused as fuel [140]. In both cases the oxygen reduction is the same as in the operation with H_2.

$$CH_4 + O^{2-} \rightarrow CO + 2H_2 + 2e^- \tag{2.31}$$

$$CH_4 + 4O^{2-} \rightarrow CO_2 + 2H_2O + 8e^- \tag{2.32}$$

The disadvantages of these reactions is that they may allow carbon deposition by hydrocarbon pyrolysis (Eq. 2.33).

$$CH_4 \rightarrow C + 2H_2 \tag{2.33}$$

Carbon deposition deactivates the nickel catalyst, causing the degradation of the fuel cell. Thus, the SOFC is operated by mixing the hydrocarbons with steam, which prevents the pyrolysis. However, under those conditions the direct oxidation is not favored. Therefore, instead of the direct use by oxidation, the methane is normally used in the SOFC after being reformed to hydrogen and carbon monoxide. All types of fuel cells can operate with hydrogen resulting from the reformate of hydrocarbons in an external processor (in PEMFC, AFC and PAFC fuel cells after removing the CO in order to prevent the fuel cell gifting by this chemical specie). The advantage of SOFCs is that this process can take place directly at the anode bulk, which simplifies the system design and cost. Furthermore, contrary to other fuel cell types, the CO does not have to be removed since it can be used as fuel. Additionally, the hydrogen is better distributed along the cell and the achieved methane conversion rate is high, since this chemical reaction is favored by the high temperatures present in SOFCs [145]. The process is carried out by steam reforming described by Eq. 2.34 to Eq. 2.36. Under suitable composition and temperature conditions, the water to gas shift reaction (WGS) also occurs as well (Eq. 2.37).

$$CH_4 + H_2O \rightleftharpoons CO + 3H_2 \tag{2.34}$$

$$CH_4 + 2H_2O \rightleftharpoons CO_2 + 4H_2 \tag{2.35}$$

$$C_nH_{2n+2} + nH_2O \rightleftharpoons nCO + (2n+1)\,H_2 \tag{2.36}$$

$$CO + H_2O \rightleftharpoons CO_2 + H_2 \tag{2.37}$$

Steam reforming of hydrocarbons represent endothermic reactions. If they take place in the fuel cell, the necessary heat is provided by the exothermic electrochemical reaction, resulting in high global efficiencies [139]. The water needed for the reactions can be either externally provided or obtained by recycling the anode flue gas, which contains the water obtained as product of the electrochemical reaction. This latter design investigated in the group by Carré [52] will be explained in detail in the next sections.

The catalyst needed in order to carry on the involved reactions can be provided externally (indirect internal reforming) or the nickel present at the fuel cell anode can be used (direct internal reforming). The advantages of the direct internal reforming compared to the indirect are a simpler system design and higher efficiencies. The drawbacks of the direct reforming are higher temperature differences along the fuel cell and the fact that the nickel activates the decomposition of the long hydrocarbons (Eq. 2.50), both effects resulting in the stack degradation [140].

2.2 SOFC for combined heat and power applications

This section is devoted to the SOFC applied to Combined Heat and Power Systems (CHP). Firstly, the interest of CHP for the energy production is shown. Then, the different technologies for CHP are compared to the SOFC. Finally, the characteristics of a SOFC for CHP applications are described, focusing on the different components constituting the system.

2.2.1 Combined heat and power systems or CHP

Combined heat and power (CHP), also named co-generation of heat and power, is the decentralized, simultaneous production of thermal and electrical energy. The energy conversion takes place next to the consumption area. Therefore, not only the electricity, but also the heat can be used, for example for room and water heating at residential and commercial buildings or at industrial processes involving heat. The produced electrical energy can be either self-consumed or fed to the grid.

Three efficiencies can be defined in relation to CHP systems: electrical, thermal and global efficiency (Eq. 2.38 to Eq. 2.40) [145]. The electrical efficiency relates the produced electricity to the consumed fuel power, while the thermal efficiency is the ratio of the useful heat production to the consumed power. The global efficiency is the sum of the thermal and electrical efficiencies, and accounts for the total useful energy in comparison to the consumed. When referring to a fuel, the efficiencies can be related to the higher or to the lower heating value (HHV and LHV respectively), in this case the definition respect to the HHV has been chosen. The difference between them is that the HHV includes the heat of vaporization of the water contained in the combustion products, while LHV does not. The definition of both physical properties is explained in detail in latter chapters.

$$\eta_{th} = \frac{\dot{Q}}{HHV_{fuel}\dot{n}_{fuel}} \tag{2.38}$$

$$\eta_{el} = \frac{P_{el}}{HHV_{fuel}\dot{n}_{fuel}} \tag{2.39}$$

$$\eta_{tot} = \eta_{th} + \eta_{el} \tag{2.40}$$

The conventional energy production model is based on independent production of heat and power. The needed heat is usually produced at the consumption point by using a gas boiler, with efficiencies attaining values up to 98 % in case of condensing gas boilers [23]. On the other side, the power is mainly generated in a centralized power plants and then transported to the end consumer. At the moment, the efficiency of the common power plants in Germany is of 43-45 % (expected to increase to 50 % until 2020 [138]), being the major losses in form of thermal energy. Additionally, the transport losses have to be accounted, which represents a 9.6 % in Germany [125]. Thus, although the heat production reaches a high efficiency, the power generation implies about 60 % of losses.

In comparison, CHP systems use the energy more efficiently, as a consequence of the short distance between the production and the consumption point. Firstly, the heat generated during the process is not waste, but useful energy. Additionally, the electricity transport costs become negligible. Consequently, the primary energy consumption and the CO_2 emissions are reduced. For example, at the report *Neue Kraftwerke mit fossilen Brennstoffen* published by *Verein Deutscher Ingenieure (VDI)* it is shown that a CHP system with $\eta_{el} = 30\,\%$ and $\eta_{th} = 68\,\%$ results in a decrease in the primary energy consumption of 24.6 % and in the CO_2 emissions of 23.3 % [37].

The environmental impact of the energy production has become a central topic for the governments of most countries. For instance, the European Union has set a target for the reduction of the CO_2 emissions of 80-95 % by 2050 (in comparison to 1990) and for the reduction of the primary energy consumption of 20 % by 2020 (compared to projection of 2007) [21]. Additionally, higher efficiency results in lower dependence from external countries for the energy supply.

From the point of view of the end user, the decentralized energy production has the advantage of a higher independence from the grid (which ensures access to the electricity even in case of grid blackout) and a reduction of the costs in the energy production.

Consequently, the different governments implemented several laws in order to promote the CHP. For instance, the European Union recommends to its Member States to promote the installation of decentralized cogeneration systems [21] since the "promotion of high-efficiency cogeneration based on a useful heat demand is a Community priority given the potential benefits of cogeneration with regard to saving primary energy, avoiding network losses and reducing emissions, in particular of greenhouse gases. In addition, efficient use of energy by cogeneration can also contribute positively to the security of energy supply and to the competitive situation of the European Union and its Member States" [4].

Following these recommendations, the government of Germany fixed the targets until 2020 of reducing the greenhouse emissions of 40 % in comparison to the levels of 1990 and of decreasing the primary energy and electricity consumption 20 % and 10 % respectively compared to the values of 2008 [26]. One of the measures to reach the objectives, is the target of increasing the electricity production by CHP to 25 % of the total until 2020 [26]. In order to promote private investments in CHP, the Germany Government supports financially new CHP systems which accomplish defined characteristics [26]. For all these reasons combined heat and power systems have become an interesting topic for public and private researchers, who have been developing various technologies allowing its implementation. They are discussed and compared in the next section.

2.2.2 Fuel cells compared to other CHP technologies

There are different technologies competing against fuel cells for combined heat and power applications. The most important ones are listed below.

- **Combustion engines**: based on conventional Diesel and Otto engines. The chemical energy of the fuel is transformed into mechanical energy, used to drive a generator producing electricity. They are run mostly in lean operation to

achieve lower emissions, which is the most important challenge for this technology. Other disadvantages are the need of continuous cooling, high maintenance costs and noise levels. However, they are an extended technology due to their high reliability, fast start-up and relative low investment costs.

- **Steam turbines**: the thermodynamical process under which steam turbines operate is the Rankine cycle. The heat source, result of the combustion of any type of fuel, provides thermal energy to produce high pressure steam. The expansion of the steam in successive steam turbines produces electricity. They are characterized by a long start-up process and low electrical efficiency, but at the same time by a long life-time and high reliability.

- **Gas turbines**: they operate following the Brayton cycle. The atmospheric air is compressed by a turbo compressor and mixed with the fuel in the combustion camber. The temperature is increased by combustion of the fuels. Then, the gas is fed to the expansion turbine, which drives a turbo compressor producing electricity. The gas turbines are high reliable devices, which can operate without cooling and, due to the low amount of moving parts, do not require frequent maintenance. On the other side, they are only available in large power ranges (from 500kW) and are not efficient at partial load.

- **Microturbines**: they are smaller versions of gas turbines. Thus, they have most of their characteristics. However, microturbines require higher investments and maintenance costs together with a fuel cleanup in order to work efficiently. The advantages on gas turbines result from the smaller power range: they operate with a better performance in part load and have a small size and weight, and can be used for small/middle size applications.

The typical cost and performance characteristics from these technologies compared with the fuel cells (including SOFC and MCFC) are presented in Tab. 2.2.

The main advantage of the fuel cells with respect to the other technologies is their high electrical efficiency. The main reason is that, as explained in the last section, the conversion of chemical and energy to electricity takes place in a single step. On the contrary, all the other processes consist in successive steps, including a combustion reaction, one or more thermodynamical transformations which result in mechanical energy, transformed finally into electricity. Each energy transformation is accompanied by process losses. In consequence, the less steps involved in the process, the higher is the potential of achieving high global efficiencies. Furthermore, all thermodynamical cycles have a maximal efficiency, resulting from the Second Law of Thermodynamics. It is called the Carnot efficiency, and depends on the high and low temperature levels between which the device operates, T_h and T_l respectively (Eq. 2.41). Since the fuel cell generates power by electrochemical conversion, the electrical efficiency does not have this limitation.

$$\eta_{\text{Carnot}} = 1 - \frac{T_l}{T_h} \tag{2.41}$$

Another difference between of fuel cells from other technologies for energy conversion is that, since the system contains few moving parts, the noise level is very low. Furthermore, it results into low maintenance requirements. Regarding the emissions, the levels achieved by fuel cell systems are negligible in comparison to the other technologies. Additionally, the size of the fuel cells make them suitable for many different applications, from residential to power plants. Moreover, the fuel flexibility of SOFC's allows their use under several different conditions.

The main disadvantages of solid oxide fuel cells are still the high investment costs together with the limited lifetime. Additionally, they require long start-up processes and limited number of cycles, which results in a need of almost non-stop operation.

Table 2.2 – Comparison between the main CHP technologies [6, 9]. The efficiencies are based on the LHV of the used fuels.

technology	η_{el} *in* %	η_{th} *in* %	*noise level*	*emissions (CO, NOx)*	*power range in* kW_{el}	*investment costs*	*maintenance costs*	*partial load performance*
fuel cell	30 - 63	25 - 50	low	very low	0.3 - 2000	high	low	high
combustion engine	22 - 40	30 - 58	high	high	100 - 3300	low	high	medium
steam turbine	15 - 38	42 - 65	high	high	50 - 250000	low	very low	medium
gas turbine	22 - 36	34 - 63	medium	low	500 - 250000	low	low	low
microturbine	18 - 27	38 - 57	medium	low	30 - 250	medium	high	medium

2.2.3 Subsystems and components of a SOFC system for CHP applications

Together with the SOFC stack, other components are needed to complete the SOFC system for CHP applications, which together represent the so-called the Balance of Plant (BoP). The subsystems forming it are the following:

- **Fuel processing subsystem**: although SOFC can operate with several fuel types, when used for CHP applications they normally use natural gas. The gas needs to be compressed, cleaned up from the components damaging the stack and reformed to H_2 and CO. These processes take place in the fuel processing subsystem, which is not always included in the BoP. The different possibilities to apply the reforming are described later.

- **Air management subsystem**: the oxidant consumed at the cathode side is usually the oxygen contained in atmospheric air. Before entering the system, the particles contained in the air have to be removed and its pressure increased.

- **Thermal management subsystem**: in order to achieve the required temperature levels for each process at the system the heat produced at the exothermic reactions is transferred to the gases which need to work at higher temperatures. This function corresponds to the heat exchangers, which have to be accurately dimensioned and installed at the optimal position in the overall process. The unused fuel at the stack reacts in a burner with air in a combustion reaction, so that thermal energy is produced which, together with the heat produced in the stack, is used for the system heat up and for heat recovering.

- **Power conditioning subsystem**: the power produced by the fuel cell is DC power. In case of current controlled subsystems, which are the most common configuration, the current is transferred to the system as a set point and the cell voltage varies depending on the cell performance, resulting in a variable voltage

outlet. In order to obtain the useful power, the voltage should be constant and, depending on the targeted application, alternating current is required. This is the reason why the power conditioning subsystem is implemented. It consists in a voltage regulator (used to stabilize the voltage) and an inverter (to convert the DC power into AC). In order to connect both components, the use of a DC-DC boost converter is often necessary, so that the voltage is adjusted to the level of the AC converter inlet [145].

Some of the named subsystems can be integrated with each other in multi-functional components in order to optimize the system, regarding efficiency and/or size. For instance, it is usual that the operations of thermal management and of fuel/air processing are carried out in an integrated component.

The natural gas reforming is one of the critical functions in a SOFC system. There are three main catalytic reforming technologies which are currently implemented: catalytic partial oxidation (CPOX, Eq. 2.42), steam reforming (SR, Eq. 2.43) and oxidative steam reforming (OSR, Eq. 2.44). The different processes are briefly described in the next paragraphs, based on [139], where the reader can refer for deep knowledge on the topic.

$$C_nH_{2n+2} + 0.5nO_2 \rightleftharpoons nCO + (n+1)H_2 \tag{2.42}$$

$$C_nH_{2n+2} + nH_2O \rightleftharpoons nCO + (2n+1)H_2 \tag{2.43}$$

$$C_nH_{2n+2} + mH_2O + 2\,(n-m)\,O_2 \rightleftharpoons nCO + (n+m+1)\,H_2 \tag{2.44}$$

For partial oxidation reforming a mixture of hydrocarbons and oxygen are transformed into carbon monoxide and hydrogen in an exothermic reaction. It takes place

typically between 700 °C and 1000 °C [139], requiring noble metals or nickel as catalyst. The main advantages of this method are fast reaction kinetics and the possibility to operate without water. However, per each molecule of hydrocarbon less combustible molecules are formed than with steam reforming. For example, in CH_4 reforming three molecules are formed with catalytic partial oxidation ($1CO + 2H_2$) and four with steam reforming ($1CO + 3H_2$). Additionally, addition of oxygen to the fuel reduces the partial pressure of the hydrogen/carbon monoxide at the anode bulk, resulting in a lower Nernst potential [106]. Consequently, this method is usually applied when the simplicity is prioritized over the efficiency, for example in portable applications.

Steam reforming has already been described for SOFC (Sect. 2.1). The physical principle at the prereformer is exactly the same: hydrocarbons react with water forming carbon monoxide and hydrogen in an endothermic reaction. In comparison to CPOX, the steam reaction is an efficient process, but the need of steam increases the complexity of the system. Additionally, the start-up process is slower than for CPOX and it requires a higher thermal management effort.

Oxidative steam reforming (OSR) is a mixture of both methods described previously: both oxygen and steam are provided in order to transform the hydrocarbons into hydrogen and carbon monoxide. As it can be observed in Eq. 2.44 several stoichiometries are possible. Depending on the proportions of the reactants the alkanes react rather with oxygen or with steam, resulting consequently in an exothermic or an endothermic reaction. A special case of this process is the auto-thermal reforming, characterized by being isothermal. It is the consequence of a specific mixture of the reactants, which results in a compensation of the needed heat at the exothermic reactions by the heat produced by the endothermic. OSR combines the advantages and disadvantages of the both methods described previously. It has a fast start-up and a higher reformate rate than CPOX, but still lower than SR. The process needs steam feeding, resulting in a higher complexity than CPOX. However, the thermal management becomes more simple, due its auto-thermal characteristic.

Most SOFCs are designed so that the production of hydrogen and carbon monoxide takes mostly place in the stack, by internal reforming. Then, the described reforming processes occurs in a prereformer, in order to reform the long hydrocarbons to single-carbon molecules. They should not reach the stack because, at the usual operating temperature of SOFCs, nickel catalyst activates the carbon formation from long hydrocarbons [124]. Details about carbon formation are given in the next section.

The subsystems and specific components forming the SOFC system object of study are presented in Chap. 5.1.

2.3 Solid oxide fuel cell system with anode offgas recycle (AOR)

A usual configuration for SOFC systems is the design which incorporates an anode flue recycle loop, shown in Fig. 2.8. In this kind of system part of the anode flue, still containing unburned fuel, is mixed with the inlet natural gas and fed to the prereformer again. The first advantage caused by this configuration is the possibility of implementing hydrocarbon steam reforming (both at the prereformer and as internal reforming) without necessity of a water management system. The steam necessary for the process is produced by the electrochemical reaction in the stack and introduced to the fuel path through the recycled flue gas [79]. As detailed in the previous sections, steam reforming is the method with the highest conversion efficiency.

Additionally, the electrical efficiency of the system is increased. The reason is that, in order to avoid starvation, every stack has a limit for fuel utilization (explained in detail in the next sections). Thus, there is a part of the fuel which remains unused after the electrochemical reaction in the stack and can be only used as heat after its combustion at the afterburner. However, when the anode flue gas is reintroduced in the system inlet, part of this unburned fuel can be used at the stack again and

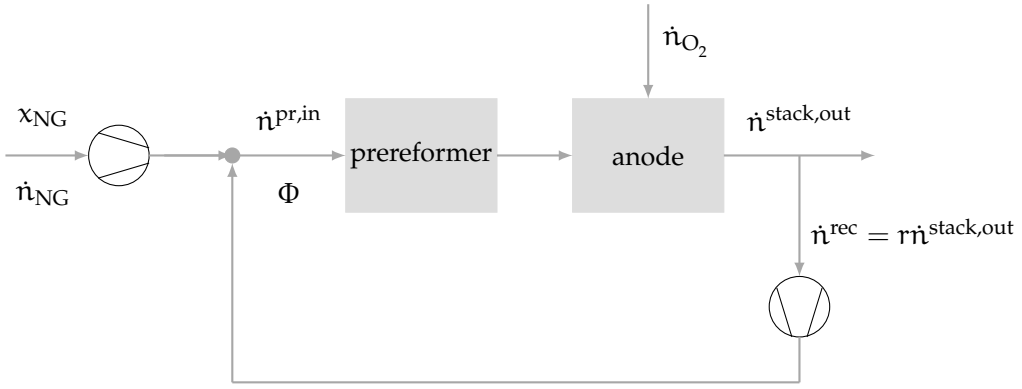

Figure 2.8 – Mass balance in the anode path for a fuel cell system with anode gas recycle.

converted into electrical energy. Carré [52] reported a 12 % increase of the electrical efficiency between a system with external water supply and a system with anode flue recycle. Peters et al. [127] calculated an electrical efficiency of 50 % for a system without anode recycle loop and of 66 % when it was incorporated.

A challenge for these systems is the physical implementation of the recycle loop, since the temperature and humidity conditions of the anode flue gas make it difficult to use a standard blower. Additionally, a sufficient amount of water has to be provided in order to avoid carbon formation [79]. The indicator used to evaluate if this condition is fulfilled is the oxygen to carbon ratio (Φ). This is one of the operating parameters related to a SOFC system with anode recycle path. Φ, together with the other operating parameters, is defined in detail in the next paragraphs.

The recycle rate (r) is defined as the percentage of the flue which is recycled. Its value has to be optimized depending on the operating point. Too low recycle rate can cause carbon deposition because of the lack of water and can decrease the system efficiency. On the other side, the higher the r value, the more diluted is the fuel at the stack inlet, the lower the Nernst voltage and consequently the lower cell voltage [57, 70].

$$r = \frac{\dot{n}^{rec}}{\dot{n}^{stack,out}} \tag{2.45}$$

The fuel utilization, FU, is defined as the ratio of consumed electrons over the potential amount of electrons provided by the fuel. The FU is the most important indicator for the efficiency of the system. It can be defined for the whole system or for the stack, as follows:

$$\mathrm{FU}^{\mathrm{sys}} = \frac{\dot{n}^{\mathrm{sys}}_{e^-,\mathrm{cons}}}{\dot{n}^{\mathrm{sys}}_{e^-,\mathrm{prov}}} \tag{2.46}$$

$$\mathrm{FU}^{\mathrm{stack}} = \frac{\dot{n}^{\mathrm{stack}}_{e^-,\mathrm{cons}}}{\dot{n}^{\mathrm{stack}}_{e^-,\mathrm{prov}}} \tag{2.47}$$

The stack fuel utilization has a maximal value, provided by the manufacturer, in this work 60 %. If this value is exceeded starvation condition can be attained, resulting in degradation of the stack. The main reason is the difference of fuel molecules concentration between the anode bulk and the TPB, where the reaction actually takes place, as explained in Sect. 2.1.3. This means that not all fuel molecules which enter the stack and are accounted for the potential electrons release, can actually be used in the electrochemical reaction. Thus, if the electrochemical reaction rate (directly proportional to the produced current) is too high for the supplied fuel amount, starvation situation is attained. The first consequence is a sharp voltage drop. Additionally, part of the oxygen ions cannot react with fuel molecules as usual, but they oxidize the anode causing permanent damage [73].

For conventional configurations, the system fuel utilization has the same value as the stack fuel utilization. However, if the anode recycle path is implemented, they vary from each other. Due to the reuse of part of the unburned fuel the system fuel utilization increases while the stack fuel utilization remains limited to its maximum value, achieving a higher efficiency without damaging the stack. Both operating parameters can be related by applying a mass balance in the recycle circuit. The resulting expression (Eq. 2.48) has been developed by Carré [52] depending on the recycle rate.

$$FU^{stack} = \frac{(1-r)FU^{sys}}{1-rFU^{sys}} \tag{2.48}$$

Another phenomenon which can cause the stack degradation, as well as the prereformer damage, is the carbon deposition. As previously explained, there are some undesired parallel reactions to the steam reforming which can result in carbon deposition. The most important are the hydrocarbon decomposition (Eq. 2.49 for methane and Eq. 2.50 for any alkane), the Boudouard reaction (Eq. 2.51) and the CO reduction reaction (Eq. 2.52) [139].

$$CH_4 \rightarrow C + 2H_2 \tag{2.49}$$

$$C_nH_{2n+2} \rightarrow nC + (n+1)H_2 \tag{2.50}$$

$$2CO \rightleftharpoons C + CO_2 \tag{2.51}$$

$$CO + H_2 \rightarrow C + H_2O \tag{2.52}$$

Mogensen et al. [117] reported several consequences of carbon deposition. On the one hand, it results on the reduction of the catalyst activity due to the covering of its surface. Additionally, the anode pores become blocked, which reduces the mobility of the reactants and products and increases the pressure. Finally, the structure of the catalyst can be destroyed.

The common method to avoid the carbon formation is to ensure that the anode bulk/ prereformer is fed with additional steam compared to the necessary for the reaction

[136]. This ensures that the hydrocarbons react with steam in the reforming reaction (Eq. 2.36) and the carbon monoxide in the water-gas-shift (Eq. 2.37) [106].

The oxygen to carbon ratio, Φ, is a parameter defined to quantify this additional steam amount depending on the hydrocarbons forming the fuel, defined by Eq. 2.53.

$$\Phi = \frac{\dot{n}_{O}}{\dot{n}_{C}} \tag{2.53}$$

Eguchi et al. presented in [68] different carbon deposition zones in C-H-O phase diagrams, depending on the temperature. For 400 °C the limit is equivalent to $\Phi = 2$. In this work it is assumed that it is the minimal value for Φ to avoid the carbon deposition.

In order to guarantee that carbon deposition does not occur, Φ should be evaluated at the inlet of each catalyst of the system, that is to say, at the inlet of the prereformer and of the stack anode. However, since between these points neither the carbon nor the oxygen content vary (there is not any flow entering or leaving the system), the evaluation in one of the points is sufficient. In this case it has been chosen the prereformer inlet.

Similarly to the fuel utilization, the air utilization (AU) is defined as the ratio between the amount of oxygen necessary for the electrochemical reaction and the amount which is available (Eq. 2.54). Its maximal value is given by the stack manufacturer, and should be respected in order to avoid oxygen starvation and the resulting voltage decrease. However, the air utilization is not a critical operating parameter for SOFC, since usually large amounts of air are needed for the cooling which provides oxygen for the electrochemical reaction.

$$\mathrm{AU} = \frac{\dot{n}_{O_2,cons}}{\dot{n}_{O_2,prov}} \tag{2.54}$$

It can be observed that, contrary to FU, in use of AU it has not been specified if it refers to the stack or to the system. The reason is that, since the system design does not include cathode flue gas recycling, the calculation for the system does not differ from the calculation for the stack.

Another operating parameter found in SOFC systems is the air-fuel equivalence ratio (λ). It is usually applied to combustion reactions, in the analyzed system for example at the afterburner. λ is defined as the ratio between the amount of air in the mixture related to the amount of air which would be necessary to carry on an stoichiometric combustion (Eq. 2.55).

$$\lambda = \frac{\dot{n}_{air}}{\dot{n}_{air,stoich}} \tag{2.55}$$

If $\lambda = 1$ the combustion takes place under stoichiometric conditions. In case of $\lambda < 1$ the mixture is classified as rich (there is more fuel available that it can be burned) and in the opposite case it is a lean mixture. Sometimes λ is defined for the stack instead of the AU [57], but it is not usually the case.

The electrical efficiency of the system, η_{el}, is one of the most important parameters regarding economical feasibility and emissions reduction. It has been defined as the relation between the electrical produced energy and the energy provided to the system in form of fuel (Eq. 2.39). However, different specific definitions can be applied depending on the chosen limits of the system, that is, the kind of losses taken into account. For example, the electricity consumed by the BoP (for instance the blowers) or the electrical losses at the DC/AC converter. In this work these losses are not considered, so that the electrical efficiency (related to the lower heating value) can be defined by Eq. 2.56.

$$\eta_{el} = \frac{P_{el,DC}}{\dot{n}_{fuel} LHV_{fuel}} = \frac{N_{cells} I U_{cell}}{\dot{n}_{fuel} LHV_{fuel}} \tag{2.56}$$

3 State of the art

In this chapter the previous work on SOFC systems modelling and control is briefly reviewed, focusing on the topics which are developed in later chapters and pointing out these fields which can be deeper analyzed respect to the state of the art.

3.1 Modelling of solid oxide fuel cell systems

In the last decades several authors focused their research in the modelling of solid oxide fuel cells. Various criteria can characterize a model, depending on its application. In case of fuel cells the most important ones have been defined by Haraldsson and Wipke [80] and are listed below. These criteria were already used by Zabihian et al. [157] to classify models of hybrid solid oxide fuel cell systems.

- **Model approach**: it can be theoretical or semi-empirical. For engineering purposes the semi-empirical approach can provide a model with a low time-investment. However, this is only possible if enough experimental data are available. Thus, its re-usability is limited and it can only be applied to already existing systems. On the contrary a theoretical approach, based on physical equations, is recommendable if the purpose is to acquire a deep understanding of the system or in case of lack of experimental data.

- **State**: the behavior of the system can be analyzed in an equilibrium point (steady-state) or under transient conditions. This second analysis is necessary, for example, if start-up and shut-down procedures are of interest.
- **System boundary**: it defines the area of interest of the model. In case of fuel cells systems, it can be a cell layer, a single cell, a stack or the complete system. The system boundary has a strong influence on the details of the model.
- **Spatial dimension**: the models can be spatially discretized from zero (lumped-model) to three dimensions.
- **Complexity/details**: the effects which are taken into account and the assumptions and simplifications which are applied determine the complexity of the system.
- **Accuracy and simulation speed**: they are two criteria inversely proportional to each other. Thus, a compromise has to be found depending on the use of the model.
- **Flexibility**: the flexibility of a model defines its range of validity, which is always limited.
- **Validation**: a model has to be validated in order to ensure its correctness and define its validity range.

Additionally, most of the models are limited to one of the two main SOFC geometries: tubular or planar fuel cell (defined in Sect. 2.1.2).

It is not an aim of this work to make a wide review of the existing SOFC models. Some comprehensive works regarding this topic are these from Hajimolana et al. [78] (subdividing the fuel cell in five subsystems and analyzing them separately), Kakaç et al. [95] (with literature reviews differentiated between macro- and micro-modelling)

or Bhattacharyya et al. [41] (focused on dynamic models). However, some representative models, all based on a physical approach, are presented in Tab. 3.1 and classified under the parameters defined previously.

Most of models are limited to the cell or stack level. The spatial discretization varies from simple 0D models to detailed fluid dynamics models in 3D. The considered effects and assumptions are different in each case, depending on the purpose of the model. The influence of several modelling aspects have been analyzed in detail, for example the effect of neglecting the radiation [48], neglecting the CO oxidation [77] or the momentum conservation equation [42]. Thus, it can be affirmed that the modelling of SOFC cells and stacks has been widely analyzed.

On the contrary, only a few authors analyze the complete SOFC system, with different levels of accuracy. In some cases the complete system is simulated, but actually only the stack is modeled in detail. For the other components standard models from general libraries are used, so that the characteristics of the actual components are not accounted for. In this case the systems are not validated with experimental data. Some examples are Riensche et al. [131] or Carl et al. [50].

Other authors do model each component specifically, the stack and all elements of the BoP, but applying a 0D assumption. In some of them the results are validated with experimental data (for instance Carré [52] or Carl et al. [51]). However, in most cases only simulation results are shown [108, 113] or only the stack is validated, while the other components are not experimentally tested or only validated for the stack [46, 92, 96].

Another usual approach is the integration of a discretized stack model in a 0D BoP model. This is for example the case of Kattke et al. [99]. Additionally, the thermal losses of these components are often neglected, for instance in the work of Kazempoor et al. [100].

However, there are some works where entire SOFC systems are modeled with spatial discretization. Slippey [141] modeled different SOFC system configurations, including a tubular stack and a POX reformer. Although the components are discretized in the flow direction, it is limited to two nodes per component and the adiabatic behavior of the components is assumed. Furthermore, the simulation results are not compared with experimental data. Stiller [146] modeled an hybrid system formed by a SOFC and a gas turbine in one dimension, with the purpose of designing and testing a control strategy. Again, the interaction between components is not examined and the results are not validated. Mueller et al. [119] modeled and validated a tubular stack SOFC system with a implementing one dimensional discretization of the BoP, but assuming adiabatic components.

As it has been shown, modeling of complete system designs is not usual for SOFC. The inclusion of the spatial discretization of the BoP, the interaction between components and the experimental validation require an improvement with respect to the current SOFC system modeling.

Table 3.1 – Comparison between some representative SOFC models (I).

model	*geometry*	*state*	*boundary*	*discretization*	*validation*
[28]	planar	transient	stack	3D	no
[30]	planar	transient	cell	1D+1D	no
[42]	tubular	steady state	cell	1D+1D	yes
[46]	planar	transient	system	1D+1D stack, 0D system	stack[1]
[48]	planar	transient	stack	1D+1D	no
[49]	planar	steady state	cell	2D	no
[52]	planar	transient	system	0D	yes
[56]	planar	transient	cell	1D	no
[60]	tubular	transient	stack	1D+1D	no
[63]	planar circular	steady state	stack	2D	yes

continued on next page...

Table 3.1 – Comparison between some representative SOFC models (II).

model	*geometry*	*state*	*boundary*	*discretization*	*validation*
[74]	planar	transient	cell	1D	yes
[77]	tubular	transient	cell	0D	no
[81]	planar	transient	stack	1D+1D	yes
[92]	general	steady state	system	0D	stack
[98]	tubular	steady state	cell	1D+1D	yes
[99]	planar	steady state	system	1D+1D stack, 0D system	no
[100]	planar	steady state	system	1D+1D stack, 0D system	no
[113]	planar	steady state	system	0D	no
[122]	tubular	transient	cell	1D+1D	yes[1]
[142]	tubular	steady state	stack	1D+1D	yes[1]

3.2 Control of fuel cell systems

Many works have been published in the last decades on the control of SOFC systems for residential applications. The first purpose of these control strategies is the maximization of the electrical efficiency. Additionally, safety and long term operation of the system imply constraints for the operation of the system which have to be fulfilled. The constraints implemented in the control strategy depend on the system configuration, the robustness of the different components and the operating strategy. A usual limitation is the stack temperature, including the cell temperature itself or the temperature difference between the inlet and the outlet (a large gradient can result in thermal stresses which cause the stack degradation). Additionally, the fuel utilization

[1] validated with literature data

and air utilization of the stack (FU^{stack} and AU respectively) have to be kept below a maximum value in order to avoid starvation (as detailed in the previous chapter). The oxygen to carbon ratio, Φ, should be maintained over a minimal value in the prereformer and the stack, otherwise carbon deposition can take place. Finally, all burners in the system should operate in a determined range of equivalent fuel to air ratio (λ) which ensures the desired combustion characteristics (rich or lean) and the flame stability.

The typical manipulated inputs of a SOFC system for CHP application are the fuel flow rate ($\dot{n}_{fuel}^{sys,in}$), the air flow rate ($\dot{n}_{air}^{sys,in}$), the current (I) or voltage (U_{cell}) of the cell and, if the system includes an anode flue recycle loop, the recycle rate (r). Additionally, in some cases the temperature of the inlet gases is also controlled (for instance Inui et al. [90]).

Different approaches have been used in order to implement SOFC control strategies. The most common is the use of PID controllers in different loops in order to achieve the targets of the different operating parameters. However, some authors determined on applying predictive control (MPC) on SOFC systems.

A comparison between various representative control strategies for SOFC systems is presented in Tab. 3.2 regarding the controlled outputs, the manipulated variables and the control approach. For wider comparisons the reader is referred to the reviews of Kirubakaran et al. [103] (who publishes a section on control in a general review about SOFC), Huang et al. [88] (focused on dynamic modelling and control of SOFC for CHP applications), Bavarian et al. [39] (steady state/dynamic models and control strategies for PEM and SOFC systems are reported) or Leung et al. [110] (focused on control strategies for CHP, APU and SOFC-GT hybrid systems).

The control strategy which is the starting point for this work is based on the one developed by Carré in [52]. The controlled variables are the FU^{stack}, AU, Φ and λ^{ab} and the manipulated variables $\dot{n}_{fuel}^{sys,in}$, $\dot{n}_{air}^{sys,in}$, I and r.

Table 3.2 – Comparison between some representative SOFC system control strategies.

control strategy	*controlled outputs*	*manipulated inputs*	*controller*
[31]	T_{stack}, FU, AU	$\dot{n}_{fuel}^{sys,in}$, $\dot{n}_{air}^{sys,in}$	PID
[55]	U	$x_{H_2,stack}^{in}$	PI
[57]	FU_{stack}, λ_{stack}	$\dot{n}_{fuel}^{sys,in}$, $\dot{n}_{air}^{sys,in}$	MPC
[73]	FU_{stack}	$\dot{n}_{fuel}^{sys,in}$	PID
[90]	T_{stack}	AU, $T_{fuel,in}$	PID
[119]	FU_{stack}	$\dot{n}_{fuel}^{sys,in}$	not specified
[134]	T_{stack}^{out}, I, $x_{H_2,stack}^{out}$	$\dot{n}_{fuel}^{sys,in}$, $\dot{n}_{air}^{sys,in}$, U_{cell}	MPC
[144]	$T_{stack}^{in} - T_{stack}^{out}$	$\dot{n}_{fuel}^{sys,in}$, $\dot{n}_{air}^{sys,in}$	PI
[156]	T_{stack}	$\dot{n}_{fuel}^{sys,in}$, $\dot{n}_{air}^{sys,in}$	MPC
[158]	FU_{stack},T_{stack}, P_{el}	$\dot{n}_{fuel}^{sys,in}$, $\dot{n}_{air}^{sys,in}$, I	MPC

In Carré's strategy two control loops are defined, one for the air path and the other for the fuel path. For the air path, a closed-loop control is implemented with a PID controller. It compares the set point stack temperature with the measured value and has as output the air flow rate. The minimal and maximal values of $\dot{n}_{air}^{sys,in}$ are restricted by the maximal AU and the minimal and maximal λ^{ab}. The AU for a cell has been defined in Chap. 2.1.3 as the relation between the consumed and the provided oxygen ions (Eq. 2.54). For the global electrochemical reaction 0.5 moles of O_2 are consumed per mole of H_2. Thus, the calculation of the consumed oxygen molecules in all the cells forming the stack can be described by Eq. 3.1 depending on the electrochemical reaction rate (Eq. 2.6).

$$\dot{n}_{O_2,cons} = \frac{\xi_{elech} N_{cells}}{2} = \frac{I N_{cells}}{4F} \tag{3.1}$$

The oxygen molecules are supplied by the air entering the stack. Thus, by inverting Eq. 3.1 in Eq. 2.54 the AU can be related to the inlet air flow rate by Eq. 3.2.

$$AU = \frac{IN_{cells}}{4F x^{in}_{O_2,air} \dot{n}^{sys,in}_{air}} \tag{3.2}$$

For the anode path control loop the manipulated variables are $\dot{n}^{sys,in}_{fuel}$, $\dot{n}^{sys,in}_{air}$, I and r. The controlled variables are FU^{stack} and Φ (defined at the reformer inlet). It is implemented with an open-loop controller. The generated current I is an input variable, which can be freely chosen. The other manipulated variables are dependent on I so that the constraints for FU^{stack} and Φ are fulfilled. The expressions are developed in the next paragraphs.

The fuel utilization of the system, in case that it incorporates an anode recycle path, has been defined by Eq. 2.46 as the ratio between the provided and the consumed electrons molar flow. Two electrons are consumed in the electrochemical reaction for each mole of reacted H_2. Thus, the flow rate of consumed electrons at the stack can be calculated depending on the electrochemical reaction rate by applying Eq. 3.3. The electrons are supplied by the fuel, depending on its composition (Eq. 3.4).

$$\dot{n}_{e^-,cons} = 2\xi_{elech} N_{cells} = \frac{IN_{cells}}{F} \tag{3.3}$$

$$\dot{n}_{e^-,prov} = \sum x_j N_{e^-,j} \tag{3.4}$$

$N_{e^-,j}$ is the amount of released electrons per molecule j, whose value varies depending on the fuel molecule assuming complete steam reforming. In this case, the fuel is natural gas, abbreviated as NG. By combining Eq. 3.3 and Eq. 3.4 with Eq. 2.46 the expression for the calculation of the fuel utilization of the system depending on the inlet fuel flow rate is obtained (Eq. 3.5).

$$FU^{sys,set} = \frac{IN_{cells}}{F \dot{n}_{NG} \sum_j x_{j,NG} N_{e^-,j}} \tag{3.5}$$

In systems with anode recycle path the system fuel utilization and the stack fuel utilization have different values. The aim of the control strategy is to control the stack fuel utilization, which is related with the system fuel utilization. By replacing the stack set point ($FU^{stack,set}$) in Eq. 2.48 the $FU^{sys,set}$ can be calculated (Eq. 3.6).

$$FU^{sys,set} = \frac{FU^{stack,set}}{1 - r^{set} + r^{set} FU^{stack,set}} \tag{3.6}$$

Replacing this value in Eq. 2.46 the set point of $\dot{n}_{NG}^{sys,set}$ is obtained (Eq. 3.7).

$$\dot{n}_{NG}^{sys,set} = \frac{IN_{cells}}{FU^{sys,set} F \sum_j x_{j,NG} N_{e^-,j}} \tag{3.7}$$

The only variable which remains unknown is the recycle rate set point. If applying a mass balance at the anode recycle path, it can be calculated depending on the set point values for FU^{stack} and Φ by applying Eq. 3.8.

$$r^{set} = \frac{\Phi^{set} - k_{O_2}}{FU^{stack,set} \left(k_\Phi + k_{O_2} - \Phi^{set}\right) - k_{O_2} + \Phi^{set}} \tag{3.8}$$

where k_Φ and k_{O_2} are two constants depending on the gas compositions, defined by Eq. 3.9 and Eq. 3.10 respectively. $N_{C,j}$ is the amount of carbon atoms contained in the molecule j.

$$k_\Phi = \frac{\sum_j x_{j,NG} N_{e^-,j}}{2 \sum_j x_{j,NG} N_{C,j}} \tag{3.9}$$

$$k_{O_2} = \frac{2 \left(x_{O_2,NG} + x_{CO_2,NG}\right)}{\sum_j x_{j,NG} N_{C,j}} \tag{3.10}$$

In order to apply this control strategy the composition of the natural gas entering the system has to be known. It is necessary in order to calculate the amount of released

electrons in Eq. 3.7 as well as the values of the constants k_Φ and k_{O_2}. In the work of Carré the composition $x_{j,NG}$ is assumed as constant, using methane as fuel gas.

The influence on SOFC systems of the fuel fluctuating composition has been regarded only in few works. One of them is an analysis for the *U.S. Department of Energy Laboratory* about the integration of the fuel cells with coal and biomass gasification. Although a quantitative evaluation is not provided, it is concluded that the main challenge for these systems is the variation of the fuel composition. Van Herle et al. [82] studied a simple SOFC system (without anode recycle path) fed with biogas (composed by a mixture of CO_2 and CH_4). The percentage of CO_2 was varied from 30 % to 50 % for a constant fuel flow, in order to analyze the effect on the electrical output. The electrical power decreased 2 kW_{el} for a 1 % increase in CO_2 content (for an electrical power of 140 kW by 30 % of CO_2). The cell voltage, the current density and the electrical efficiency were little affected by these variations. An analysis of the other system operation characteristic values was not reported.

Most of control strategies are not robust against fuels with varying compositions. For this reason, the systems have to operate at a fuel utilization below its maximal value in order to avoid the stack starvation, resulting in lower electrical efficiency. An alternative is to measure the gas composition online, which currently implies complex and cost-intensive methods. However, a few authors designed control strategies to hold for variable natural gas compositions. Kaneko et al. [97] developed a control method for a SOFC-GT hybrid system fueled by biogas, composed by CH_4 mixed with CO_2 in a proportion variable over the time. By applying a control strategy designed for pure methane, power variations up to 13 % were shown for a 5 % change in the CH_4 concentration. In order to compensate this effect, a PID controller for the fuel flow rate was implemented. The result was a stable power output and a slight variation of the FU_{stack}. However, this strategy could not be applied to a system with anode recycle path, since no set point for the recycle rate was provided. Furthermore, the oxygen to carbon ratio (Φ), which is a crucial parameter to guarantee the lifetime

of the fuel cell, was not taken into account. Additionally, it was tested exclusively with biogas.

Massa Gray [75] designed a control strategy for SOFC systems without anode recycling. It was based on calculating the oxygen content of the system exhaust for some reference gases and comparing it with the real value. If the gas entering the system did coincide with one of the reference gases, the fuel flow rate was adapted correctly. However, as it will be explained in the next chapter, in reality too many possible natural gas compositions are to be found for applying this strategy.

Daly et al. [66] patented a control method based on the use of a hydrogen sensor at the anode outlet. However, this strategy does not account neither for fuel cells operating with CO as fuel nor for configurations which include anode flue recycling. Very similar methods, with identical limitations, were developed by Balliet et al. [38] and by Hallum [132].

As it can be seen, none of the control strategies reported up to now are effective for SOFC systems with anode flue recycling operating with natural gas with fluctuating composition. Additionally, there is not any of the methods which has been tested in the reality.

4 Natural gas composition in Germany and its effects on SOFC CHP systems

One of the results of the review presented in Chap. 3 was the lack of thorough studies referred to the effects of variable gas composition on SOFC CHP systems. This chapter is focused on this issue. First, an analysis of the natural gas distribution system in Germany has been carried out in order to achieve a conclusion about the variability of the gas composition in this country. Then, these results have been applied to the SOFC CHP system, by evaluating their influence on the system operating parameters.

4.1 Natural gas composition in Germany

The natural gas provided to the end consumers by German grids is a mixture of gases from different origins, mainly imported from other countries. Russia has traditionally been the most important gas supplier. Nevertheless other countries like the Netherlands and Norway are increasing the gas exports to Germany. The origin of the consumed gas in Germany over time can be seen in Fig. 4.1.

Only a small fraction of the gas demand, about 11 % in 2011, is covered by gas produced in Germany, mainly extracted from the sources in the north. Nevertheless the percentage of biogas (mainly produced in the country) is predicted to rise constantly, as shown in Fig. 4.2.

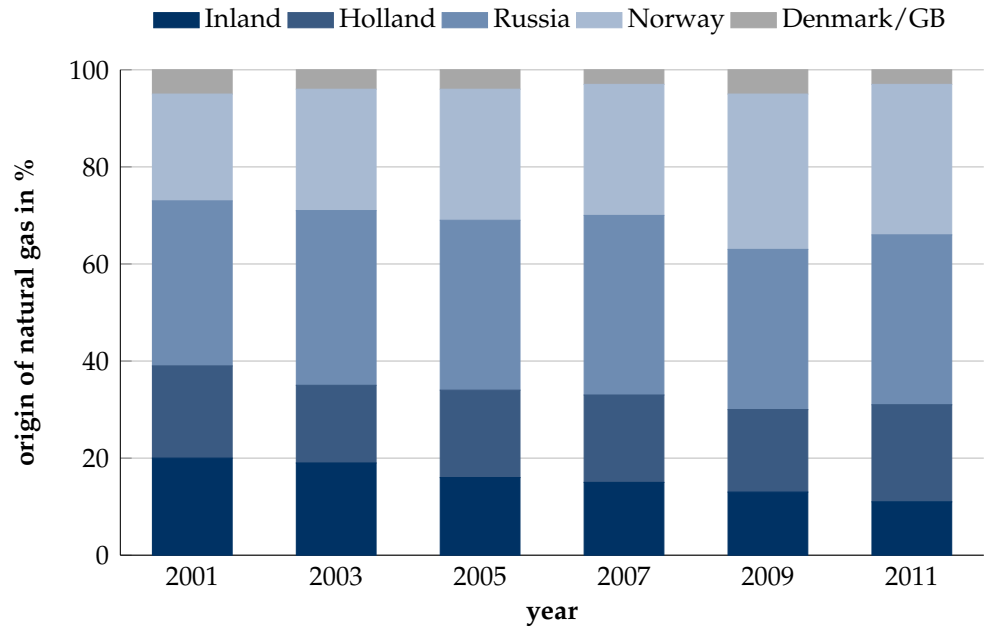

Figure 4.1 – Origin of the natural gas consumed in Germany, from 2001 to 2011 [22].

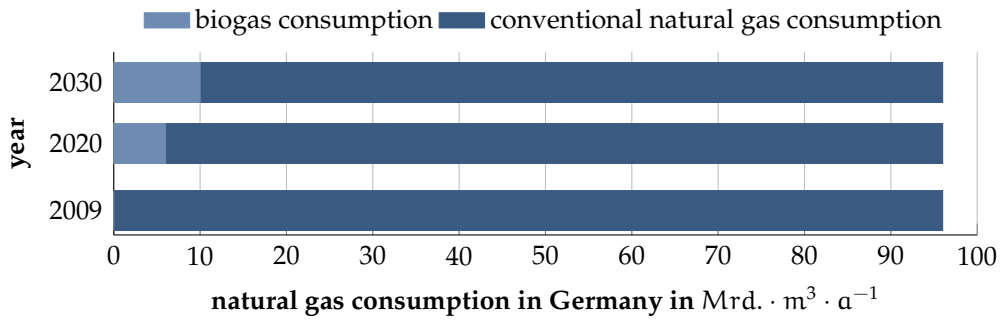

Figure 4.2 – Prediction of the consumption of biogas in Germany in the next years [10].

Finally, there are some special gases which are a mixture between a conventional gas and Liquefied Petroleum Gas (LPG) or Air: Russia+Propane/Air, Holland I+Butane/Air, etc. These gases are used to shift the demand from the consumption peaks to periods with low demand. This is a common strategy in the power market known as "peak shaving".

As a result the gas imported/extracted in Germany has significantly variable compositions, as presented in Fig. 4.3. The main gas components are alkanes (mostly methane) and nitrogen, containing residual amounts of CO_2 and O_2 in some cases. It can be observed that only hydrocarbons up to butane are shown. Actually, traces of other longer alkanes can be found. However, since they values remain below $0.25\,\mathrm{mol\,\%}$ they are not regarded.

The most important characteristic of the natural gas for the operation of SOFC systems is the amount of electrical energy which can be produced by consuming this gas. The electrical energy is generated by the electrons contained in the fuel gas, which are released at the electrochemical reaction.

In order to quantify this magnitude a new variable is defined, $\bar{N}_{e^-,NG}$, as the mean amount of electrons potentially released per molecule of fuel. For the natural gases imported/extracted in Germany the value of $\bar{N}_{e^-,NG}$ is indicated in the right axis of Fig. 4.3. For a H_2 or CO molecule the value of $\bar{N}_{e^-,NG}$ is equal to 2. Since all alkanes are reformed into these species, for each C and each H_2 contained in an alkane molecule two electrons can be released. The resulting value for methane is 8, for ethane 14, for propane 20 and for butane 26 [52]. Since the fuel is a mixture of these different molecules, the resulting $\bar{N}_{e^-,NG}$ is the weighted average of the values of the different compounds:

$$\bar{N}_{e^-,NG} = 8x_{CH_4,NG} + 14x_{C_2H_6,NG} + 20x_{C_3H_8,NG} + 26x_{C_4H_{10},NG} \tag{4.1}$$

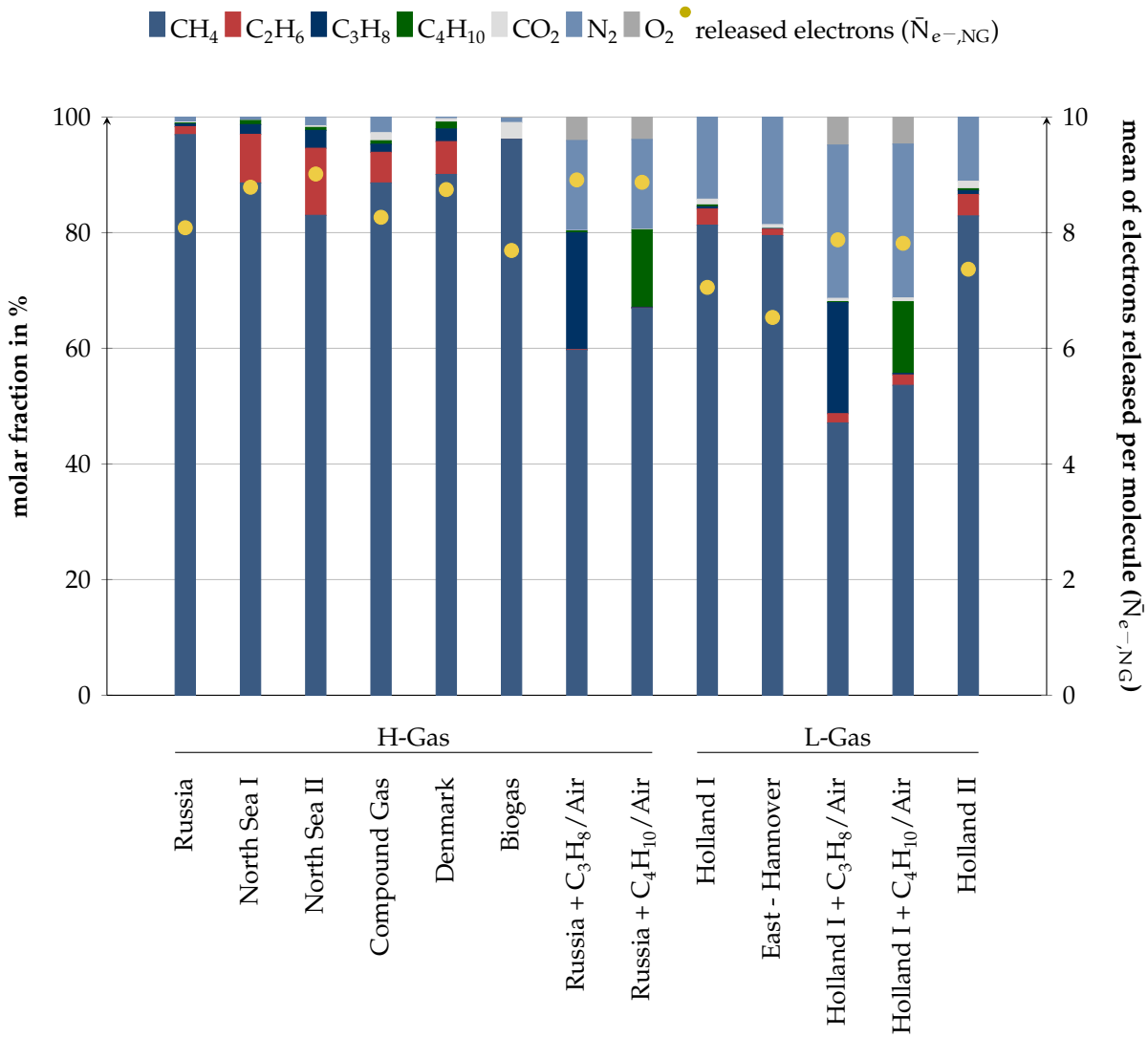

Figure 4.3 – Composition of the imported/produced gases in Germany [3, 18].

In Germany the quality of natural gas is regulated in the *DVGW Arbeitsblatt G260* [18], document where the quality standards for the natural gas in Germany are specified. These quality standards set limits for the Wobbe-Index (Ws), the higher heating value (HHV), the density (ρ) and the maximal amount of oxygen and sulfur.

The limits for these values are given separately for H-Gas (natural gas with high energetic content) and L-Gas (with low energetic content). All natural gases in Germany are classified in one of these groups, depending on their Wobbe index. For each of the groups it exists an independent grid. In most regions there is either L-Gas distribution or H-Gas distribution, and all the gas-consuming devices have to be adapted accordingly. In some areas both grids can be found, but each consumption point is only connected to one of them.

The *DVGW Arbeitsblatt G260* is the only standard concerning natural gas quality in Germany. As long as the gas fulfills the given limits every composition is possible. Furthermore, since there is only one L-Gas and one H-Gas grid for the whole country it is possible for every consumer to be supplied with gas coming from any source (Russia, Norway, etc). The structure of the natural gas market strengthens this situation: the different gas suppliers interchange gas depending on their own demand and on the selling prices of the competitors. As a result, mixtures of the different origin gases are provided to the consumer, with variable compositions and $\bar{N}_{e^-,NG}$ values (shown in Fig. 4.3).

Fig. 4.4 shows some examples of natural gas compositions in Germany, measured by the gas distributors in different locations. They are mixtures of the different origin gases presented previously. Therefore, the fluctuation of the composition is more moderate. However, the percentage of methane still changes from 85 % to 97 % and the potential amount of electrons released per molecule ($\bar{N}_{e^-,NG}$) varies from 8 to 9 in case of H-Gases and from 7 to 7.5 for L-Gases.

The data presented in Fig. 4.4 are directly obtained from the gas suppliers. They ana-

lyze the gas composition and publish a monthly mean value. However, the gas composition is not actively controlled, but exclusively monitored in several measurement points distributed over Germany in order to ensure that the limits given by *DVGW* are respected.

Online measurements at consumption points are discarded at the moment, since they can only be carried out with cost- and time-expensive methods. Consequently, it is impossible to know the composition of the consumed gas in advance. Most devices do not suffer from this this circumstance, as long as the Wobbe-Index remains stable. On the contrary, in the case of a fuel cell system (FCS) it would be desirable to have a fixed gas composition, since as seen in Chap. 3, most control strategies cannot hold for variable gas compositions.

Additionally to the geographical change it exists a fluctuation of the gas composition over the time, like in the examples for Oldenburg (L-Gas, Fig. 4.5) and Stuttgart (H-Gas, Fig. 4.6) during 2011.

It can be observed that the change in the composition can be significant, being a difference in the molar fraction of methane of 7 % between January and June in Stuttgart.

The most detailed gas analysis about the natural gas compositions which could be obtained so far were monthly mean values. However, sources of *Open Grid Europe* affirmed, in the context of oral interviews, that in some regions the energy content of the natural gas could change from the minimal to the maximal limit (which is a 30 % of the HHV) in a period of 10 min. In order to obtain an indicator about the short-time fluctuations the change of the higher heating value (HHV) over time is analyzed. These data are published by some gas suppliers, calculated from measurements at different locations with a frequency of 1 measurement/hour. An example of one-day measurement in Freiburg is presented in Fig. 4.7. In that case the heating value varies significantly fast, being the difference between the daily maximal and minimal value of 4 %.

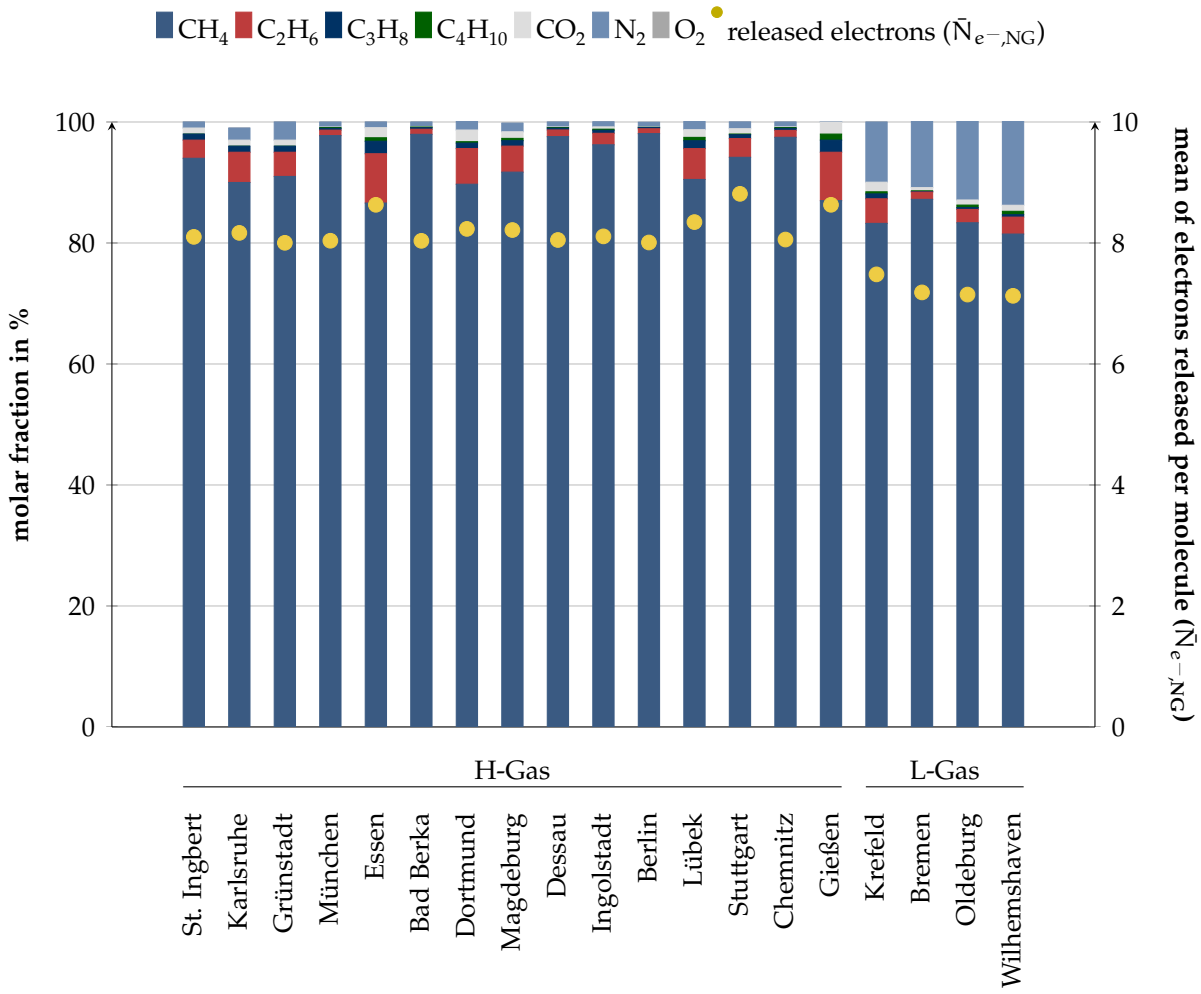

Figure 4.4 – Composition of the natural gas analyzed in different cities [3, 18].

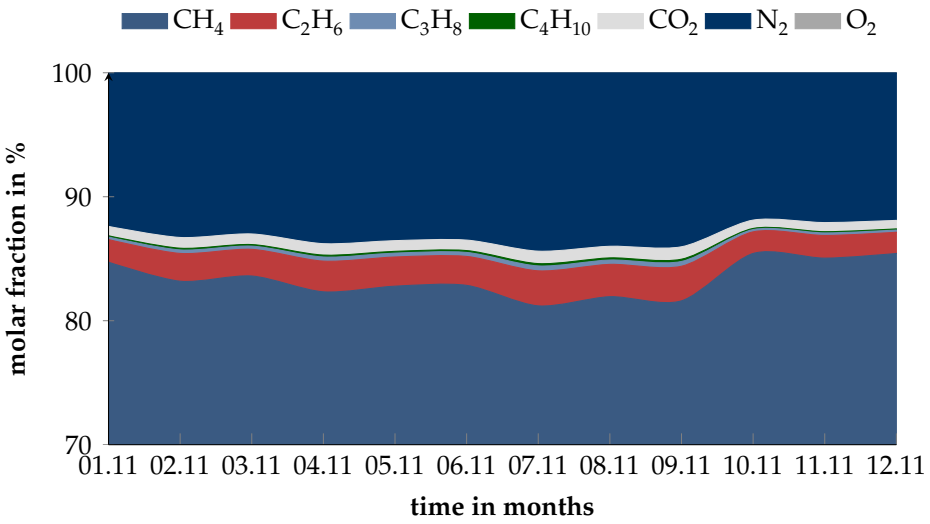

Figure 4.5 – Composition of the natural gas in Oldenburg in 2011 [25].

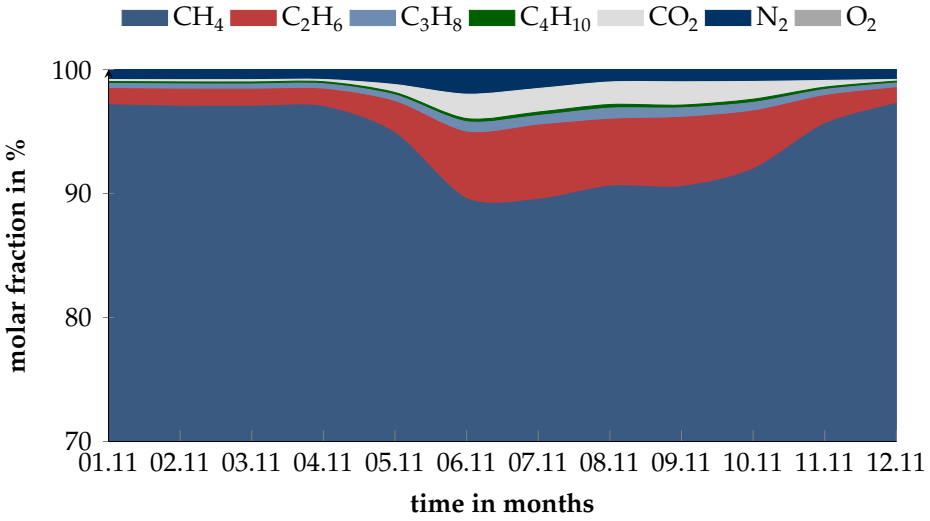

Figure 4.6 – Composition of the natural gas in Stuttgart in 2011 [17] .

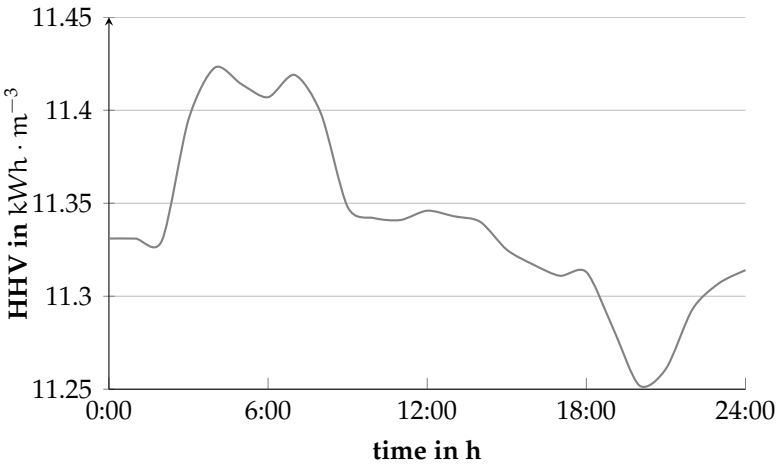

Figure 4.7 – Higher heating value of the natural gas in Freiburg (06.11.11) [19].

To sum up, it can be affirmed that the natural gas composition in Germany varies significantly, both geographically and over time. The only limit applied to these variations by the German regulations is at the energetic content, which is allowed to vary up to 30 % between the maximal and minimal value. With the current natural gas distribution system, these variations are not known in advance, since neither the providers nor the consumers measure the gas composition online.

4.2 Influence of the natural gas composition on the system operation characteristic variables

In this section the sensitivity analysis of the system to the change of gas composition is presented. The FCS is calibrated for one gas, normally methane, since it is the main component of natural gas. As long as the system is fed with exactly this gas, it achieves its maximal efficiency while the conditions of the system operation characteristic variables related to the system lifetime remain fulfilled. However, since the gas composition changes over time, the calibration is not at its optimal value during most of the operating time. In this chapter the influence of the gas composition

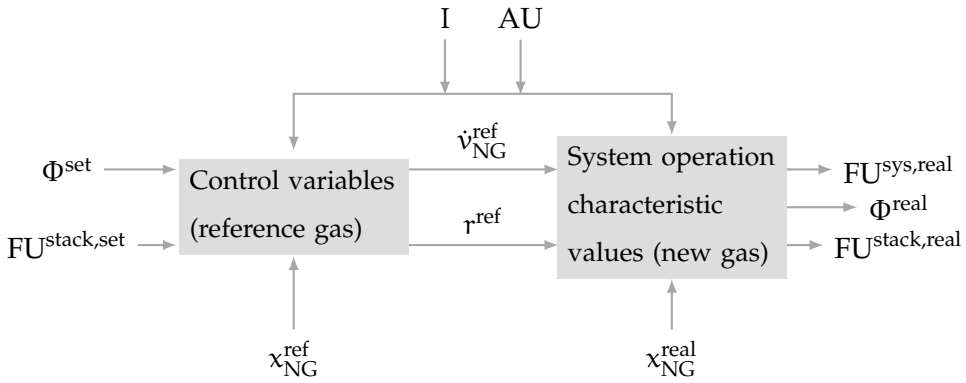

Figure 4.8 – Diagram of the calculations implemented in the tool.

fluctuations on the operating parameters of the system (FU^{stack} and Φ) is quantified. This first analysis is carried out with a steady state model (no dynamic change of the composition is taken into account).

Fig. 4.8 shows the steps of the calculation tool. The input parameters for the calculation are the set points for the stack fuel utilization and oxygen to carbon ratio ($FU^{stack,set}$ and Φ^{set} respectively) and the composition of the calibration gas (x_{NG}^{ref}). The operating point of the system is also defined in terms of air utilization and generated current, and kept constant for all the calculations. The input parameters and operating conditions are shown in Tab. 4.1.

In the first step the control variables for the actuators of the system are calculated by using the reference control strategy, developed by Carré in [52] and which has been detailed in Sect. 3.2 (Eq. 3.6 to Eq. 3.10). They are the volumetric flow of the natural gas blower and the recycle rate, indicated in Fig. 4.8 as $\dot{v}_{NG}$ and r respectively. In the second step the composition of the natural gas is changed and, without modifying the volumetric flow rates, the new characteristic values of the system are calculated (indicated with the superscript real in Fig. 4.8).

The following assumptions have been taken for the following calculation:

- Steady state.

- The alkanes contained in the natural gas are limited to CH_4, C_2H_6, C_3H_8, C_4H_{10}. If the analyzed natural gas contains longer alkanes, their molar fraction is added to the C_4H_{10} molar fraction. The CO_2 and N_2 molar fractions are considered.
- Sulphide and other impurities (H_2S, COS, CS_2, ...) are not taken into account.
- Blowers always deliver the desired flow, even if the gas composition is changing.
- Complete steam reforming of all alkanes.

This model has been used to calculate the system operating parameters (FU^{stack} and Φ) of the different natural gases supplied in Germany, whose compositions have been shown in Fig. 4.3. Another important parameter is η_{el}. However, with the model used in this section it cannot be evaluated, since the stack performance depends on the gas properties.

As mentioned before, the usual calibration gas is methane. However, a simple method to adapt a basic strategy to variable gas composition is to take as reference gas the mean composition of all origin gases, which in principle would result in a better system behavior. That is the reason why in this analysis the composition of the calibration natural gas is the mean value of the composition of all gases from different sources presented in Fig. 4.3. The gases have been separated into two groups: H-Gas

Table 4.1 – Parameters and operating point used in the calculations.

parameter	*unit*	*value*	*description*
$FU^{stack,set}$	%	60	fuel utilization in the stack
Φ^{set}	$mol \cdot mol^{-1}$	2	oxygen to carbon ratio
I	A	25	generated current
AU	%	35	air utilization

and L-Gas. For each of them has been defined a reference gas and volumetric flows, shown in Tab. 4.2.

The system operating parameters (FU^{stack} and Φ) obtained in these conditions for the different gases are shown in Fig. 4.9 and Fig. 4.10, with the corresponding set point values. It can be observed that the values change considerably with the gas used. The gas for which the parameters have the minimal values is *Holland I + Propane/Air*, reaching a FU^{stack} value of 52 % and a Φ value of 1.8. The maximal values of the parameters correspoind to the *Biogas*, resulting on a $FU^{stack} = 74\,\%$ and a $\Phi = 2.35$. The difference between the values resulting from both gases attains 29 % for FU^{stack} and 25 % for Φ of . The maximal deviation from the reference point is from 23 % in the case of the FU_{stack} and 15 % in the case of Φ.

Thus, it can be concluded that the fluctuation of the system operating parameters from gas to gas is significantly high. Furthermore, the values obtained present large deviations from the set point values, so that the conditions which guarantee the stack lifetime are not fulfilled. Consequently, it can be concluded that the basic control strategy cannot be applied to systems which are to be implemented in a region with a natural gas distribution system with the characteristics of the German one. Therefore, Chap. 6 deals with this issue by developing new control methods.

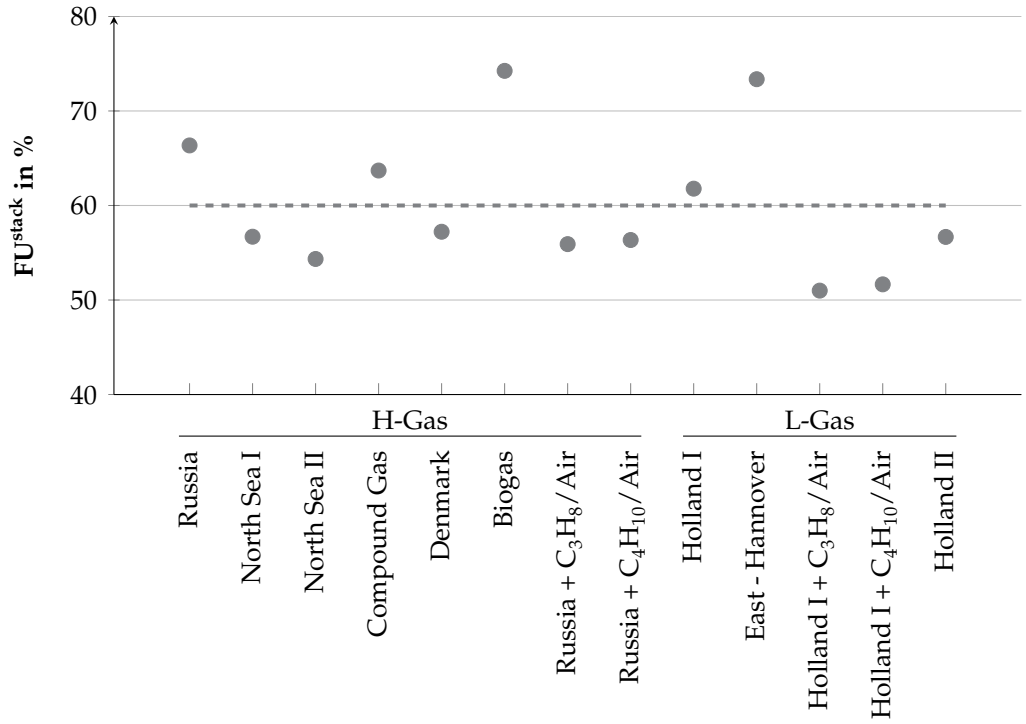

Figure 4.9 – Stack fuel utilization for natural gas coming from different sources. For this example $FU^{stack,set}$ = 60 % (dashed line).

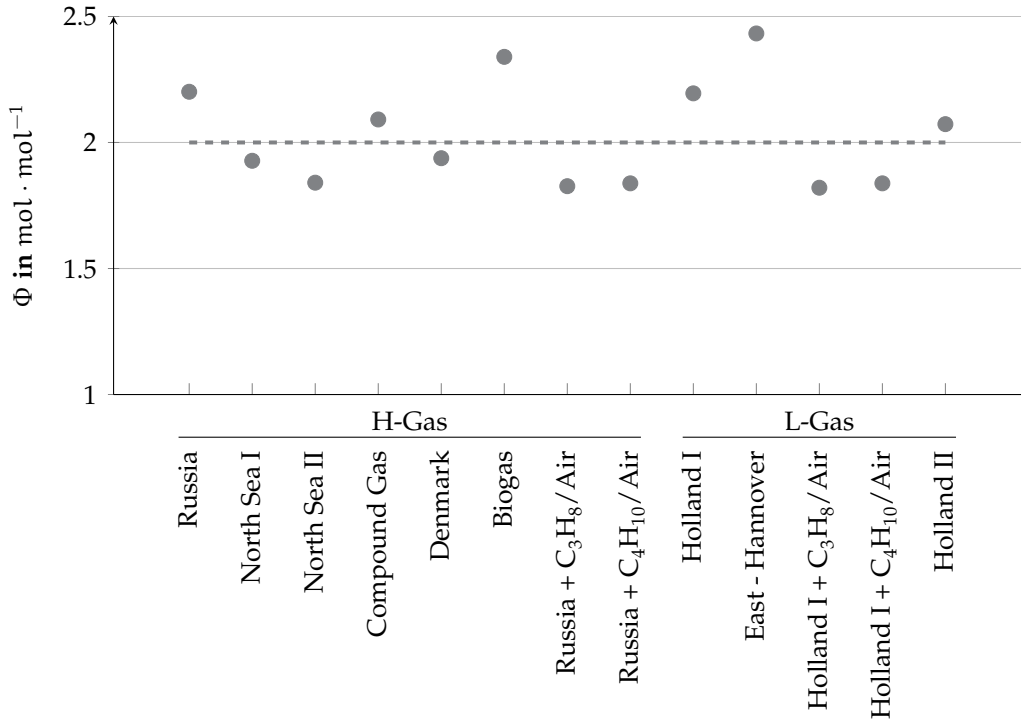

Figure 4.10 – Φ ratio for natural gas coming from different sources. For this example Φ^{set}=2 (dashed line).

Table 4.2 – Composition of the reference gases (H-Gas and L-Gas) and resulting set point values for the manipulated variables (under operation conditions and set points presented in Tab. 4.1).

variable	*H-Gas*	*L-Gas*	*variable*	*H-Gas*	*L-Gas*
x_{CH_4} in %	85.6	73.5	x_{N_2} in %	3.6	1.4
$x_{C_2H_6}$ in %	4.7	2.0	x_{O_2} in %	0.6	7.3
$x_{C_3H_8}$ in %	2.9	3.0	$\dot{v}_{NG}$ in $Nl \cdot min^{-1}$	23.0	26.9
$x_{C_4H_{10}}$ in %	1.5	1.9	r in $mol \cdot mol^{-1}$	0.65	0.625
x_{CO_2} in %	1.1	0.8			

5 Modelling of a SOFC system

In this section the system model is described. First, the configuration of the specific modeled system is presented. Then, the structure of the model is described, including the modeling tool, the main assumptions and the general structure of the components. They are the basis for the sub-component models, including heat exchangers, prereformer, afterburner and stack. Finally, the optimization of the discretization (as a balance between accuracy and calculation time) and the parameterization and validation of the system are presented.

The development of the model, including its parameterization and validation, has been carried out together with Stefanie Wahl in the frame of her PhD [151]. The results of the collaboration work have been published in the common paper *Modeling of a thermally integrated 10 kWe planar solid oxide fuel cell system with anode offgas recycling and internal reforming by discretization in flow direction* [152].

5.1 System configuration and description

The SOFC system is formed by different subsystems, including the stack, the fuel processing, the air management, the thermal management and the power conditioning. The main components are the stack, the fuel processor and the air processor, being the thermal management subsystem integrated in these two latter components. Additionally three blowers, the start-up burner and a heat exchanger coupled with a

condensation trap are considered. The power conditioning subsystem also forms part of the system, but it is not regarded in this work, since it is more focused on dealing with heat management. The system configuration is presented in Fig. 5.1.

The fuel (in this case natural gas) enters the system pressurized by a blower. It is heated up in the first heat exchanger (HE_1) to the reforming temperature. The function of the prereformer is the reaction of the long alkanes with water to form methane, hydrogen and carbon monoxide, since their presence in the fuel cell could result in carbon deposition and consequently on the stack degradation. On the contrary, methane can be reformed at the anode bulk, while at the prereformer it can be created or reformed depending on the temperature and composition. The temperature of the reformed gas is increased in HE_2 in order to achieve the stack inlet temperature. At the anode the CH_4 contained in the gas inlet is completely reformed. The produced H_2 and CO react electrochemically with O_2, generating electrical power and heat. Part of the anode flue is recycled to be reused in the fuel processor in order to increase the pre-reforming temperature and to provide the water molecules necessary for the reforming reaction at the prereformer. The rest of the anode flue gas enters the afterburner, to react with the cathode exhaust gas in a combustion reaction.

The air used in the system is obtained from the environment. After being filtered in order to remove the particles, it is heated up in HE_3 to the stack temperature. Part of the oxygen, quantified by the air utilization (AU), reacts in the electrochemical exothermic reaction. Then, the cathode output gas enters the afterburner to provide the necessary oxygen for the combustion. The resulting flue gas is used to increase the temperature of the fresh air in HE_3 and to increase the temperature of the heating water in the heat recovering heat exchanger (HE_4). Since it is possible that the mixture reaches the water condensing temperature, the heat exchanger is coupled with a condensation trap in order to remove the condensate.

The start-up burner is used exclusively during the start-up procedure. Its purpose is the production of CO at an incomplete combustion to be supplied to the anode while

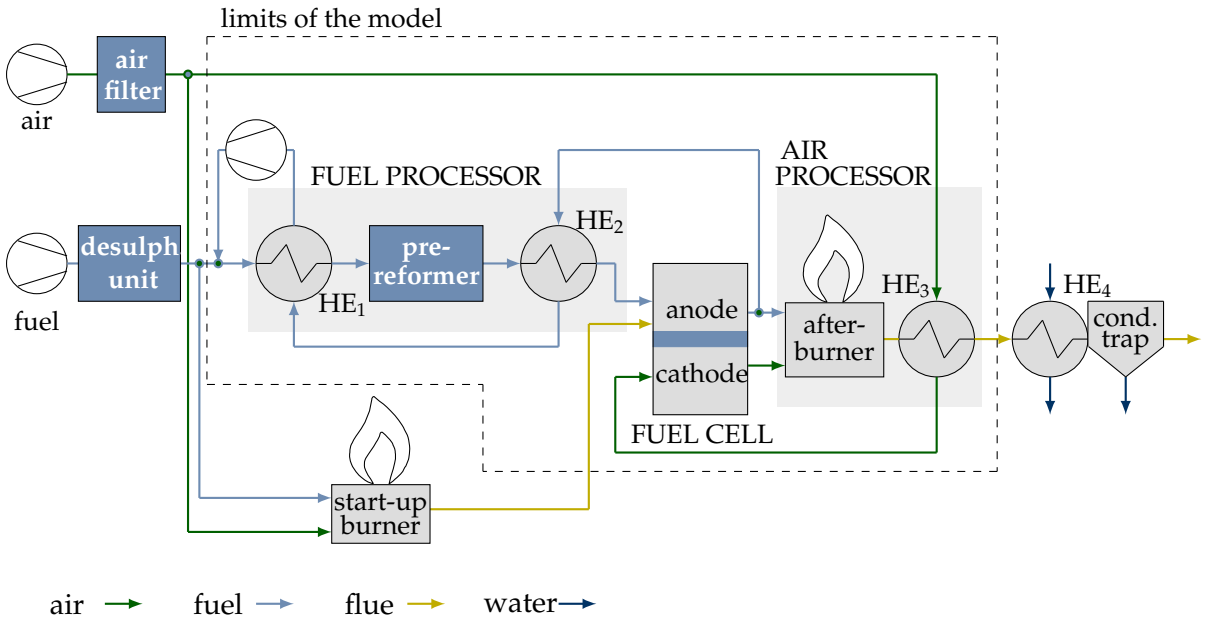

Figure 5.1 – Flow diagram of the system layout.

the reforming reactions do not take place. The start-up procedure is not relevant to this work, but in subsequent chapters the start-up burner will be referred.

In Fig. 5.1 the *fuel processor* and the *air processor* are indicated. In the first case it is a component which contains HE_1, the prereformer and HE_2. The air processor is constituted by the afterburner and HE_3. Both are constructive solutions in order to thermally integrate several components and minimize the heat losses.

The limits of the model are shown with the dashed lines. The components which are not considered significant for the purposes of the simulation, like the blowers, the air filter, the desulphurization unit or the start-up burner, have not been included in order to reduce the complexity and the calculation time of the model.

5.2 Model structure

5.2.1 Features of the model and modeling tool

The different criteria used to classify a model have been defined in Sect. 3.1. In this work the SOFC model has the following characteristics:

- **Model approach**: the model should be reusable (to be utilized in different applications and configurations) and developed with a limited amount of experimental data. Accordingly, a theoretical approach has been chosen.
- **State**: one of the applications of the model, on which this work is focused, is the design of a control strategy. Consequently, a dynamic model is necessary.
- **System boundary**: the complete SOFC system is modeled. The specific model boundaries have been shown in Sect. 5.1.
- **Spatial dimension**: a 1D+1D discretization has been chosen, explained in detail in Sect. 5.2.3.
- **Complexity/details**: the assumptions applied to the different effects modeled are detailed in the next sections.
- **Accuracy and simulation speed**: there are two criteria inversely proportional to each other. Thus, a compromise has to be found depending on the use of the model. The calculation times are presented in Sect. 5.4.
- **Flexibility**: this model is built so that it can be used for system comparison and optimization, as well as under different operating conditions and control strategies.
- **Validation**: the parameterization and validation of the model is presented in Sect. 5.5.

In order to fulfill these requirements the chosen modeling language is Modelica®. Modelica® is an open-source, equation based language designed for the modeling of complex systems [24]. Its is a object-oriented modeling language appropriate for the multi-domain modeling: different physical effects (thermodynamical, electrical, chemical...) and the interactions between them can be combined in the same model [72].

Most simulation tools are based on a causal approach. With this approach the systems are modeled in computational block diagrams, where the interactions between variables are decided a priory and described by explicit equations. On the contrary, with an acausal approach, like in the Modelica®-based tools, the relation between variables is described by physical laws. Neither the input/output variables nor the sequence of the equations are defined by the modeler, since the solver is capable to re-order the equations depending on the boundary conditions [53, 61, 69].

Another characteristics of Modelica® is the modularity. That means that the variables defining the state of a component are calculated in a module, depending only on its inlets and not on internal variables of other modules. The first advantage is the reduction of the modeling complexity due to the subdivision of the system [133]. Furthermore, it is possible to apply changes on single components without changing the entire system and to reuse the modules in new systems or new system configurations [61].

The process of system simulation by using Modelica®-based tools consists in two steps: the compilation and the simulation. During the compilation process, the modular structure of the model is destroyed, becoming a global equations system. Additionally, the implicit equations are transformed into explicit, so that the standard ODE solvers can be applied [160]. This mathematical process is the main feature of the Modelica® tools, but it is significantly time-consuming. The result is a compiled code, which can be simulated in a efficient way.

5.2.2 Relevant phenomena and assumptions

In a FCS for CHP applications multiple physical phenomena occur involving many different scientific fields. For the purpose of this work the chemical, electrochemical, thermodynamical and fluid mechanics effects have been modeled, being the most relevant listed below.

- Pressure losses in the volumes.
- Heat transfer between gas and solid components by convection phenomena in the flow direction.
- Heat transfer through solid components by conduction phenomena.
- Energy storage in the solid components.
- Electrochemical reaction in the stack.
- Chemical reactions in the prereformer, burner and the anode/cathode bulk.
- Thermal interaction between components: the subcomponents are not considered adiabatic but the heat exchanged between them has been modeled [99].

The system is modeled under the following assumptions:

- Dalton model of ideal mixture of ideal gases is applied to gas flows [129].
  - Each component behaves as an ideal gas.
  - The mixture behaves as an ideal gas (no interaction between gases is regarded).
  - All components have the same temperature.
  - All components occupy the entire volume.

  - The total pressure of the mixture is the sum of the partial pressures of all components.

- The wall to wall heat transfer by radiation phenomena is generally neglected. There are two components with temperatures achieving values for which the effect of the radiation has to be taken into account: the afterburner and the stack. In the first case, the radiation is implemented. On the contrary, for the stack this effect is neglected, as justified in Sec. 5.3.4.

5.2.3 Model discretization

The FCS has been modeled in a quasi-2D or 1D+1D approach. In one dimensional models the system is discretized in one spatial direction, for example in the flow direction. Accordingly, the variables which define the state of the system have a different value for each node. Thus, if the physical magnitudes vary strongly in one direction the use of a discretized model is necessary in order to achieve a high accuracy. The latter is true for the FCS. Regarding the heat exchangers forming the air processor and the fuel processor, the high temperature gradients justify the discretization. Furthermore, it is possible to distinguish between co- and counterflow. In case of the stack, the value of temperatures, gas compositions, cell voltage and current density change significantly in the flow direction [30, 31, 33].

Several authors (for instance [46] or [64]) report a high thermal and electrochemical agreement between one-dimensional SOFC models (discretized in the flow direction) and experimental results. If lumped models are compared to one-dimensional models the improvement of the quality of the results by one-dimensional approach is remarkable. For instance, Cheddie and Munroe [56] reported deviations over 20 K on the cathode and anode outlet temperatures between the 0D and the 1D models (discretized into 21 nodes). Another example is provided by Karcz [98]. The lumped

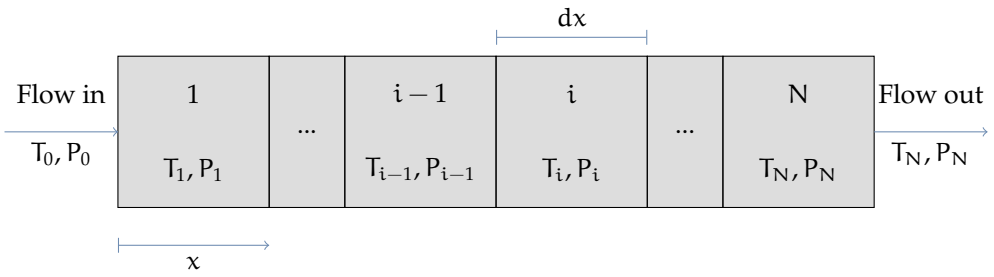

Figure 5.2 – Diagram of the one-dimensional model discretization, for the variables temperature (T) and pressure (P).

model gives an overestimation of the cell voltage of 0.05 V in comparison to the one-dimensional model with 20 discretization compartments. On the contrary, the influence of the other spatial directions is low in comparison to the flow direction, while the calculation time is significantly increased. For instance, Andersson et al. [35] showed a two-dimensional temperature profile for a planar SOFC. While between the fuel inlet and outlet the temperature difference attained 90 K, on the orthogonal direction the deviation was lower than 10 K.

Similar results have been reported for steam reformers. Schaedel et al [137] presented the simulation results of a two-dimensional cylindrical prereformer at 327 °C, 452 °C and 577 °C. The gas composition varies significantly in the axial direction, but the change is not representative in the radial position. Regarding the temperature, variations up to 150 K between the inlet and the outlet of a planar prereformer (200 mm longitude) have been shown experimentally [126].

In conclusion, a one-dimensional approach has been proofed to be a good approximation of the behavior of the main components of SOFC systems.

Each compartment is modeled as a continuous stirred-tank reactor (CSTR). Under this approximation, the variables defining the state of the node have the value of the output variables. Fig. 5.2 illustrates the model approximation with N nodes for the variables P and T.

From this point all equations used to describe the behavior of the system have to be applied to each discretization segment. However, the sub-index i is not included in order to simplify the reading of the document.

In a quasi-2D model the components are not only divided into segments in the flow direction, but they are composed of several control volumes. Each volume of control represents either a volumetric chamber or a solid material layer. By applying this modeling strategy the flow streams can be separated and different material properties simulated. As a result the behavior of the system can be simulated more precisely. Consequently, this is the chosen discretization approach for the model of this work.

The difference with a two-dimensional model is that the discretization segments can only be freely chosen in the flow direction, while in the other directions the volumes of control are defined by the structure of the model and remain fixed. The volumes of controls which compose the components of the system are detailed in Sect. 5.3.

5.2.4 General structure of a subcomponent

The models of the single components are built by using basic blocks, which are combined to each other in order to reproduce the structure of the component. There are three types of blocks: *heat transfer blocks*, *volumetric blocks* and *solid blocks*. In order to connect the different blocks two kind of connectors have been defined: *flow pins* (thermodynamical properties of the gas, Tab. 5.1) and *heat pins* (necessary properties for the calculation of the heat transfer, Tab. 5.2).

In Modelica® language there are two kinds of variable in connectors: non-flow variables (for electrical potential, energy level, pressure, etc.) and flow variables (for variables like electrical current, heat flow rate, volumetric flow, etc.). When two connectors of the same type become coupled, automatically certain conditions are set.

Table 5.1 – Flow pin variables.

variable	*unit*	*description*	*type of variable*	*dimension*
$\dot{n}$	$mol \cdot s^{-1}$	molar flow	flow	scalar
T	K	temperature	non-flow	scalar
P	Pa	pressure	non-flow	scalar
$\dot{H}$	W	enthalpy flow rate	flow	scalar
$\dot{S}$	$W \cdot K^{-1}$	entropy flow rate	flow	scalar
$\dot{G}$	W	Gibb's free energy rate	flow	scalar
$\dot{c}_p$	$W \cdot K^{-1}$	heat capacity rate	flow	scalar
x	$mol \cdot mol^{-1}$	molar fraction	non-flow	vector

Table 5.2 – Heat pin variables.

variable	*unit*	*description*	*type of variable*	*dimension*
T	K	temperature	non-flow	vector
$\dot{Q}$	W	heat flow	flow	vector

In case of the non-flow variables the equality condition is imposed and for the flow variables the sum-to-zero condition [72].

Fig. 5.3 shows a general component, formed by two chambers separated by a wall which interchange heat with each other. It is formed by two volumetric blocks, with two flow pins for the inlet and outlet flows (in gray). Each one of them is connected through a heat pin (in red) to a heat transfer block. Both blocks are connected to a solid block, which represents the wall.

The volumetric blocks are used to model a chamber of a component. The following paragraphs describe the basic equations implemented in every volumetric block. In order to model the system subcomponents this basic block is adapted to the specific geometry. Furthermore, if at the component chemical reactions take place, the block

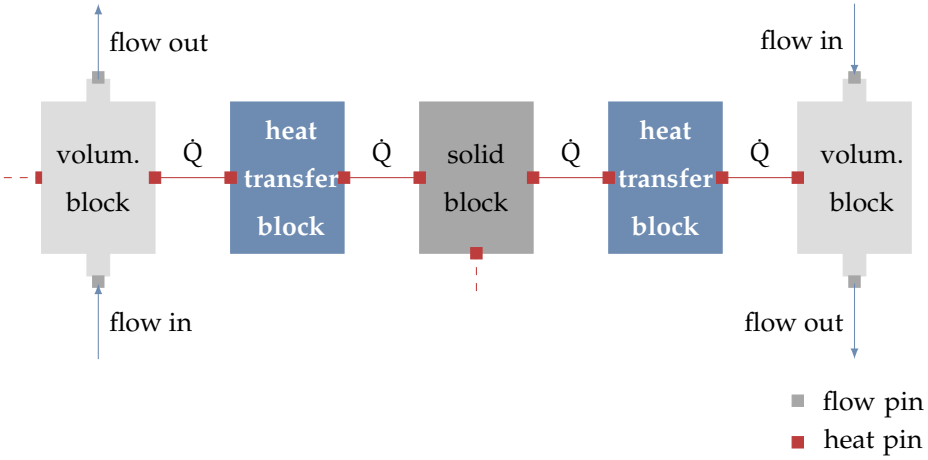

Figure 5.3 – Diagram of a general component, showing the generic blocks and connectors. The dashed lines show possible connections to other components.

is enlarged and the corresponding equations are integrated. They are described in Sect. 5.3.

Each volumetric block includes two flow pins (for the inlet and the outlet flows) and the amount of heat pins necessary in order to implement the heat exchange with this chamber. In each discretization compartment of the chamber all thermodynamical properties (Tab. 5.1) are actualized by applying the energy balance (Eq. 5.1), momentum balance (Eq. 5.5), overall mass balance (Eq. 5.10) and species mass balance (Eq. 5.11).

The energy balance takes into account the heat losses to the environment and the other components ($\dot{Q}_{hex}$), the heat generated or consumed at the endothermic and exothermic reactions ($\dot{Q}_{chem}$) and the electrical power generated by the electrochemical reactions (P_{el}). On the contrary, the potential and kinetic energy and other types of work can be neglected. Thus, the energy balance is calculated by

$$n c_p^{out} \frac{dT}{dt} = \dot{n}^{in} h^{in} - \dot{n}^{out} h^{out} + \sum_i \dot{Q}_{hex,i} + \sum_i \dot{Q}_{chem,i} - P_{el} \tag{5.1}$$

The molar enthalpy, entropy and heat capacity are calculated by using the NASA polynomials [116] depending on gas composition and temperature and referred to the standard conditions ($T^0 = 298.15\,K$ and $p^0 = 101325\,Pa$).

$$h(T) = \sum_j x_j h_j^{NASA}(T) \tag{5.2}$$

$$cp(T) = \sum_j x_j cp_j^{NASA}(T) \tag{5.3}$$

$$s(T) = \sum_j x_j s_j^{NASA}(T) \tag{5.4}$$

Eq. 5.5 shows the integrated form of the linear momentum equation applied to a fluid under the assumptions of steady and incompressible flow in a streamline. τ_o is the resisting force due to viscous friction at the flow boundary, A_{cross} the cross section area and L_P the perimeter of the wall.

$$\frac{dP}{dx} A_{cross} = -\tau_o L_P \tag{5.5}$$

By applying the definition of the hydraulic diameter D_h (Eq. 5.6), the previous equation results in Eq. 5.7.

$$D_h = \frac{4A_{cross}}{L_P} \tag{5.6}$$

$$\frac{dP}{dx} = -\frac{4\tau_o}{D_h} \tag{5.7}$$

The Darcy friction factor, λ_p, is defined by

$$\lambda_p = \frac{8\tau_o}{\rho v^2}. \tag{5.8}$$

Combining Eq. 5.7 and Eq. 5.8 the Darcy-Weisbach equation is obtained. If its extended with the minor losses (z_k) and applied to a section of length L, it results in Eq. 5.9 [54].

$$p^{in} - p^{out} = 0.5\rho v^2 \left(\frac{L}{D_h}\lambda_p + \sum_k z_k \right) \tag{5.9}$$

The Darcy-Weisbach friction factor can be calculated from experimental correlations depending on geometric parameters and on the Reynolds number. The minor pressure losses, z_k, are caused by the hydraulic components which induce a change in the streamline, for instance a valve, an elbow or the variation on the pipe cross section. The minor loss caused by each hydraulic component can be calculated depending on the geometry. Nevertheless, the geometrical parameters are often not known. In this case the minor losses can be parameterized experimentally.

The mass balance for each discretization node is applied in its molar form, resulting in Eq. 5.10. If it is applied to each gas component Eq. 5.11 is obtained, in which ξ_i is the reaction rate of the reaction i and ν_{ij} the stoichiometric coefficient of the reaction i for specie j.

$$\frac{dn}{dt} = \dot{n}^{in} - \dot{n}^{out} + \sum_j \sum_i \xi_i \nu_{ij} \tag{5.10}$$

$$\frac{dn_j}{dt} = \dot{n}_j^{in} - \dot{n}_j^{out} + \sum_i \xi_i \nu_{ij} \tag{5.11}$$

There are two types of heat conduction blocks, in order to implement the two heat transfer phenomena that are considered in the model: convection and conduction. The convective heat flow is calculated by using Eq. 5.12.

$$\dot{Q}_{conv} = h_{conv} A_{cont} \left(T_{solid} - T_{fluid}\right) \tag{5.12}$$

A_{cont} is the contact area between the solid and the fluid. h_{conv} is the convection coefficient, which is calculated depending on the Nusselt number (Nu) and the characteristic length (l_{char}):

$$h_{conv} = \frac{Nu\lambda}{l_{char}} \tag{5.13}$$

The thermal conductivity (λ) of the gases is calculated depending on the temperature by using the polynomial laws developed by Todd and Young [147]. The authors reported errors below 10 % for the range between 273 K and 1473 K.

The characteristic length and the Nusselt number depend on the geometrical characteristics. Nusselt number Nu can be calculated by using different experimental correlations, for example that developed by Churchill and Chu for vertical and horizontal cylinders [58, 59]. Another influence factor is the type of convection. In case of forced convection (between the solid and a flowing fluid) the Nusselt number is calculated depending on the Prandlt and the Reynolds numbers (Pr and Re respectively, Eq. 5.14). On the contrary, for free convection (with an fluid with velocity zero), the Grashof number (Gr) influences the value of Nu (Eq. 5.15).

$$Nu_{forced} = f\left(Re, Pr\right) \tag{5.14}$$

$$Nu_{free} = f\left(Gr, Pr\right) \tag{5.15}$$

The expression of the heat transferred by thermal conduction through a solid layer is shown in Eq. 5.16. It depends on the temperature difference between the two sides, the material characteristics (in particular on its thermal conduction coefficient, λ) and

the geometrical characteristics of the solid (summarized in a geometrical coefficient K_{geo}).

$$\dot{Q}_{\lambda} = \lambda \, (T_1 - T_2) \, K_{geo} \tag{5.16}$$

For a planar wall of area A and thickness δ the geometrical factor K_{geo}^{planar} is calculated by applying Eq. 5.17 and in case of a cylinder of length L, inner diameter D_{in} and outer diameter D_{out} by Eq. 5.18

$$K_{geo}^{planar} = \frac{A}{\delta} \tag{5.17}$$

$$K_{geo}^{cyl} = \frac{2\pi L}{\ln\left(\frac{D_{out}}{D_{in}}\right)} \tag{5.18}$$

The *solid block* is used to model a solid material. The main physical phenomena which has been implemented is the accumulation of energy, depending on the heat capacity of the solid (cp). Since the model has been discretized in the flow direction, the effect of the heat transfer by conduction in this direction (from node to node) has been taken into account. Assuming the impermeability of the solid (no gas molecules are transported through it), only the thermal balance is applied, modeled by Eq. 5.19.

$$\frac{dT}{dt} = \frac{1}{cp}\left(\dot{Q}_{\lambda}^{in} - \dot{Q}_{\lambda}^{out} + \sum_{k} \dot{Q}_{loss,k}\right) \tag{5.19}$$

$\dot{Q}_{loss}$ represents the heat flows interchanged with the other components through the k heat pins.

5.3 Sub-models approach

In this section the specific models for the main system components are described in detail, including their function in the system, the model structure based on the basic blocks and the assumptions which have been made in each case.

5.3.1 Heat exchangers

In a SOFC system optimal thermal management is a crucial issue in order to run each process at its optimal temperature. For this purpose the system incorporates four heat exchangers. All of them are based on shell-and-tube heat exchangers, a design which consists in a cylindrical shell, with a bundle of round tubes mounted in it so that they are parallel to the shell [94]. One of the fluids flows through the tubes and the other along the shell, taking place the heat exchange through the tubes walls. There are different kinds of tubes and shells configurations. In this case the design consists in a one-pass shell with straight tubes, operating in counter-flow. The structure of such a heat exchanger is presented in Fig. 5.4. In the system the heat exchangers are thermally integrated with other components in order to optimize the thermal behavior. In case of HE_1 and HE_2 they are parts of the fuel processor, together with the prereformer. Heat exchanger HE_3 is integrated with the afterburner forming the air processor.

The heat exchanger is modeled by using exclusively the basic blocks presented in Sect. 5.2.4. The model structure is shown in Fig. 5.5. The tube and the shell are built by using a volumetric component, which implements an energy, momentum and mass balance. In both cases the volumes are limited by their walls, thermal conductors which interchange heat with the fluid by forced convection. Since this heat exchange takes place with one fluid in each tube side, the heat exchange between both gases is

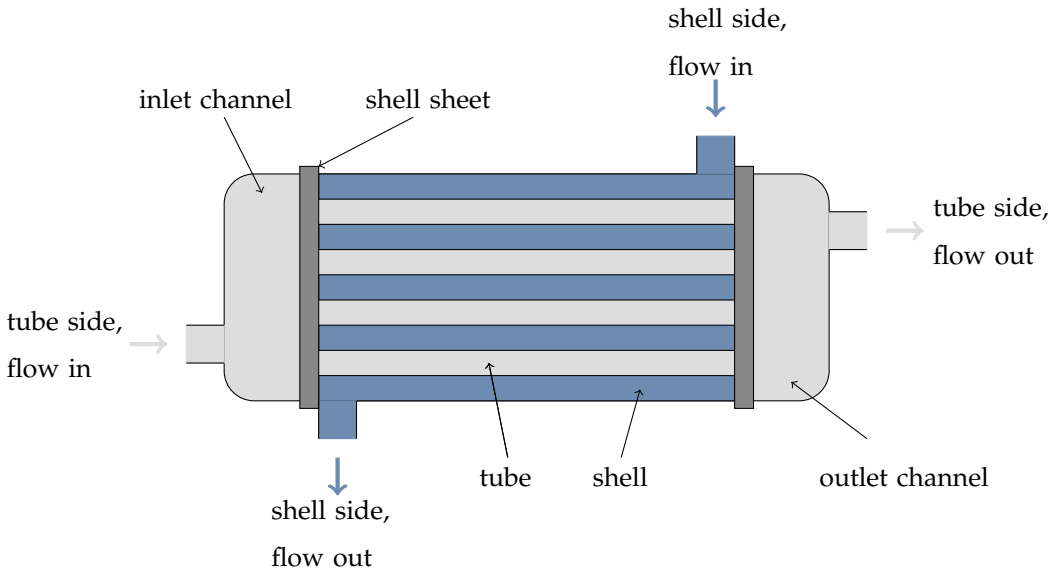

Figure 5.4 – Diagram of a shell-and-tube heat exchanger (straight tube with one pass tube-side), based on [107] and [154].

attained. Finally, the shell wall is in contact with the environment or with other components, which results in a new heat transfer source. All components are discretized in the flow direction.

The following assumptions have been taken in the modeling of the shell-and-tube heat exchanger:

- The behavior of the flow in each of the tubes is identical. Accordingly, only one tube is modeled and the results extended to all tubes. In order to model the correct heat transfer between both sides of the heat exchanger, the heat released/adsorbed by the shell side ($\dot{Q}$) is calculated as the heat flow from one tube ($\dot{Q}_{tube}$) multiplied by the amount of tubes (N_{tubes}).

- Under the assumption of 1D modeling, the variations in the radial direction are not regarded. This relies upon two assumptions: first, a negligible temperature difference between the center of the shell and the external area. Additionally,

Table 5.3 – Parameters for the Nusselt number correlation.

parameter	*value*	*unit*
K_{Nu}	0.57	-
m_{Nu}	0.9	-
n_{Nu}	0.3	-

the distance between the tubes is considered large enough so that the velocity and temperature gradient between two tubes can be neglected.

- The inlet and outlet channels are not modeled, since the losses generated in this area are not examined.
- The gas in the shell side is constantly parallel to the tubes along the complete heat exchanger.

For most components the calculation of heat transfer coefficients h_{conv} can be carried out by using standard experimentally-determined Nusselt correlations. However, this is not the case for the inner side of the heat exchanger, since it consists of an irregular geometry with laminar flow [150]. Because of this reason, a generic form for the calculation of Nu (Eq. 5.20, [83]) has been used, being the parameters obtained from experimental measurements (Tab. 5.3).

$$Nu = K_{Nu} Re^{m_{Nu}} Pr^{n_{Nu}} \tag{5.20}$$

5.3.2 Prereformer

The purpose of the prereformer is to reform the long alkanes into hydrogen and carbon monoxide, since their presence in the anode side of the stack could contribute to its degradation. Additionally, since the mixture contains H_2, CO, H_2O and CH_4,

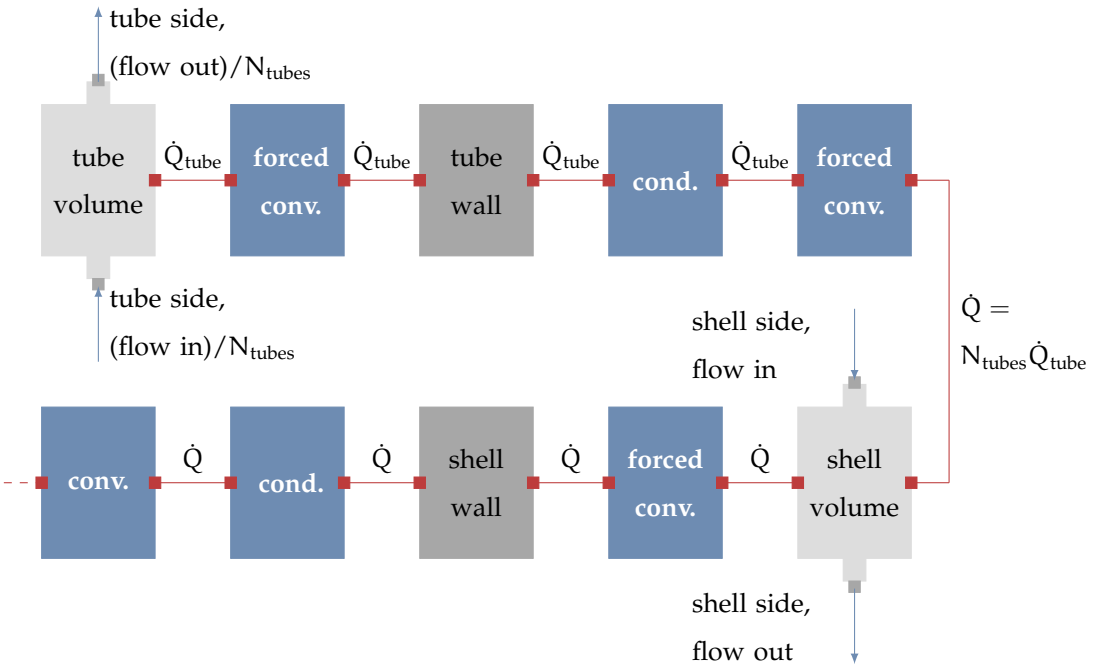

Figure 5.5 – Structure of the model of a shell-and-tube heat exchanger.

methane is reformed or created depending on temperature. The prereformer is a component integrated in the fuel processor, together with the heat exchangers HE_1 and HE_2 (see Fig. 5.1).

The prereformer model is based on a general volumetric component (Sect. 5.2.4). Thus, energy, momentum and mass balances (Eq. 5.1, Eq. 5.5 and Eq. 5.10) are applied to the gas mixture. The reforming reactions and water gas shift reaction or WGS (listed in Tab. 5.4) are added to the base model. The species which are taken into account are the natural gas components (CH_4, C_2H_6, C_3H_8, C_4H_{10}, CO_2, N_2) and the components of the recycled gas (H_2O, H_2, CO). The other components of the gas (C_5H_{12}, C_{6+} and S) have been neglected, since their molar fraction remain below 0.25 % [18].

There are other reactions which could take place in the prereformer as detailed in Chap. 2.3. The most important are these which cause carbon deposition: the decomposition of hydrocarbons (Eq. 2.50), the Boudouard reaction (Eq. 2.51) and the carbon monoxide hydrogenation (Eq. 2.52) [136]. However, if there is enough water avail-

Table 5.4 – Chemical reactions implemented in the prereformer chamber.

reaction index i	*reaction name*	*reaction formula*
1	methane-steam reforming	$CH_4 + H_2O \rightleftharpoons CO + 3H_2$
2	methane-steam reforming	$CH_4 + 2H_2O \rightleftharpoons CO_2 + 4H_2$
3	water gas shift reaction (WGS)	$CO + H_2O \rightleftharpoons CO_2 + H_2$
4	ethane-steam reforming	$C_2H_6 + 2H_2O \rightleftharpoons 2CO + 5H_2$
5	propane-steam reforming	$C_3H_8 + 3H_2O \rightleftharpoons 3CO + 7H_2$
6	butane-steam reforming	$C_4H_{10} + 4H_2O \rightleftharpoons 4CO + 9H_2$

able, they can be avoided, because in this case the methane-steam reforming reactions dominate over the others [135]. Assuming that the oxygen to carbon ratio is actively kept in a high level at the prereformer inlet by the control strategy, these three reactions can be safely neglected.

In case of the methane-steam reforming reactions and the WGS reaction the reaction rates are calculated by applying the kinetics model of Xu and Froment [155], which has been used by other several authors in the SOFC system modelling [32], [96], [153]. This models is based on a Langmuir-Hinshelwood model (which describes bimolecular reactions on surfaces) and assumes that the rate limiting step is the formation of adsorbed carbon species, which is generally agreed [91]. The experiments for the determination of the parameters were carried out in the range 500 °C-575 °C. However, Haberman and Young [76] compared extrapolated data from the model of Xu and Froment with the curve obtained by fitting the data from Lehnert et al. [109] and reported a very good agreement by temperatures up to 900 °C. Thus, the model is assumed applicable under this temperature condition. The reaction rates ξ_1^{pr}, ξ_2^{pr} and ξ_3^{pr} are calculated by applying Eq. 5.21, Eq. 5.22 and Eq. 5.23 respectively, depending on the partial pressure of the reactants and products.

$$\xi_1^{pr} = \frac{\frac{C_{ki,1}\,a_c}{p_{H_2}^{2.5}}\left(p_{CH_4}p_{H_2O} - \frac{p_{H_2}^3 p_{CO}}{C_{eq,1}}\right)}{DEN^2} \tag{5.21}$$

$$\xi_2^{pr} = \frac{\frac{C_{ki,2}\,a_c}{p_{H_2}^{3.5}}\left(p_{CH_4}p_{H_2O}^2 - \frac{p_{H_2}^4 p_{CO_2}}{C_{eq,2}}\right)}{DEN^2} \tag{5.22}$$

$$\xi_3^{pr} = \frac{\frac{C_{ki,3}\,a_c}{p_{H_2}}\left(p_{CO}p_{H_2O} - \frac{p_{H_2}p_{CO_2}}{C_{eq,3}}\right)}{DEN^2} \tag{5.23}$$

$$DEN = 1 + C_{ads,CO}p_{CO} + C_{ads,H_2}p_{H_2} + C_{ads,CH_4}p_{CH_4} + \frac{C_{ads,H_2O}p_{H_2O}}{p_{H_2}} \tag{5.24}$$

a_c is the catalyst activity, $C_{eq,i}$ the equilibrium constant of the reaction k, calculated in dependence of the temperature by applying Eq. 5.25. $C_{ki,i}$ is the kinetic constant, obtained by the Arrhenius equation (5.26). The adsorption constant of the component j is calculated depending on its enthalpy of formation by applying Eq. 5.27. All parameters needed for these calculations are obtained from [155] as well, and are found in Tab. 5.5 and Tab. 5.6.

$$C_{eq,i} = exp\left(\frac{-\Delta G_i}{RT}\right) \tag{5.25}$$

$$C_{ki,i} = c_i exp\left(-\frac{E_{act,i}}{R}\left(\frac{1}{T} - \frac{1}{T_{ref}}\right)\right) \tag{5.26}$$

$$C_{ads,j} = C_{ads,j}^{T_R} exp\left(\frac{-H_{j,ads}}{R}\left(\frac{1}{T} - \frac{1}{T_{ref,j}}\right)\right) \tag{5.27}$$

Table 5.5 – Parameters for the calculations of the reforming reaction rates.

reaction index i	c_i	$E_{act,i}$ in $kJ \cdot mol^{-1}$	T_i^{ref} in K
1	$1.842 \cdot 10^{-4}$	240.10	648
2	7.558	67.13	648
3	$2.193 \cdot 10^{-5}$	243.90	648

Table 5.6 – Adsorption constants and enthalpy for the species taking part in the reforming reactions.

specie index j	$C_{ads,j}^{T_R}$ in bar^{-1}	$H_{ads,j}$ in $kJ \cdot mol^{-1}$	T_j^{ref} in K
CO	40.91	-70.65	648
H_2	0.0296	-82.90	648
CH_4	0.1791	-38.28	823
H_2O	0.4152	88.68	823

For the conversion of the long alkanes a simplified model for the reaction rates has been chosen, since complete reforming is assumed for the usual operating temperatures. Schaedel et al. [137] reported a conversion rate (c_r) of ethane, propane and butane, in a mixture with methane, beginning at 200 °C and reaching a value of 100 % for temperatures over 450 °C (for a $\Phi = 2.5$). Between these temperatures the conversion rate is assumed to behave with a smooth transition between 0 and 100 % (Eq. 5.28), in this case modeled with a sinus function. Thus, the reaction rate can be calculated depending on this conversion rate and on the inlet molar flow of the corresponding alkane by using Eq. 5.29.

$$c_r(T) = \begin{cases} 0 & \text{if } T < T_{min}^{ref} \text{ °C}, \\ -\frac{1}{2}\sin\left(0.5\frac{\left(T - T_{min}^{ref}\right)}{\left(T_{max}^{ref} - T_{min}^{ref}\right)}\pi\right) & \text{if } T_{min}^{ref} < T < T_{max}^{ref}, \\ 1 & \text{if } T > T_{max}^{ref} \text{ °C}. \end{cases} \tag{5.28}$$

Being $T_{min}^{ref} = 200\,°C$ and $T_{max}^{ref} = 450\,°C$.

$$\xi_i = \dot{n}_j^{in} c_r\,(T)\,, \text{ for i =4, 5, 6 and the corresponding j=}C_2H_6, C_3H_8, C_4H_{10} \qquad (5.29)$$

In case of butane, the results of Acvi et al. [36] are consistent with these data: they reported conversion rates of 67 % for $\Phi = 3$ by using nickel catalyst. For the other alkanes no data were found.

5.3.3 Afterburner

The function of the afterburner is the combustion of the part of the anode flue which is not recycled to the inlet of the system. The anode exhaust contains unburned fuel components, since the fuel is not fully oxidized in the stack in order to prevent the degradation of the anode. The oxygen necessary for the combustion comes from the cathode off-gas. The afterburner is part of the air processor and thermally integrated with HE_3 (see Fig. 5.1), the heat exchanger where the heat transfer between the afterburner exhaust gas and the system inlet air takes place.

The afterburner model is based on a volumetric component, including the energy, momentum and mass balance. The species which have been regarded are H_2, CO, CH_4, O_2, H_2O, CO_2 and N_2. The long alkanes are assumed to be reformed at the prereformer, since their presence at the anode would result in its degradation. Accordingly, they are not to be found in the afterburner. The methane entering the fuel cell is usually totally reformed, due to the high temperatures and water concentration. However, the anode flue gas can contain residual amounts of CH_4. In addition, several experiments were carried out on the air processor using methane as fuel. Consequently it is necessary to include this component in the model in order to be able to reproduce these experiments in the simulation.

The reactions implemented in the model are the combustion of the CO, CH_4 and H_2 (Tab. 5.7). It is assumed that if the ignition conditions are fulfilled, as detailed below, a

Table 5.7 – Chemical reactions implemented in the afterburner chamber.

index	*reaction name*	*reaction formula*
1	carbon monoxide combustion	$CO + 0.5O_2 \rightarrow CO_2$
2	methane combustion	$CH_4 + 2O_2 \rightarrow CO_2 + 2H_2O$
3	hydrogen combustion	$H_2 + 0.5O_2 \rightarrow H_2O$

Table 5.8 – Self-ignition temperature and flammability range of the different fuels considered in the afterburner model ($T = 20\,°C$, $p = p_{atm}$) [93].

fuel	*self-ignition temperature*	*lower flammability limit*	*upper flammability limit*
CO	605 °C	12.5 % in gas-air mixture	74.2 % in gas-air mixture
CH_4	610 °C	5.0 % in gas-air mixture	15.0 % in gas-air mixture
H_2	560 °C	4.0 % in gas-air mixture	75.0 % in gas-air mixture

complete combustion of all components takes place. The kinetics of the reactions have not been regarded. Thus, the reaction rates can be calculated by applying Eq. 5.30, being j the burned component in the reaction i.

$$\xi_i^{ab} = \dot{n}_j^{in} \tag{5.30}$$

The combustion is induced by an external flame, which causes an increase in the temperature of the mixture close to the flame. As soon as the ignition temperature is attained, if the mixture is in the flammability range, the auto-ignition conditions are fulfilled (Tab. 5.8). Then, the flame is propagated until complete combustion of the mixture. If the composition of the mixture is under the lower flammability limit (LFL) or over the upper flammability limit (UFL) the combustion takes place locally at the flame area, but it is not propagated and most part of the gas remains unburned [93]. In the model the flammability range is used, but the ignition mechanisms are assumed to be instantaneous and homogeneous in the burner chamber.

5.3.4 Stack

The modeled stack is a planar, co-flow, anode-supported fuel cell stack, whose physical behavior has been detailed in Chap. 2.

The heat losses are different for each individual cell. However, the difference between the central cells is negligible. This is the reason because, in order to simplify the model, the cells are divided in three groups: the top external cell, middle cells and the lower external cell. The external cells are modeled individually, while the group of middle cells are modeled by a single cell, which behavior is expanded for the $(N_{cells} - 2)$ forming the group. The models used in all cases are identical, except for the boundary conditions. The following assumptions are applied:

- Perfect fuel and air distribution between all the cells forming the stack.
- All middle cells have an identical behavior.
- Stack isolation is directly in contact with the stack. Consequently, the losses are modeled as caused by conduction and free convection phenomena. Forced convection and radiation do not take place.
- External cells are in contact with the stack isolation through the side walls and the top/below side, for the middle cells this contact is exclusively effective by the side walls.
- Between the external cells and the middle cells heat exchange occurs: the exchanged heat is divided equally among the cells forming the middle block.

The structure of one individual cell is presented in Fig. 5.6 from the plane perpendicular to the flow direction. It can be seen that six different components form the cell: anode bulk, cathode bulk, anode, electrolyte, cathode and interconnect. Assuming that all channels of a cell behave identically, a single channel unit is modeled and the results are extended to the other channel units. The consequence is a reduction of the

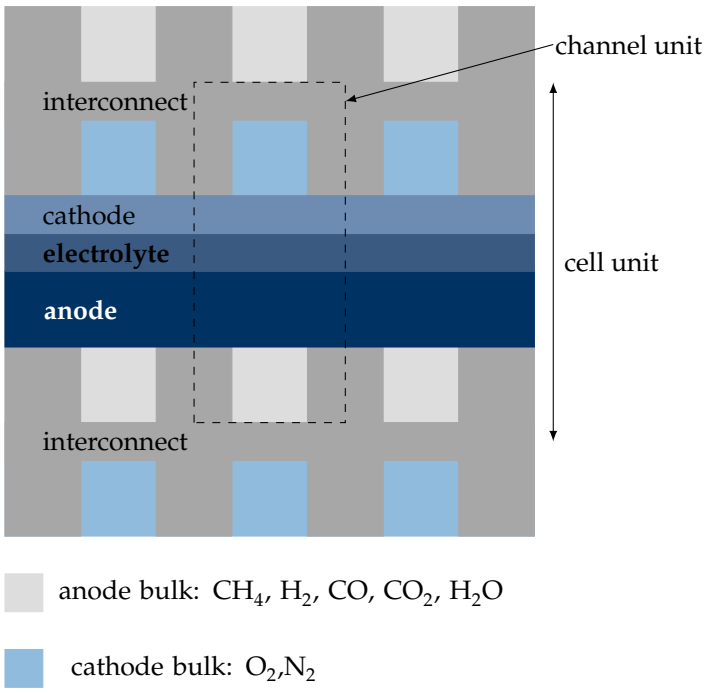

Figure 5.6 – Schematic side view of a typical co-flow planar anode-supported fuel cell, with its main components (not in scale). The cell unit and the channel unit are indicated (for non-side elements).

model complexity without neglecting the geometrical characteristics of the channel. The latter is important to consider, since it influences directly on the calculation of the heat transfer coefficients and of the pressure losses.

The six components forming the cell are reduced to 4 control volumes in the model: anode bulk, cathode bulk, interconnect and PEN (Positive-Electrolyte-Negative). The PEN is formed by the anode, the cathode and the electrolyte. By summarizing the three layers in one component, the following assumptions are automatically taken:

- The temperature does not vary between the anode, the cathode and the electrolyte.
- The material properties required for the calculations are in general calculated as a weighted mean of these from each one of the materials depending on the thickness of the layer.

- The PEN is treated as a solid. Consequently, the mass transport rates through the porous electrodes by diffusion are not modeled in detail. However, not considering the mass limiting effect can result in inaccuracies in the prediction of the polarization curve [42]. Thus, this effect is included in the electrochemical model through the limiting current.

Each control volume is discretized in the flow direction, constituting the quasi-2D approach mentioned before. Fig. 5.7 shows the mentioned control volumes, as well as the heat transfer mechanisms between them. Between the anode, the cathode bulk and the walls the heat transfer occurs due to convection, and between the solid elements by conduction. All mechanisms have been modeled by using the general blocks described in Sect. 5.2.4. The dotted lines represent the boundaries of the channel unit.

The convection coefficients are not assumed to be constant, but calculated for each discretization segment depending on the local gas properties. This complex calculation is important, since in fuel cells with internal reforming the convection coefficients can vary significantly along the bulk due to the change of the temperature. For example, Sánchez et al. reported a variation of the heat transfer coefficient of $300\,W \cdot m^{-2} \cdot K^{-1}$ along the anode bulk and of $175\,W \cdot m^{-2} \cdot K^{-1}$ along the cathode channel [143].

It can be observed that radiation has not been implemented. Two kinds of radiation phenomena nevertheless have to be analyzed. The first one is the radiation between the gases and the surfaces (PEN and interconnect). In case of air, it is formed by non-polar molecules (oxygen and nitrogen), and consequently it can be treated as transparent under the usual SOFC operating temperatures and pressures. On the contrary, the components forming the anode gas are actively contributing species [67]. Even though, Hajimolana et al. [77] reported a little significant temperature change (2.6 K) if the cell is operated under 0.3 bar overpressure, since the emissivity coefficient of gray gases decreases with their partial pressure. Damm and Federov [67] come to

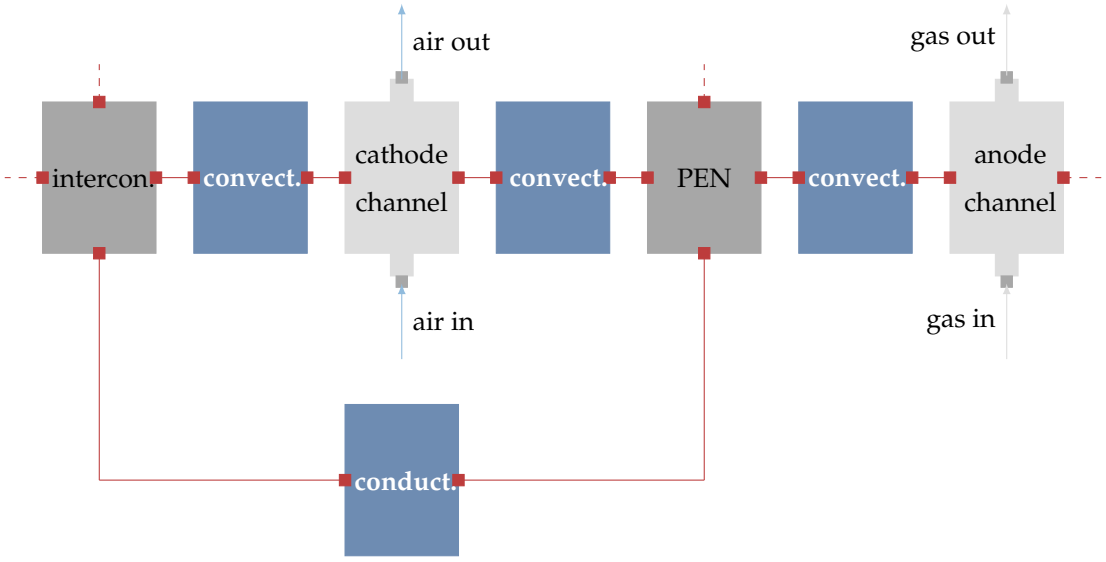

Figure 5.7 – Control volumes forming a single cell model.

the same conclusion, limited to steady-state conditions. The second kind of radiation phenomena is the called surface-to-surface, which in the fuel cell takes place between the channels and the PEN. For of planar fuel cells, the temperature differences between these elements are small, which results in a limited contribution of the radiation in the heat exchange [67]. Burt et al. reported a voltage change below to 3.6 % resulting from the influence of the radiation [47].

The species considered in the air flow are O_2 and N_2. The molar fraction of the other species (mainly Ar, CO_2, Ne) remains under 1 % [2], and consequently they can be safely neglected. The assumption of dry air is also made. The gas flow is considered to be formed by CH_4, H_2O, CO, CO_2, H_2 and N_2. Although the system operates with natural gas, it is assumed that the long alkanes are reformed in the prereformer. Nitrogen is not usually regarded in the anode channels, but in this case is also considered because it can be found in natural gas.

The anode and cathode bulk models are based on the volumetric component described in Sect. 5.2.4. Thus, Eq. 5.5 describes their momentum balance, Eq. 5.1 their energy balance, Eq. 5.10 their mass balance and Eq. 5.11 their species balance. In the

Table 5.9 – Chemical and electrochemical reactions implemented in the cell model.

reaction index	*reaction name*	*reaction formula*	*control volume*
1	hydrogen oxidation	$H_2 + O^{2-} \rightarrow H_2O + 2e^-$	PEN
2	oxygen reduction	$\frac{1}{2}O_2 + 2e^- \rightarrow O^{2-}$	PEN
3	methane-steam reforming	$CH_4 + H_2O \rightleftharpoons CO + 3H_2$	anode bulk
4	methane-steam reforming	$CH_4 + 2H_2O \rightleftharpoons CO_2 + 4H_2$	anode bulk
5	WGS	$CO + H_2O \rightleftharpoons CO_2 + H_2$	anode bulk

balances the effects of the reactions implemented in the model, listed in Tab. 5.9, are included. These reactions are the two electrochemical half-reactions, the methane steam reforming and the water-gas-shift reaction.

In order to simplify the model the oxidation of CO (Eq. 2.29) has not been considered. Hajimolana et al. [78] presented several reasons which justify this assumption. First, since the kinetics of the WGS is considerably faster than the CO oxidation, most CO molecules are consumed in the first reaction [87]. Furthermore, in systems where both H_2 and CO are oxidized, the reaction rate of the first oxidation at 750 °C is 1.9-2.3 times higher than from the second as a result of the larger diffusion resistance of CO [115]. In order to evaluate the effect of this assumption on the results, Ho et al. [85] compared the same 2D fuel cell model (co-flow configuration) with and without considering of CO oxidation. The differences in the resulting current density curve along the bulk were negligible and in the temperature curve remained below 1 K.

The electrochemical half reactions take place at the interfaces between the electrolyte and the corresponding electrode. The location of the heat released in the global reaction has been a discussion topic [86]. The possibilities are the anode or the cathode layers, and since they are modeled in the same control volume, it is clear that they are modeled in the PEN. The consumed oxygen comes from the cathode bulk, and the conversion of hydrogen to water occurs in the anode bulk. The electrochemical reaction rate, defined in Eq. 2.6 for a single cell, is enlarged to the reaction rate for the

entire stack by Eq. 5.31.

$$\xi_{elech} = \frac{N_{cells} I}{2F} \tag{5.31}$$

WGS and methane reforming occur at the surface between the anode and the anode bulk, since the presence of the catalyst is necessary for the occurrence of the reactions. However, in the model, the mentioned surface has been included in the control volume of the anode bulk, being the heat generation/consumption resulting from these reactions placed in the same control volume [133]. The corresponding reaction rates are calculated by applying the same model as in the prereformer (Sect. 5.3.2).

A SOFC stack model involves various time scales for the transient behavior, related to the several phenomena which take place simultaneously. While electrical and electrochemical phenomena have time scales of 10^{-5} to 10^{-3} s, the transient of species transport is the order of magnitude of 1 s and for the thermal processes about 10^{3} s [74]. Thus, it is assumed that the thermal process is the dominant phenomena in the transient behavior, and the transient behavior of the other processes is neglected (except for the kinetics of the reforming reactions, Sect. 5.3.2).

The interconnect is modeled as a solid component: heat conduction in the flow direction (Eq. 5.16) and heat accumulation are taken into account (Eq. 5.19). The heat conduction in the perpendicular direction is included in the conduction block between the PEN and the interconnect. The latter is assumed to be impermeable, consequently only electrons transport is considered. Since its material is characterized by a high electrical conductivity, the interconnect is treated as an equipotential surface and the heat released by the joule effect is neglected.

The PEN model is based on the solid component model, presented previously, but extended with the electrochemical model. It is modeled in one dimension. Assuming that the interconnect is an isopotential surface (Eq. 5.32), its equivalent electrical circuit becomes that shown in Fig. 5.8.

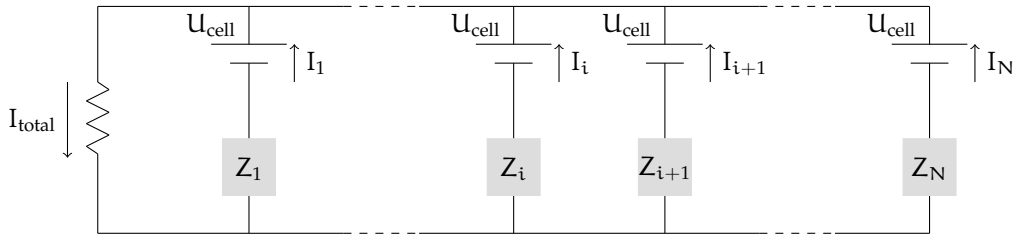

Figure 5.8 – Equivalent electrical circuit of the PEN, based on [114].

$$U_{cell,i} = U_{cell} \tag{5.32}$$

The stack is controlled by the total cell current, which is a command variable. Thus, if one assumes that I_{cell} reaches its set point value, it can be considered to have a known value. On the contrary, the cell current in each discretization node is variable and depending on the temperature and gas composition at the anode and cathode bulk, as detailed in the next paragraphs. However, a restriction which can be deduced from the electrical circuit, is that the total cell current can be calculated as the sum of the current at each discretization volume.

$$I_{tot} = \sum_i I_i \tag{5.33}$$

From this point of the section, all equations regarding the electrochemical model are applied to each discretization compartment of the cell. Even though, the usual index *i* is omitted in order to facilitate the reading.

Instead of the electrical current, *I*, the current density *j* is usually referred to characterize a fuel cell (Eq. 2.7), as detailed in Chap. 2.1.3.

The cell voltage and the current density are related to each other through the irreversible cell losses: the voltage is calculated by subtracting to the Nernst voltage (Eq. 5.35) the overpotentials generated in the cell, which are dependent on the current

density. Three loss phenomena take place in the SOFC: ohmic, activation and concentration losses (Eq. 5.34). The Nernst or reversible voltage is calculated depending on the standard cell voltage ($U_{OC}^{r,0}$, the maximal thermodynamically possible voltage, Eq. 5.36) and the partial pressures of the species participating in the electrochemical reaction (Eq 5.35). The equations are these detailed in Chap. 2.1.3 assuming that the number of transferred electrons is equal to 2.

$$U_{cell} = U_{Nernst} - \vartheta_{ohm}(j) - \vartheta_{act}^{an}(j) - \vartheta_{act}^{cath}(j) - \vartheta_{conc}^{an}(j) - \vartheta_{conc}^{cath}(j) \tag{5.34}$$

$$U_{Nernst} = U_{OC}^{r,0} - \frac{RT}{2F} \ln\left(\frac{p_{H_2O,an}}{p_{H_2,an} p_{O_2,cat}^{1/2}}\right) \tag{5.35}$$

$$U_{OC}^{r,0} = \frac{-\Delta G^0}{2F} \tag{5.36}$$

The ohmic losses are consequence of the resistance found by the electrons and the oxygen anions in their movement through the components of the cell. It is calculated by using second Ohm's Law, which relates the current, the potential and the ohmic resistance. The latter is calculated depending on the electrical conductivity of the materials and the length of the paths of the electrons and ions. Their lengths are simply considered to be the thickness of each layer, assuming that conduction only occurs in the direction perpendicular to the bulk [62]. Five contributions to the ohmic overpotential have been regarded: from the anode, the cathode, the electrolyte, the interconnect and the contact resistance. The first four layers are accounted by most authors. On the contrary, the contact resistances are neglected by most of them. However, their contribution in the total ohmic resistance can be relevant (as for example as shown by Zhu and Deevi in [159]), and consequently they should be regarded. By applying these assumptions to Eq. 2.24 and Eq. 2.25 the ohmic losses are calculated by using Eq. 5.37.

$$\vartheta_{ohm} = \left(\frac{\delta^{an}}{\sigma^{an}} + \frac{\delta^{elect}}{\sigma^{elect}} + \frac{\delta^{cath}}{\sigma^{cath}} + \frac{\delta^{ic}}{\sigma^{ic}} + \frac{\delta^{cont}}{\sigma_{cont}} \right) j \tag{5.37}$$

The electrical conductivity of the different solid materials *k* is calculated as function of the temperature by applying Arrhenius equation (Eq. 5.38 for the anode, the cathode and the interconnect and Eq. 5.39 for the electrolyte). In case of the anode and the cathode the effect of their porosity is taken into account in the calculation of the resistivity, by applying Eq. 5.40 [78].

$$\sigma_{solid,k} = \frac{A_k}{T} exp\left(\frac{B_k}{T} \right), \text{ for } k = an, cath, ic \tag{5.38}$$

$$\sigma_{solid,el} = A_{electrl} exp\left(\frac{B_{electr}}{T} \right) \tag{5.39}$$

$$\sigma_{porous} = \sigma_{solid} \left(1 - \epsilon\right)^{1.5} \tag{5.40}$$

In case of the interconnect a third-grade polynomial has been fitted to the temperature-dependent resistivity curve, included in the technical data sheet from the material provider [7]:

$$\sigma_{ic} = -0.001250249T^3 + 4.185429T^2 - 4857.595T + 2.859824 \cdot 10^6 \tag{5.41}$$

Several parameters for the calculation of the electrical conductivity and the porosity for the different materials are presented in Tab. 5.10. They have been partially obtained from the literature and partially from internal sources, and several of them fitted to the experimental data (Sect. 5.5.1).

The activation loss at each electrode is described by the Butler-Volmer equation (Eq. 2.23). It depends on j_0, the equilibrium exchange current density. This is the current produced/consumed at the electrodes when the current density is zero, that is, when the electrochemical reactions and their reverse take place at the same rate [106].

Noren and Hoffman [120] detailed the adaption of this general equation to that usually considered in SOFC models. α_1 and α_2, the charge transfer coefficients, could be calculated if the intermediate steps of these reactions were known by applying Eq. 5.42 and Eq. 5.43. They depend on the number of electrons transferred in the global reaction (n_{e^-}), the number of electrons transferred before the rate determining step (n_b), the number of times that the rate determining step takes place in the global reaction (n_t), the number of electrons transferred in the rate determining step (n_d) and the symmetry factor (β).

$$\alpha_1 = \frac{n_{e^-} - n_b}{n_t} - n_d\beta \tag{5.42}$$

$$\alpha_2 = \frac{n_b}{n_t} + n_d\beta \tag{5.43}$$

Assuming that the reaction happens in one unique step, the reaction becomes automatically the rate determining step, so that n_b=0, n_t=1 and n_{e^-}=n_d. Thus, the transfer coefficients at Eq. 2.23 could be replaced by Eq. 5.44 and Eq. 5.45 and the generally used simplification of the Butler-Volmer equation (Eq. 5.46) would be obtained.

$$\alpha_1 = (1-\beta)\, n_{e^-} \tag{5.44}$$

$$\alpha_2 = \beta n_{e^-} \tag{5.45}$$

$$j = j_0 \left(exp\left((1-\beta) \frac{F \cdot n_{e^-} \vartheta_{act}}{RT} \right) - exp\left(-\beta \frac{F n_{e^-} \vartheta_{act}}{RT} \right) \right) \tag{5.46}$$

In order to simplify the equation, the symmetry factor is often assumed to be $\beta = 0.5$ for both the cathode and the anode. Thus, $\alpha_1 = \alpha_2$, and consequently Eq. 5.46 can be approximated by the hyperbolic sinus function. By applying again the assumption of a unique step and defining $1 - \beta = \alpha$, the Butler-Volmer equation can be rewritten in an explicit form as Eq. 5.47. In [120] a good agreement is shown between the results obtained from Eq. 5.47 and Eq. 5.46, also if after the simplification α was varied between 0.1 and 0.9.

$$\vartheta_{act}^{an/cath} = \frac{RT}{\alpha n_{e^-} F} \sinh^{-1}\left(\frac{j}{2 j_0^{an/cath}} \right) \tag{5.47}$$

The symmetry factor is related to the electrochemical reaction rate, and n_{e^-} is the number of transferred electrons in the reaction. However, since the assumption in which the equation simplification is based is not correct (it is usually considered that the reactions are not single step reactions [34]), the parameters loose their physical meaning. Thus, a new parameter α_{eff} is defined, named effective charge transfer coefficient (Eq. 5.48). If it is replaced in Eq. 5.47 a new definition of the activation overpotential results (Eq. 5.49). α_{eff} is a parameter to be obtained from fitting of the experimental data, for the anode and the cathode.

$$\alpha_{eff} = \alpha n_{e^-} \tag{5.48}$$

$$\vartheta_{act}^{an/cath} = \frac{RT}{\alpha_{eff}^{an/cath} F} \sinh^{-1}\left(\frac{j}{2 j_0^{an/cath}} \right) \tag{5.49}$$

The calculation of the exchange current density for the anode and cathode (j_0^{an}, j_0^{cath}) is presented in Eq. 5.50 and Eq. 5.51. It is expressed depending on the partial pressures

of the components taking part in the reaction (H_2 and H_2O at the anode and O_2 at the cathode), on the frequency factors (γ^{an} and γ^{cath}) and on the Arrhenius equation [63]. Many different values for the parameters of the last equations are found in the literature. In case of the frequency factors and the activation energy the used values are listed in Tab. 5.10. The exponents for the anode current density are calculated from the data from Bieberle et al. [43], resulting $a = 0.12$ and $b = 0.7$. The exponent for the cathode is $c = 0.25$ [28].

$$j_0^{an} = \gamma^{an} \left(\frac{p_{H_2}}{p^0}\right)^a \left(\frac{p_{H_2O}}{p^0}\right)^b exp\left(\frac{-E_{act}^{an}}{RT}\right) \tag{5.50}$$

$$j_0^{cath} = \gamma^{cath} \left(\frac{p_{O_2}}{p^0}\right)^c exp\left(\frac{-E_{act}^{cath}}{RT}\right) \tag{5.51}$$

The concentration losses result from the concentration gradients between the anode/cathode bulk and the TPB's, which cause a difference between the calculated Nernst voltage and its actual value (Eq. 2.27). The thicker the electrode and the lower the diffusivity coefficient, the higher the concentration losses (Eq. 2.26). In general they take place at both the anode and the cathode (for the H_2 and H_2O diffusion and for the O_2 diffusion respectively). However, this latter can be neglected in case of anode supported fuel cells, because the thickness of the cathode is very small compared to that of the anode [46]. Then, the anode concentration losses can be calculated as follows [140]:

$$\vartheta_{conc}^{an} = -\frac{RT}{2F} \ln\left(1 - \frac{j}{j_{lim}^{an}}\right) + \frac{RT}{2F} \ln\left(1 + \frac{p_{H_2,an} j}{p_{H_2O} j_{lim}^{an}}\right) \tag{5.52}$$

The anode limiting current density, j_{lim}^{an}, is the current density at which the hydrogen concentration at the triple-phase-boundary is zero. In this case starvation occurs, which results in a drastic voltage drop and contributes to the degradation of the fuel cell. If it is assumed that the triple-phase-boundary is located exclusively

at the electrode-electrolyte interface, the limiting current density can be calculated dependent on the anode thickness δ^{an} [102].

$$j_{lim}^{an} = \frac{2Fp_{H_2}^{an} D_{eff}^{an}}{RT\delta^{an}} \tag{5.53}$$

In order to calculate the diffusion coefficient it has been used the expression developed by Petersen [128]. It accounts for binary and Knudsen diffusion, and is calculated as function of the hydrogen molar fraction by applying an experimental correlation (Eq. 5.54). It is adapted to the current pressure and temperatures by using Eq. 5.55, being $T^{ref} = 750\,°C$ and $P_{ref} = 1\,atm$. Finally, the effect of the anode porosity, ϵ^{an}, and tortuosity, τ^{an} is accounted in the calculation of the effective diffusion coefficient by using Eq. 5.56.

$$D_{exp} = dx_{H_2} + e \tag{5.54}$$

$$D^{an} = D_{exp} \left(\frac{T}{T^{ref}} \right)^{\frac{7}{4}} \frac{P^{ref}}{P} \tag{5.55}$$

$$D_{eff}^{an} = \frac{D^{an} \epsilon^{an}}{\tau^{an}} \tag{5.56}$$

5.4 Optimization of the discretization

The decision of modeling the system in one dimension has been taken assuming that it contributes to improve the quality of the model. A disadvantage of the discretization is the increase in the modeling process complexity. Additionally, the simulation

Table 5.10 – Parameters used in the electrochemical model.

parameter	*value*	*unit*	*equation*	*experimental fitting*
A^{electr}	33400 [45]	$S \cdot m^{-1}$	Eq. 5.39	no
A^{an}	$9.5 \cdot 10^7$ [45]	$S \cdot K \cdot m^{-1}$	Eq. 5.38	no
A^{cath}	$4.2 \cdot 10^7$ [45]	$S \cdot K \cdot m^{-1}$	Eq. 5.38	no
A^{ic}	$9 \cdot 10^5$ [7]	$S \cdot K \cdot m^{-1}$	Eq. 5.38	no
B^{electr}	-10300 [45]	K	Eq. 5.39	no
B^{an}	-1150 [45]	K	Eq. 5.38	no
B^{ic}	0 [7]	K	Eq. 5.49	no
B^{cath}	-1200 [45]	K	Eq. 5.49	no
δ^{electr}	10	μm	Eq. 5.39	no
δ^{an}	260	μm	Eq. 5.38	no
δ^{cath}	50	μm	Eq. 5.49	no
δ^{ic}	1	mm	Eq. 5.49	no
ϵ^{an}	0.4	–	Eq. 5.40	no
ϵ^{cath}	0.4	–	Eq. 5.40	no
τ^{an}	2.5	–	Eq. 5.56	no
α_{eff}^{an}	1 [120]	–	Eq. 5.49	yes
α_{eff}^{cath}	1[120]	–	Eq. 5.38	yes
E_{act}^{an}	$100 \cdot 10^3$ [64]	$J \cdot mol^{-1}$	Eq. 5.50	yes
E_{act}^{cath}	$117 \cdot 10^3$ [49]	$J \cdot mol^{-1}$	Eq. 5.51	yes
γ^{cath}	$7 \cdot 10^8$ [49]	$A \cdot m^{-2}$	Eq. 5.51	yes
γ^{an}	$5.5 \cdot 10^8$ [64]	$A \cdot m^{-2}$	Eq. 5.50	yes
a	0.12 [43]	–	Eq. 5.50	no
b	0.7 [43]	–	Eq. 5.50	no
c	0.25 [28]	–	Eq. 5.51	no
d	$-4.107 \cdot 10^{-5}$ [128]	–	Eq. 5.54	no
e	$8.704 \cdot 10^{-5}$ [128]	–	Eq. 5.54	no

becomes more time consuming. In this section the dependence between discretization nodes, accuracy of the results and calculation time is analyzed, with the purpose of finding an optimal number of discretization nodes.

Fig. 5.9 shows the outlet temperatures of the hot and the cold side of the air processor ($T_{9,a}$ and $T_{3,a}$ respectively in Fig. 5.14). In order to obtain these data the fuel processor parameters, as well as the inlet gases properties, have been maintained constant while the number of discretization nodes (N) has been varied. It can be observed that the difference between a 0D model (N=1) and the 1D model is significant, up to the point that in the first case the temperature at the cold side outlet is lower than at the hot side and for N>1 it happens the opposite. Both temperatures change with the number of discretization nodes, but it can be seen that the deviation becomes lower with higher N until they converge for N=15 ($\Delta T < 2\,K$ between N=15 and N=16). However, from N=6 the temperatures can be considered stable ($\Delta T < 10\,K$ between N=6 and N=7).

Additionally, the calculation time of the model is presented depending on N. It can be seen that the order of magnitude is of 0.1 s and that it varies lineally with N. The compilation time, which is not shown, has an order of magnitude of 100 s.

The same data are presented for the fuel processor in Fig. 5.10. In this case the cold side corresponds to $T_{5,f}$ in Fig. 5.16 and the hot side to $T_{8,f}$. Compared to the air processor, the temperatures converge for a lower number of discretization nodes ($\Delta T < 2\,K$ for N=10). The reason is that the temperature gradients are significantly lower. On the other side, since this component consists of a higher number of subcomponents, the calculation time is considerably longer (order of magnitude of 10 s). Additionally, the fuel processor contains the fuel pre-reformer, in which chemical reactions take place, increasing significantly the complexity of the model and consequently the calculation time. The same happens with the compilation time, which reaches an order of magnitude of 500 s.

In case of the stack, the variable observed for the optimization of the discretization has

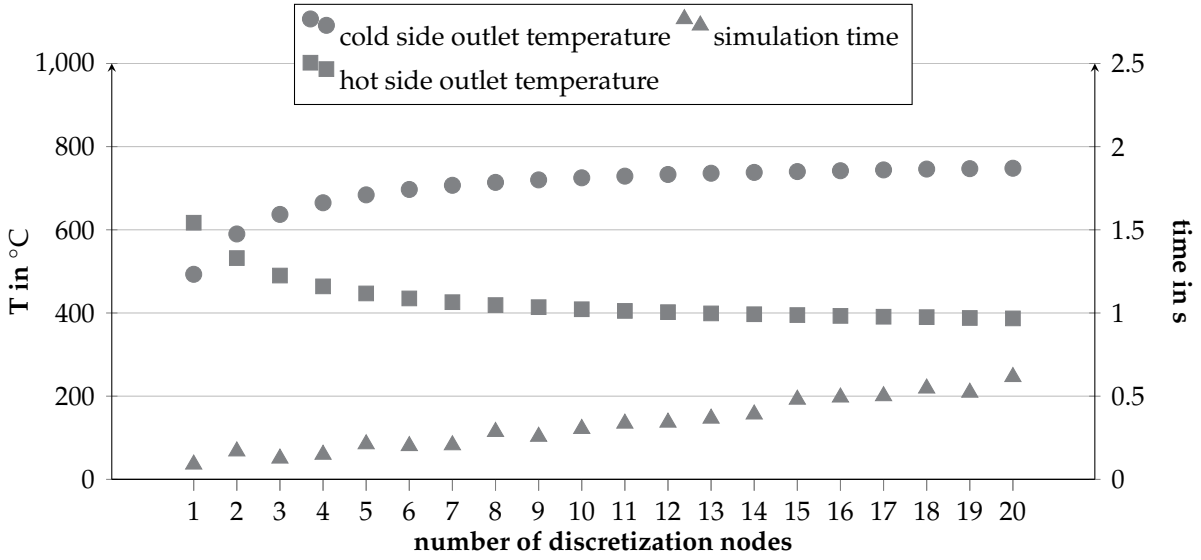

Figure 5.9 – Temperatures of the air processor and simulation time corresponding to 7200 s (time to reach the steady-state) depending on the number of discretization nodes.

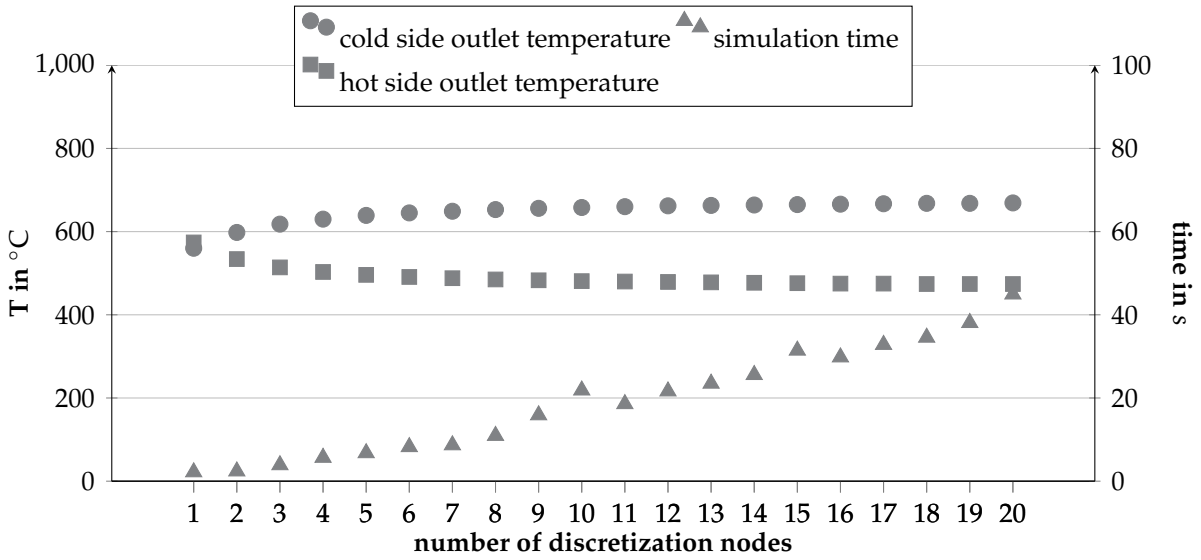

Figure 5.10 – Temperatures of the fuel processor and simulation time corresponding to 7200 s (time to reach the steady-state) depending on the number of discretization nodes.

been the current density (j). In Fig. 5.11 is presented the current density distribution over the stack length depending on the number of discretization nodes. Due to the CSTR assumption (the value of a variable in a discretization volume corresponds to the outlet value) there is not any value corresponding to the first discretization node in any case. It can be observed that for N>2 the curves present the same form, varying exclusively for the maximum value. As for the air and fuel processors, the change in the model predictions decreases for higher values of N. On the contrary, the curve obtained from N=2 does not represent the real current density profile over the cell, and its maximal value and value at the output differ from the other curves substantially.

The calculation time of the stack model for the different numbers of discretization nodes are shown in Fig. 5.12. The order of magnitude is of 10 s and it can be observed that it remains below 20 s until N=3 and from then it increases linearly. The calculation time corresponding to the stack is long compared to the other components, due to the high number of equations and non-linearities which describe its behavior. An example is the simultaneous calculation of the current density j and the different voltage losses for each discretization node, values depending on each other related by non-linear equations. Regarding the compilation time the same effect is observed: approximately 1000 s are required.

When the components are connected to each other in order to model the entire system the calculation time becomes significantly larger than to this of the single models. The reason is that the coupling between components through the different flows, including the anode flue recycling. For example, for a calculation corresponding to 50000 s the calculation time for the air processor with N=4 is of 0.15 s, 5.75 s for the fuel processor and 29.15 s for the stack. However, in case of the simulation of the complete system, the calculation time is increased to 158 s. The compilation time becomes significantly larger as well, attaining of 5400 s for N=4. For this reason the number of discretization nodes per component has to be limited. In case of the air processor and

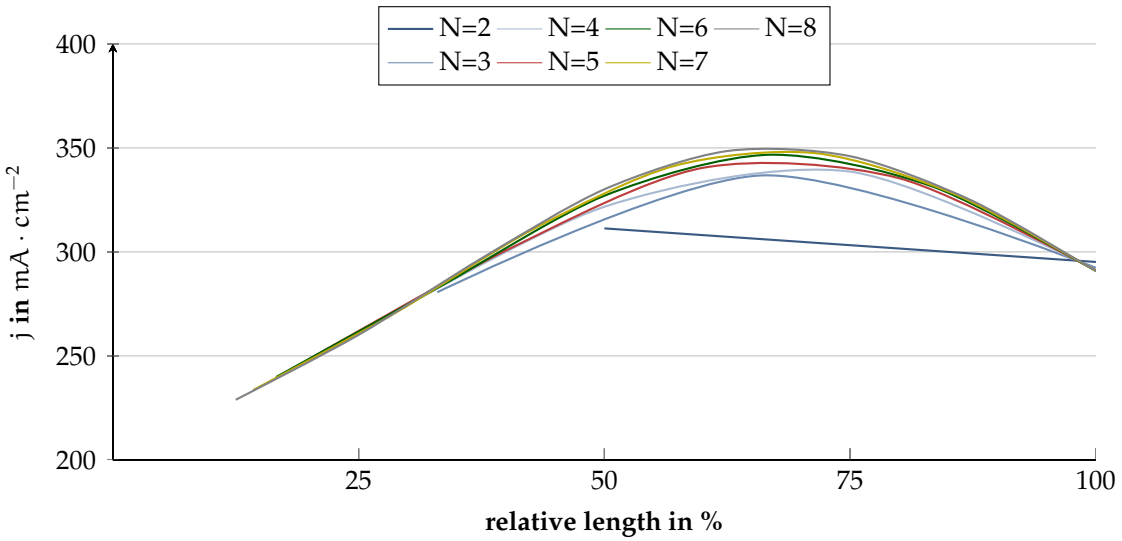

Figure 5.11 – Current density along the fuel cell for different amount of discretization nodes.

the fuel processor, the value considered as a compromise between calculation time and accuracy is N=8 and for the stack N=3. In the following, all models used in this work have been discretized in the flow direction with this number of nodes.

5.5 Parameterization and validation

In order to adapt the theoretical models of the stack and the other components to the real behavior, some of the parameters have been fitted to experimental values. For the stack these parameters are indicated in Tab. 5.10, while for the air and fuel processors they are geometrical and material parameters. In this section the procedure of the parameterization is described. Additionally, simulation results obtained with the model are compared to experimental values in order to validate the model.

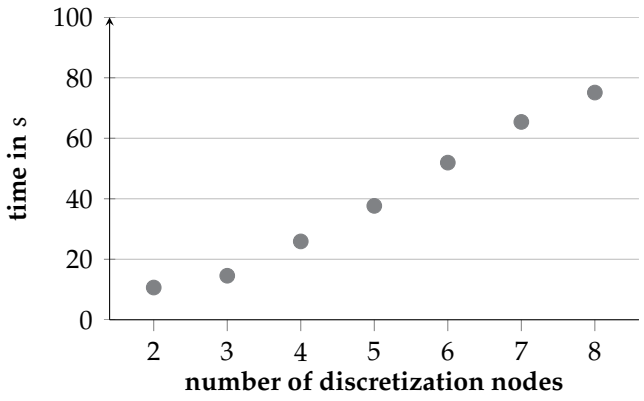

Figure 5.12 – Calculation time of the stack corresponding to 7200 s (time to reach the steady-state) depending on the number of discretization nodes.

5.5.1 Parameterization and validation of the electrochemical model of the stack

The aim of the electrochemical model is not to calculate the different losses mechanisms with precision, but to predict a polarization curve which characterizes the behavior of the fuel cell. For this purpose, the values resulting from the tests carried out by the department *CR/ARC* at *Robert Bosch GmbH* are used. The tests have been carried out with a stack run with different fuels (reformate and hydrogen), at different temperatures (680 °C, 720 °C, 750 °C and 770 °C), and different fuel utilizations (FU). For each operation conditions, the cell voltage has been measured for various current densities in order to generate polarization curves. In total 47 pairs of values U-j have been obtained experimentally.

As detailed in the previous section, several parameters are taken from the literature. In Tab. 5.10 these parameters are presented, together with the values which have been assumed for each one and the corresponding sources. Some of the parameters have been chosen to be fitted, with the criteria of being the most uncertain parameters of each losses mechanism.

The stack model has been discretized in 3 nodes, since it is the optimal value regard-

ing simultaneously accuracy and time-economy (Sect. 5.4). For the parameterization 11 pairs of values U-j have been used, corresponding to the tests run with reformate by a FU=70 % at each of the mentioned temperatures. In order to fit the data, the combination of parameters which minimize the difference between the experimental and simulation results for each of point n has been found (Eq. 5.57). The variation of the parameters from the original literature values has been restricted to 20 %.

$$f_{min} = \min\left(\sum_{n=1}^{11} \text{abs}\left(U_{sim,n} - U_{exp,n}\right)\right) \tag{5.57}$$

In order to validate the parameterized model, the experimental and the simulation values for the remaining 36 U-j pairs of values have been compared. As example, the results for 720 °C and 750 °C are presented in Fig. 5.13. It can be observed that the simulation reproduces the trend of the experiments with a good accordance in all cases. It is to be remarked that even for the experiments run with H_2 the divergence remains low. The maximal error between the experimental and simulation data, on the 47 operating points and calculated by applying Eq. 5.58, is of 1.8 % and the mean error is near 0.5 %.

$$\epsilon_{sim,n} = \frac{U_{exp,n}\left(j_n\right) - U_{sim,n}\left(j_n\right)}{U_{exp,n}\left(j_n\right)} \tag{5.58}$$

5.5.2 Parametrization and validation of the air processor

The air processor consists in the afterburner and a heat exchanger, which are thermally integrated with each other. Since several geometrical and material properties of the components are not possible to measure with enough precision, a fitting with experimental data becomes necessary. For this purpose a specific experimental test is carried out for the air processor. A diagram of the test bench, including the actuators and the sensors, is presented in Fig. 5.14.

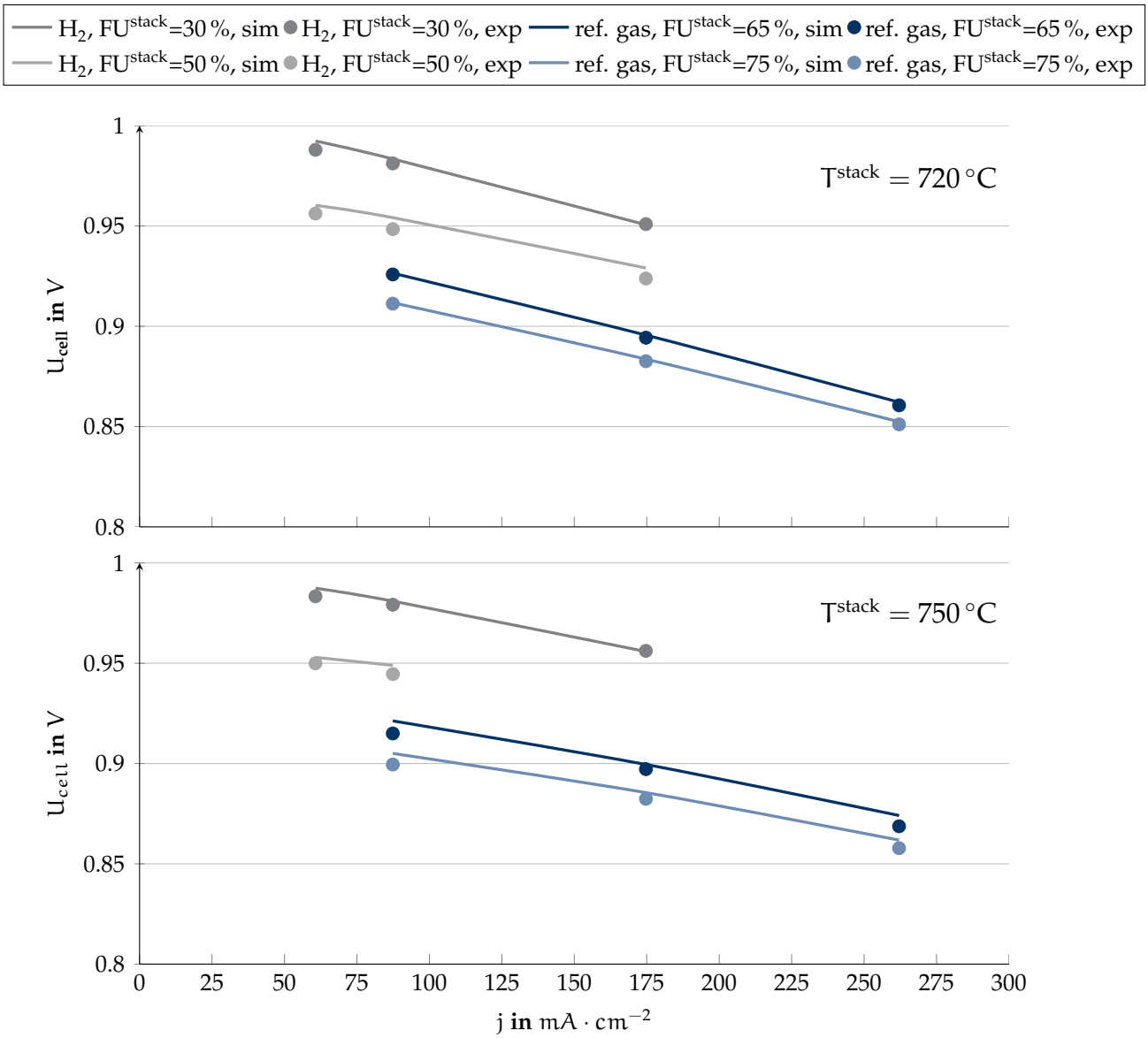

Figure 5.13 – Validation of the electrochemical characteristics, for various stack temperatures, fuels and values of FU^{stack}.

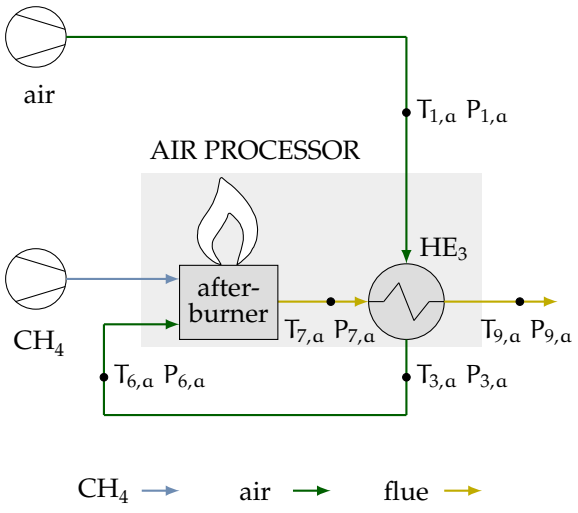

Figure 5.14 – Test bench for the parameterization of the air processor, with the nomenclature corresponding to the complete system presented in Fig. 5.18

The control variables are the methane volumetric flow and the air to fuel ratio. λ is varied between 7.01 and 8.1 and $\dot{v}_{CH_4}$ between 3.6 $Nl \cdot min^{-1}$ and 8.1 $Nl \cdot min^{-1}$. In total 14 different operating points are tested, measuring in all cases the temperature and the pressure in all points of the system. Nine of them are used for the parameterization and the other five for validation.

The parameterization of the model has been carried out by minimizing the error between the experimental and simulated temperatures. This procedure is not straightforward, since there is not only an output variable, but in this case they are four T_m (T_{3a}, T_{6a}, T_{7a} and T_{9a}, since T_{1a} is taken as input variable). Furthermore, they cannot be fitted independently from each other due to the high thermal integration of the components. Thus, an error function has been defined for each operating point n, as the maximum of the deviation committed in each of the m points of the system (Eq. 5.59):

$$\Delta_{max,n} = \max\left(\text{abs}\left(T_{m,sim,n}\left(\lambda_n, \dot{v}_{CH_4,n}\right) - T_{m,exp,n}\left(\lambda_n, \dot{v}_{CH_4,n}\right)\right)\right), \text{ for m=2,3,4,5} \tag{5.59}$$

The combination of parameters which has been adopted is the combination which minimizes Δ_{max} for the 9 operation points. Then, by applying the chosen combination, the model has been validated by comparing the experimental and the simulation results for 5 new operating points. The results for the operating points with the maximal and minimal volumetric flows, are presented in Fig. 5.15. It can be seen that the trend of the experimental data is accurately reproduced by the simulated values, except for the temperature of point 4, corresponding to the afterburner temperature. The reason is that, while in the model this temperature is equivalent to the adiabatic flame temperature, in the real system the sensor is located outside the combustion chamber. Thus, they cannot be compared directly and consequently this measurement point is not taken into account in the evaluation. The maximal committed deviation Δ_{max} for the 14 operation points is of 29.8 K (Eq. 5.60). However, the mean deviation is of 10.18 K (Eq. 5.61). With these results, the air processor model is considered thermally validated.

$$\Delta^{T}_{max} = \max\left(\text{abs}\left(T_{m,sim} - T_{m,exp}\right)\right), \text{ for m=2,3,5} \tag{5.60}$$

$$\Delta^{T}_{mean} = \frac{\sum_n \sum_m \text{abs}\left(T_{m,sim,n} - T_{m,exp,n}\right)}{m \cdot n}, \text{ for m=2,3,5} \tag{5.61}$$

The geometrical characteristics influence both the temperatures and the pressure losses of the system. Since the temperature is the most relevant property, and at the same time the most sensitive due to the thermal integration, the fitting of the geometrical parameter has been made only regarding the temperatures. After that, and in order to ensure a correct simulation of the pressure losses, the minor losses (z_k in Eq. 5.9) are fitted by applying the same method to the temperatures. The results of the validation of two operation points are shown in Fig. 5.15. In this case the agreement is good for all four system points. If the 14 operating points are treated, a maximal divergence between experimental and simulation results of 2.38 mbar (10.22 % regarding

relative pressure) is attained (Eq. 5.62). The mean discrepancy between simulation and experimental results, by using Eq. 5.63, is of 1.13 mbar (8.28 % of error). Thus, it is confirmed that the model reproduces the behavior of the pressure drop at the air processor with a high accuracy.

$$\Delta^{P}_{max} = \max\left(abs\left(P_{m,sim} - P_{m,exp}\right)\right), \text{ for m=2,3,5} \tag{5.62}$$

$$\Delta^{P}_{mean} = \frac{\sum_n \sum_m abs\left(P_{m,sim,n} - P_{m,exp,n}\right)}{m \cdot n}, \text{ for m=2,3,5} \tag{5.63}$$

5.5.3 Validation of the fuel processor

In case of the fuel processor it has not been possible to realize specific tests for the parameterization, due to restrictions of the test bench. However, since the construction of the air processor and of the fuel processor are very similar, the values obtained from the parameterization of the first are applied to the fuel processor.

In order to validate the behavior of the fuel processor, the experiments carried out at the complete system have been used. Two operating points have been run: at full load and at 56 % of the design operating point. Then, the characteristics of the inlet fuels of the parameterized component (shown in Fig. 5.16) are taken from the experimental values and kept constant for the simulations. Thus, the effects of the fuel processor parameters can be analyzed.

Fig. 5.17 presents the experimental data together with the simulation results, for the operation at 56 % of the design operating point. The temperature and pressure curves are presented for the hot and the cold side of the fuel processor. The measurement

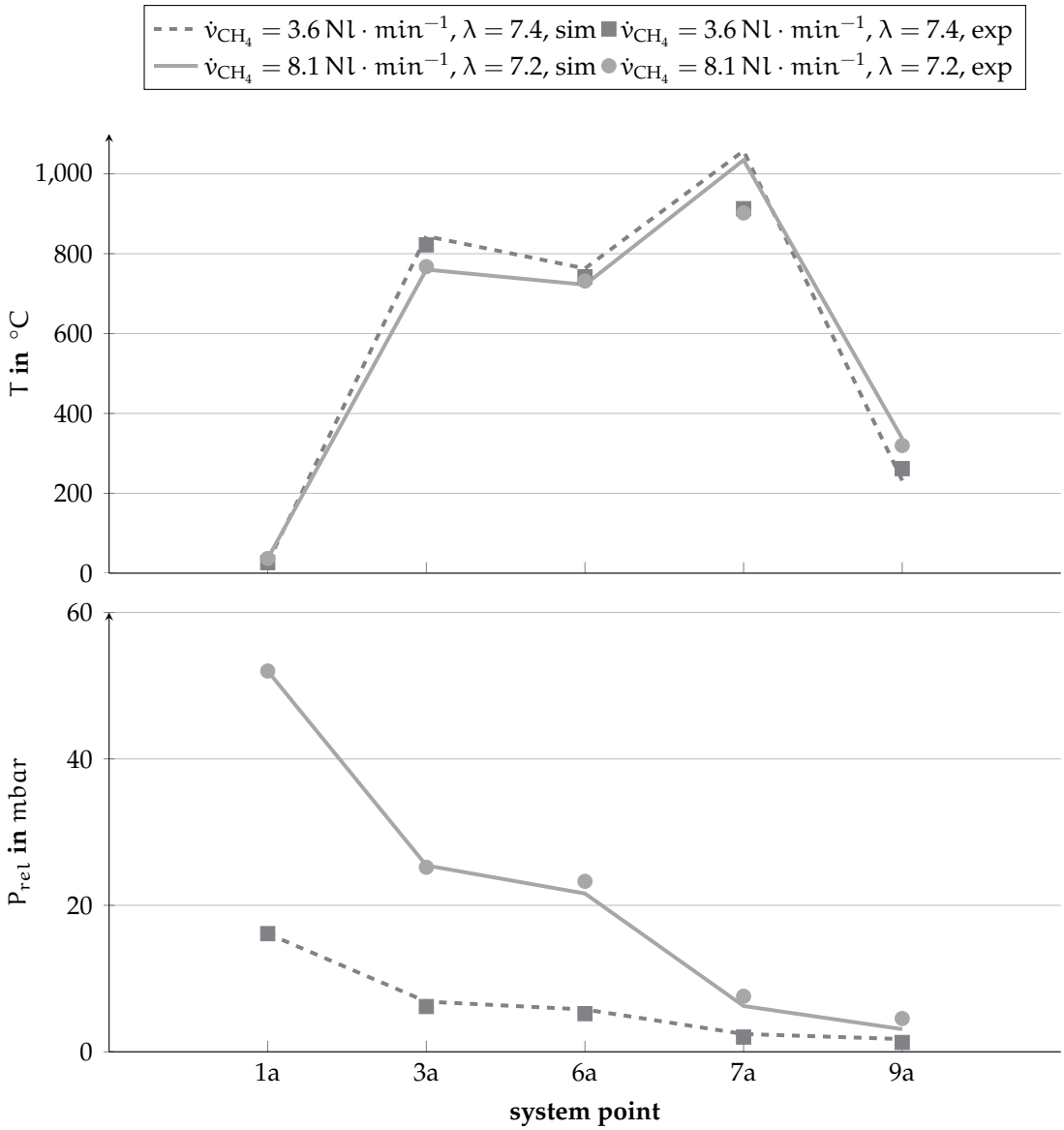

Figure 5.15 – Validation of the temperature and relative pressure behavior of the air processor.

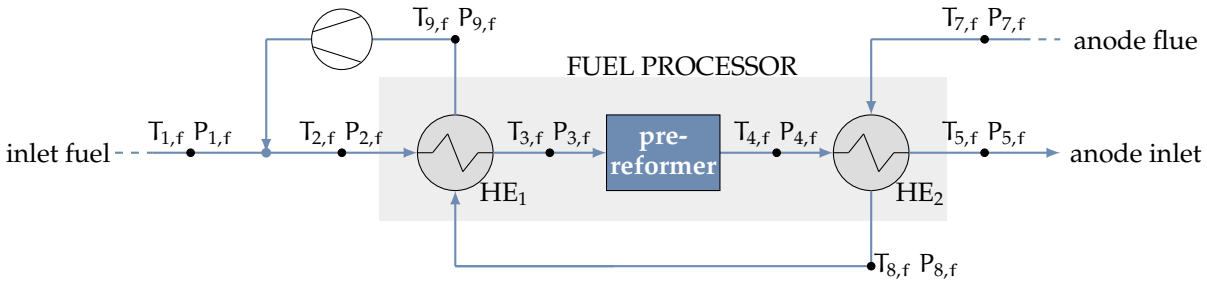

Figure 5.16 – Measurement points of the fuel processor, with the nomenclature corresponding to the complete system presented in Fig. 5.18.

points are referenced in Fig. 5.16. It can be observed that in general the model reproduces the fuel processor behavior accurately, for both the temperatures and the pressure drops. However, for the temperature at point 3 of the hot side a high deviation is to be seen. It is assumed to be result of a defect temperature sensor, since otherwise this effect should be observed in other points of the component, as consequence of the high thermal integration. If the measurements at this point are not included, the maximal deviation in the temperatures is of 47.2 K (Eq. 5.60) and the mean discrepancy is of 22.75 K (Eq. 5.61). Regarding the pressures, the maximal difference between experimental and simulation results is of 2.5 mbar (Eq. 5.62), corresponding to an error of 5.15 %, and the mean value of 1.6 mbar (Eq. 5.63), which corresponds to a mean error of 4.80 %. Consequently, the fuel processor can be considered thermally validated.

Regarding the prereformer behavior, no experimental data are available to be compared with the simulation results. Thus, the prereformer outlet temperatures and compositions have been compared with the data generated by a second model. It is created with Cantera©, an open-source software used for solving chemical problems. By using Cantera, it is possible to calculate the thermodynamical properties and the final composition of a mixture in equilibrium. The properties which are regarded are pressure, temperature, density, enthalpy, entropy and internal energy. Two of these properties have to be given as constant, so that the software can solve the problem. In this case it is assumed an adiabatic behavior (the prereformer is well insulated) and

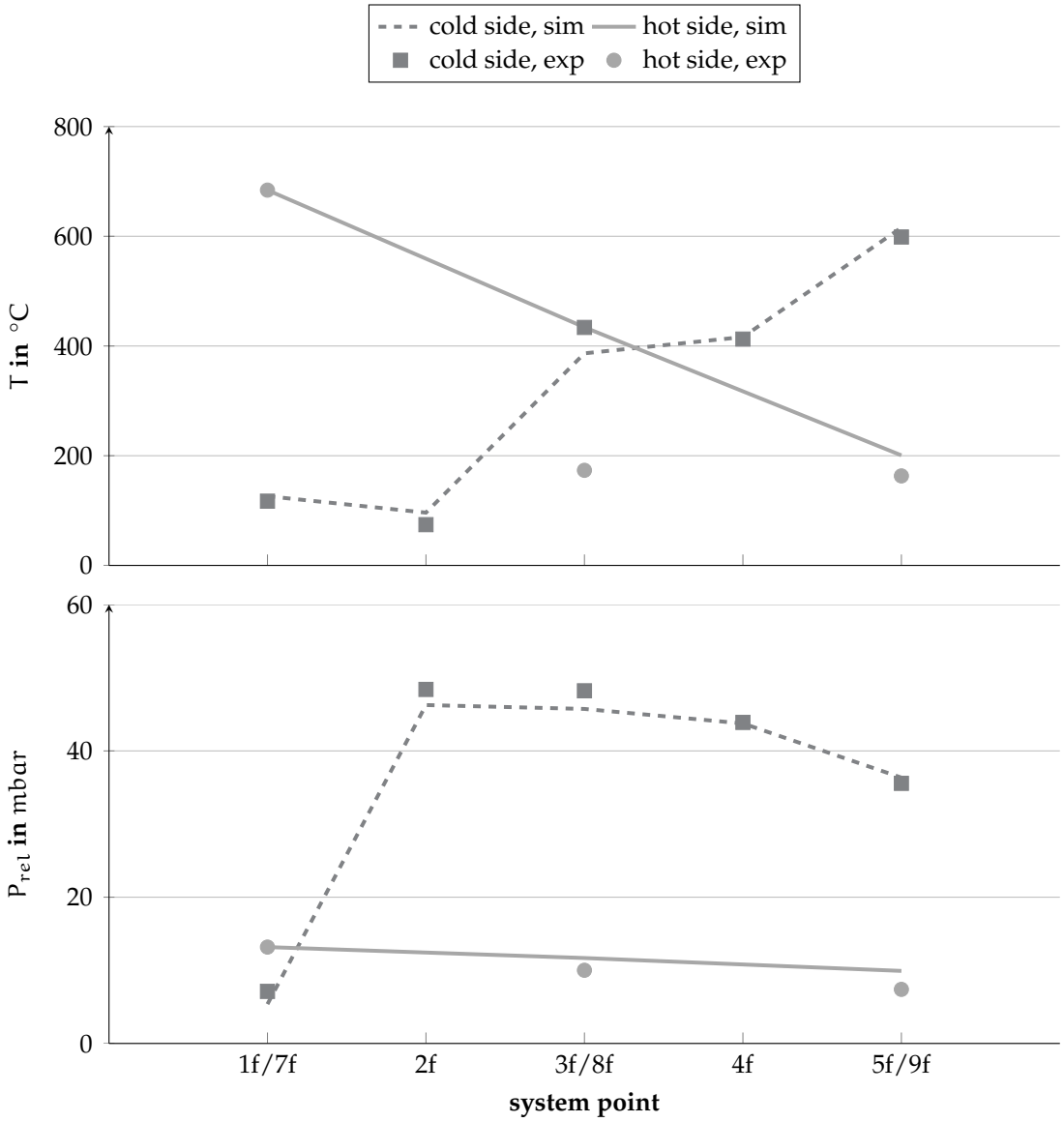

Figure 5.17 – Validation of the temperature and relative pressure behavior of the fuel processor for the second test set at part load (56 % of maximal current).

Table 5.11 – Values of the prereformer output gas resulting from the Modelica® model and from the Cantera® model.

property	*inlet*	*outlet (Modelica)*	*outlet (Cantera)*	*deviation in %*
T in °C	466.50	504.87	503.88	0.13
x_{CH_4} in $mol \cdot mol^{-1}$	0.131	0.139	0.139	0.13
x_{H_2O} in $mol \cdot mol^{-1}$	0.373	0.325	0.322	0.91
x_{CO} in $mol \cdot mol^{-1}$	0.079	0.037	0.035	3.38
x_{CO_2} in $mol \cdot mol^{-1}$	0.206	0.249	0.251	-0.59
x_{H_2} in $mol \cdot mol^{-1}$	0.192	0.236	0.239	-1.22
x_{O_2} in $mol \cdot mol^{-1}$	0.014	0.014	0.014	-0.88
$x_{C_2H_6}$ in $mol \cdot mol^{-1}$	0.004	0.000	0.000	0.00
$x_{C_3H_8}$ in $mol \cdot mol^{-1}$	0.001	0.000	0.000	0.00

a constant pressure (the effects on the results of the measured pressure drop at the prereformer are negligible) [84].

Tab. 5.11 shows the comparison of the prereformer output values resulting from both models, for a typical operating point. The deviation between the results obtained with both models is negligible. The tested operating points include different Φ, temperatures and gas compositions (containing all the species regarded in the prereformer model). Thus, the prereformer is assumed as validated in equilibrium.

5.5.4 Validation of the system model

The system has been validated for the same operating points as the fuel processor. Fig. 5.19 shows the comparison between the experimental and the simulation results for the fuel and for the air path at part load (56 % of the design point) and Fig. 5.20 for full load. It can be observed that in both cases the temperature paths are very similar. The only difference is that in full load the temperatures are between 10 K and 30 K

higher than in part load. The reason is that the system operates producing a higher electrical power and consequently the amount of released heat becomes higher as well, increasing the temperature at each point of the system.

It can be observed that the trend of the experimental results is correctly followed by the simulation results, specially at full load (system design point). In the case of part load, however, the stack temperatures resulting from the simulation are lower than these measured at the experiments. The maximal deviation observed is of 86.4 K (Eq. 5.60), while the mean deviation is of 30.5 K (Eq. 5.61).

The reason which can explain these differences is that the tests have been carried out with the same stack, but at different degradation states. The stack parameterization and validation has been realized with tests obtained with a new stack. On the contrary, the system experiments have been realized with a degraded stack, which presented a reduction of the voltage of approximately 5 % between the tests for the calibration of the stack and the system tests. Thus, in the second case the losses are larger and consequently the temperature higher. Wahl [151] extended the stack model with a degradation model and the results show a temperature increase of the order of magnitude of 100 K between the begin and the end of the stack lifetime. Thus, it can be considered that the model reproduces effectively the behavior of the SOFC CHP system.

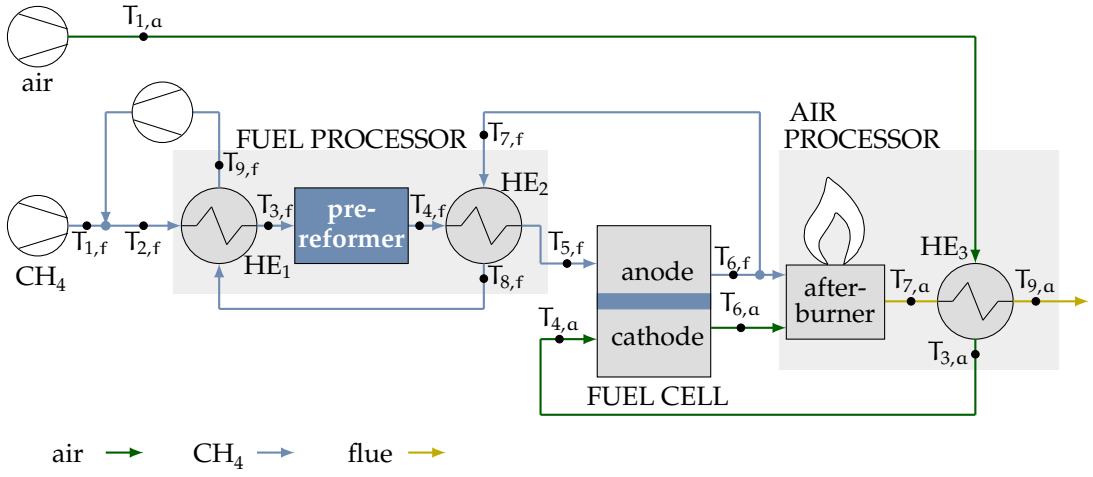

Figure 5.18 – Temperature measurement points for the validation of the complete system. With $T_{k,f}$ is indicated the temperature of the point k in the fuel path and with $T_{k,a}$ of the air path.

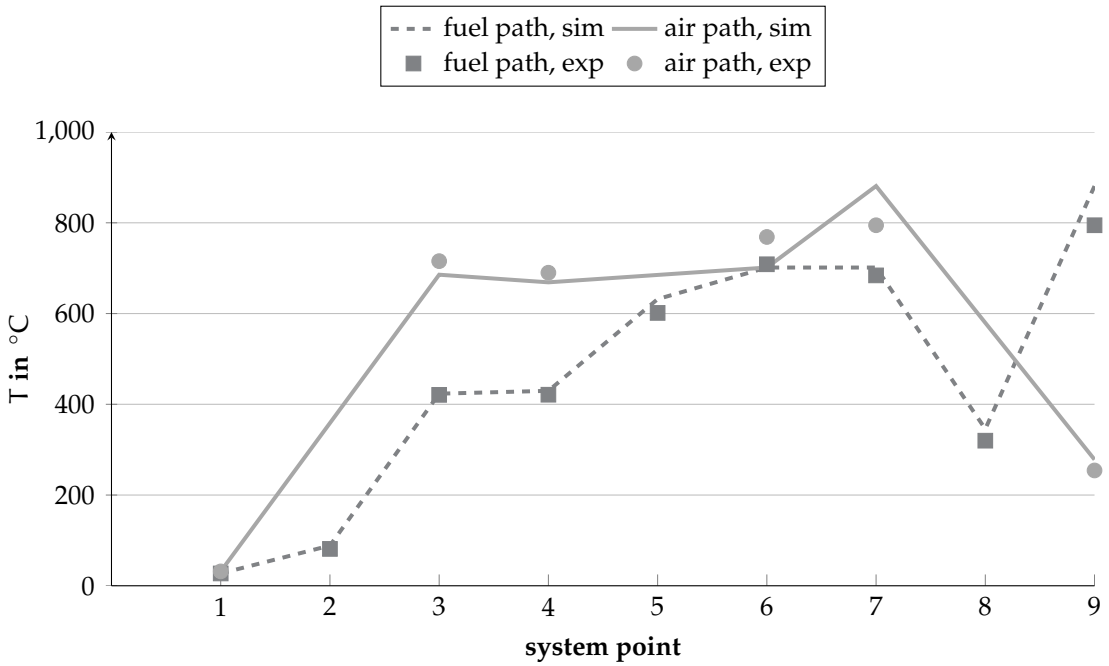

Figure 5.19 – Validation of the temperature behavior of the SOFC system at part load (56 % of maximal current).

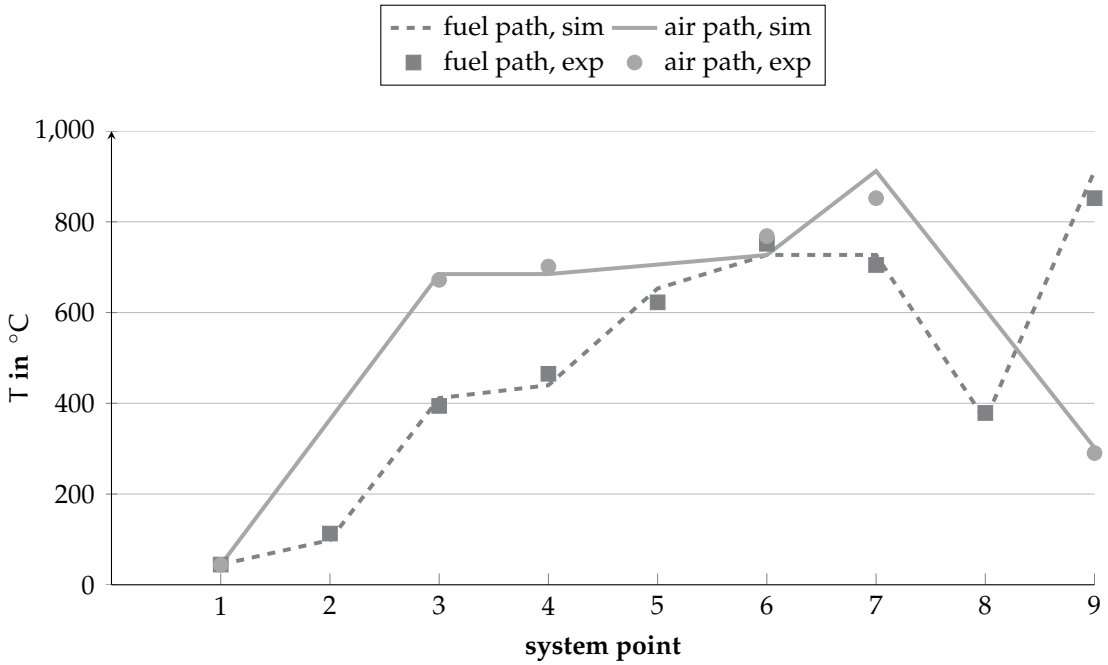

Figure 5.20 – Validation of the temperature behavior of the SOFC system at full load.

6 Robust control strategies to fluctuating natural gas composition

The effect of the fluctuation of the natural gas composition on the FCS has been shown in Chap. 4. It has been concluded that the variation of the system operating parameters resulting of this disturbance factor was not acceptable, since important differences between the real and the set point values were observed. The different methods which have been developed in order to avoid this problem are presented in this chapter.

The control loop of the air path, based on the stack temperature control by manipulating the air inlet flow, is not the focus of this work. Therefore, the strategy developed by Carré in [52] is implemented as described in Chap. 3.

The control strategy can be summarized in three steps, as shown in Fig. 6.1. In the first one, the mean number of carbon atoms per fuel molecule ($\bar{n}$) is determined. As explained in Chap. 4, the mean amount of free electrons per molecule of fuel is determinant for the stack performance, since the electrical energy produced by the elec-

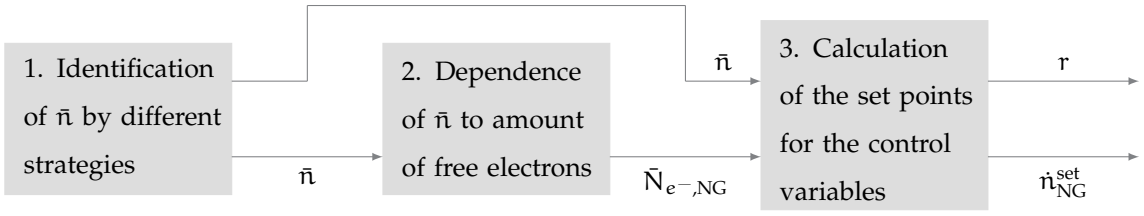

Figure 6.1 – Steps of the robust control strategy robust to variable gas composition.

trochemical reaction is directly generated by these electrons. As it will be explained later, $\bar{N}_{e^-,NG}$ and $\bar{n}$ depend directly from each other. Therefore, $\bar{n}$ is a key factor for the control strategies. The method to calculate this variable is different for each strategy, and actually characterizes each one of them. Once $\bar{n}$ is known, the mean amount of potentially released electrons per molecule of fuel ($\bar{N}_{e^-}$) can be calculated, since it exists a dependence between both variables. Finally the set points of the natural gas and recycling molar flows can be calculated, by adapting the control strategy developed by Carré [52] as described in Sect. 3.2.

6.1 Identification of the mean of carbon atoms per molecule ($\bar{n}$)

Five different solutions have been developed in order to identify the mean of carbon atoms per molecule ($\bar{n}$), which are summarized in Fig. 6.2 and listed below:

- Option a): Measurement of the natural gas calorific value by using a sensor placed at the natural gas inlet.
- Option b): Measurement of the oxygen molar content at the flue gas of the start-up burner.
- Option c): Measurement of the flue gas temperature at the start-up burner.
- Option d): Measurement of the oxygen content in the system flue gas.
- Option e): Measurement of the oxygen content in the system and at the cathode flue gas.
- Option f): Measurement of the carbon dioxide and water content at the after-burner flue gas.

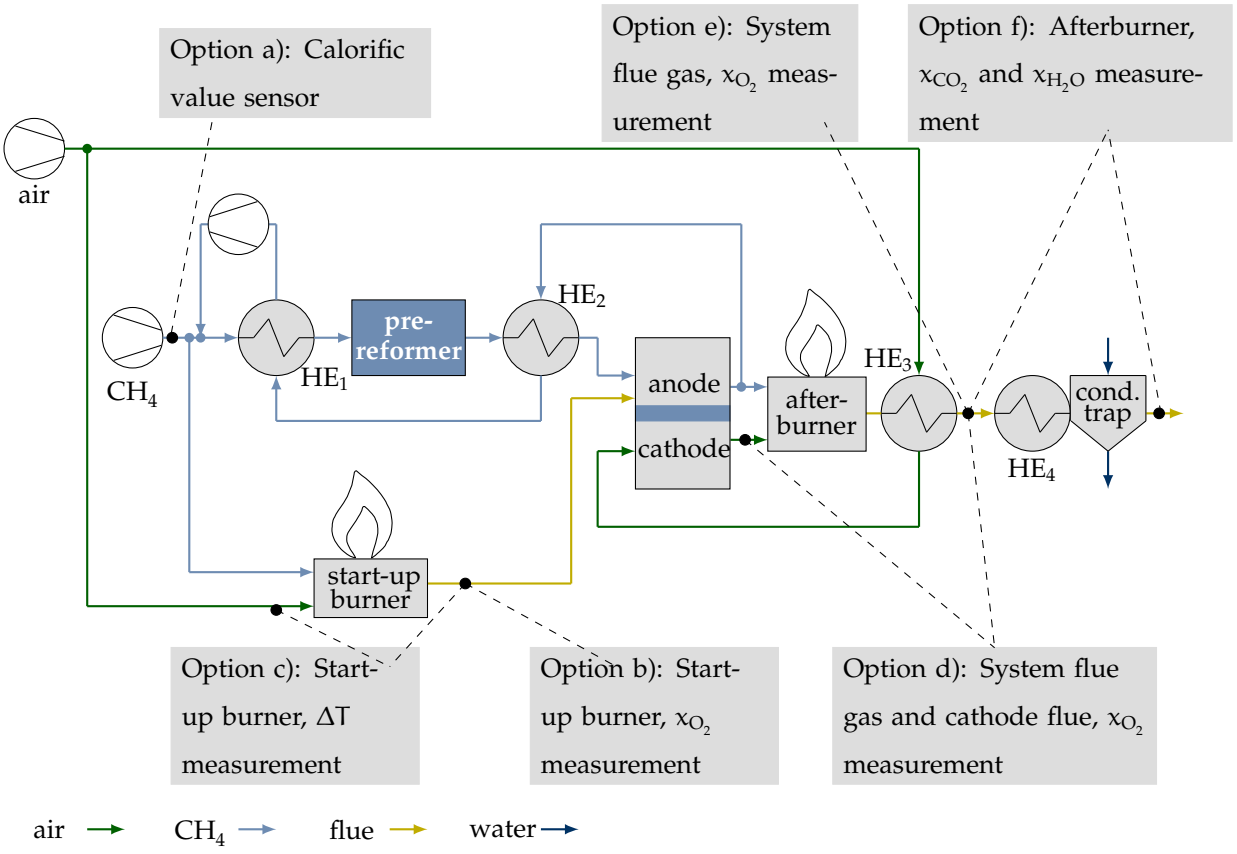

Figure 6.2 – Proposed strategies for the determination of $\bar{n}$, with the necessary sensors placed in the system.

The detailed description of the listed solutions is given in the following sections.

6.1.1 Measurement of the calorific value of the natural gas

The calorific value of a fuel is the specific amount of heat which is released during its complete combustion. For each substance two calorific values can be defined: the higher and the lower calorific value (HHV and LHV). The HHV is calculated under the assumption that the products are in the gaseous state except for the water, which is liquid. The LHV includes the effect of the latent vaporisation of the water: all reactants and products are to be found in gaseous state [40]. The relation between LHV and HHV depending on the latent heat of vaporization of water is presented in Eq. 6.1.

$$\mathrm{HHV} = \mathrm{LHV} + \frac{\dot{n}_{H_2O}}{\dot{n}_{\mathrm{fuel}}} \Delta h^0_{\mathrm{vap},H_2O} \tag{6.1}$$

Fig. 6.3 presents the higher heating value of some hydrocarbons contained in the natural gas depending on the amount of carbon atoms per molecule of alkane (n_j). It can be observed that both properties are proportional. In the following paragraphs the analytical relation between HHV and the mean amount of carbon atoms per molecule of fuel ($f(\mathrm{HHV}) = \bar{n}$) is developed.

The bond-dissociation energy of a bond between two atoms (D_0) is a measure of its strength. Its value is different for each pair of atoms and has been determined experimentally for most common bonds. During a chemical reaction the bonds of the reactant molecules are broken by consuming heat (endothermic process) and the bonds of the product molecules are formed (exothermic process), resulting in a heat release [149]. The difference between the bond-dissociation energy of the reactants and the products, both in gaseous state, determines the overall enthalpy change of

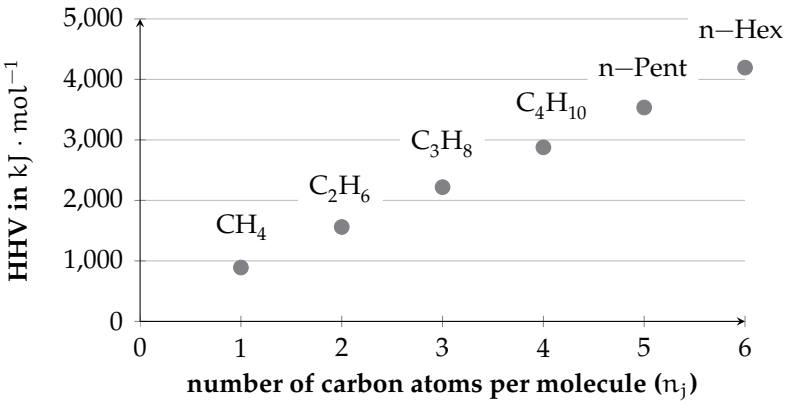

Figure 6.3 – Higher heating value of some alkanes with not-cyclic structure contained in the natural gas [89]. The exact values are to be found in Tab. 0.7 .

the reaction [111]. Thus, for the combustion reaction the lower calorific value can be calculated by Eq. 6.2:

$$\mathrm{LHV} = \sum \mathrm{D}_0^{\mathrm{prod}} - \sum \mathrm{D}_0^{\mathrm{react}} \tag{6.2}$$

Consequently, the lower calorific value can be calculated depending on the amount of bonds of each type in the reactant and products sides.

The chemical reaction of the complete combustion of an alkane j is described in Eq. 6.3:

$$\mathrm{C}_{n_j}\mathrm{H}_{2n_j+2} + \frac{3n_j+1}{2}\mathrm{O}_2 \rightarrow n_j\mathrm{CO}_2 + (n_j+1)\,\mathrm{H}_2\mathrm{O} \tag{6.3}$$

n_j is the amount of carbon atoms per molecule of the alkane j, being $n_1 = 1$ for methane, $n_2 = 2$ for ethane and so on. The internal bonds contained in the species taking part on the reaction are presented in Tab. 6.1. In total they are only 5 kinds of internal bonds, which bond-dissociation energies are to be found in Tab. 6.2.

Table 6.1 – Chemical formula, structural formula and internal bonds of the molecules which take part in the combustion reactions of the considered alkanes.

component	*chemical formula*	*structural formula*	*internal bonds*
oxygen	O_2	O=O	$1 \times$ O=O
water	H_2O	H−O−H	$2 \times$ H−O
carbon dioxide	CO_2	O=C=O	$2 \times$ O=C
methane	CH_4	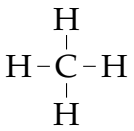	$4 \times$ C−H
ethane	C_2H_6	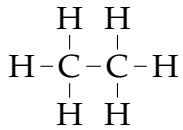	$6 \times$ C−H $1 \times$ C−C
propane	C_3H_8	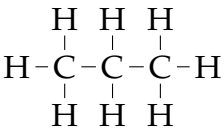	$8 \times$ C−H $2 \times$ C−C
butane	C_4H_{10}	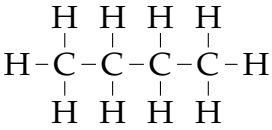	$10 \times$ C−H $3 \times$ C−C
non-cyclic alkane	C_nH_{2n+2}	different possibilities	$(2n+2) \times$ C−H $(n-1) \times$ C−C

Table 6.2 – Molar bond-dissociation energy for the different internal bonds [118].

internal bond	*C—H*	*C—C*	*O=O*	*C=O*	*H—O*
$D_0\left(kJ \cdot mol^{-1}\right)$	413.24	345.83	497.81	803.86	463.06

If Eq. 6.2 is rewritten specifically for the combustion of the alkane j (Eq. 6.3) its calorific value can be calculated as follows:

$$\begin{aligned} LHV_j &= \sum D_0^{prod} - \sum D_0^{react} \\ &= n_j \sum_k D_0^{k\in CO_2} + (n_j+1) \sum_k D_0^{k\in H_2O} - \sum_k D_0^{k\in C_{n_j}H_{2n_j+2}} - \left(\frac{3n_j+1}{2}\right) \sum_k D_0^{k\in O_2} \end{aligned} \tag{6.4}$$

$\sum_k D_0^{k\in CO_2}$ is the sum of the bond-dissociation energy of all the bonds contained by the molecule CO_2 and so on. The internal bonds of each molecule have been defined in Tab. 6.1. By applying them to Eq. 6.4, the lower calorific value for a general alkane can be obtained as follows:

$$LHV_j = 2n_j D_0^{C=O} + 2\,(n_j+1)\, D_0^{H-O} - (n_j-1)\, D_0^{C-C} - (2n_j+2)\, D_0^{C-H} - \left(\frac{3n_j+1}{2}\right) D_0^{O=O} \tag{6.5}$$

The bond-dissociation energy of the internal bonds is defined in Tab. 6.2. The released energy resulting from the complete combustion of a fuel gas molecule is independent from the participation from its neighboring molecules in other reactions [44]. Accordingly the heat of combustion of the natural gas can be calculated as the sum of the heat of combustion of the different gases contained in the mixture weighted according to their molar fraction ($x_{j,NG}$) [2]:

$$LHV_{NG} = \sum_j x_{j,NG} LHV_j \tag{6.6}$$

Therefore, for a mixture of alkanes, the heat value can be calculated by

$$\begin{aligned} LHV_{alk} = &- \sum_{j} x_{j,alk} \left(n_j - 1\right) D_0^{C-C} - \sum_{j} x_{j,alk} \left(\frac{3n_j + 1}{2}\right) D_0^{O=O} \\ &+ \sum_{j} x_{j,alk} 2 \left(n_j + 1\right) D_0^{H-O} - \sum_{j} x_{j,alk} \left(2n_j + 2\right) D_0^{C-H} + \sum_{j} x_{j,alk} 2 n_j D_0^{C=O} \end{aligned} \tag{6.7}$$

Where $x_{j,alk}$ is the molar fraction of the specie j in the alkane mixture. It is related to $x_{j,NG}$ by Eq. 6.8, being x_{alk} defined as the sum of molar fractions of alkanes (Eq. 6.9).

$$x_{j,NG} = x_{alk} x_{j,alk} \tag{6.8}$$

$$x_{alk} = \sum_{j=alk} x_{j,NG} \tag{6.9}$$

As shown in Sect. 4 most of natural gases contain some inert species (CO_2, O_2 and/or N_2). In this case the natural gas calorific value can be defined as follows:

$$LHV_{NG} = x_{alk} LHV_{alk} + x_{inert} LHV_{inert} \tag{6.10}$$

x_{inert} is defined as the sum of molar fractions of the inert species contained in the gas.

$$x_{inert} = \sum_{j=inert} x_{j,NG} \tag{6.11}$$

The calorific value for inert species is zero, since they do not take part in the combustion. Applying this condition and replacing Eq. 6.7 to Eq. 6.10, the calorific value of a general natural gas can be rewritten:

$$\begin{aligned} LHV_{NG} &= x_{alk} LHV_{alk} \\ &= 2x_{alk}\bar{n}_{alk} D_0^{C=O} + 2x_{alk}\left(\bar{n}_{alk}+1\right) D_0^{H-O} - \left(\frac{3\bar{n}_{alk}+1}{2}\right) x_{alk} D_0^{O=O} \\ &- \left(\bar{n}_{alk}-1\right) x_{alk} D_0^{C=C} - \left(2\bar{n}_{alk}+2\right) x_{alk} D_0^{C-H} \end{aligned} \tag{6.12}$$

$\bar{n}_{alk}$ is the mean amount of carbon atoms per molecule of alkane, defined in Eq. 6.13.

$$\bar{n}_{alk} = \sum_{j=alk} x_{j,alk} n_j \tag{6.13}$$

By replacing Eq. 6.8 in Eq. 6.13,

$$\bar{n}_{alk} = \frac{\sum_{j=alk} x_{j,NG} n_j}{x_{alk}} \tag{6.14}$$

The mean amount of carbon atoms per molecule of fuel is defined by Eq. 6.15, related to $\bar{n}_{alk}$ with the total molar fraction of alkanes x_{alk}.

$$\bar{n} = x_{alk}\bar{n}_{alk} \tag{6.15}$$

In Eq. 6.1 the relation between LHV and HHV depending on the water molar fraction has been defined. As shown in Eq. 6.3 per each reacted mole of alkane $\bar{n}_{alk}+1$ moles of water are produced. For a general fuel, the total alkanes molar fraction x_{alk} is taken into account. As a result the relation between LHV_{NG} and HHV_{NG} is the following:

$$HHV_{NG} = LHV_{NG} + x_{alk}\left(\bar{n}_{alk}+1\right)\Delta h^0_{vap,H_2O} \tag{6.16}$$

Tab.6.3 presents the HHV_{NG} of the reference gases (defined in Fig. 4.3) obtained by applying Eq. 6.12 and Eq. 6.16. They are compared with two reference values. $HHV^{ref}_{NG,1}$

Table 6.3 – Higher heating value for several reference natural gases calculated with the method described in this section. The values are compared with two references. The calorific value is given in $kJ \cdot mol^{-1}$ and the error ϵ_j in %.

natural gas	HHV_{NG}	$HHV^{ref}_{NG,1}$ *[18],[3]*	ϵ_1 *in %*	$HHV^{ref}_{NG,2}$ *[89]*	ϵ_2 *in %*
Russia	894	904	1.100	900	-0.724
North Sea I	977	984	0.725	978	-0.098
North Sea II	1002	1008	0.662	1003	-0.167
Verbundgas	920	928	0.869	920	-0.047
Denmark	973	976	0.362	973	-0.076
Biogas	857	855	-0.228	856	0.090
Holland I	785	791	0.660	785	0.014
East-Hannover	728	734	0.852	727	0.064
Holland II	820	823	0.329	820	-0.007

is obtained directly from [18] and [3]. $HHV^{ref}_{NG,2}$ is calculated as the weighted sum of the higher calorific values of the natural gas components (Tab. 0.7) by applying Eq. 6.6. The error between the calculated and the reference HHV (ϵ_j) is obtained by Eq. 6.17.

$$\epsilon_j = \frac{HHV^{ref}_{NG,j} - HHV_{NG,j}}{HHV^{ref}_{NG,j}} 100 \tag{6.17}$$

It can be observed that for both references of calorific value the maximal deviation has a value of 1.1 %.

Replacing Eq. 6.16 in Eq. 6.12 the mean amount of carbon atoms per molecule ($\bar{n}$) can be expressed dependent exclusively on the higher calorific value and the total alkane molar fraction:

$$\bar{n} = \frac{HHV + x_{alk}\left(-\Delta h^0_{vap,H_2O} - 2D_0^{H-O} + 0.5D_0^{O=O} - D_0^{C-C} + 2D_0^{C-H}\right)}{\Delta h^0_{vap,H_2O} + 2D_0^{C=O} + 2D_0^{H-O} - 1.5D_0^{O=O} - D_0^{C-C} - 2D_0^{C-H}} \tag{6.18}$$

In opposite to n, the value of $\bar{n}$ is not an integer corresponding to specific alkanes, but a real value which identifies the calorific value of a natural gas formed by a mixture of different alkanes. The importance and use of this variable will be explained in Sec. 6.2.

The higher calorific value can be measured by using a sensor placed at the system gas inlet. The total alkanes molar fraction can be, in a first instance, assumed as a fixed parameter.

6.1.2 Measurement of the oxygen content in the start-up burner flue gas

The molar fraction of oxygen in the flue gas of a burner can be related to the carbon atoms of the molecule by stoichiometric relations. For this purpose the start-up burner is used, which has the function of protecting the system during the start-up procedure by producing CO in an incomplete combustion of the gas. Since the air and the natural gas volumetric flows can be determined independently, during the normal operating time a complete combustion of the gas can be forced.

The general complete combustion of an alkane $C_{n_j}H_{2n_j+2}$ has been described in Eq. 6.3, being its speed of reaction ($\xi_{comb}^{C_nH_{2n+2}}$) the alkane molar flow.

The combustion of a mixture of alkanes is a chemical reaction which can be approximated as the parallel combustions of the different gases [44]. The main alkanes contained by the natural gas are methane, ethane, propane and butane (Sec. 4.1). The specific combustion reactions for those alkanes are listed below.

$$CH_4 + 2O_2 \rightarrow CO_2 + 2H_2O$$

$$C_2H_6 + \frac{7}{2}O_2 \rightarrow 2CO_2 + 3H_2O$$

$$C_3H_8 + 5O_2 \rightarrow 3CO_2 + 4H_2O$$

$$C_4H_{10} + \frac{13}{2}O_2 \rightarrow 4CO_2 + 5H_2O$$

Assuming that these reactions take place at the same time, they can be added in a single expression as follows, being j the type of alkane:

$$\left(\sum_{j=1}^{4} x_j C_{n_j} H_{2n_j+2}\right) + \left(\sum_{j=1}^{4} x_j \frac{3n_j+1}{2}\right) O_2 \rightarrow \left(\sum_{j=1}^{4} x_j\, n_j\right) CO_2 + \left(\sum_{j=1}^{4} x_j\,(n_j+1)\right) H_2O \tag{6.19}$$

A fictive alkane molecule can be defined as $C_{\bar{n}_{alk}} H_{2\bar{n}_{alk}+2}$, which contains the mean amount of carbon atoms per molecule of alkane $\bar{n}_{alk}$ (Eq. 6.13). The combustion reaction for this fictive molecule can be described by rewriting Eq. 6.19:

$$C_{\bar{n}_{alk}} H_{2\bar{n}_{alk}+2} + \left(\frac{3\bar{n}_{alk}+1}{2}\right) O_2 \rightarrow \bar{n}_{alk} CO_2 + (\bar{n}_{alk}+1)\, H_2O \tag{6.20}$$

Considering the reaction described in Eq. 6.20 a mass balance on the burner is applied in order to calculate the output oxygen molar fraction:

$$x_{O_2}^{bu,out} = \frac{\dot{n}_{air}^{bu,in} x_{O_2,air} + \dot{n}_{NG}^{bu,in} x_{O_2,NG} - 0.5\xi_{comb}\,(3\bar{n}_{alk}+1)}{\dot{n}_{air}^{bu,in} + \dot{n}_{NG}^{bu,in} + 0.5\xi_{comb}\,(\bar{n}_{alk}-1)} \tag{6.21}$$

ξ^{comb} is the speed of reaction for the combustion. Assuming a complete combustion it can be determined by

$$\xi_{comb} = \dot{n}_{alk}^{bu,in} = x_{alk}\dot{n}_{NG}^{bu,in} \tag{6.22}$$

Eq. 6.21 is rewritten by applying the definition of $\bar{n}_{alk}$ (defined in Eq. 6.14) and ξ_{comb} (Eq. 6.22). After some mathematical arrangements the mean amount of carbon atoms per molecule can be defined by

$$\bar{n} = \frac{\dot{n}_{air}^{bu,in}x_{O_2,air} + \dot{n}_{NG}^{bu,in}\left(x_{O_2,NG} - 0.5x_{alk}\right) - x_{O_2}^{bu,out}\left(\dot{n}_{air}^{bu,in} + \dot{n}_{NG}^{bu,in}\left(1 - 0.5x_{alk}\right)\right)}{\dot{n}_{NG}^{bu,in}\left(0.5x_{O_2}^{bu,out} + 1.5\right)} \tag{6.23}$$

The air and natural gas inlet molar flows ($\dot{n}_{air}^{bu,in}$ and $\dot{n}_{NG}^{bu,in}$) are measured with flow meters, the inlet oxygen molar fractions are considered constants. The oxygen molar fraction in the flue gas can be measured measured with a oxygen sensor, for example a *lambda-sonde*.

6.1.3 Temperature measurement of the start-up burner flue gas

An alternative to the measurement of the calorific value with a specific sensor is the determination of this property indirectly by using other measurements. For this purpose different methods can be used including analytical, correlative, stoichiometric, state reconstruction and calorimetry methods [148]. In this latter case a sample of the gas is burned in order to determine the calorific value of the gas. The strategy described in this section is based on this principle, making use of the start-up burner, as proposed in Sect. 6.1.2. In this case the flue gas temperature is measured in order to determine the calorific value of the gas and the mean amount of carbon atoms per molecule ($\bar{n}$). The details of the calculations are shown in the following paragraphs.

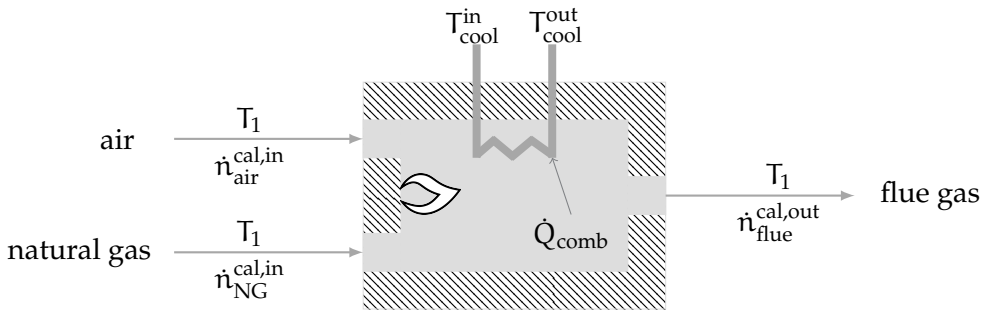

Figure 6.4 – Isothermal flow calorimeter, based on [71].

Consider an isothermal flow calorimeter, as the one shown in Fig. 6.4. This kind of calorimeters are based in the complete combustion of a fuel, for example natural gas, in an open flame. The heat generated in the process Q_{comb} is transferred completely to a cooling fluid with a heat exchanger, increasing its temperature from T^{in}_{cool} to T^{out}_{cool}. Thus, the outlet gas temperature is equal to the inlet level (T_1). The First Law of Thermodynamics is applied to a general combustion in a calorimeter as the described. The contribution of the potential and kinetic energy can be neglected and, since the volume is constant, the work produced by the gases is assumed to be zero [71]. Thus, the steady state energy balance of the calorimeter can be expressed as in Eq. 6.24 to calculate the enthalpy of combustion per mole at the inlet temperature $\Delta h_{comb}(T_1)$.

$$\begin{aligned}\dot{Q}_{comb} &= \Delta h_{comb}(T_1)\,\dot{n}^{cal,in}_{NG} = \dot{n}^{cal,out}_{flue} h_{flue}(T_1) - \dot{n}^{cal,in}_{NG} h_{NG}(T_1) - \dot{n}^{cal,in}_{air} h_{air}(T_1) \\ &= \dot{H}_{flue}(T_1) - \dot{H}_{air}(T_1) - \dot{H}_{NG}(T_1)\end{aligned} \tag{6.24}$$

$h_j(T_1)$ is the molar enthalpy of compound j at temperature T_1. As mentioned in the previous chapter, all referred enthalpies are relative to standard conditions ($T^0 = 298.15\,K$ and $p^0 = 101325\,Pa$).

The lower calorific value (LHV) is defined by ISO 6976 [2] as "The amount of heat which would be released by the complete combustion in air of a specified quantity of gas, in such a way that pressure p1 at which the reaction takes place remains constant,

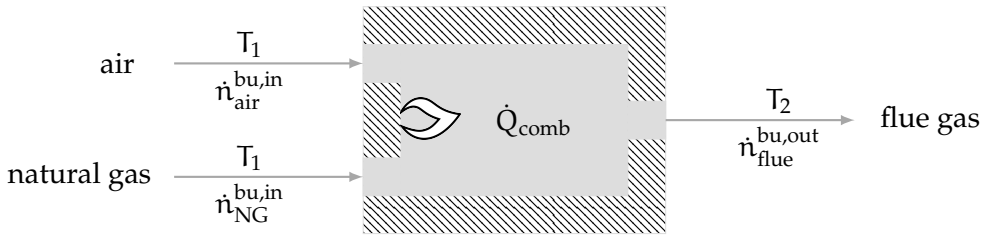

Figure 6.5 – Adiabatic start-up burner.

and all the products of combustion are returned to the same specified temperature t1 as that of the reactants, all of these products being in the gaseous state". By applying this definition the LHV at temperature T_1 can be calculated by replacing Eq. 6.24. The negative sign comes from the convention, which establishes that "a positive heat release is taken to be a numerically identical negative enthalpy increment" [2].

$$LHV = -\frac{\dot{H}^{cal,out}_{flue}(T_1) - \dot{H}^{cal,in}_{air}(T_1) - \dot{H}^{cal,in}_{NG}}{\dot{n}^{cal,in}_{NG}} \tag{6.25}$$

In the start-up burner the reaction is a complete combustion under constant pressure. In contrast to the calorimeter the reaction is not isothermal but adiabatic (Fig. 6.5). Hence, the enthalpy balance at the start-up burner is the following:

$$\dot{H}^{bu,out}_{flue}(T_2) - \dot{H}^{bu,in}_{air}(T_1) - \dot{H}^{bu,in}_{NG}(T_1) = 0 \tag{6.26}$$

If the same inlet conditions for the calorimeter and the burner are assumed ($\dot{n}^{bu,in}_{air} = \dot{n}^{cal,in}_{air}, \dot{n}^{bu,in}_{NG} = \dot{n}^{cal,in}_{NG}, T_{1,bu} = T_{1,cal}$) the inlet enthalpies can also be considered as equal ($\dot{H}^{0,bu,in} = \dot{H}^{0,cal,in}$). Additionally, since the chemical reactions are the same in both cases, $\dot{n}^{cal,out}_{flue} = \dot{n}^{bu,out}_{flue}$. Thus, Eq. 6.25 and Eq. 6.26 can be combined and the lower calorific value can be expressed depending on the flue enthalpy flow at the inlet and outlet temperatures T_1 and T_2 (Eq. 6.27).

$$\mathrm{LHV} = -\frac{\dot{H}_{\mathrm{flue}}(T_2) - \dot{H}_{\mathrm{flue}}(T_1)}{\dot{n}_{\mathrm{NG}}} = -\frac{\dot{n}_{\mathrm{flue}}^{\mathrm{bu,out}}}{\dot{n}_{\mathrm{NG}}^{\mathrm{bu,in}}}\left(h_{\mathrm{flue}}(T_2) - h_{\mathrm{flue}}(T_1)\right) \tag{6.27}$$

The enthalpy flow can be calculated by using the NASA polynomial [116] depending on the temperature and the composition (Eq. 5.2). Applying the equation to the flue gas:

$$h_{\mathrm{flue}}(T) = x_{O_2,\mathrm{flue}} h_{O_2}^{\mathrm{NASA}}(T) + x_{N_2,\mathrm{flue}} h_{N_2}^{\mathrm{NASA}}(T) + x_{CO_2,\mathrm{flue}} h_{CO_2}^{\mathrm{NASA}}(T) + x_{H_2O,\mathrm{flue}} h_{H_2O}^{\mathrm{NASA}}(T) \tag{6.28}$$

Temperature T_2 is measured with a sensor. T_1 can be measured or assumed as equal to the ambiance temperature. The flue gas composition is calculated by applying a mass balance in the burner, similarly to Sect. 6.1.2. Taking into account that the natural gas is a mixture of alkanes and inert species, the molar fraction for the different species can be calculated depending on $\bar{n}$ and x_{alk} as follows:

$$x_{O_2,\mathrm{flue}} = \frac{x_{O_2,\mathrm{air}}^{\mathrm{bu,in}} \dot{n}_{\mathrm{air}}^{\mathrm{bu,in}} + x_{O_2,\mathrm{NG}}^{\mathrm{bu,in}} \dot{n}_{\mathrm{NG}}^{\mathrm{bu,in}} - \frac{3}{2}\left(\bar{n} + x_{\mathrm{alk}}\right) \dot{n}_{\mathrm{NG}}^{\mathrm{bu,in}}}{\dot{n}_{\mathrm{flue}}^{\mathrm{bu,out}}} \tag{6.29}$$

$$x_{N_2,\mathrm{flue}} = \frac{x_{N_2,\mathrm{air}}^{\mathrm{bu,in}} \dot{n}_{\mathrm{air}}^{\mathrm{bu,in}} + x_{N_2,\mathrm{NG}}^{\mathrm{bu,in}} \dot{n}_{\mathrm{NG}}^{\mathrm{bu,in}}}{\dot{n}_{\mathrm{flue}}^{\mathrm{bu,out}}} \tag{6.30}$$

$$x_{CO_2,\mathrm{flue}} = \frac{x_{CO_2,\mathrm{NG}}^{\mathrm{bu,in}} \dot{n}_{\mathrm{NG}}^{\mathrm{bu,in}} + \bar{n} \dot{n}_{\mathrm{NG}}^{\mathrm{bu,in}}}{\dot{n}_{\mathrm{flue}}^{\mathrm{bu,out}}} \tag{6.31}$$

$$x_{H_2O,\mathrm{flue}} = \frac{\left(\bar{n} + x_{\mathrm{alk}}\right) \dot{n}_{\mathrm{NG}}^{\mathrm{bu,in}}}{\dot{n}_{\mathrm{flue}}^{\mathrm{bu,out}}} \tag{6.32}$$

The flue gas molar flow is also obtained from the mass balance:

$$\dot{n}_{flue}^{bu,out} = \dot{n}_{air}^{bu,in} + \dot{n}_{NG}^{bu,in}\left(1 + \frac{\bar{n} - x_{alk}}{2}\right) \tag{6.33}$$

The mean amount of carbon atoms per molecule ($\bar{n}$) can be calculated by replacing Eq. 6.27 in Eq. 6.18.

$$\bar{n} = \frac{h_{flue}(T_2) - h_{flue}(T_1) + x_{alk}\left(-2D_0^{H-O} + 0.5D_0^{O=O} - D_0^{C-C} + 2D_0^{C-H}\right)}{2D_0^{C=O} + 2D_0^{H-O} - 1.5D_0^{O=O} - D_0^{C-C} - 2D_0^{C-H}} \tag{6.34}$$

6.1.4 Measurement of the oxygen molar fraction at the system flue gas

The control strategy based on calculating $\bar{n}$ by measuring the oxygen molar fraction in the start-up burner (Sec. 6.1.2) can also be applied to the whole system. The reason is that regarding the mass balance the SOFC system behaves like a burner. In order to justify this statement in the next paragraphs a simple FCS, operated with H_2 and without anode flue gas recycling is analyzed. The conclusions can be then extended to all fuel systems.

Fig. 6.6 presents a fuel cell CHP system composed by a stack (anode and cathode) and an afterburner. The heat exchangers required for the thermal management of the system have been omitted since they are not relevant for this purpose. The molar flows entering the system, oxygen and hydrogen, are delivered to the cathode and anode respectively. There take place the oxidation (Eq. 2.4) and the reduction (Eq. 2.5) reactions, generating heat and electrical power. The product of the reaction is water, which together with the unburnt hydrogen and the rest of the oxygen are brought to the afterburner. Finally a complete combustion oxidizes the rest of the hydrogen into water producing heat.

If the whole electrochemical reaction is considered instead of the two half-reactions, then one finds that reaction taking place in the fuel cell is described by the same stoichiometry as the hydrogen combustion. Therefore, independently of the fraction of hydrogen which is oxidized at the fuel cell and at the burner, the outlet molar flow and composition do not vary. This means that, considering only these properties, the whole system can be treated as a burner. Regarding other variables, for example the temperature or the generated power, this is not generally true.

Consequently the control strategy based on the measurement of the flue gas oxygen molar fraction, which had been designed to be applied to the start-up burner (Sect. 6.1.2), can be also implemented to the complete system. Eq. 6.23 for this case

yields to the following relation:

$$\bar{n} = \frac{\dot{n}_{air}^{sys,in} x_{O_2,air} + \dot{n}_{NG}^{sys,in} \left(x_{O_2,NG} - 0.5 x_{alk}\right) - x_{O_2,flue}^{sys} \left(\dot{n}_{air}^{sys,in} + \dot{n}_{NG}^{sys,in} \left(1 - 0.5 x_{alk}\right)\right)}{\dot{n}_{NG}^{sys,in} \left(0.5 x_{O_2,flue}^{sys} + 1.5\right)} \tag{6.35}$$

Assuming that the intern controller of the gas blower has an ideal behavior (the measured flow is equal to the set point) the natural gas system inlet flow ($\dot{n}_{NG}^{sys,in}$) can be replaced by its set point value ($\dot{n}_{NG}^{set}$). This value is calculated depending on $\bar{n}$, as will be shown in the following section. Thus, Eq. 6.35 can be rewritten as Eq. 6.36.

$$\bar{n} = \frac{\dot{n}_{air}^{sys,in} x_{O_2,air} + \dot{n}_{NG}^{set}(\bar{n}) \left(x_{O_2,NG} - 0.5 x_{alk}\right) - x_{O_2,flue}^{sys} \left(\dot{n}_{air}^{sys,in} + \dot{n}_{NG}^{set}(\bar{n}) \left(1 - 0.5 x_{alk}\right)\right)}{\dot{n}_{NG}^{set}(\bar{n}) \left(0.5 x_{O_2,flue}^{sys} + 1.5\right)} \tag{6.36}$$

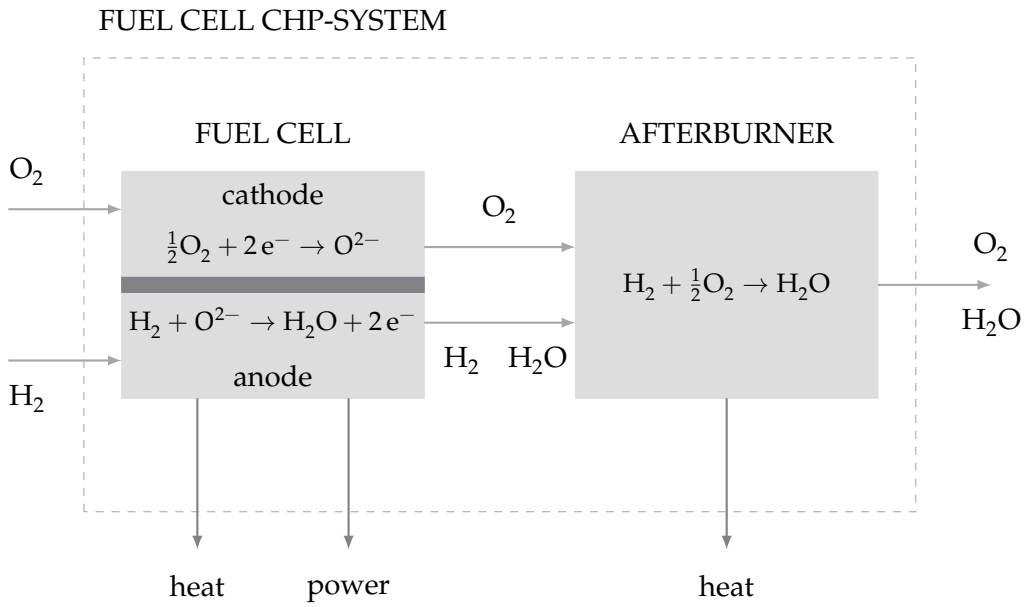

Figure 6.6 – Simple FCS operating with H_2, composed by a fuel cell and an afterburner. Note that if the whole system is considered the gas inlet and outlet flows are the same as for a burner.

6.1.5 Measurement of the oxygen content in the system and at the cathode flue gas

During the electrochemical reaction in the stack, the oxygen anions migrate from the cathode bulk through the electrolyte to the anode, resulting in a reduction in the oxygen molar fraction at the cathode outlet respect to the inlet. The electrochemical reaction at the stack has been given by Eq. 2.1,

$$H_2 + 0.5O_2 \rightarrow H_2O$$

and its reaction rate has been defined as ξ_{elech}. Thus, the amount of O_2 at the output of the stack can be calculated by

$$\dot{n}^{out}_{O_2,cath} = \dot{n}^{in}_{O_2,cath} - 0.5\xi_{elech} = \dot{n}^{in}_{air,sys} x^{in}_{O_2,cath} - 0.5\xi_{elech} \tag{6.37}$$

Similarly, the total molar flow at the cathode outlet is reduced respect to the inlet due to the migration of oxygen to the anode as well. Consequently,

$$\dot{n}^{out}_{air,cath} = \dot{n}^{in}_{air,cath} - 0.5\xi_{elech} = \dot{n}^{in}_{air,sys} - 0.5\xi_{elech} \tag{6.38}$$

Combining both equations, the oxygen molar fraction at the cathode outlet can be calculated by

$$x^{out}_{O_2,cath} = \frac{\dot{n}^{in}_{air,sys} x^{in}_{O_2,cath} - 0.5\xi_{elech}}{\dot{n}^{in}_{air,sys} - 0.5\xi_{elech}}. \tag{6.39}$$

Replacing the expression of the reaction rate in Eq. 6.39 by Eq.2.6, the following expression is obtained

$$x^{out}_{O_2,cath} = \frac{\dot{n}^{in}_{air,sys} x^{in}_{O_2,cath} - 0.5\frac{IN_{cell}}{F}}{\dot{n}^{in}_{air,sys} - 0.5\frac{IN_{cell}}{F}}. \tag{6.40}$$

From this expression, the inlet system air flow ($\dot{n}^{in}_{air,sys}$) can be calculated depending exclusively on the generated electrical current (I) and the oxygen molar fraction at the cathode outlet ($x^{out}_{O_2,cath}$):

$$\dot{n}^{sys,in}_{air} = \frac{0.5\frac{IN_{cell}}{F}\left(1 - x^{out}_{O_2,cath}\right)}{x_{O_2,air} - x^{out}_{O_2,cath}} \tag{6.41}$$

$x^{out}_{O_2,cath}$ can be easily measured by using an oxygen sensor, for example a *lambda-sonde*. As a result the air flow sensor would not be necessary. Thus, Eq. 6.36 is replaced by

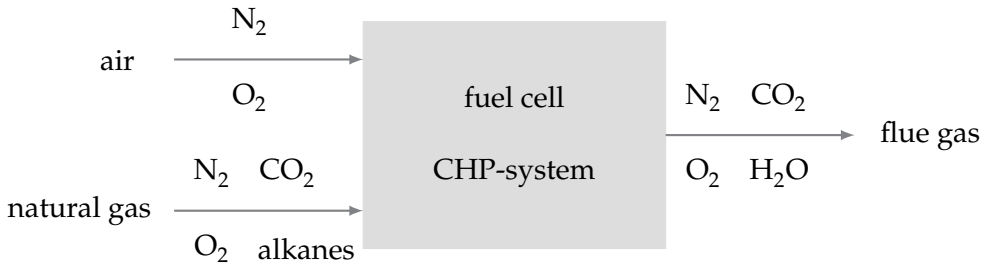

Figure 6.7 – Inlet and outlet gases of the FCS, with the chemical species which contain each of them.

$$\bar{n} = \frac{\dot{n}_{air}^{sys,in}\left(I, x_{O_2,cath}^{out}\right) x_{O_2,air} + \dot{n}_{NG}^{set}(\bar{n})\left(x_{O_2,NG} - 0.5x_{alk}\right)}{\dot{n}_{NG}^{set}(\bar{n})\left(0.5x_{O_2,flue}^{sys} + 1.5\right)} - \frac{x_{O_2,flue}^{sys}\left(\dot{n}_{air}^{sys,in}\left(I, x_{O_2,cath}^{out}\right) + \dot{n}_{NG}^{set}(\bar{n})\left(1 - 0.5x_{alk}\right)\right)}{\dot{n}_{NG}^{set}(\bar{n})\left(0.5x_{O_2,flue}^{sys} + 1.5\right)} \tag{6.42}$$

6.1.6 Measurement of the carbon dioxide and water content at the system flue gas

In section 6.1.4 the equivalence of the mass balance of the FCS to that of a combustion reaction has been justified. In the method described in this section this equivalence is used again for the identification of $\bar{n}$ based on the CO_2 molar fraction and the humidity at the flue gas of the system.

A mass balance of the FCS can be applied to each of the elements, considering the molecules shown in Fig. 6.7. Assuming the absence of water in the inlet natural gas (like in the standard gas compositions described in [18] and [3]), the mass balance for the carbon and hydrogen atoms is described by Eq. 6.43 and Eq. 6.44 respectively.

$$\dot{n}_C^{sys,in} = \dot{n}_C^{sys,out} \Rightarrow \dot{n}_{CO_2,NG} + \bar{n}_{alk}\dot{n}_{alk} = \dot{n}_{CO_2,flue} = \dot{n}_{flue}x_{CO_2,flue} \tag{6.43}$$

$$\dot{n}_H^{sys,in} = \dot{n}_H^{sys,out} \Rightarrow (2\bar{n}_{alk} + 2)\,\dot{n}_{alk} = 2\dot{n}_{H_2O,flue} = 2\dot{n}_{flue}x_{H_2O,flue} \tag{6.44}$$

$\bar{n}_{alk}$ is the mean amount of carbon atoms per molecule of alkane, as defined in Eq. 6.14. Dividing Eq. 6.43 by Eq. 6.44:

$$\frac{\dot{n}_{CO_2,NG} + \bar{n}_{alk}\dot{n}_{alk}}{(\bar{n}_{alk} + 1)\,\dot{n}_{alk}} = \frac{\dot{n}_{flue}x_{CO_2,flue}}{\dot{n}_{flue}x_{H_2O,flue}} \tag{6.45}$$

The molar fraction of CO_2 in the natural gas ($\dot{n}_{CO_2,NG}$) is nearly zero for most of the gases ([18], [3]) and reaches a maximal value of 5 % in the gases which are provided in Germany. Accordingly it is approximated to zero. Applying this simplification, and after some mathematical arrangements:

$$\frac{\bar{n}_{alk}}{\bar{n}_{alk} + 1} = \frac{x_{CO_2,flue}}{x_{H_2O,flue}} \tag{6.46}$$

Eq. 6.46 expresses the relationship between $\bar{n}_{alk}$, x_{CO_2} and the humidity of the system flue gas. $\bar{n}_{alk}$ can be calculated by applying Eq. 6.47, independently of the inlet molar flows.

$$\bar{n}_{alk} = \frac{x_{CO_2,flue}}{x_{H_2O,flue} - x_{CO_2,flue}} \tag{6.47}$$

The molar fraction of CO_2 can be measured with different sensors. A general restriction for these sensors is their maximal temperature, with a value of about 60 °C. This restriction represents an additional a difficulty to the implementation of the strategy, since the only point of the system where this restriction is fulfilled would be the flue outlet (Fig. 6.8), placed after the condensation trap. For the measurement of the H_2O molar fraction a relative humidity (RH) sensor can be used. Their maximal operating temperature is about 180 °C. Therefore, regarding exclusively the temperature it should be installed downstream of the condensation trap. However, in this case part

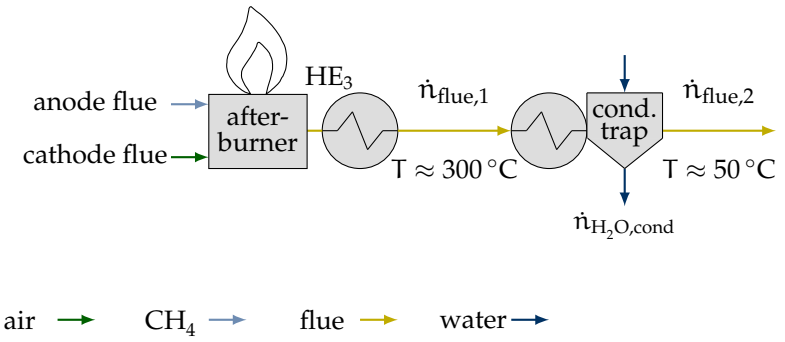

Figure 6.8 – Flue gas outlet of the system. The stack, the afterburner and the cooling system are indicated.

of the water contained in the flue gas may not be detected by the sensor. A solution is to cool down the flue gas by using a heat exchanger with the inlet air in the cold side and a sample of the flue gas in the hot side. The resulting system is detailed in Fig. 6.9.

In order to be able to apply Eq. 6.46 it is necessary to know the H_2O and CO_2 molar fractions in the flue gas ($x_{CO_2,flue}$, $x_{H_2O,flue}$). They correspond to the molar fractions in points 1 or 3. The molar fractions at point 2 are not the corresponding ones in the flue gas due to water condensation.

Fraction $x_{H_2O,flue}$ can be calculated with the sensors placed in point 3 from Fig. 6.9. The relative humidity (RH) is defined as follows:

$$RH_3 = \frac{p_{H_2O,3}}{P_{sat,H_2O,3}(T_3)} \tag{6.48}$$

The partial pressure of water ($p_{H_2O,3}$) can be expressed with the water molar fraction:

$$p_{H_2O,3} = P_3 x_{H_2O,3} \tag{6.49}$$

Combining Eq. 6.48 and Eq. 6.49 yields:

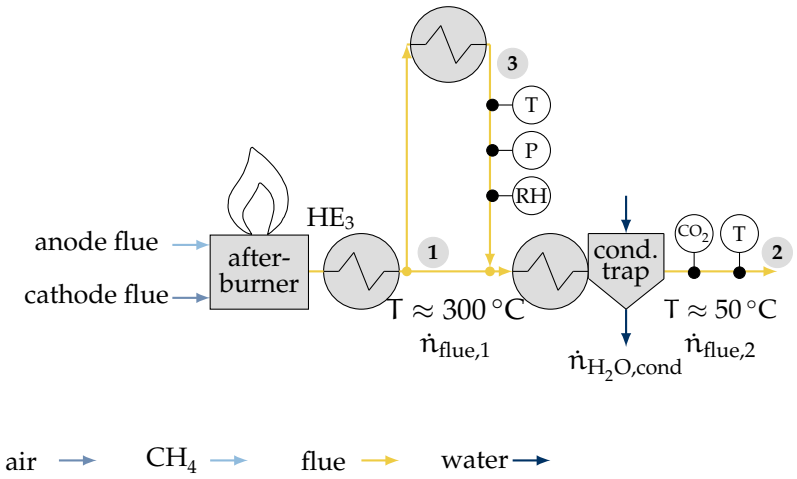

Figure 6.9 – Flue gas outlet of the system the integration of the sensors required for this control strategy. A heat exchanger has been added to cool a sample of the flue gas in order to make the humidity measurement possible.

$$x_{H_2O,flue} = x_{H_2O,3} = x_{H_2O,1} = \frac{RH_3 P_{sat,H_2O,3}(T_3)}{P_3} \tag{6.50}$$

The saturation pressure (P_{sat}) can be calculated by applying Antoine Equation [130]:

$$\log_{10}\left(P_{sat,H_2O,2}\right) = A - \frac{B}{C + T_3} \tag{6.51}$$

A, B and C are tabulated parameters and T_3 can be measured with a temperature sensor.

In case of the CO_2 molar fraction the measurement can only be obtained at the point 2 due to the high temperatures in points 1 and 3. Consequently it is necessary to apply a mass balance to calculate x_{CO_2} with the available data.

The value of the CO_2 molar flow is the same in the point 2 and in the point 1:

$$\dot{n}_{CO_2,flue,1} = \dot{n}_{CO_2,flue,2} \Rightarrow x_{CO_2,1} = \frac{x_{CO_2,2}\dot{n}_{flue,2}}{\dot{n}_{flue,1}} \tag{6.52}$$

The difference between the two molar flows is the molar flow of the condensed water in the condensation trap, since it is the only specie which condensates:

$$\dot{n}_{flue,1} = \dot{n}_{flue,2} + \dot{n}_{H_2O,cond} \tag{6.53}$$

Replacing $\dot{n}_{flue,1}$ in Eq. 6.52 with Eq. 6.53 yields:

$$x_{CO_2,1} = \left(1 - \frac{\dot{n}_{H_2O,cond}}{\dot{n}_{flue,1}}\right) x_{CO_2,2} \tag{6.54}$$

Applying a mass balance for the water:

$$\dot{n}_{H_2O,1} = \dot{n}_{H_2O,2} + \dot{n}_{H_2O,cond} \Rightarrow \dot{n}_{flue,1} x_{H_2O,1} = \dot{n}_{flue,2} x_{H_2O,2} + \dot{n}_{H_2O,cond} \tag{6.55}$$

Inserting Eq. 6.53 in Eq. 6.55 and after some mathematical arrangements:

$$\frac{\dot{n}_{H_2O,cond}}{\dot{n}_{flue,1}} = \frac{x_{H_2O,1} - x_{H_2O,2}}{1 - x_{H_2O,2}} \tag{6.56}$$

Applying Eq. 6.56 on Eq. 6.54:

$$x_{CO_2,flue} = x_{CO_2,1} = \left(1 - \frac{x_{H_2O,1} - x_{H_2O,2}}{1 - x_{H_2O,2}}\right) x_{CO_2,2} \tag{6.57}$$

$x_{CO_2,2}$ is directly measured by the sensor, and $x_{H_2O,1}$ can be calculated by applying Eq. 6.50. The vapor fraction at the point 2 ($x_{H_2O,2}$) can be calculated depending on the temperature. Since the water in this point is in liquid-vapor equilibrium (RH = 100 %), its partial pressure is the saturation pressure for the temperature in this point:

$$p_{H_2O} = P_{sat,H_2O,2}(T_2) \rightarrow x_{H_2O,2} = \frac{P_{sat,H_2O,2}(T_2)}{P_2} \tag{6.58}$$

P_2 is the absolute pressure, in this case the atmospheric pressure. The saturation pressure can be calculated by applying Antoine Equation (Eq. 6.51) at point 2.

Finally, if Eq. 6.57 is replaced in Eq. 6.46, and the definition of $\bar{n}$ (Eq. 6.15) is applied:

$$\bar{n} = x_{alk}\bar{n}_{alk} = x_{alk}\frac{\left(1-\frac{x_{H_2O,1}-x_{H_2O,2}}{1-x_{H_2O,2}}\right)x_{CO_2,2}}{x_{H_2O,1}-\left(1-\frac{x_{H_2O,1}-x_{H_2O,2}}{1-x_{H_2O,2}}\right)x_{CO_2,2}} \tag{6.59}$$

6.2 Dependence between $\bar{N}_{e^-,NG}$ and $\bar{n}$

The variable $N_{e^-,j}$ has been defined as the potentially amount of released electrons by the molecule k. If the electrochemical half-reactions at the anode fuel cell are analyzed, it can be observed that the value of N_{e^-,H_2} and $N_{e^-,CO}$ are equal to 2 (Eq. 6.60 and Eq. 6.61).

$$H_2 + O^{2-} \rightarrow H_2O + 2e^- \Rightarrow N_{e^-,H_2} = 2 \tag{6.60}$$

$$CO + O^{2-} \rightarrow CO_2 + 2e^- \Rightarrow N_{e^-,CO} = 2 \tag{6.61}$$

Accordingly, each molecule of H_2 and of CO can release 2 electrons. The fuel supplied to the stack is not composed by these compounds, but by alkanes, oxygen, nitrogen and carbon dioxide. The alkanes are reformed into H_2 and CO, therefore they are the molecules which potentially release electrons. In case of methane (CH_4), the number of potentially released electrons electrons is 8, as shown in Eq. 6.62.

$$CH_4 + H_2O \rightleftharpoons CO + 3H_2 \Rightarrow N_{e^-,CH_4} = N_{e^-,CO} + 3N_{e^-,H_2} = 8 \tag{6.62}$$

This calculation for the other alkanes studied in the work is shown in Tab. 6.4. The calculation can be generalized for any molecule of an alkane with non-cyclic structure:

$$C_{n_j}H_{2n_j+2} + n_jH_2O \rightarrow n_jCO + (2n_j+1)H_2 \Rightarrow N_{e^-,j} = 6n_j + 2 \tag{6.63}$$

Table 6.4 – Reforming reaction for the considered alkanes and the resulting amount of potential free electrons per molecule [52].

alkane	*reforming reaction*	$N_{e^-,j}$
C_2H_6	$C_2H_6 + 2H_2O \rightarrow 2CO + 5H_2$	$N_{e^-,C_2H_6} = 2N_{e^-,CO} + 5N_{e^-,H_2} = 14$
C_3H_8	$C_3H_8 + 3H_2O \rightarrow 3CO + 7H_2$	$N_{e^-,C_3H_8} = 3N_{e^-,CO} + 7N_{e^-,H_2} = 20$
C_4H_{10}	$C_4H_{10} + 4H_2O \rightarrow 4CO + 9H_2$	$N_{e^-,C_4H_{10}} = 4N_{e^-,CO} + 9N_{e^-,H_2} = 26$

The mean amount of potentially released electrons by a natural gas with a general composition is defined in Eq. 6.64:

$$\bar{N}_{e^-} = \sum_j x_{j,NG} N_{e^-,j} \tag{6.64}$$

Thus, in principle it seems necessary to know the composition of the natural gas for calculating this value. However, in the next paragraphs it will be shown that it is enough to provide the variable $\bar{n}$, which has been identified by different methods in the last section.

The previous expression can be split up into a part corresponding to the alkanes and another corresponding to the inert gases as follows

$$\bar{N}_{e^-,NG} = \sum_{j=alk} x_{j,NG} N_{e^-,j} + \sum_{j=inert} x_{j,NG} N_{e^-,j} \tag{6.65}$$

Taking into account that for inert gases $N_{e^-,j=\mathtt{inert}} = 0$ and applying Eq. 6.63, Eq. 6.65 can be rewritten as

$$\bar{N}_{e^-,NG} = \sum_{j=alk} x_{j,NG} \left(6n_j + 2\right) \tag{6.66}$$

Finally, by applying the definition of x_{alk} (Eq. 6.9) , the definition of $\bar{n}_{alk}$ (Eq. 6.14) and the dependence between $\bar{n}$ and $\bar{n}_{alk}$ (Eq. 6.15), a relation between $\bar{N}_{e^-,NG}$ and $\bar{n}$ is

obtained.

$$\bar{N}_{e^-,NG} = 6 \sum_{j=alk} x_{j,NG} n_j + 2x_{alk} = 6\bar{n}_{alk}\bar{n}_{alk} + 2x_{alk} = 6\bar{n} + 2x_{alk} \tag{6.67}$$

If the fuel is composed only by alkanes this term takes a value of 1. Otherwise x_{alk} becomes an unknown value which changes, for the considered natural gases, between 0.8 and 1.

In conclusion, the variable $\bar{n}$ has been identified as sufficient for calculating $\bar{N}_{e^-,NG}$, instead of the complete natural gas composition. This awareness simplifies significantly the necessary efforts for controlling a FCS with variable gas composition.

6.3 Calculation of the molar flow set points in dependence of $\bar{N}_{e^-,NG}$

The expressions used to calculate the set point values of the system manipulated variables (the natural gas inlet flow and the recycle rate) are based on [52] and have been described in Sect. 3.2. They have been modified so that they are valid for a general fuel, including those containing oxygen and carbon dioxide.

They have been modified so that the variables calculated in dependence of the gas composition are rewritten depending on $\bar{n}$ and $\bar{N}_{e^-,NG}$. For instance, the constants necessary for the calculation of the recycle rate (k_Φ and k_{O_2}) can be calculated by using Eq. 6.68 and Eq. 6.69.

$$k_\Phi = \frac{\bar{N}_{e^-,NG}}{2\left(\bar{n} + x^{ref}_{CO_2,NG}\right)} \tag{6.68}$$

$$k_{O_2} = \frac{2\left(x^{ref}_{O_2,NG} + x^{ref}_{CO_2,NG}\right)}{\bar{n} + x^{ref}_{CO_2,NG}} \tag{6.69}$$

$x^{ref}_{CO_2,NG}$ and $x^{ref}_{O_2,NG}$ are the carbon dioxide and oxygen molar fractions in the natural gas. Since their values are unknown, they are considered parameters and take the value of the reference gas. Thus, the recycle rate (original equation Eq. 3.8) can be calculated independently of the gas composition by using Eq. 6.70

$$r^{set} = \frac{\Phi^{set} - k_{O_2}(\bar{n})}{FU^{stack,set}\left(k_\Phi(\bar{n}) + k_{O_2}(\bar{n}) - \Phi^{set}\right) - k_{O_2}(\bar{n}) + \Phi^{set}} \tag{6.70}$$

The expression for the calculation of the $FU^{sys,set}$ has been developed in Chap. 3.2 (Eq. 3.6). With the new relationships, it can be calculated by Eq. 6.71.

$$FU^{sys,set} = \frac{FU^{stack,set}}{1 - r^{set}(\bar{n}) + r^{set}(\bar{n})\, FU^{stack,set}} \tag{6.71}$$

The expression for the calculation of the natural gas inlet molar flow set point has been previously developed depending on the produced current, the set point of the system fuel utilization and the gas composition. The expression involving $\bar{N}_{e^-,NG}$ is developed in Eq. 6.72.

$$\dot{n}^{set}_{NG} = \frac{IN_{cells}}{FU^{sys,set}(\bar{n})\, F\bar{N}_{e^-,NG}(\bar{n})} \tag{6.72}$$

The summary of the control strategy is presented in Fig. 6.10. It is based on Fig. 6.1, showing the variable dependences which have been developed in this section. The tests of the developed control strategies are carried on in the next chapter by using simulation methods.

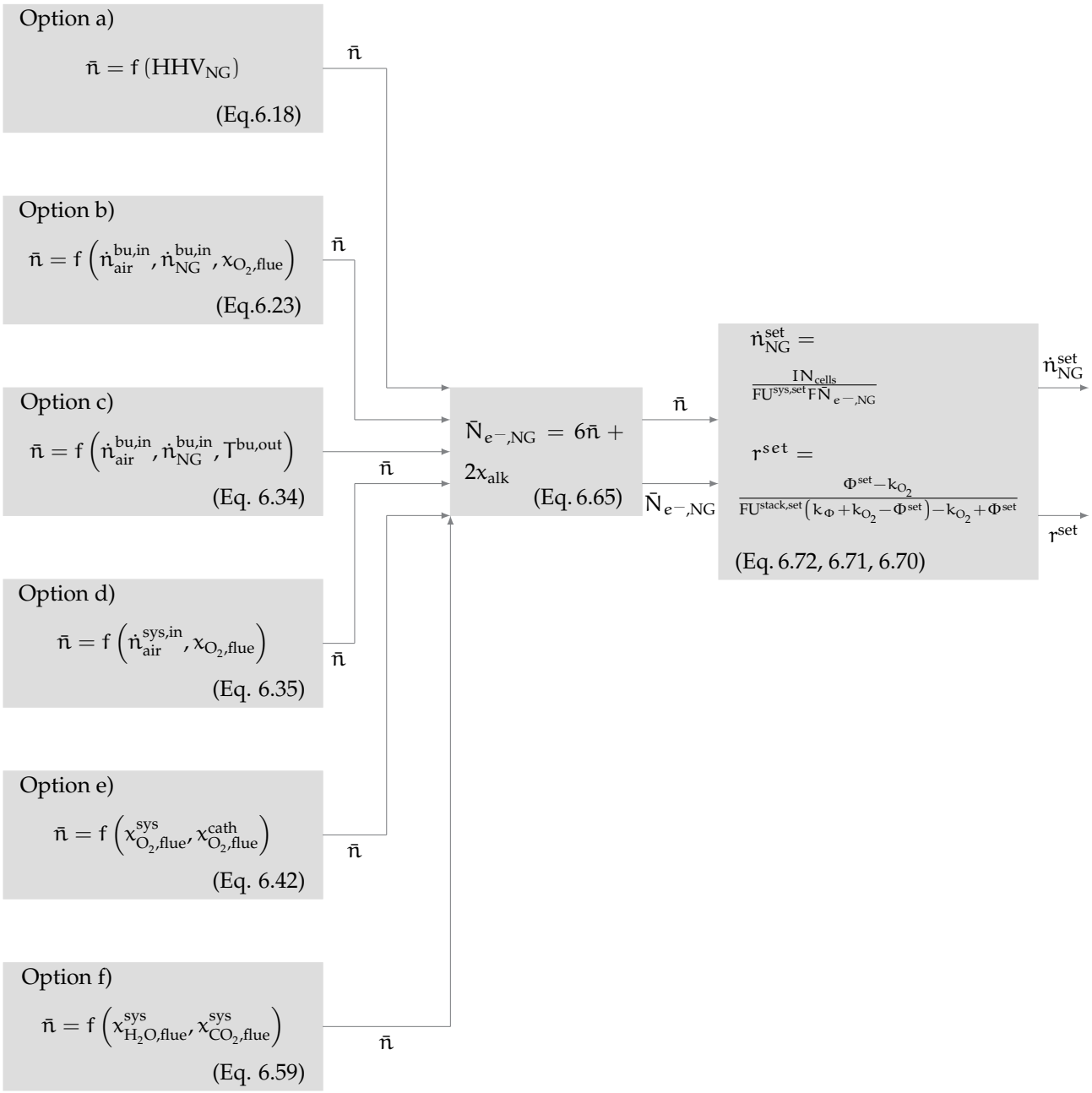

Figure 6.10 – Summary of the system control for the different natural gas detection strategies.

7 Evaluation of the control strategies with simulation methods

In this chapter the different detection methods for the adaption of the control strategies are evaluated by using the system model. Firstly, the strategies to be evaluated are selected by applying technical and economical criteria. Then, the system evaluation parameters for the reference gases resulting from each strategy are shown and compared.

7.1 Choice of the control strategies to be evaluated

There are different reasons to choose or discard a control strategy to be tested with simulation methods, including technical and economical criteria.

The main technical factor is the accuracy in the detection of the inlet natural gas. In order to carry on a first evaluation of the deviation between the real value of $\bar{n}$ and the values detected by the control strategy, an analysis of the error propagation in the calculation of $\bar{n}$ is applied. For this purpose, the standard deviation of $\bar{n}$ is calculated from the variance of the measured signals by the sensors (Tab. 7.2).

$$\sigma_{\bar{n}} = \sqrt{\sum_{k} \left(\frac{\partial \bar{n}}{\partial y_k} \right)^2 \sigma_{y_k}^2} \tag{7.1}$$

$\sigma_{\bar{n}}$ is the standard deviation of $\bar{n}$, and represents its variation from the real value. The deviation or error can be also expressed as a relative error by

$$\epsilon_{\bar{n}} = \frac{\sigma_{\bar{n}}}{\bar{n}^{\text{real}}} \tag{7.2}$$

y_k are the variables and parameters used for the calculation of $\bar{n}$ and consequently which are an uncertainty source. The relative error (Eq. 7.2) has been calculated for all reference natural gases (Fig. 4.3) by using the expressions for the calculation of $\bar{n}$ developed in Chap. 6. The maximal and the mean value of them (ϵ_{max} and ϵ_{mean} respectively, defined by Eq. 7.3 and Eq. 7.4) are presented in Tab. 7.1 for each strategy as indicator of the accuracy.

$$\epsilon_{\text{max}} = \max\left(\epsilon_{\bar{n}}\right), \text{for the 13 reference gases} \tag{7.3}$$

$$\epsilon_{\text{mean}} = \frac{\sum_{\bar{n}}\left(\epsilon_{\bar{n}}\right)}{13} \tag{7.4}$$

Another fact to be taken into account is the consumption of natural gas for the detection method, which results in a decrease of the system efficiency. The use of the start-up burner in the strategy implies the combustion of natural gas which otherwise could be consumed in the system. This fuel volumetric flow has to reach a minimal value in order to ensure the operation of the burner. In case of a calorific value sensor different measuring principles can be used, but most of them consume a small amount of natural gas. On the contrary, in the strategies where the complete system is regarded, the efficiency is not affected by the detection strategy.

The economical criteria include the investment (cost of the additional sensors) and the possibility of operating without the air flow sensor in the system, which would result in a costs decrease.

Table 7.1 – Evaluation of the detection strategies to be tested, on the basis of technical and economical criteria. The deviations are calculated by assuming the sensor errors referred in Tab. 7.2.

strategy	*sensors*	ϵ_{max}	ϵ_{mean}	*NG consumption*	*cost*	*air flow sensor*
a)	HHV_{NG}	0.54 %	0.52 %	small flow	€€€	no
b)	$\dot{n}_{air}^{bu,in}$, $\dot{n}_{NG}^{bu,in}$, $T^{bu,out}$	24.5 %	11.3 %	large flow	€	yes
c)	$\dot{n}_{air}^{bu,in}$, $\dot{n}_{NG}^{bu,in}$, $T^{bu,out}$	14.1 %	13.4 %	large flow	0	yes
d)	$\dot{n}_{air}^{sys,in}$, $x_{O_2,flue}$	13 %	12 %	no	€	no
e)	$x_{O_2,flue}^{sys}$, $x_{O_2,cath}^{out}$	14.9 %	13.9 %	no	€	yes
f)	$x_{H_2O,flue}^{sys}$, $x_{CO_2,flue}^{sys}$	15.3 %	12.1 %	no	€€	no

In Tab. 7.1 the evaluation for the different strategies is presented. It can be observed that the control strategy based on the measurement of the higher heating value (a) is optimal regarding precision, which could partly compensate the fact that a small amount of natural gas is consumed in the process and the high investment costs.

In case of the strategies based of the continuous use of the start-up burner (b, c) the main argument against their choice is the large consumption of natural gas related to the measurement method. In addition, the used sensors are not precise in the $\bar{n}$ detection and an air flow sensor is necessary. Nevertheless the strategies could be considered due to their low costs.

On the contrary, the strategies based on gas measurements at the system exhaust gas do not mean an additional fuel consumption. In case of the measurement of the oxygen molar fraction at the flue gas (e), the precision is only moderate and an air flow sensor is necessary. However, the alternative to this strategy characterized by the calculation from the oxygen molar fraction at the cathode outlet (d) does not present these disadvantages. Finally, in case of the water and the carbon dioxide molar fraction measurement (f), the accuracy of the results is acceptable and the presence of air

Table 7.2 – Measurement errors of the reference sensors (MV=Measured Value, EV=End Value).

measured variable	*physical principle*	*measurement error*
HHV	nondispersive infrared sensor + thermal conductivity	$\pm$0.4 %MV [27]
$\dot{v}_{CH_4}$	constant temperature anemometer	$\pm 1.5\,\%\,\mathrm{MV} \pm 0.3\,\%\,\mathrm{EV}$ [14]
$\dot{v}_{air}$	calorimetric flow meter	$\pm\,(3\,\%\,\mathrm{MV} \pm 0.3\,\%\,\mathrm{EV})$[12]
x_{O_2}	lambda-sonde	$\pm$3.14 %MV[5]
P	differential pressure transducer	$\pm$0.5 %MV [8]
T	resistance temperature detector	$\pm$0.4 K[11]
RH	capacitive humidity sensor	$\pm$1 %RH [13]
x_{CO_2}	nondispersive infrared sensor	$\pm max(1\,\%\mathrm{MV}, 0.002 mol \cdot mol^{-1})$ [16]

flow sensor is not necessary. The disadvantage of this strategy are the medium costs caused by its implementation.

Taking into account the mentioned criteria, strategies (b) and (c) are discarded, while the other methods are tested by using the system model.

7.2 System operating parameters resulting of the control strategies

The detection strategies described previously are evaluated in this section. For this purpose, they are implemented at the model described in Chap. 5 and the system operation with the variable gas composition is simulated. The resulting system operation characteristic variables are compared: the oxygen to carbon ratio (Φ), the stack

Table 7.3 – Values of the parameters used for the evaluation of the strategies.

parameter	*value*
Φ^{set}	2
$FU^{stack,set}$	60 %
x_{alk} (H-gas)	0.95
x_{alk} (L-gas)	0.80

fuel utilization (FU^{stack}) and the electrical efficiency of the system (η_{el}^{sys}), all defined in Chap. 2.3. The set points for the system operation characteristic variables are kept constant for all strategies, as well as the value of the parameter x_{alk} (Tab. 7.3). The air side control strategy (detailed in Sect. 3.2) does not vary either.

The results for the different control strategies are shown in Fig. 7.1. They are calculated for the reference gases presented in Chap. 4.3, classified under H-Gas and L-Gas groups. In case of Φ and FU^{stack} the set point is shown with a red line. In order to ensure the lifetime of the stack, the actual value of Φ should be above the set point and for FU^{stack} below its set point. Regarding the electrical efficiency there is not a specific set point, but the aim is to maximize its value. The results are presented compared to these obtained by from applying the reference strategy, calculated with the gases referred in Tab. 4.2. The results obtained from the reference strategy are presented in dark blue. They fluctuate depending on the inlet gas, achieving a difference between the maximal and minimal values of 26.1 % regarding Φ, 35.1 % if FU^{stack} is considered and 33.3 % in case of η_{el}.

On the contrary, the values resulting from the use of the detection method based on the calorific value sensor (in yellow) show a significantly lower variation from natural gas to natural gas. In case of Φ the variation in the results between the maximal and minimal points attain 5.7 % and for the FU^{stack} and η_{el} remains under 2 %. Furthermore, both conditions to guarantee the lifetime of the stack are continuously fulfilled. In addition, the set point for the stack fuel utilization is met in all cases. The con-

sequence is a maximization of the electrical efficiency, kept over 63 %, in contrast to the reference values.

The parameters resulting from applying the detection strategies based on the oxygen measurement are shown in green. The mean amount of carbon atoms per molecule is calculated depending on the methane and air flows and on the oxygen molar fraction at the system exhaust. In the first case the air flow is directly measured with a sensor (Eq. 6.34) and in the second it is calculated depending on the oxygen molar fraction at the cathode flue gas by using Eq. 6.42. If ideal sensors are assumed, the values of Φ, FU^{stack} and η_{el} are the same for both strategies, since they are based on the same principle. The variation of the parameters values is negligible, being the difference between the minimal and maximal Φ of 4.76 %, 3 % for FU^{stack} and 5.5 % for η_{el}.

Comparing the calorific value strategy and the oxygen strategies, it can be seen that the results are very similar. For H-Gases, the parameters have the same values for each gas. On the contrary, for L-Gases a difference can be observed, specially for the efficiency. The reason is that in case of L-Gases a low value of x_{alk} should be assumed in order to avoid starvation. In case of the strategy based on the calorific value its influence is negligible, but for the oxygen strategies the influence is higher, causing the efficiency decrease. It can be affirmed that these gas identification strategies are adequate methods for adaptation of the control strategy to fluctuating gas compositions.

Finally, the values resulting from applying the detection strategy based on the measurement of water and carbon dioxide at the system flue gas are presented in light blue. It can be observed that the variation in the values is comparable to these from the reference strategy. The values of Φ change up to 29.8 %, up to 47.2 % for FU^{stack} and 18.3 % in case of η_{el}. The reason is the influence of the parameter x_{alk}. As it can be seen in Eq. 6.59, the calculation of $\bar{n}_{alk}$ is directly proportional to the alkanes molar fraction. It results in considerable errors in the detection, which causes a deviation between the actual values of the system operation characteristic values and the set

points. Thus, with the current configuration, the strategy based on the measurement of CO_2 and H_2O cannot be applied to adapt the control strategy to gases with variable composition.

Last results showed the system system operation characteristic values if ideal sensors where assumed. In reality, each sensor generates a measurement error, which results in a stronger deviation between the set points and the actual values. The results obtained by regarding the sensor errors are shown in Fig. 7.2, Fig. 7.3, Fig. 7.4 and Fig. 7.5 for each strategy. The sensor errors are obtained from the data sheet of each sensor and listed in Tab. 7.2.

In case of calorific value strategy, the results of the sensor errors are very similar to these obtained considering ideal sensors. On the contrary, for the strategies based on the oxygen measurement, it can be seen that the error range becomes wide, achieving Φ and FU^{stack} values which result in the stack degradation and the efficiency varying on $\pm 3\,\%$. The reason is that three and four different sensors are used respectively, so that the error generated by each one of the sensors is propagated resulting in worst cases with very high errors. On the contrary, if the strategy based on the measurement of the calorific value is analyzed, it can be seen that it needs only one sensor, which is at the same time a sensor with a high accuracy which results in a narrow error range. It can also be observed that results from both control strategies (*Option d)* and *Option e)* are very similar, if the sensor errors are also regarded. The reason is that the errors resulting from the flow air sensor and from the oxygen sensor for its calculation are not significantly different.

For the strategy based on the measurement of the humidity and carbon dioxide molar fraction at the system outlet the error margins are broad too. It can be concluded that the correction does not fulfill the objectives, since the resulting FU^{stack} and Φ differ significantly from the set points. Again, several sensors are necessary in order to implement the strategy, resulting in a propagation of the error. Furthermore, the high values of FU^{stack} forced a change in the χ_{alk} values. Otherwise, in some operation

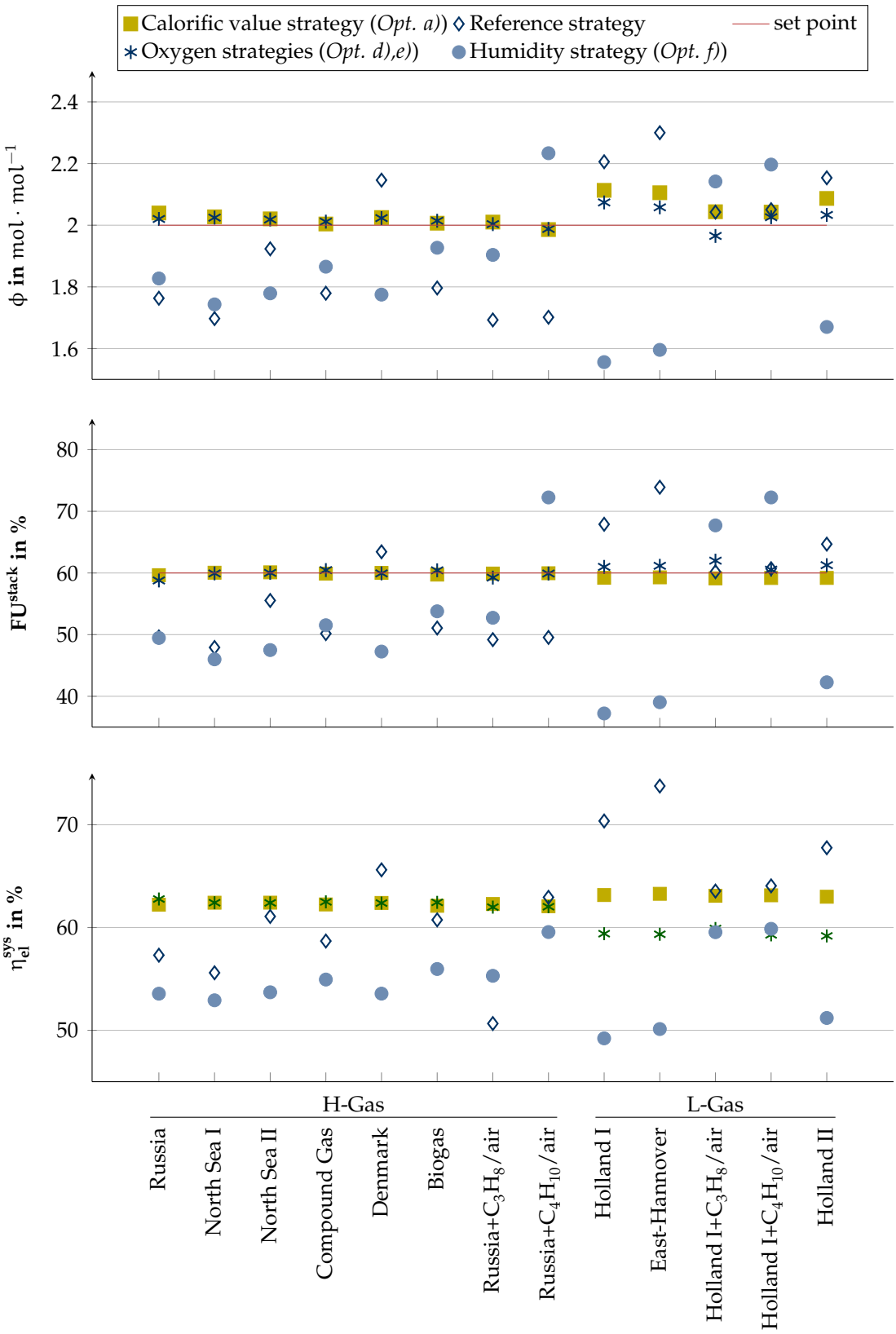

Figure 7.1 – System operation characteristic values by applying the different control strategies (ideal sensors; $x_{alk} = 0.95$ for H-Gases and $x_{alk} = 0.80$ for L-Gases).

points the stack run into a situation of starvation, which resulted in a too low voltage. In this situation the simulation breaks up and the obtention of steady state results becomes impossible. Therefore, the standard values used in the other simulations are changed to x_{alk}=0.87 for H-Gases and x_{alk}=0.70 for L-Gases.

To sum up, simulation results show that, if ideal sensors are considered, three strategies are effective in order to adapt the control strategies to natural gases with fluctuating gas composition: the strategy based on the measurement of the calorific value, these on the measurement of oxygen molar fraction at the system exhaust gas and on the measurement of the oxygen molar fraction at the anode and at the system flue gases. On the contrary, the method consisting on measuring the humidity and the carbon dioxide molar fraction at the system outlet did not show satisfactory results. In the next chapter, two of the strategies are experimentally evaluated in order to extract solid conclusions.

In the next paragraphs the differences in the system behavior operating with or without a gas detection method are analyzed for better understanding of the results. As example is taken the strategy based on the measurement of the calorific value for the H-Gas, but the results can be extended to the other strategies and gases.

In Fig. 7.2 it has been observed that the efficiency of the system operating with the calorific value strategy is maintained constant for all gases, whereas for the reference strategy it fluctuates. The electrical efficiency has been defined as the ratio between the electrical power produced by the system (P_{el}^{out} from Fig. 7.6) and the inlet power through the fuel (P^{in} from Fig. 7.6) by Eq. 2.56. In Fig. 7.7 the system inlet power and the electrical outlet power, for the reference and the calorific value strategies are presented. It can be observed that for both methods the produced electrical power is nearly constant of around 9.25 kW_{el} for all gases. The reason is that the produced current I is a manipulated variable which has not been varied, and the changes on the power output U_{cell} are slight. On the contrary, P^{in}, in case of the reference strategy, fluctuates between 15 kW and 18 kW. However, for the calorific value, in opposite, it

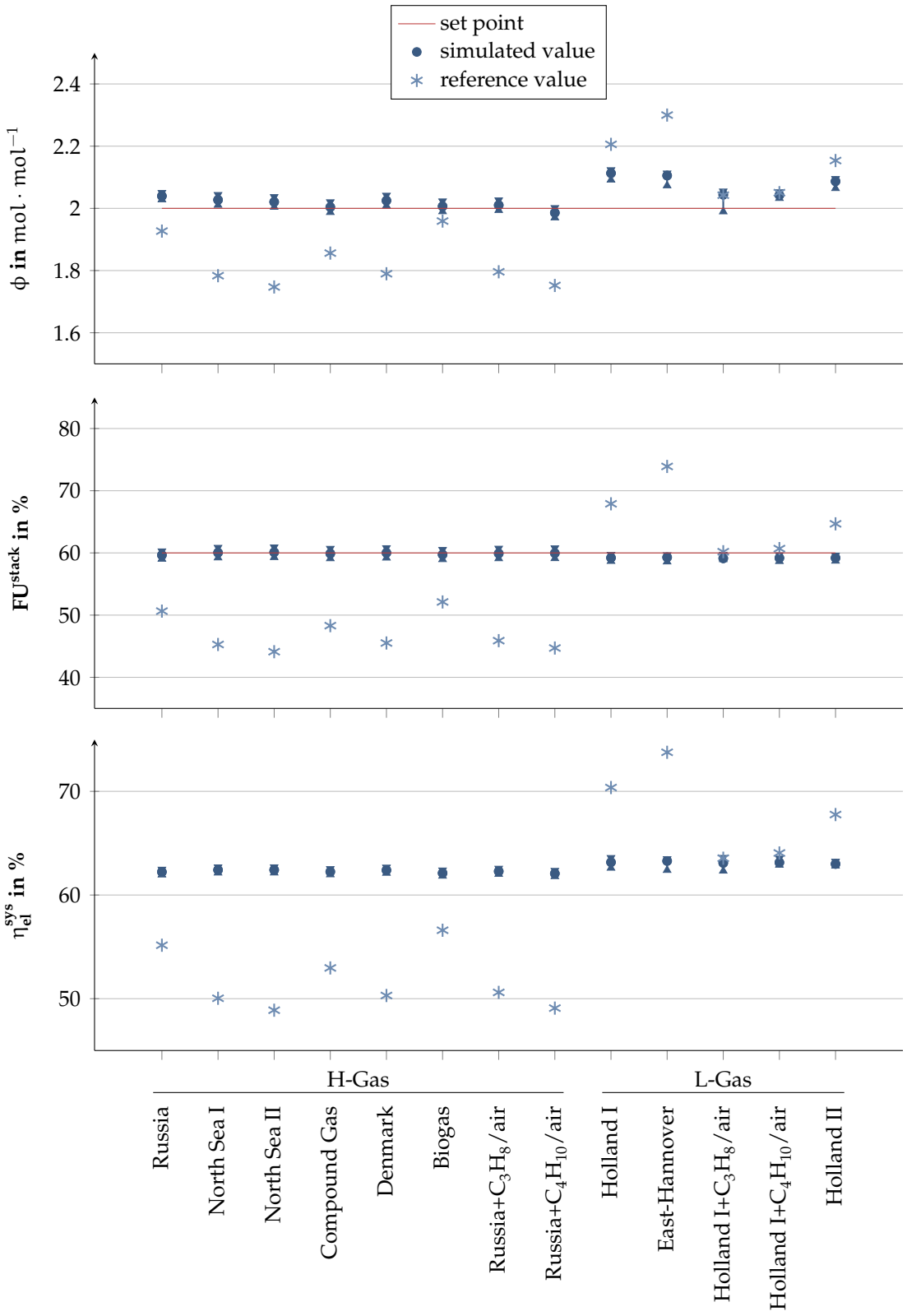

Figure 7.2 – System operation characteristic values resulting from the control strategy *Calorific value strategy, Opt. a)*, assuming $x_{alk} = 0.95$ for H-Gas and $x_{alk} = 0.80$ for L-Gas. The sensor errors are considered.

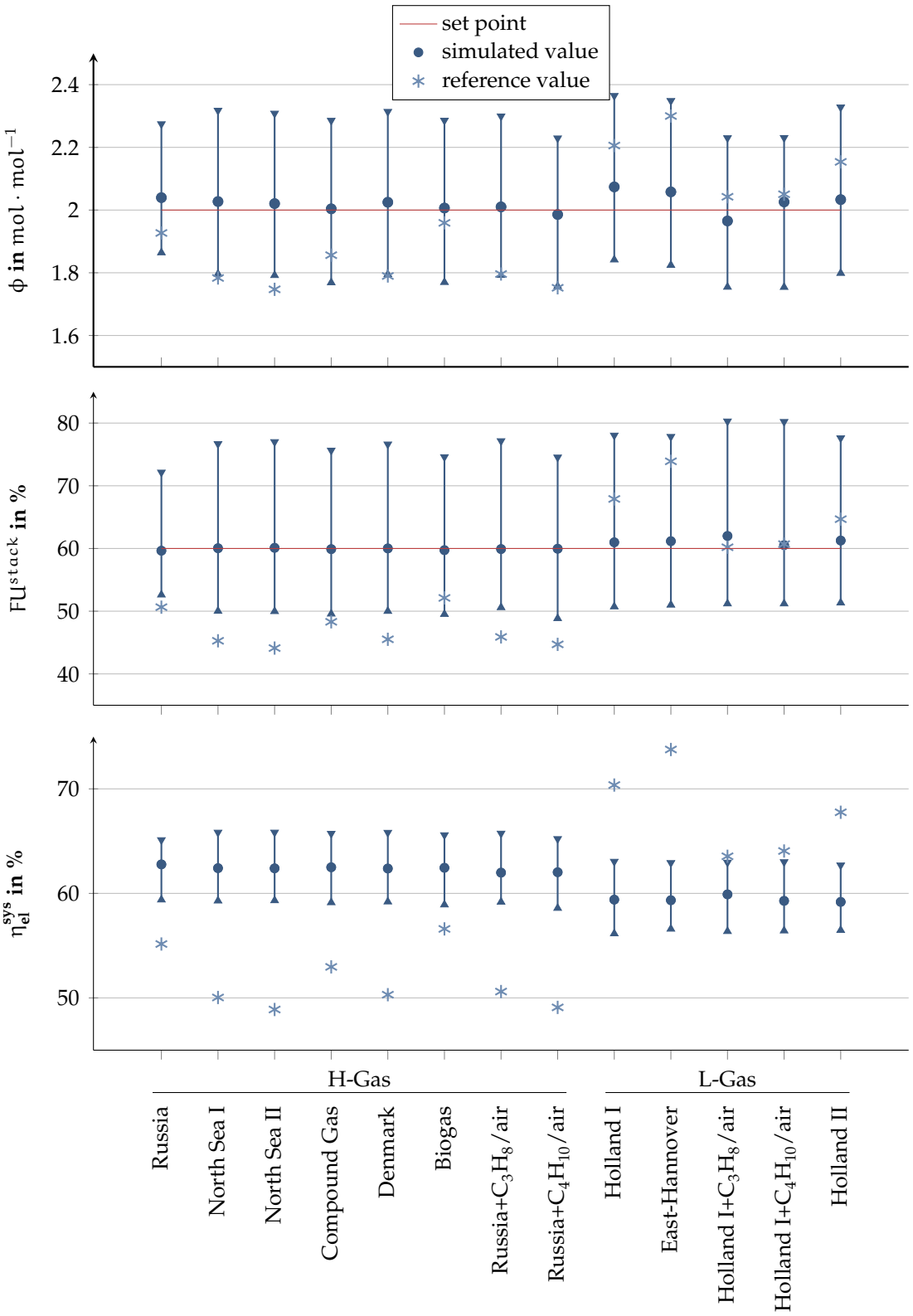

Figure 7.3 – System operation characteristic values resulting from the control strategy *Oxygen strategy I, Opt. d)*, assuming $x_{alk} = 0.95$ for H-Gas and $x_{alk} = 0.80$ for L-Gas. The sensors errors are considered.

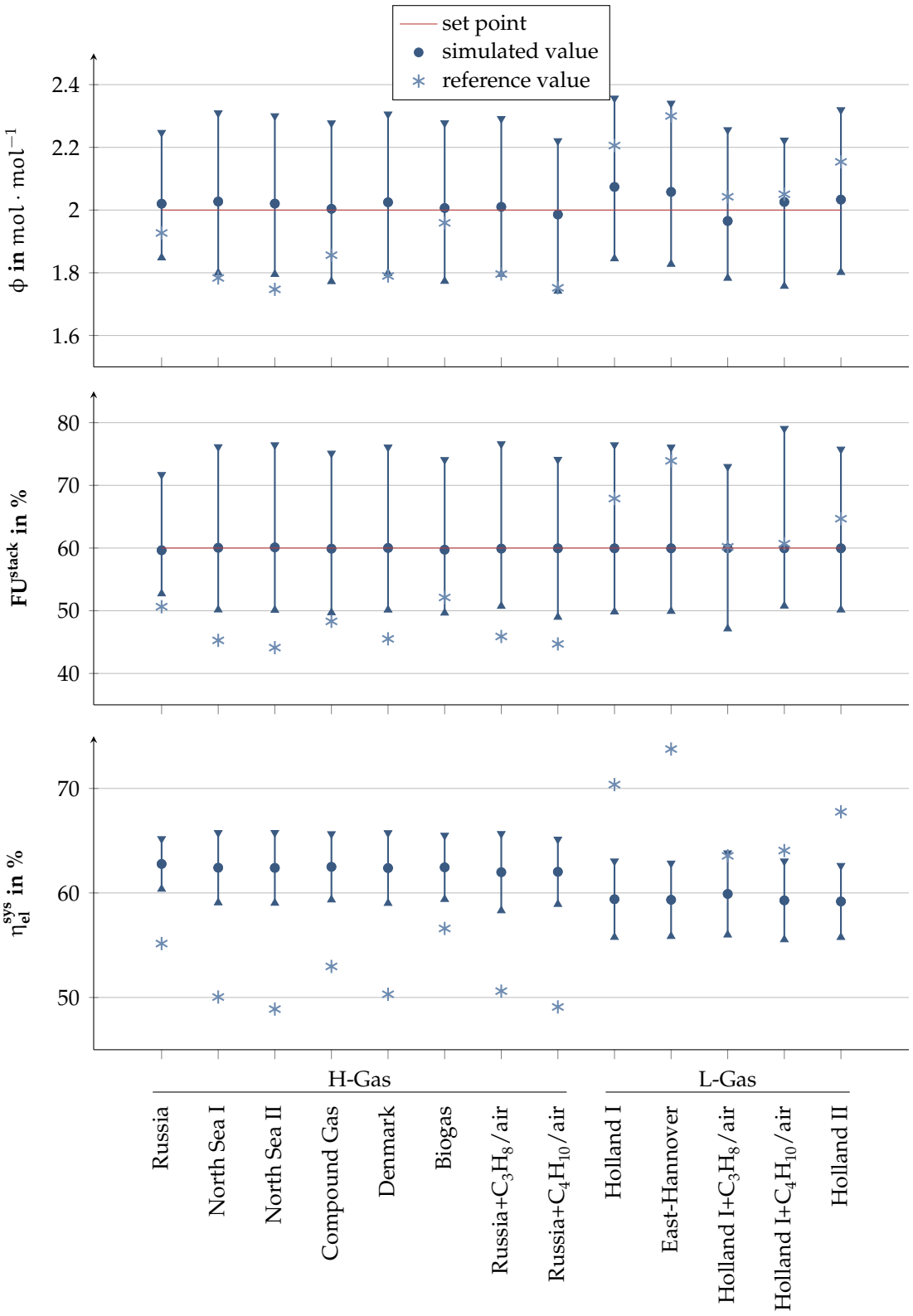

Figure 7.4 – System operation characteristic values resulting from the control strategy *Oxygen strategy II, Opt. e)*, assuming $x_{alk} = 0.95$ for H-Gas and $x_{alk} = 0.80$ for L-Gas. The sensors errors are considered.

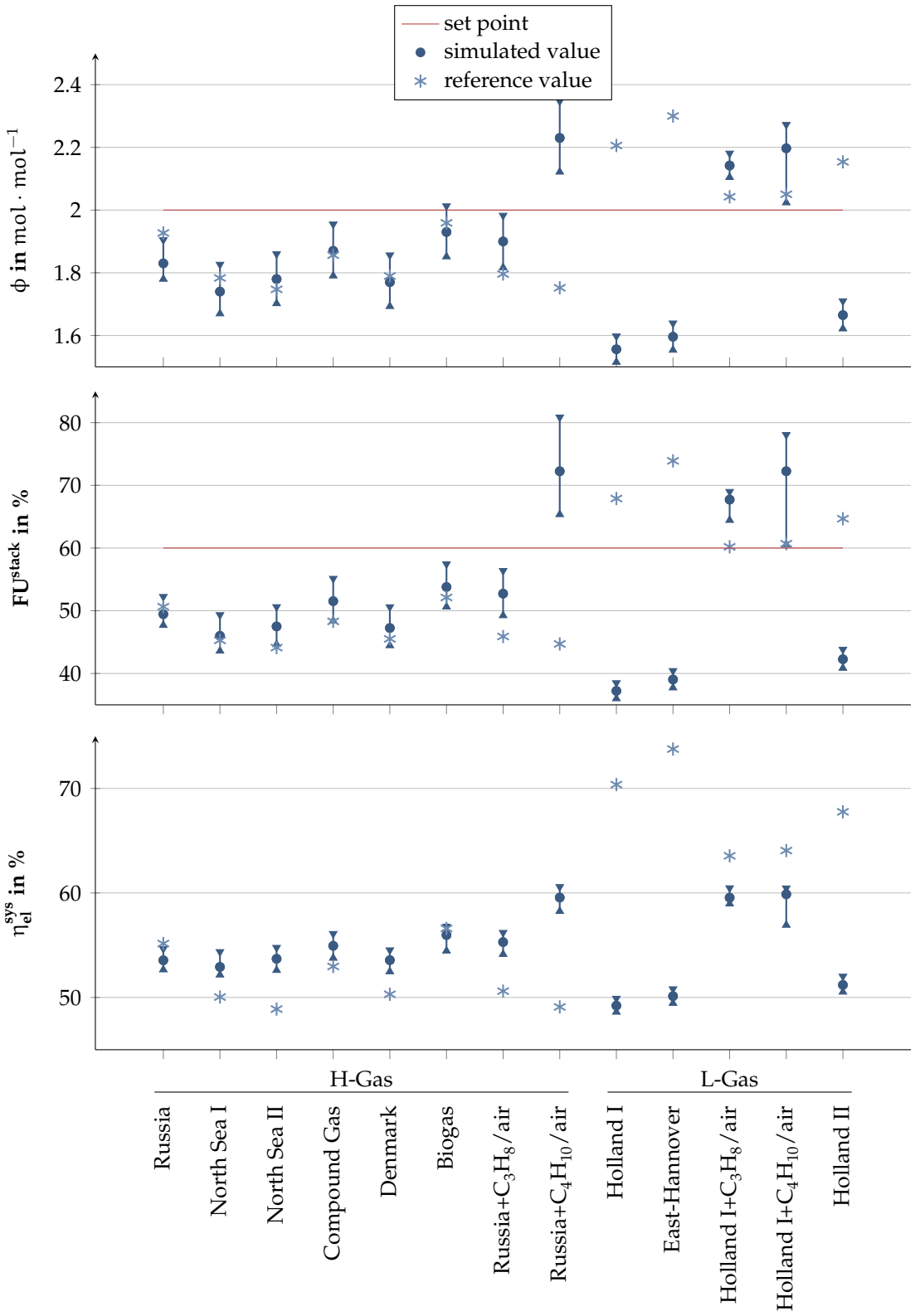

Figure 7.5 – System operation characteristic values resulting from the control strategy *Humidity strategy, Opt. f)*, assuming $x_{alk} = 0.87$ for H-Gas and $x_{alk} = 0.80$ for L-Gas. The sensors errors are considered.

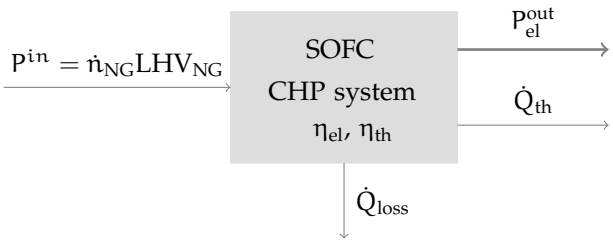

Figure 7.6 – Inlet power, outlet power and losses for the SOFC CHP system.

has a slightly fluctuating value of 16 kW. Thus, the quotient of both variables results constant in the latter case and fluctuating in the first one.

The reason of the different behavior in the entering power can be understood if the properties of the entering fuel flow are analyzed. The lower calorific value of the fuel (LHV) and the molar flow rate are presented for both strategies and all H-Gases in Fig. 7.8. Since the analyzed gases are the same, the inlet LHV does not vary with the strategies considered. However, if the molar flow rate is observed differences can be found. While for the reference strategy it has a fixed value, for the calorific value it varies depending on the gas. This is the expected behavior, because in the first case the set point for the fuel flow is calculated for a reference gas and kept constant independently on composition of the actual fuel. On the contrary, the detection method compensates the gas fluctuations adapting the molar flow so that, since the power is defined as the product between both properties, the result (P^{in}) becomes constant, which results in constant η_{el} and FU^{stack} values.

The oxygen to carbon ratio, Φ, has been defined as the ratio between carbon and oxygen molar flow at the prereformer inlet (Eq. 2.53). In Fig. 7.2 its values for the analyzed strategies have been presented. In case of the reference strategy Φ has a different value for each gas, being often below the minimum value to guarantee the stack lifetime. On the other side, the values of Φ obtained by applying the calorific value strategy is maintained constant at the set point.

In Fig. 7.9 and Fig. 7.10 are presented the oxygen and carbon molar flow with respect

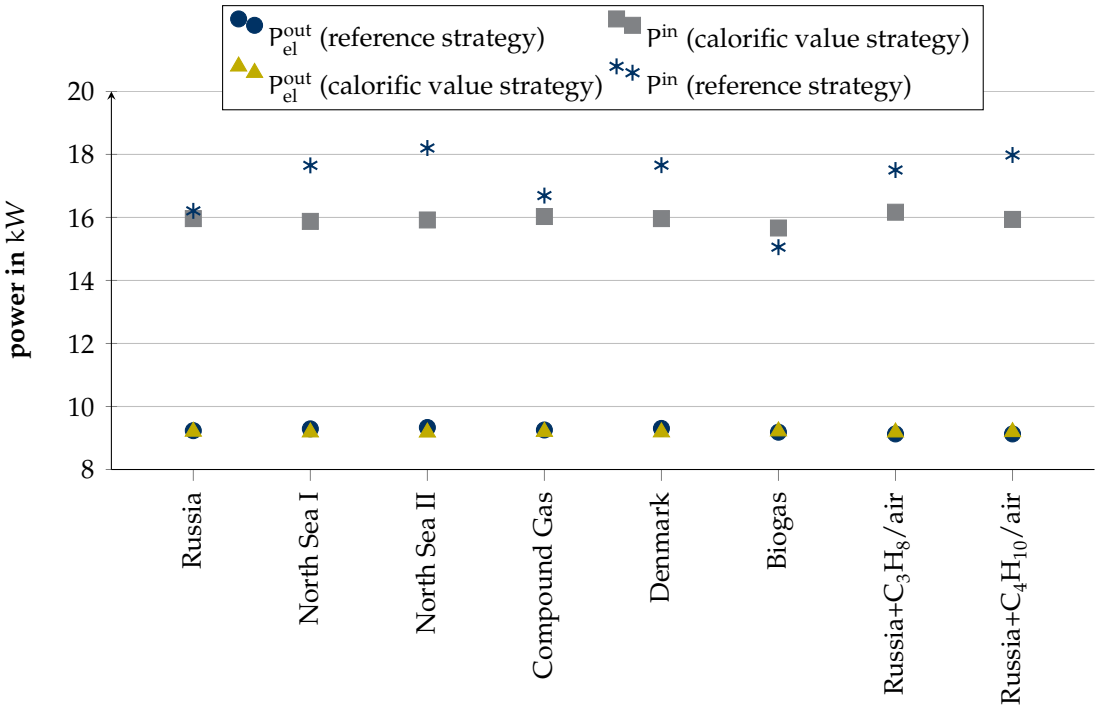

Figure 7.7 – Inlet and outlet power for the reference strategy and for the detection method based on the measurement of the calorific value.

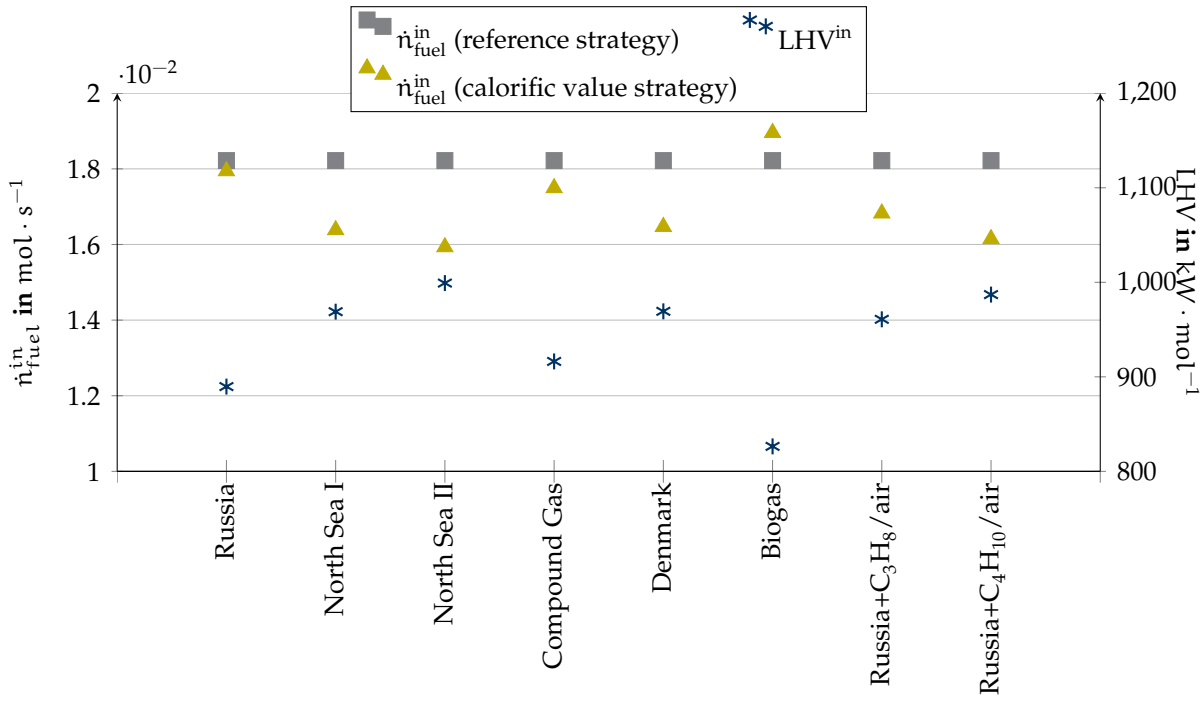

Figure 7.8 – Inlet fuel molar flow and inlet calorific value for the reference strategy and for the detection method based on the measurement of the calorific value.

to the total molar flow at the prereformer inlet. It can be observed that, when the carbon molar flow increases, for the case of the reference strategy the oxygen molar flow decreases. The reason is that the oxygen transfer to the anode flow, which takes place at the stack through the electrochemical reaction, is actually constant (it depends directly on the produced current, which is set constant). The recycle rate r is maintained fixed for all gases, as can be seen in Fig. 7.11. Thus, if the absolute amount of carbon atoms is increased by a change in the inlet gas, the relative oxygen content decreases and consequently so does the value of Φ.

On the contrary, the calorific value strategy is capable to detect the change in the gas composition. Consequently the recycle rate is adapted, so that it increases with the carbon molar flow (Fig. 7.11). This results in a higher oxygen molar flow (Fig. 7.10), which compensates the higher carbon molar flow and guarantees that the Φ is kept over its minimum value.

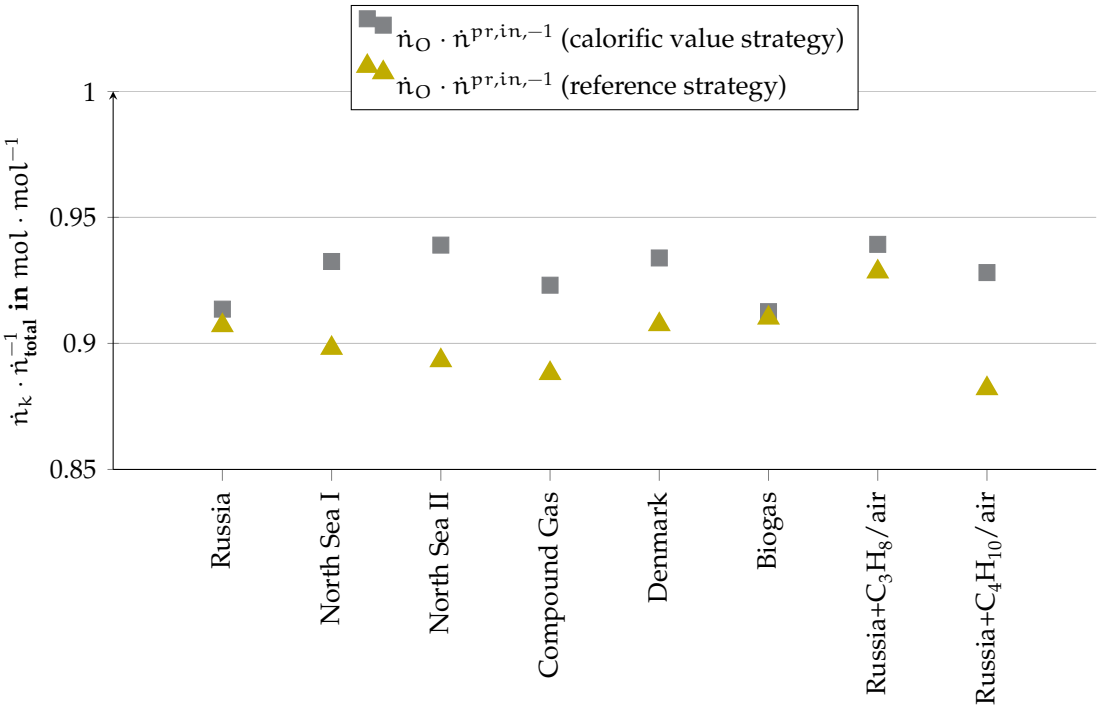

Figure 7.9 – Oxygen molar flow with respect to the total molar flow at the prereformer inlet for the reference strategy and the strategy based on the measurement of the calorific value.

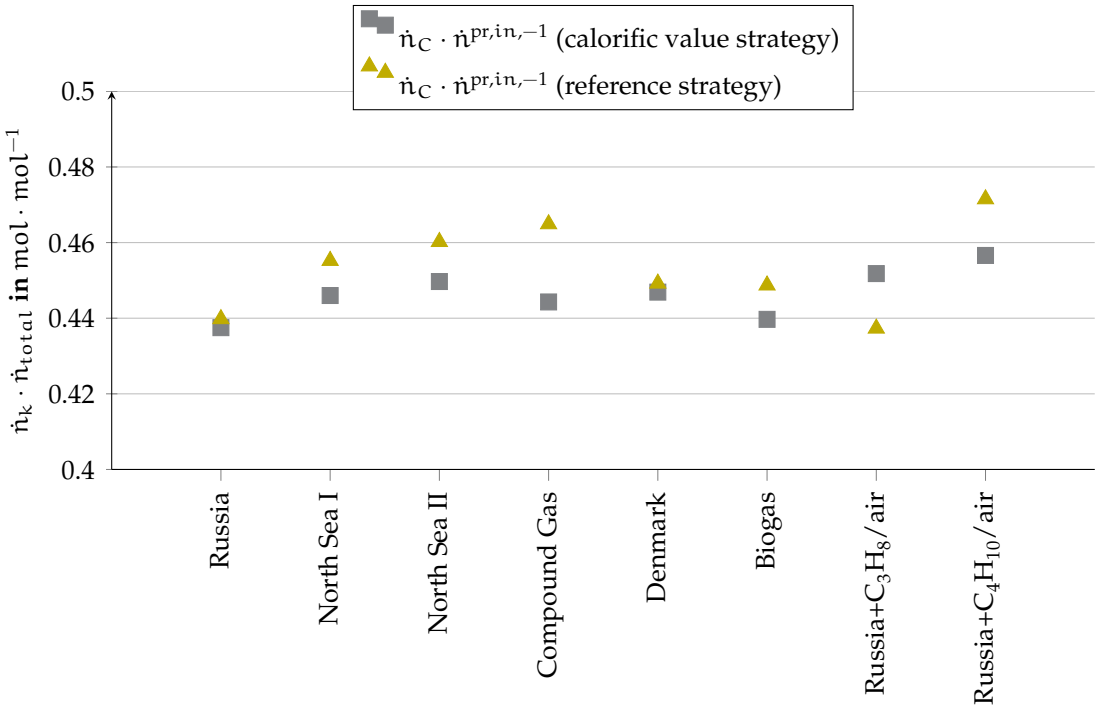

Figure 7.10 – Carbon molar flow with respect to the total molar flow at the prereformer inlet for the reference strategy and the strategy based on the measurement of the calorific value.

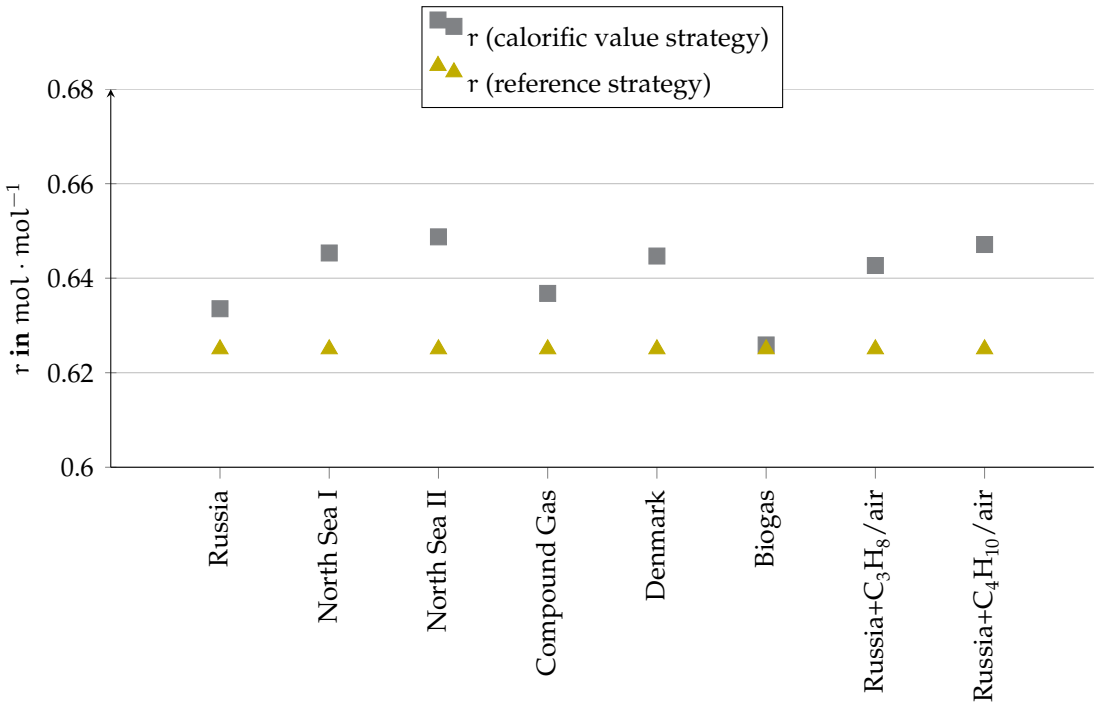

Figure 7.11 – Recycle rate for the reference strategy and the calorific value strategy.

The stack fuel utilization is defined as the percentage of the provided electrons which react in the electrochemical reaction producing electricity (Eq. 2.47). Similarly to the other operating parameters, with the reference strategy the fuel utilization changes depending on the natural gas and with the calorific value strategy is kept constant at the set point (Fig. 7.2).

This behavior can be explained by comparing the electrons molar flows in both cases, as presented in Fig. 7.12. The amount of consumed electrons depends exclusively on the produced current, which is constant for all gases with both strategies. Consequently, the electrons molar flow consumed at the stack is constant as well. The electrons are provided by the gas entering the stack, which is a mixture between the fresh natural gas and the recycled anode flue. It can be observed that with the reference strategy the flow is fluctuating, which is the expected behavior, since in the previous figures it has been observed that while the energetic content of the inlet fuel changes depending on the gas, neither the inlet gas flow nor the recycle gas vary

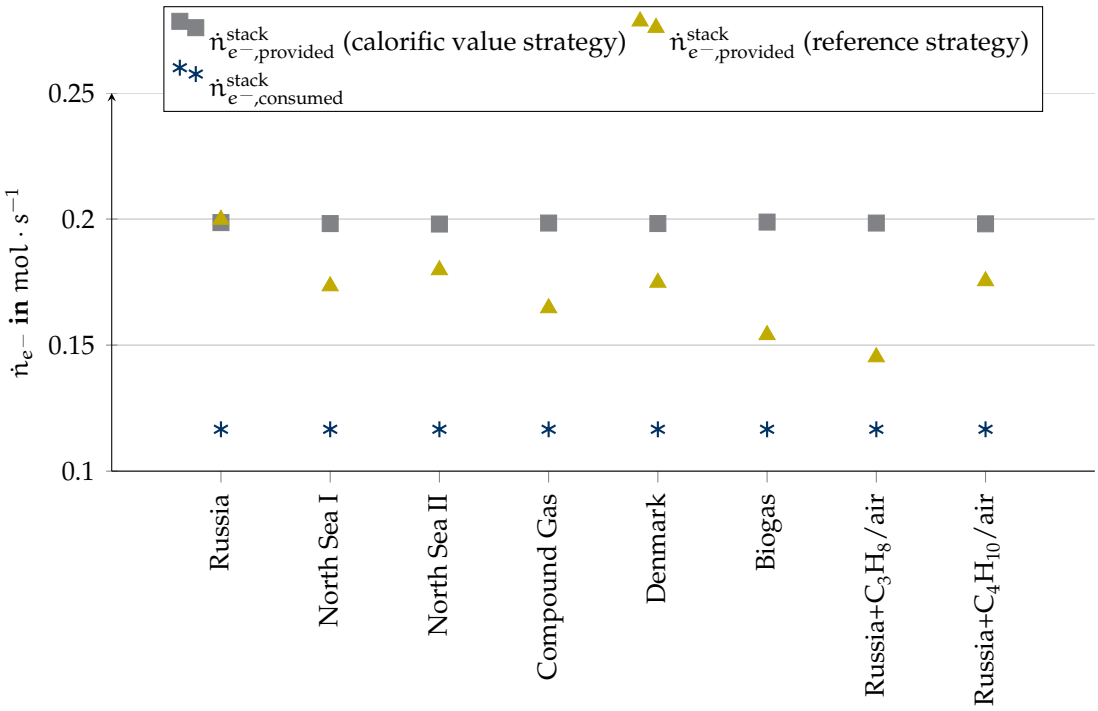

Figure 7.12 – Provided and consumed electrons molar flow at the stack for the reference and the calorific value strategies.

consequently. In contrast, with the calorific value strategy, a constant molar flow of provided electrons is achieved, resulting in the adaptation of the manipulated variables to the gas composition.

8 Evaluation of the control strategies with experimental methods

In Chap. 7 the different methods for adaptation of the control strategy to variable gas composition have been evaluated by using simulation methods. In the next sections two of the strategies are experimentally tested. The aim is to compare the mean amount of carbon electrons per molecule of fuel ($\bar{n}$) with the value detected by the different procedures.

From the four methods implemented in the simulation model only two have been chosen to be tested: the solution based on the measurement of the oxygen molar fraction at the system exhaust (Option d) in Chap. 6) and the one based on the measurement of the carbon dioxide and the water molar fraction at the system flue gas (Option f) in Chap. 6). The other two methods could not be tested experimentally for different reasons. In case of the calorific value sensor, the high prices of the devices which are to be found at the moment at the market prevent its implementation in the system. If in future low-cost heating value sensors are to be found in the market this strategy should be taken into account. On the contrary, the strategy which uses two oxygen sensors (at the cathode and the system outlet) would suppose a low investment.The disadvantage of this method is that it can only be tested in the complete SOFC system, which at this point is not possible because there is no access to the stack.

8.1 Experimental procedure

In Chap. 6 the relation between $\bar{n}$ and the energy content of a natural gas has been detailed. As a consequence, if $\bar{n}$ is known, the SOFC system control strategy can be adapted to inlet fuels with fluctuating calorific value. The aim of the experiments is to evaluate the precision of the detection methods by comparing the real value of $\bar{n}$ for gases with variable HHV and the obtained value by applying the different detection procedures.

The diagram of the test bench used for this purpose is presented in Fig. 8.1. It can be observed that instead of carrying out the experiment in the complete SOFC system, it has been limited to the air processor and the HE_4. In Sect. 6.1.4 it has been shown that, regarding the species and mass balance, a FCS is equivalent to a burner operating in complete combustion. Thus, since the control strategies are based on stoichiometric relations, it is assumed that the results for the reduced system can be extended to the entire system.

The used fuel is a mixture of methane and nitrogen mixed in different proportions in order to emulate natural gas with different HHV contents, due to limitations in the test bench.

The normalized volumetric flow of the gases entering the system is determined by the Mass Flow Controllers (MFC). The variation of the fuel heating value is achieved by mixing methane and nitrogen in different proportions. The air flow is heated up in the HE_3. In the complete system, the hot air would enter the cathode bulk. On the contrary, in the test bench, it is delivered to the afterburner, where it is mixed with the fuel. There, a complete combustion takes place, ensured by an operation in lean mixture ($\lambda > 1$). Before the exhaust gas is cooled down in a first heat exchanger the measurement of the oxygen molar fraction is performed, since for the sensor it is optimal to operate at high temperatures. On the contrary, the relative humidity (RH) needs to be measured at temperatures slightly over the condensation point. There is

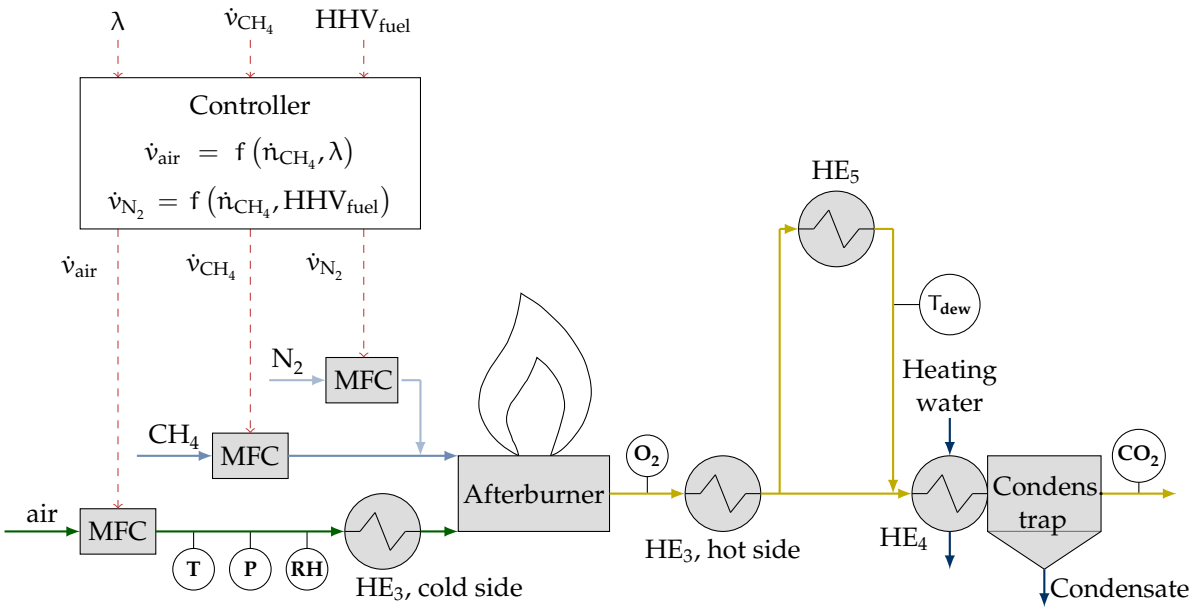

Figure 8.1 – Diagram of the test bench where the experiments were carried out. The white circles show the location of the sensors.

not any point in the system which fulfills this condition. Thus, a flue gas sample is extracted from the system and brought to the desired temperature at the HE_5, to finally measure the gas humidity, temperature and pressure. These are the data needed for the posterior calculation of the water molar fraction. Then the flue gas is cooled down in HE_4. At its outlet it is located the carbon dioxide sensor, which operates at maximal temperatures of about $T = 50\,°C$.

The control variables of the system, presented in Fig. 8.1, are the higher heating value (HHV_{fuel}), the methane molar flow ($\dot{n}_{CH_4}$) and the air-fuel ratio (λ). The value of λ can be calculated by applying Eq. 2.55. The nitrogen volumetric flow, $\dot{v}_{N_2}$, is determined depending on the methane flow and the resulting heating value by

$$\dot{v}_{N_2} = \left(\frac{HHV_{CH_4}}{HHV_{fuel}} - 1 \right) \dot{v}_{CH_4} \tag{8.1}$$

The aim of the experiment is not only to vary the heating value of the inlet gas, but the operating conditions of the system as well. A change of the methane molar flow res-

ults in a variation of the exhaust volumetric flow and the burner power. The change in the λ alters the exhaust volumetric flow, its composition and the burner temperature. Thus, it can be analyzed if the change of these factors influences the result of the control strategies or if, on the contrary, they are robust against these disturbances.

The ranges of the control variables are presented in Tab. 8.1, for the test bench depicted in Fig. 8.1 and for the real system presented in Fig. 5.1. Several differences can be observed between the values for each case. The HHV depends on the gas mixture. In case of the real system, it is fed with natural gas. Under its components it is usual to find long alkanes, whose heating value is higher than this from methane (Tab. 0.7). On the contrary, in the mixture fed to the test bench, the gas with the highest energy content is the methane, since other alkanes are not available. Thus, its heating value ($890.63\,\mathrm{kJ \cdot mol^{-1}}$) is the maximum obtained. The difference between the lowest and the highest values is larger in case of the test bench. The reason is that the range of the composition of the methane-nitrogen mixture is limited due to the precision of the MFC's.

The maximal value of the methane volumetric flow depends on the power of the burner. The device is the same for the test bench and for the system. However, the composition of the gas entering the burner varies: while in case of the test bench the fuel is provided directly to the burner, in the system it has been previously partially oxidized in the fuel cell, reducing its energy content.

On addition, λ is limited due to another factor. The burner temperature has to be kept between 900 °C and 950 °C in order to ensure its optimal operation. Thus, if the energy content of the fuel gas is increased, a higher value of λ is necessary in order to achieve the same temperature level.

The restrictions in the test bench result on smaller molar fractions of all components at the flue gas than under the system operating conditions. This fact implies less

Table 8.1 – Ranges of the control variables for the SOFC system and for the test bench, including their limiting factors.

variable	*range*	*test bench*	*limiting factor*
HHV	$[710, 1010]\ \mathrm{kJ \cdot mol^{-1}}$	$440, 590, 893\ \mathrm{kJ \cdot mol^{-1}}$	gas mixture
$\dot{v}_{CH_4}$	$[0, 25]\ \mathrm{Nl \cdot min^{-1}}$	$3, 4.5, 6\ \mathrm{Nl \cdot min^{-1}}$	burner power
λ	$[3, 4]$	$6.5, 6.75, 7$	burner temperature

exactitude in their measurement. Consequently, it can be assumed that the precision in the detection of $\bar{n}$ in the system is at least as high as in the test bench.

The experiments are carried out by applying a three-level full-factorial design, for the values presented in Tab. 8.1, resulting in 29 steady-state operation points. The reference operating point (the middle value for each variable) is investigated three times: at the beginning, at the middle and at the end of the experiments, in order to detect possible changes in the operating conditions.

8.2 Experimental results

In this section the results of the experiments are presented. Firstly, the exactitude of the measurements is evaluated by comparing the theoretical (calculated from set points for air, nitrogen and methane volumetric flows) and the measured values of the oxygen, water and carbon dioxide molar fraction. Then, the correctness of detection of the mean amount of carbon atoms per molecule for the different methods is evaluated.

8.2.1 Accuracy of the gas measurements

The first analysis which is carried on with the experimental data is an statistical analysis. The aim is to identify all influence factors on the molar fraction measurements, and to determine if the control variables are the only significant effects or if there are interference factors which should be taken into account. Therefore, the software Cornerstone® is used. For each of the responses (the molar fractions x_{CO_2}, x_{O_2} and x_{H_2O} at the measurement points indicated in Fig. 8.1) a statistical model (multiple regression with a third degree polynomial including all interaction terms) has been developed. The control variables (HHV, $\dot{v}_{CH_4}$ and λ) have been taken as predictors. The resulting coefficient of determination for the three responses, R_j^2, is shown in Tab. 8.2 (regression 1). The coefficient of determination quantifies how well the statistical model fits the experimental data. It takes a value between 0 and 1, indicating a perfect model fit for $R^2 = 1$ and a worse prediction of the response as it approaches the value 0. Thus, it can be used for detecting which input variables have to be taken into account for the calculation of the outputs. For x_{CO_2} and x_{O_2} it has values near to 1. It indicates that the variables included in the statistical model (the control variables) are the most sensitive variables and that by considering them the quantitative behavior of the outputs can be predicted. On the contrary, for x_{H_2O} R^2 takes a value of 0.2. Thus, the considered inputs are not sufficient for obtaining a model for predicting the output. After analyzing the behavior, the water molar fraction at the inlet air ($x^{in}_{H_2O,air}$) has been included in the model. The resulting R^2 value is presented in Tab. 8.2 (regression 2). It can be observed that the value is increased to 0.9976, resulting in a high quality statistical model. Additionally, $x^{in}_{H_2O,air}$ is also regarded for the other responses. In both cases their R^2 is increased, taking a value nearer to 1. It indicates that the inlet air humidity is a sensitive input for all three outputs and has to be included to any model for predicting their behavior.

In Fig. 8.2 the predicted response graph of the measured variables (x_{CO_2}, x_{O_2} and x_{H_2O}) is presented with respect to each predictor (HHV, λ, $\dot{v}_{CH_4}$ and $x_{H_2O,air}$). The diagram

Table 8.2 – Determination coefficients of the responses for different regressions.

regression	$R^2_{x_{CO_2}}$	$R^2_{x_{O_2}}$	$R^2_{x_{H_2O}}$
regression 1 (x_{H_2O} neglected)	0.8547	0.9236	0.2005
regression 2 (x_{H_2O} considered)	0.9951	0.9847	0.9976

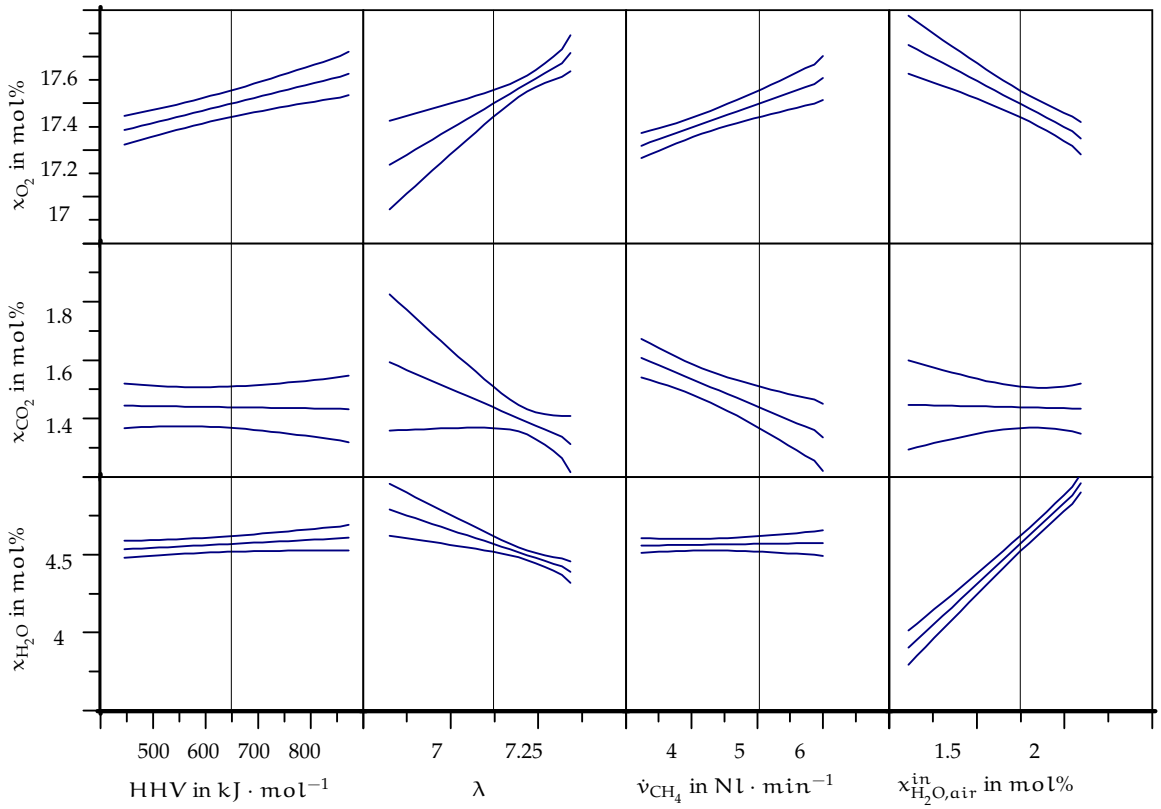

Figure 8.2 – Predicted response of the measured variables (x_{CO_2}, x_{O_2} and x_{H_2O}) for the predictors HHV, λ, $\dot{v}_{CH_4}$ and $x_{H_2O,air}$ (interval of confidence = 95 %).

shows how the response changes with the variation of one parameter, keeping the other predictors at a constant value, in this case the corresponding to the middle value of the range. For each interaction three curves are presented. The curve in the middle indicates the predicted response, while the other show the interval of confidence of 95 %. It can be observed that, effectively, the water content of the inlet air is the most influent factor for the water molar fraction at the exhaust. This can be explained by the fact that the air flow is considerably larger than the fuel flow, and therefore a larger proportion of the water at the exhaust has its origin on the inlet air. In case of the carbon dioxide, the methane flow is one of the determinant factors, which is coherent, since each molecule of CO_2 at the outlet has its origin in one molecule of CH_4 at the system inlet. However, it can be observed that the value of λ has as much influence as $\dot{v}_{CH_4}$. The reason is that the higher the λ, the larger the air flow, the more diluted are the CO_2 molecules in the exhaust and consequently the smaller its molar fraction. For the response of x_{O_2} all predictors have a strong influence. The amount of oxygen introduced to the system is proportional to the air flow, which depends directly of λ and $\dot{v}_{CH_4}$. The higher the HHV, the lower the N_2 flow for the same amount of CH_4, and consequently the less diluted is the oxygen at the outlet. Finally, the influence of the air humidity is explained by the fact that the higher is the water content of the inlet air, the lower is its oxygen molar fraction.

Once the influence variables have been identified and the dependences understood, a physical model to calculate the theoretical values of the responses has been developed to be compared with the results obtained in the experiments. The theoretical values of O_2, CO_2 and H_2O are calculated by applying a mass balance in the burner:

$$x_{O_2} = \frac{x_{O_2,air}\dot{n}_{air} - 2\dot{n}_{CH_4}}{\dot{n}_{air} + \dot{n}_{CH_4} + \dot{n}_{N_2}} \tag{8.2}$$

$$x_{CO_2} = \frac{\dot{n}_{CH_4}}{\dot{n}_{air} + \dot{n}_{CH_4} + \dot{n}_{N_2}} \tag{8.3}$$

$$x_{H_2O} = \frac{2\dot{n}_{CH_4} + x_{H_2O,air}\dot{n}_{air}}{\dot{n}_{air} + \dot{n}_{CH_4} + \dot{n}_{N_2}} \tag{8.4}$$

The water molar fraction in the inlet air ($x_{H_2O,air}$) is calculated depending on the inlet temperature, pressure and relative humidity by applying Eq. 6.50. The oxygen molar fraction in the inlet air, $x_{O_2,air}$ is calculated regarding $x_{H_2O,air}$. The volumetric flows are measured at the test bench and converted to molar flows under the assumption of ideal gases.

Fig. 8.3 shows the experimental results of the carbon dioxide, oxygen and water molar fractions for the 29 operating points. They are compared with the corresponding theoretical value. For this latter, three different values are to be seen. The middle curve shows the corresponding to the ideal theoretical value, which results from applying directly Eq. 8.2, Eq. 8.3 and Eq. 8.4. Additionally, the maximal and minimal theoretical values are presented. These maximal and minimal values are obtained by considering that the data used for the calculations are delivered by real sensors, which have a measurement error (listed in Tab. 8.3). It can be observed that in all cases the sensor signal follows the tendency of the theoretical value and remains between the upper and the lower limits. The maximal error committed in the measurements (ϵ_{sensor}), calculated with Eq. 8.5, has a value of 8 % for CO_2, of 1.53 % for O_2 and of 1.63 % for H_2O.

$$\epsilon_{sensor} = \frac{x_j^{theo} - x_j^{meas}}{x_j^{theo}} \tag{8.5}$$

These results are consistent with those presented at Tab. 8.2 and in Fig. 8.2. The values of the water molar fraction present a high agreement between theoretical and experimental results. This is also the response with the highest coefficient of determination in the polynomial regression and with the thinnest interval of confidence in the predicted response graph. This is consequence of the high accuracy of the sensor used for its determination, a chilled mirror dew point hygrometer, which provides the dew

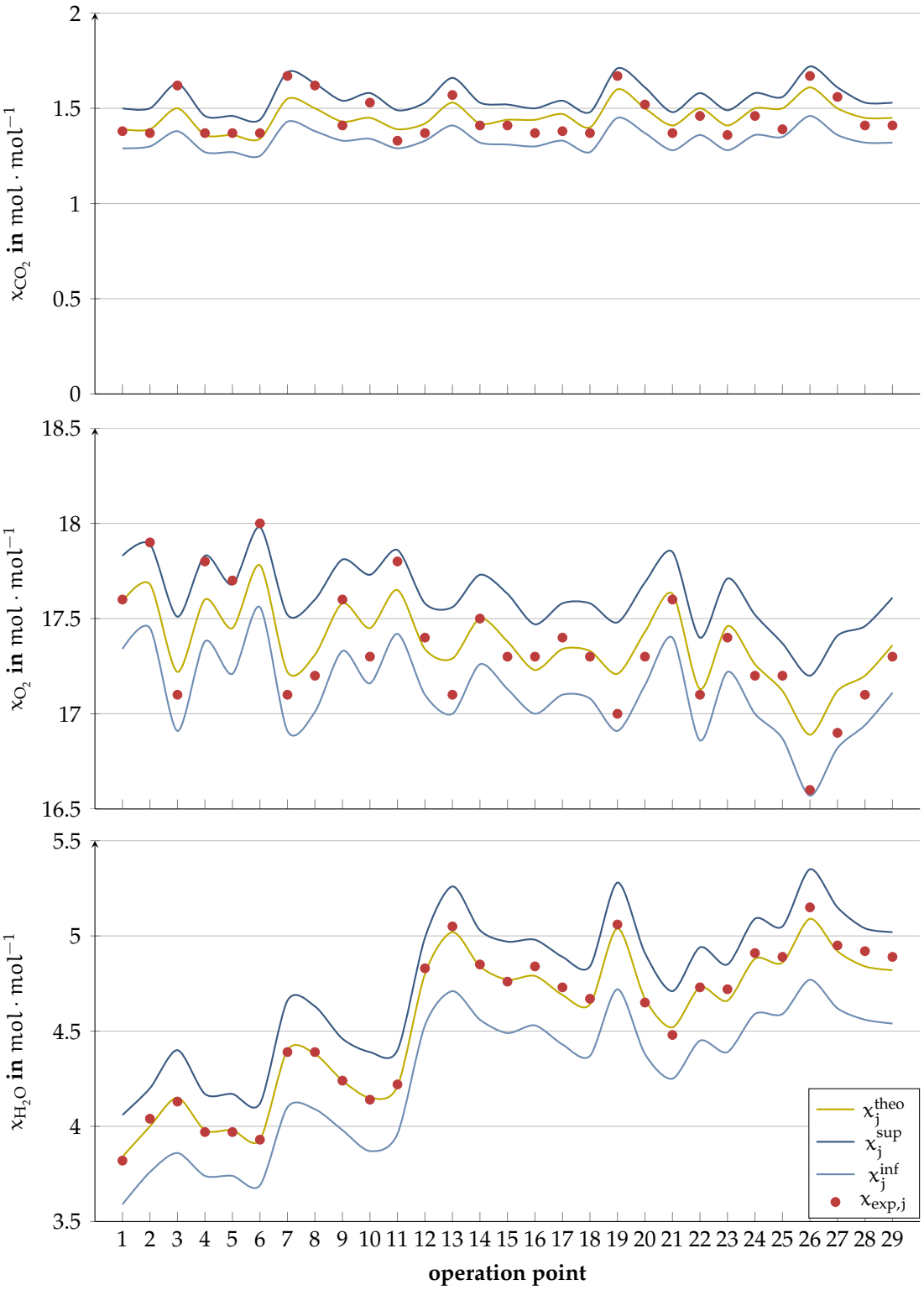

Figure 8.3 – Comparison between the theoretical and experimental results for the carbon dioxide, oxygen and water molar fraction at the burner offgas.

Table 8.3 – Measurement errors of the sensors used in the test bench (MV=Measured Value, EV=End Value).

Variable	*Physical principle*	*Measurement error*
$\dot{v}_{CH_4}$	Constant temperature anemometer	$\pm 1.5\,\%\,\mathrm{MV} \pm 0.3\,\%\,\mathrm{EV}$ [14]
$\dot{v}_{air}$	Calorimetric flow meter	$\pm\,(3\,\%\,\mathrm{MV} \pm 0.3\,\%\,\mathrm{EV})$[12]
$\dot{v}_{N_2}$	Constant temperature anemometer	$\pm 1.5\,\%\,\mathrm{MV} \pm 0.3\,\%\,\mathrm{EV}$ [14]
P	Differential pressure transducer	$\pm 0.5\,\%\,\mathrm{MV}$ [8]
T	Resistance temperature detector	$\pm 0.4\,\mathrm{K}$[11]
RH	Capacitive humidity sensor	$\pm 1\,\%\,\mathrm{RH}$ [13]
x_{O_2}	Lambda-sonde	$\pm 3.14\,\%\,\mathrm{MV}$[5]
x_{CO_2}	Nondispersive infrared sensor	$\pm max\left(1\,\%\,\mathrm{MV}, 0.002\,\mathrm{mol}\cdot\mathrm{mol}^{-1}\right)$[16]
T_{dew}	Chilled mirror dew point hygrometer	$\pm 0.2\,\mathrm{K}$ [20]

point with a maximal error of 0.2 K (Tab. 8.3). The same dependence between accuracy of the sensor, coefficient of determination, interval of confidence and accordance between theoretical and experimental values can be observed for the values of x_{O_2} and x_{CO_2}. Other results can be extracted from comparing both diagrams. For example, in Fig. 8.2 it can be observed that intervals of confidence for the three responses are the wider at lower λ values, corresponding to high values of x_{CO_2} and x_{H_2O} and low values of x_{O_2}. If these points are identified in Fig. 8.3 (operating points 3, 7, 8, 10, 13, 19, 20, 26 and 27) it is to be seen that in most cases the corresponding measured values present a high deviation with respect to the theoretical in comparison with other operating points.

In summary, by applying a regression analysis the influence factors on the values of x_{CO_2}, x_{O_2} and x_{H_2O} have been determined. Then, a physical model depending on the identified predictors has been written. It shows a good agreement with the experimental values and predicts behaviors which are consistent with those predicted by the regression model. Additionally, if the uncertainty resulting from the sensor errors

is incorporated, the experimental results are completely explained. In conclusion, the behavior of the system has been understood and physically described and the resulting experimental data can be well explained. Consequently, they can be safely used as input data for the detection methods.

8.2.2 Experimental evaluation of the gas detection strategies

In this section the precision of the $\bar{n}$ detection is evaluated by applying the strategies specified previously. For this purpose, the value identified by the detection strategies ($\bar{n}^{calc}$) is compared with the theoretical value ($\bar{n}^{theo}$) for each operating point. The fuel is a mixture of nitrogen and methane, whose n_k numbers are 0 and 1 respectively. Thus, the mean amount of carbon atoms per molecule of fuel can be calculated by

$$\bar{n}^{theo,ideal} = n_{CH_4} \frac{\dot{v}_{CH_4}}{\dot{v}_{CH_4} + \dot{v}_{N_2}} = \frac{\dot{v}_{CH_4}}{\dot{v}_{CH_4} + \dot{v}_{N_2}} \tag{8.6}$$

In order to take into account the deviation consequence of the flow sensors errors (defined in Tab. 8.3) two other values have been defined: $\bar{n}^{sup}$ and $\bar{n}^{inf}$.

Fig. 8.4 presents the results for the 29 operating points resulting from applying the strategy based on the oxygen measurement. In red there are shown the values resulting from applying directly Eq. 6.35, for $x_{alk} = 0.72$. This parameter is obtained as the mean value of x_{alk} regarding the 29 operating points. It can be observed that for middle values of $\bar{n}$ there is a good agreement between the measured values and the theoretical. On the contrary, for high and low levels of $\bar{n}$, a lower precision is detected. In order to reduce the discrepancy in these cases a correction can be applied:

if $\bar{n}^{calc} < \bar{n}^{inf}$ **then**

$\bar{n}^{calc} = \bar{n}^{inf}$

else if $\bar{n}^{calc} > \bar{n}^{sup}$ **then**

$\bar{n}^{calc} = \bar{n}^{sup}$

else

$\bar{n}^{calc} = \bar{n}^{calc}$

end if

For the experiments carried on at the test bench, as well as for the real system, the minimal and maximal limits of $\bar{n}$ have known values. Consequently, if the calculated value does not belong to the possible range, the result is replaced by the inferior or the superior limit of $\bar{n}^{theo}$. In case of the test bench, $\bar{n}^{sup}$=1 and $\bar{n}^{inf}$=0.5. In case of the natural gases to be found in Germany the limits can be calculated from the HHV limits ([18]), and their values are $\bar{n}^{sup}$=1.25 and $\bar{n}^{inf}$=0.67. The $\bar{n}^{calc}$ resulting from this correction is presented in Fig. 8.4 as $\bar{n}^{calc,corr}$. It can be observed that these values are to be found between the limits of $\bar{n}^{theo}$ for most operating points. The maximal deviation, calculated by applying Eq. 8.7 and regarding the 29 operating points, is of 15.6 % and the mean deviation of 2.5 %. These results confirm that the strategy based on the oxygen measurement at the system exhaust is effective to detect the entering gas.

$$\epsilon_i = \frac{\bar{n}_i^{theo} - \bar{n}_i^{calc}}{\bar{n}_i^{theo}} \tag{8.7}$$

In the next paragraphs the experimental results of the detection strategy based on measuring the carbon dioxide and the humidity at the system flue gas are presented. In Fig. 8.5 there are compared the theoretical mean amount of carbon atoms per alkane molecule ($\bar{n}_{alk}$, Eq. 6.14) with the values resulting of applying Eq. 6.59. Deviations up to 61.3 % are to be observed, being the mean difference between theoretical and measured values of 53.8 %. The reason is that the water content of the inlet air has been neglected in the calculations. However, as shown in Sect. 8.2.1, this effect is responsible for an important fraction of the water content at the exhaust. Thus,

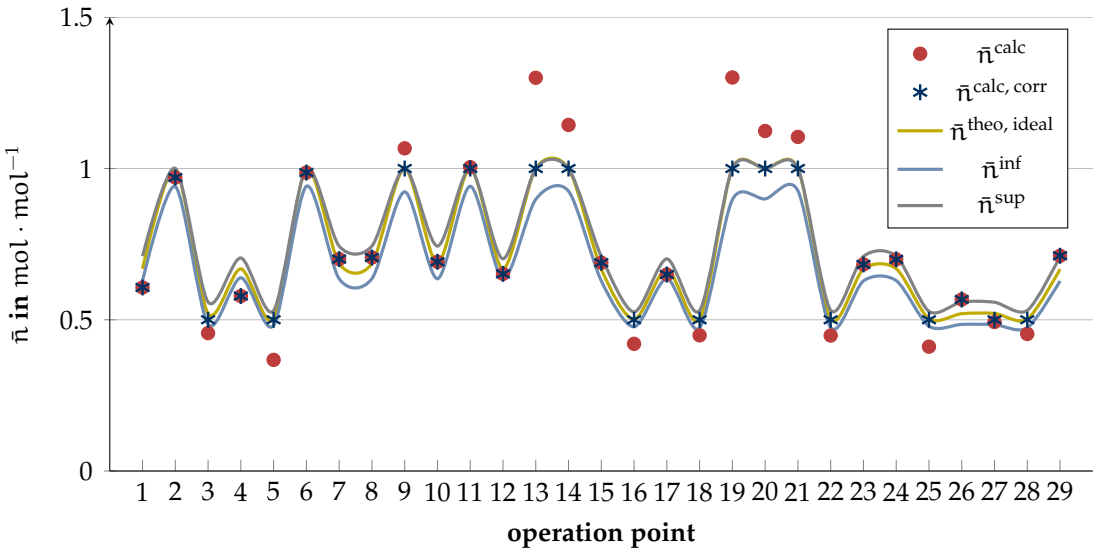

Figure 8.4 – Comparison between the calculated value of $\bar{n}$ and the theoretical value for the strategy based on measuring the oxygen molar fraction at the exhaust ($x_{alk} = 0.72$).

the equations presented in Sect. 6.1.6 are rewritten in order to take this factor into account, with the restriction of adding as less sensors as possible. The mass balance for the hydrogen atoms at the system (Eq. 6.44) can be rewritten as:

$$\dot{n}_H^{in,sys} = \dot{n}_H^{out,sys} \Rightarrow (2\bar{n}_{alk} + 2)\,\dot{n}_{alk} + 2x_{H_2O,air}\dot{n}_{air} = \dot{n}_{H_2O,flue} = 2\dot{n}_{flue}x_{H_2O,flue} \tag{8.8}$$

The mass balance for the carbon atoms is not affected and Eq. 6.43 can be used. Consequently, Eq. 6.45 can be rewritten as

$$\frac{\dot{n}_{CO_2,NG} + \bar{n}_{alk}\dot{n}_{alk}}{(\bar{n}_{alk} + 1)\,\dot{n}_{alk}} = \frac{\dot{n}_{flue}x_{CO_2,flue}}{\dot{n}_{flue}x_{H_2O,flue} - \dot{n}_{air}x_{H_2O,air}} \tag{8.9}$$

From the mass balance the flue molar flow can be calculated as

$$\dot{n}_{flue} = \dot{n}_{air} + \dot{n}_{fuel} \tag{8.10}$$

Since $\dot{n}_{air} >> \dot{n}_{fuel}$ ($\dot{n}_{fuel} \approx 0.05\dot{n}_{air}$ for the system at full load):

$$\dot{n}_{flue} \approx \dot{n}_{air} \tag{8.11}$$

Replacing Eq. 8.11 in Eq. 8.9 and after some mathematical arrangements a new expression for $\bar{n}_{alk}$ is found

$$\bar{n}_{alk} \approx \frac{x_{CO_2,flue}}{x_{H_2O,flue} - x_{H_2O,air} - x_{CO_2,flue}} \tag{8.12}$$

The results of applying Eq. 8.12 are shown in Fig. 8.5 together with the values obtained by considering dry air. It can be observed that the calculated values approximate the theoretical with a significantly higher accuracy (ϵ_{max}=21.6 % and ϵ_{mean}=7.1 %, calculated by Eq. 8.7). Therefore, it can be concluded that the water content of the inlet gas has to be included in the calculation of $\bar{n}_{alk}$ and that using Eq. 8.12 for this purpose is a good approximation.

Fig. 8.6 presents the results of $\bar{n}$ by applying method based on the CO_2 and the H_2O measurements at the flue gas. The curves represent the theoretical values assuming ideal sensors ($\bar{n}^{theo,ideal}$) and real sensors with the errors presented in Tab. 8.3 ($\bar{n}^{inf}$, $\bar{n}^{sup}$). In dots are shown the values based on the experimental measurements and calculated depending on $\bar{n}_{alk}$ and x_{alk}. $\bar{n}_{alk}$ is calculated considering humid air (Eq. 8.12) and x_{alk} is a parameter. The results for three different values of x_{alk} are compared. It can be observed that for none of the values an accurate approximation of the trend could be obtained. However, for each of the x_{alk} values, $\bar{n}$ is correctly calculated for some of the operating points. The reason is that, while $\bar{n}_{alk}$ is calculated from experimental measurements, x_{alk} takes a fixed value. Since $\bar{n}$ is directly proportional to x_{alk} (Eq. 6.14) the difference between the real value of x_{alk} and the value assumed for the parameter is directly propagated to an error in $\bar{n}_{alk}$. Thus, being the range for x_{alk} between 0.5 and 1, the error produced in $\bar{n}$ is considerable. Furthermore, since in

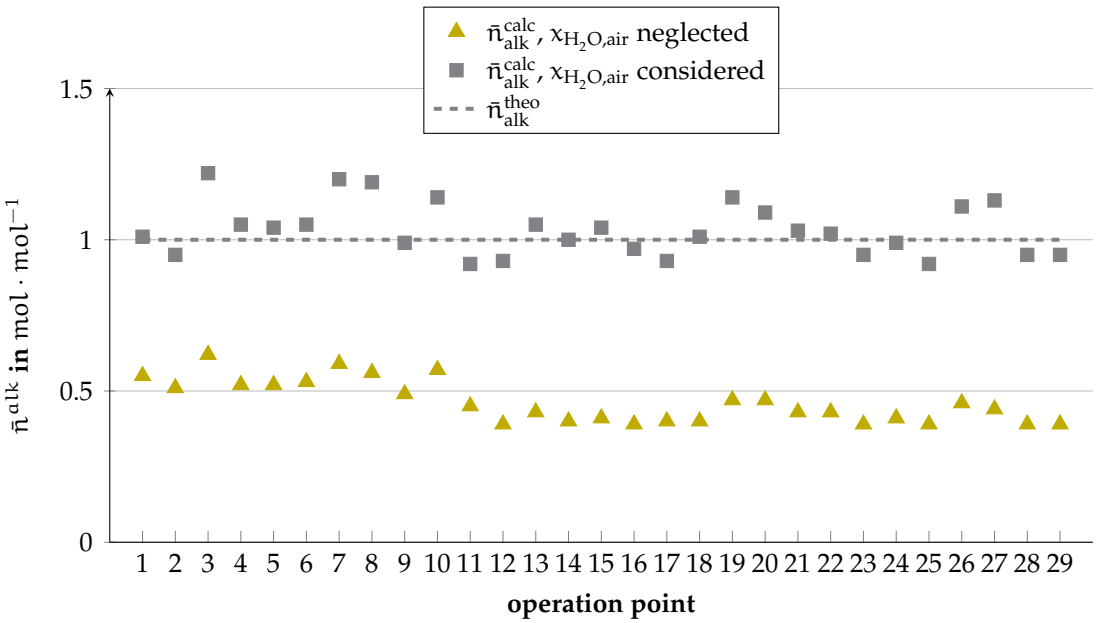

Figure 8.5 – Comparison between the real value of n_{alk} and the calculated by applying the strategy based on the measurement of x_{CO_2} and x_{H_2O}. Two values are presented: in dark blue the value obtained assuming dry air, in light blue if the air humidity is regarded.

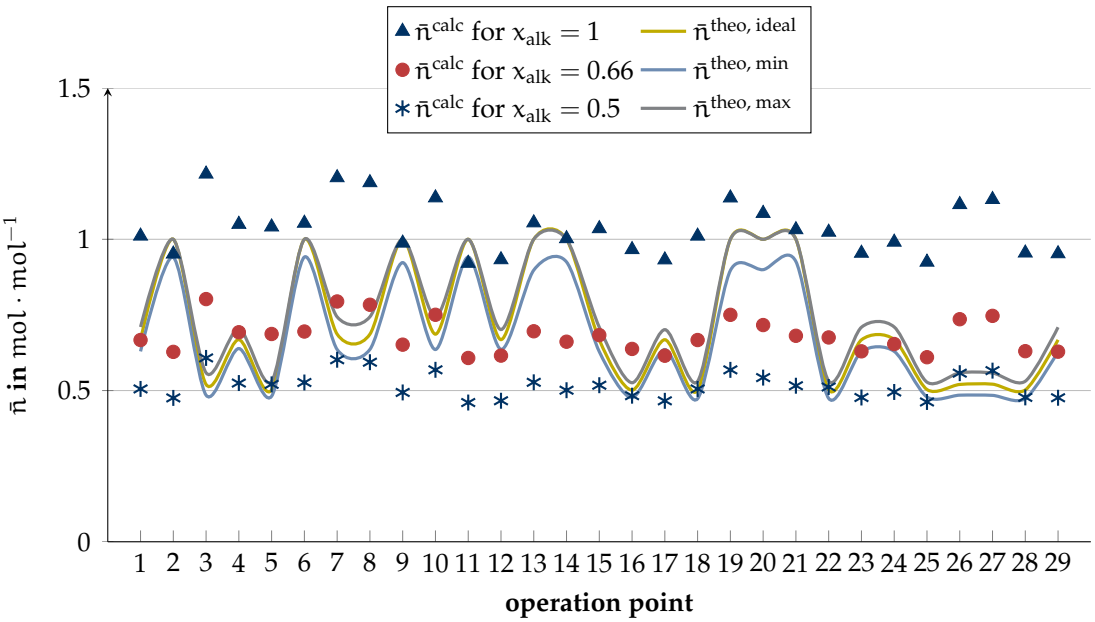

Figure 8.6 – Comparison between the calculated value of $\bar{n}$ for three different values of x_{alk} and the theoretical value for the strategy based on measuring the water and carbon dioxide molar fraction at the system exhaust.

the test bench the value of $\bar{n}_{alk}$ is constant, the fluctuation of $\bar{n}$ is caused exclusively by the variation of x_{alk}. Consequently, if it is kept constant, the trend of $\bar{n}$ cannot be detected.

On the contrary, if x_{alk} is considered variable and known for each fuel, the difference between measured and theoretical values is drastically decreased, as can be seen in Fig. 8.7. Furthermore, an improvement of the results can be achieved by applying the correction described previously. As a result, the maximal deviation from the ideal theoretical values is of 21.6 % and the mean deviation of 5.5 %.

In the test bench the control strategy has been tested for extreme conditions. In contrast to the test bench, the fluctuation of $\bar{n}$ is caused mainly by changes of $\bar{n}_{alk}$. Consequently, its trend can be better detected with a fixed value of x_{alk}. Even though, since both values are proportional, the accuracy is increased if the total alkane molar fraction is measured.

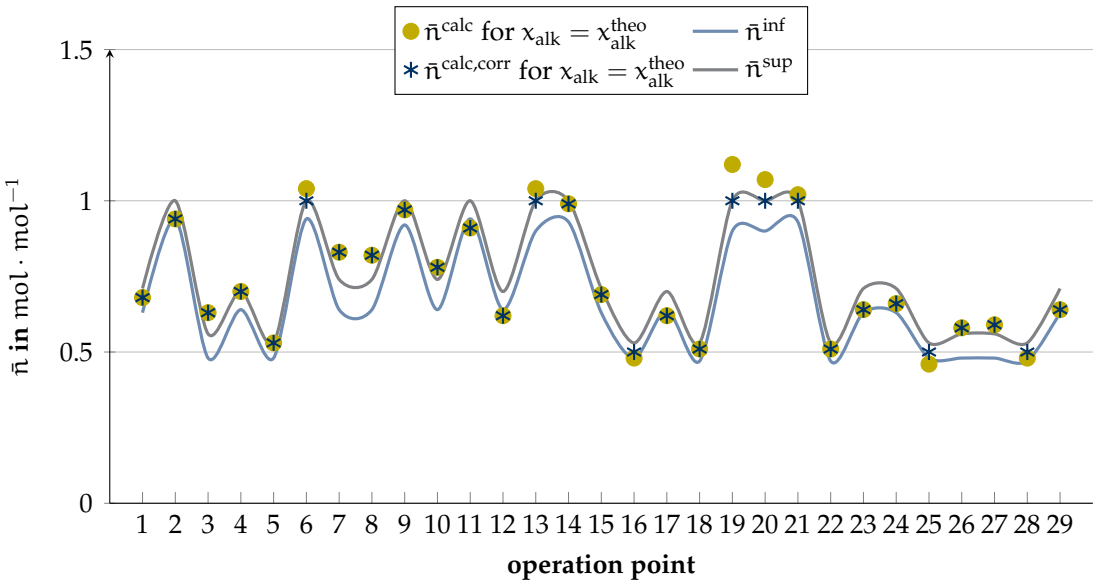

Figure 8.7 – Comparison between the calculated value of $\bar{n}$ by assuming that x_{alk} is a known value and the theoretical value for the strategy based on measuring the water and carbon dioxide molar fraction at the exhaust.

It can be concluded that both methods are appropriate for the detection of $\bar{n}$ in order to adapt the control strategy to variable natural gas composition. In case of the identification by measuring the oxygen molar fraction, the achieved mean deviation (calculated by Eq. 8.7) is 2.5 % and the maximal deviation 15.6 %. For the procedure based on the detection of x_{CO_2} and x_{H_2O} at the system flue gas, $\epsilon_{max} = 21.6\,\%$ and $\epsilon_{mean} = 5.5\,\%$. In the first case, the results have been achieved by applying directly the equations developed in Sect. 6.1.4. That is to say that the strategy can be directly implemented with its original design. On the contrary, for the second method additional measurements have to be carried on in order to obtain an acceptable accuracy. The water content in the inlet air has to be regarded for the calculation of $\bar{n}_{alk}$ and x_{alk} should not be considered as a parameter but as a variable value.

9 Review and discussion

Although the natural gas grid is an infrastructure existing in Germany since decades, and the fact that the natural gas composition is not fixed is commonly known, a quantification of these fluctuations derived of the gas distribution system in Germany could not be found by the author. That is the reason why the first step of the work was a research with the aim of collecting this information, by contacting different gas distributors in Germany. The conclusion of the research was that the calorific value and composition of the gas change considerably, both over the time and from consumption point to consumption point. The reason are the different origins of the natural gas, with variable qualities, together with the existence of a single distribution net. Additionally, since neither the composition nor the energy content of the gas is not actively controlled but just tested in single extraction points, it is not possible to predict the fluctuation in advance. Furthermore, the current methods to measure the gas composition are cost and time expensive, which makes it not feasible to implement them at each consumption point.

The data considered for these analysis were obtained from the only existing norm regarding the gas quality in Germany, the *DVGW* [18]. The composition of the different natural gases imported or extracted in Germany have been assumed as the worst case compositions. The reason is that in fact the consumed gases are a mixture of the different origin gases, so that it can be considered that their compositions do not achieve as extreme values as regarded in this documents. It may be that, by applying this approach, the assumed fluctuations are larger than they are in the reality. However, the other option would have been to use the data obtained from the gas distribution

companies. This possibility has been rejected due to two reasons. Firstly, because the data are obtained as monthly mean values and from a single point in representation of an region, which is a too low sampling rate in comparison to the geographical and dynamical variations. Thus, the worst case situations would not probably have been measured nor taken into account. To carry out the necessary measurements in order to obtain enough significant data was not feasible due to time and costs reasons. Additionally, the available data are obviously restricted to the past. On the contrary, the solid oxide fuel cell system of interest in this work is to be implemented in the future, in which it is expected that the gas fluctuations will be always larger due to the globalization of the natural gas market and the increasing significance of the biogas production. Thus, the used data are considered the most adequate in order to ensure that the worst case situations are regarded.

In order to evaluate how these fluctuations affect to the SOFC system, and if it effectively are a risk for its operation, the system operation characteristic variables related to the lifetime of the system have been analytically calculated by assuming that the system does not detect the gas composition. For this purpose, the system manipulated variables have been calculated by applying the equations of a reference control strategy, which takes as parameter the gas composition. Then, for these values of the manipulated variables, the resulting oxygen to carbon ratio and stack fuel utilization have been calculated for the natural gases referred in the previous paragraph.

The reference gas composition, needed as a parameter for the control strategy, has been calculated as the mean of the different gas compositions. Actually, at the moment the used reference gas is pure methane, since it is the gas normally used at the test units, so the first option was to use methane as reference gas in this test as well. However, the adaption of this parameter to a value which differs as little as possible from all possible composition values would be the first measure which would be adopted in order to try to solve the problem. Thus, the applied diagnosis already takes into account the predictable improvement with respect to the current situation. Even

though, the obtained results showed a strong fluctuation of the parameters, reaching levels outside of the ranges which guarantee the fuel cell lifetime. Consequently, it can be concluded that, even with a parameter optimization, the control strategies applied currently are not adequate for systems running with variable gas composition. Thus, if they are not improved with gas detection methods, the conditions to guarantee the fuel cell lifetime can not be generally fulfilled.

The fuel cell system for combined heat and power applications is constituted by several components which are chemically and thermally integrated with each others, constituting a system with a high complexity. Consequently, in order to develop and test the referred strategies, a dynamic system model had to be built. It included the fuel cell stack and the air and fuel processor units (formed by several components like heat exchanger, a fuel prereformer or a burner). Chemical, thermodynamical, heat transfer and flow mechanic effects have been regarded in the model, implemented in a modular structure which facilitates the reuse the blocks and the study of different system configurations. The assumptions taken in the model are based in several previous publications, which focused on different details of the fuel cell modelling, in order to optimize the complexity of the model. However, there are some effects which have not been regarded which would be interesting to incorporate to the model and to compare the results with and without the simplification, for instance the stack degradation, the heat transfer by radiation mechanism or the oxidation of the carbon monoxide in the fuel cell.

Similarly, the analyze of previous works indicated that an adequate spatially discretization to be applied was of the kind 1D+1D in the flow direction, since the most significant changes take place in this direction. The amount of discretization cells has been chosen as a compromise between exactitude and compilation time, by studying the change in the calculated results consequence of the increase in the discretization elements. In order to achieve adequate compilation and calculation times, the implemented number of elements was lower than the necessary to achieve a gradient zero

of the results respect to the number of elements. Consequently for future works it would be desirable to optimize the implementation of the model, regarding numerical issues, in order to increase the number of discretization cells.

Several parameters of the system components were unknown, including geometrical, chemical and electrochemical parameters. Thus, they have been obtained by fitting the simulation results to experimental data. In order to reduce the complexity of the parameterization, first the single components were parameterized and validated one by one and finally the entire system was validated with experimental data. In case of the air processor and the electrochemical behavior of the stack, the amount of available experimental data made it possible a complete parameterization and a validation for several operating conditions, achieving a good coincidence between experimental and simulation data. On the contrary, in case of the fuel processor and the entire system, only two operating points could be tested achieving the steady state. Thus, although for these cases the accordance was high as well, it would be desirable to carry out more experiments in order to validate the models for a wider range.

In order to adapt the current control strategies to natural gas fluctuations, alternative methods to the direct measurement of the gas composition had to be found. Firstly, the mean amount of released electrons per molecule of fuel ($\bar{N}_{e^-}$) was identified as a key indicator: if this gas property was known, the control strategy could be adapted so that the set points of the system operation characteristic values could be met with a negligible deviation. Furthermore, $\bar{N}_{e^-}$ could be analytically related to the natural gas heating value, which is the standard indicator for the energy content of the natural gas. The first step of all detection methods was the indirect detection of $\bar{N}_{e^-}$ by measuring several properties of the gas flow at any point of the system. Then, the calculation of the system manipulated variables was adapted to the variation of $\bar{N}_{e^-}$.

Six different adaptation strategies were developed and presented. Two of them were

directly discarded, following economical and technical criteria, while the rest were implemented in the system model in order to be tested. The inlet gas composition was varied by reproducing these of the reference gases, in order to analyze the system behavior, first assuming ideal sensors and then considering the measurement errors. The resulting parameters, regarding lifetime and efficiency, were compared to each other and with these obtained for the current strategy.

For the strategy based on the measurement of the humidity and the CO_2 fraction of the system exhaust, the values obtained were comparable to these of the reference strategy. Thus, the implementation of this method would not suppose any advantage for the adaptation to the gas fluctuations. The reason was the assumption of a variable property, the fraction of inert gases, as a constant parameter. On the contrary, for the other three strategies, good results were obtained if considering ideal sensors: the system operation characteristic values met the requirements for all cases, being their fluctuation derived of the variation of the gas composition negligible. If the sensors errors were regarded, the method based on the measurement of the gas heating value was still very satisfactory. The reason was that the strategy could be implemented by using a single sensor which, additionally, was characterized by a low error. Consequently, from the technical point of view, this strategy could be applied to combined heat and power systems with SOFC in order to adapt them to the gas fluctuations. A previous requirement would be the experimental test of the strategy, since due to financial reasons it could not be carried out in the context of this work. The reason is that at the moment the sensors used for this purpose have high economical costs. That would be the main impediment for the use of this method in the final product as well. However, it is to expect that in near future a low-cost generation of heating value sensors will be developed, so that this strategy could be successfully implemented to the systems.

In case of the other two control strategies, both based on the measurement of the oxygen content at the system flue gas, the results considering ideal sensors were very

satisfactory. However, if the sensors errors were regarded, strong deviations from the set points were achieved. It is to be pointed out that the results are referred to the worst case combination of the errors of all the sensors involved in the detection process. A statistical analysis of the actual detection error should be carried out in order to achieve more solid results. Actually, as it will be indicated later, the experiments showed that the method could detect the gas energetic content with a high accordance. Regarding the economical feasibility of the method, in this case the costs are very low compared to the investment associated to the system, therefore its implementation could be already possible.

In order to confirm the results obtained by simulation methods, two of the strategies were experimentally tested: the one based on the measurement of the humidity and the CO_2 fraction of the system exhaust) and one of these using the oxygen fraction at the system flue gas. For this purpose, the properties of the exhaust resulting from gases with different energy content (obtained by mixing methane with nitrogen) were measured. Then, the two methods were applied to the experimental measurements and the detected $\bar{N}_{e^-}$ compared to the real values.

Similar results to the obtained by simulation methods were observed. The strategy based on using the values of the humidity and the CO_2 could not detect the energetic content of the feeding gas. However, if the fraction of inert gases was not assumed as a parameter but as a detected property, the gas could be detected correctly. Thus, if the strategy included a detection method for this property (for example the detection of the total hydrocarbons fraction by using infrared sensors) it may be implemented in the systems. On the contrary, in case of the method based on the oxygen measurement at the exhaust, the gases were detected with a high precision in all cases. Thus, in principle they could be implemented to the combined heat and power systems for the detection of the gas fluctuations. However, several tests should be carried out previously, in order to confirm its optimal operation. Firstly, it should be tested with gases containing different hydrocarbons, since in this work the energy content was

varied exclusively by changing the proportion of methane and nitrogen. Additionally, the complete control strategy should be tested because, while in case of the simulation results the effects of the detection method combined with the control strategy were analyzed, in the experimental procedures only the first one was tested.

In conclusion, six different strategies for the adaptation of the control strategies to natural gas fluctuations for combined and heat systems with solid oxide fuel cells were developed. Four of them have been tested with simulation and experimental methods and all of them present possibilities to be implemented to commercial systems. From them, these based on the measurement of the oxygen content at the system exhaust present the most optimal technical and economical properties to be applied in the near future.

Bibliography

[1] United States Department of Energy. Energy Efficiency & Renewable Energy:
Fuel Cell Technologies Office: Current Technology. –
Version: August 2011

[2] ISO6976:
Natural Gas - Calculation of Calorific Values, Density, Relative Density and Wobbe Index from Composition.
1995 (corrected and revised Februar 1996)

[3] Deutscher Verein des Gas- und Wasserfaches e.V. (DVGW):
Arbeitsblatt G 260.
2000

[4] European Parliament:
Directive 2004/8/ EC of the European Parliament and of the council of 11 February 2004 on the promotion of cogeneration based on a useful heat demand in the internal energy market and amending Directive 92/42/EEC.
2004

[5] Electronic sensor:
Technische Kundenunterlage Planare Breitband Lambdasonde mit gepumpter O_2-Referenz.
2007

[6] US Environmental Protection Agency:
Catalog of CHP Technologies.
2008

[7] ThyssenKrupp VDM:
Crofer 22 H, Preliminary Material Data Sheet No. 4050.
2008

[8] WIKA Alexander Wiegand SE & Co. KG:
Druckmessumformer fuer allgemeine Anwendungen, WIKA Datenblatt PE 81.01.
2009

[9] Columbus Water Works:
Evaluation of CHP for Wastewater Facilities.
2010

[10] Wirtschafts- und Verlagsgesellschaft Gas und Wasser GmbH:
Bio-Erdgas.
2011

[11] Electronic sensor:
Characteristic line for PT 100 resistor of tolerance-classes.
2011

[12] ifm electronic gmbh:
Datenblatt Stroemungssensoren SD60.
2011

[13] Vaisala:
HMT330 Series Humidity and Temperature Transmitters for Demanding Humidity Measurement.
2011

[14] Christian Buerkert GmbH & Co. KG:

Massendurchflussregler fuer Gase, Typ 8626.
2011

[15] United Nations Framework Convention on Climate Change:
Status of Ratification of the Kyoto Protocol.
2011

[16] *Technical data sheet TDS0055*.
2011

[17] EnBW Energie Baden-Württemberg AG:
Werte Gasqualität 2011-2012 (Stuttgart).
2011

[18] Deutscher Verein des Gas- und Wasserfaches e.V. (DVGW):
Arbeitsblatt G 260.
2012

[19] terranets bw GmbH:
Brennwert vom Ergdas in Hornberg (06.11.11).
2012

[20] EdgeTech:
DewMaster Technical Specification.
2012

[21] European Parliament:
Directive 2012/27/EU of the European Parliament and of the council of 25 October 2012 on energy efficiency, amending Directives 2009/125/EC and 2010/30/EU and repealing Directives 2004/8/EC and 2006/32/EC.
2012

[22] Bundesamt für Wirtschaft und Ausfuhrkontrolle:
Entwicklung der Erdgaseinfuhr in die Bundesrepublik Deutschland.

2012

[23] Office of Energy Efficiency, Natural Resources Canada:
Heating with Gas.
2012

[24] Modelica Association:
Modelica - A Unified Object-Oriented Language for Systems Modeling, Language Specification, Version 3.3.
2012

[25] EWE Aktiengesellschaft:
Monatsdurchnitt Januar 11- Juli 12 für chemische Zusammensetzung des Erdgas (Oldenburg).
2012

[26] Bundesministerium fuer Umwelt, Naturschutz und Reaktorsicherheit:
Richtlinien zur Förderung von KWK-Anlagen bis 20 $\mathrm{kW_{el}}$.
2012

[27] elster Instromet:
Gas quality analyser Q1. Technical documentation.
2013

[28] ACHENBACH, E.:
Three-dimensional and time-dependent simulation of a planar solid oxide fuel cell stack.
In: *Journal of Power Sources* 49 (1994), Nr. 1–3, P. 333 – 348. –
Proceedings of the Third Grove Fuel Cell Symposium. The Science, Engineering and Practice of Fuel Cells

[29] ADAMSON, Kerry-Ann:
Stationary Fuel Cells. An Overview.

Oxford Amsterdam : Elsevier Ltd., 2007

[30] AGUIAR, P. ; ADJIMAN, C.S. ; BRANDON, N.P.:
Anode-supported intermediate temperature direct internal reforming solid oxide fuel cell. I: model-based steady-state performance.
In: *Journal of Power Sources* 138 (2004), P. 120–136

[31] AGUIAR, P. ; ADJIMAN, C.S. ; BRANDON, N.P.:
Anode-supported intermediate-temperature direct internal reforming solid oxide fuel cell: II. Model-based dynamic performance and control.
In: *Journal of Power Sources* 147 (2005), Nr. 1–2, P. 136 – 147

[32] AGUIAR, P. ; CHADWICK, D. ; KERSHENBAUM, L.:
Modelling of an indirect internal reforming solid oxide fuel cell.
In: *Chemical Engineering Science* 57 (2002), Nr. 10, P. 1665 – 1677

[33] ALOUI, Thameur ; HALOUANI, Kamel:
Analytical modeling of polarizations in a solid oxide fuel cell using biomass syngas product as fuel.
In: *Applied Thermal Engineering* 27 (2007), Nr. 4, P. 731 – 737. –
Energy: Production, Distribution and Conservation

[34] ANDERSSON, Daniel ; ABERG, Erik ; EBORN, Jonas ; JINLIANG, Yuan ; BENGT, Sundén:
Dynamic Modeling Of A Solid Oxide Fuel Cell System In Modelica.
In: *Proceedings of the Asme 8th International Conference on Fuel Cell Science, Engineering, and Technology 2010, Vol 2* Bd. 2 Amer Soc Mechanical Engineers, 2010, P. 65–72

[35] ANDERSSON, Martin ; YUAN, Jinliang ; SUNDÉN, Bengt:
SOFC modeling considering hydrogen and carbon monoxide as electrochemical reactants.
In: *Journal of Power Sources* 232 (2013), Nr. 0, P. 42 – 54

[36] AVCI, Ahmet K. ; TRIMM, David L. ; AKSOYLU, A E. ; ÖNSAN, Z I.:
Hydrogen production by steam reforming of *n*-butane over supported Ni and Pt-Ni catalysts.
In: *Applied Catalysis A: General* 258 (2004), Nr. 2, P. 235–240

[37] BACHOR, Andreas ; BINDE, Wulf ; BULLER, Michael ; FISCHER, Markus ; MATICS, Jens ; SMIEDER, Edgar ; SCHOLZ, Wulf-Hagen ; SELZAM, Patrick ; THOMAS, Bernd ; WEISENBERGER, Dietmar ; ZILCH, Rudi:
Neue Kraftwerke mit fossilen Brennstoffen.
2013. –
Forschungsbericht

[38] BALLIET, Ryan J. ; JARVI, Thomas D. ; PEDERSEN, Lars M. ; PERRY, Michael L. ; REISER, Carl A.:
Patent number US 6977121: Fuel cell power plant having a fuel concentration sensor cell.
2005

[39] BAVARIAN, Mona ; SOROUSH, Masoud ; KEVREKIDIS, Ioannis G. ; BENZIGER, Jay B.:
Mathematical Modeling, Steady-State and Dynamic Behavior, and Control of Fuel Cells: A Review†.
In: *Industrial & Engineering Chemistry Research* 49 (2010), Nr. 17, P. 7922–7950

[40] BEITZ, W. ; KÜTTNER, K.-H.:
Dubbel-Taschenbuch für den Maschinenbau.
Berlin : Springer-Verlag, 1990

[41] BHATTACHARYYA, Debangsu ; RENGASWAMY, Raghunathan:
A Review of Solid Oxide Fuel Cell (SOFC) Dynamic Models.
In: *Industrial & Engineering Chemistry Research* 48, Nr. 13, P. 6068–6086

[42] BHATTACHARYYA, Debangsu ; RENGASWAMY, Raghunathan ; FINNERTY, Caine:
Isothermal models for anode-supported tubular solid oxide fuel cells.
In: *Chemical Engineering Science* 62 (2007), Nr. 16, P. 4250 – 4267

[43] BIEBERLE, A ; MEIER, LP ; GAUCKLER, LJ:
The electrochemistry of Ni pattern anodes used as solid oxide fuel cell model electrodes.
In: *Journal of The Electrochemical Society* 148 (2001), Nr. 6, P. A646–A656

[44] BOSNJAKOVIC, F.:
Technische Thermodynamik Teil I.
Darmstadt : Steinkopff, 1998

[45] BOSSEL, U. G.:
Facts & Figures - Final Report on SOFC Data.
Bern : Swiss Federal Office of Energy, 1992

[46] BRAUN, Robert J.:
Optimal Design and Operation of Solid Oxide Fuel Cell Systems for Small-scale Stationary Applications, University of Wisconsin-Madison, Diss., 2002

[47] BURT, AC ; CELIK, IB ; GEMMEN, RS ; SMIRNOV, AV:
Influence of radiative heat transfer on variation of cell voltage within a stack ASME, 2003

[48] BURT, A.C ; CELIK, I.B ; GEMMEN, R.S ; SMIRNOV, A.V:
A numerical study of cell-to-cell variations in a SOFC stack.
In: *Journal of Power Sources* 126 (2004), P. 76 – 87

[49] CAMPANARI, S. ; IORA, P.:
Comparison of Finite Volume SOFC Models for the Simulation of a Planar Cell Geometry.

In: *Fuel Cells* 5 (2005), Nr. 1, P. 34–51

[50] CARL, Michael ; DJILALI, Ned ; BEAUSOLEIL-MORRISON, Ian:
Improved modelling of the fuel cell power module within a system-level model for solid-oxide fuel cell cogeneration systems.
In: *Journal of Power Sources* 195 (2010), Nr. 8, P. 2283 – 2290

[51] CARL, Michael J.:
SOFC Modeling for the Simulation of Residential Cogeneration Systems.
2005

[52] CARRÉ, Maxime:
Modeling and Control of a Domestic Solid Oxide Fuel Cell (SOFC) System with Anode Recycle for Combined Heat and Power (CHP) Generation, Stuttgart Universitaet, Diss., 2011

[53] CELLIER, François E:
Object-oriented modeling: means for dealing with system complexity.
In: *Proceedings of the 15th Benelux Meeting on Systems and Control, Mierlo, The Netherlands* Citeseer, 1996, P. 53–64

[54] ÇENGEL, Y.A. ; CIMBALA, J.M.:
Fluid Mechanics: Fundamentals and Applications.
Boston : McGraw-Hill Higher Education, 2010

[55] CHAISANTIKULWAT, A. ; DIAZ-GOANO, C. ; MEADOWS, E.S.:
Dynamic modelling and control of planar anode-supported solid oxide fuel cell.
In: *Computers & Chemical Engineering* 32 (2008), Nr. 10, P. 2365 – 2381

[56] CHEDDIE, Denver F. ; MUNROE, Norman D.:
A dynamic 1D model of a solid oxide fuel cell for real time simulation.
In: *Journal of Power Sources* 171 (2007), Nr. 2, P. 634 – 643

[57] CHIANG, Mao H. ; YU, Dung D.:
Simulation and Control for Load Change Process on a Solid Oxide Fuel Cell.
In: *Applied Mechanics and Materials* 284 (2013), P. 925–929

[58] CHURCHILL, S.W. ; CHU, H.H.S:
Correlating Equations for Laminar and Turbulent Free Convection from a Horizontal Cylinder.
In: *Int. J. Heat Mass Transfer* 18 (1975)

[59] CHURCHILL, S.W. ; CHU, H.H.S:
Correlating Equations for Laminar and Turbulent Free Convection from a Vertical Cylinder.
In: *Int. J. Heat Mass Transfer* 18 (1975)

[60] COLCLASURE, Andrew M. ; SANANDAJI, Borhan M. ; VINCENT, Tyrone L. ; KEE, Robert J.:
Modeling and control of tubular solid-oxide fuel cell systems. I: Physical models and linear model reduction.
In: *Journal of Power Sources* 196 (2011), Nr. 1, P. 196–207

[61] COLONNA, P. ; PUTTEN, H. van:
Dynamic modeling of steam power cycles.: Part I—Modeling paradigm and validation.
In: *Applied Thermal Engineering* 27 (2007), Nr. 2–3, P. 467 – 480

[62] COLPAN, C. O. ; DINCER, Ibrahim ; HAMDULLAHPUR, Feridun:
A review on macro-level modeling of planar solid oxide fuel cells.
In: *International Journal of Energy Research* 32 (2008), Nr. 4, P. 336–355

[63] COSTAMAGNA, Paola ; HONEGGER, Kaspar:
Modeling of Solid Oxide Heat Exchanger Integrated Stacks and Simulation at High Fuel Utilisation.
In: *Journal of Electrochemical Society* 145 (1998)

[64] COSTAMAGNA, Paola ; SELIMOVIC, Azra ; BORGHI, Marco D. ; AGNEW, Gerry:
Electrochemical model of the integrated planar solid oxide fuel cell (IP-SOFC).
In: *Chemical Engineering Journal* 102 (2004), Nr. 1, P. 61 – 69

[65] CRC PRESS, Taylor & Francis G.:
CRC handbook of chemistry and physics.
2013

[66] DALY, Joseph M. ; JAHNKE, Fred C. ; KOEHLER, Steven A.:
Patent number US 8062804: Flow control assembly for use with fuel cell systems operating on fuels with varying fuel composition.
11 2011

[67] DAMM, David L. ; FEDOROV, Andrei G.:
Radiation heat transfer in SOFC materials and components.
In: *Journal of Power Sources* 143 (2005), Nr. 1–2, P. 158 – 165

[68] EGUCHI, K ; KOJO, H ; TAKEGUCHI, T ; KIKUCHI, R ; SASAKI, K:
Fuel flexibility in power generation by solid oxide fuel cells.
In: *Solid State Ionics* 152–153 (2002), Nr. 0, P. 411 – 416

[69] ELMQVIST, H. ; MATTSSON, S.E. ; OTTER, M.:
Modelica-a language for physical system modeling, visualization and interaction.
In: *Computer Aided Control System Design, 1999. Proceedings of the 1999 IEEE International Symposium on*, 1999, P. 630–639

[70] FELLOWS, Richard:
A novel configuration for direct internal reforming stacks.
In: *Journal of Power Sources* 71 (1998), Nr. 1–2, P. 281 – 287

[71] FLAGAN, Richard C. ; SEINFELD, John H.:
Fundamentals of air pollution engineering.

Englewood Cliffs, New Jersey : Prentice Hall, 1988

[72] FRITZSON, Peter:
Introduction to Object-Oriented Modeling and Simulation with OpenModelica.
Tutorial for Modelica Conference 2006, 2006

[73] GAYNOR, Robert ; MUELLER, Fabian ; JABBARI, Faryar ; BROUWER, Jacob:
On control concepts to prevent fuel starvation in solid oxide fuel cells.
In: *Journal of Power Sources* 180 (2008), Nr. 1, P. 330 – 342

[74] GEMMEN, Randall S. ; JOHNSON, Christopher D.:
Effect of load transients on SOFC operation—current reversal on loss of load.
In: *Journal of Power Sources* 144 (2005), Nr. 1, P. 152 – 164

[75] GRAY, Francesco M.:
Simulation and Control of a High-Temperature Solid-Oxide Fuel Cell System for Residential Micro Combined Heat and Power.
2012

[76] HABERMAN, B.A. ; YOUNG, J.B.:
Three-dimensional simulation of chemically reacting gas flows in the porous support structure of an integrated-planar solid oxide fuel cell.
In: *International Journal of Heat and Mass Transfer* 47 (2004), Nr. 17–18, P. 3617 – 3629

[77] HAJIMOLANA, S. A. ; HUSSAIN, M. A. ; SOROUSH, M. ; WAN DAUD, W. M. A. ; CHAKRABARTI, M. H.:
Modeling of a Tubular-SOFC: The Effect of the Thermal Radiation of Fuel Components and CO Participating in the Electrochemical Process.
In: *Fuel Cells* 12 (2012), Nr. 5, P. 761–772

[78] HAJIMOLANA, S.A. ; HUSSAIN, M.A. ; DAUD, W.M.A.W. ; SOROUSH, M. ; SHAMIRI, A.:

Mathematical modeling of solid oxide fuel cells: A review.
In: *Renewable and Sustainable Energy Reviews* 15 (2011), Nr. 4, P. 1893–1917

[79] HALINEN, M ; THOMANN, O ; KIVIAHO, J:
Effect of Anode off-gas Recycling on Reforming of Natural Gas for Solid Oxide Fuel Cell Systems.
In: *Fuel Cells* 12 (2012), Nr. 5, P. 754–760

[80] HARALDSSON, Kristina ; WIPKE, Keith:
Evaluating PEM fuel cell system models.
In: *Journal of Power Sources* 126 (2004), Nr. 1–2, P. 88 – 97

[81] HENKE, M. ; WILLICH, C. ; WESTNER, C. ; LEUCHT, F. ; KALLO, J. ; BESSLER, W. G. ; FRIEDRICH, K. A.:
A validated multi-scale model of a SOFC stack at elevated pressure.
In: *Fuel Cells* 13 (2013), Nr. 5, P. 773–780

[82] HERLE, J V. ; MARÉCHAL, F ; LEUENBERGER, S ; MEMBREZ, Y ; BUCHELI, O ; FAVRAT, D:
Process flow model of solid oxide fuel cell system supplied with sewage biogas.
In: *Journal of Power Sources* 131 (2004), Nr. 1–2, P. 127 – 141

[83] HERWIG, Heinz:
Wärmeübertragung A-Z: Systematische und ausführliche Erläuterungen wichtiger Größen und Konzepte.
Berlin Heidelberg : Springer, 2000

[84] HIRSCHBERG, Sven:
Simulationsgestützte Untersuchung des Einflusses wechselnder Gaszusammensetzungen auf ein Hochtemperaturbrennstoffzellensystem.
2013

[85] HO, Thinh X. ; KOSINSKI, Pawel ; HOFFMANN, Alex C. ; VIK, Arild:

Numerical analysis of a planar anode-supported SOFC with composite electrodes.
In: *International Journal of Hydrogen Energy* 34 (2009), Nr. 8, P. 3488 – 3499

[86] HO, Thinh X. ; KOSINSKI, Pawel ; HOFFMANN, Alex C. ; VIK, Arild:
Effects of heat sources on the performance of a planar solid oxide fuel cell.
In: *International Journal of Hydrogen Energy* 35 (2010), Nr. 9, P. 4276 – 4284

[87] HOLTAPPELS, P. ; HAART, L.G.J.De ; STIMMING, U. ; VINKE, I.C. ; MOGENSEN, M.:
Reaction of CO/CO_2 gas mixtures on Ni–YSZ cermet electrodes.
In: *Journal of Applied Electrochemistry* 29 (1999), Nr. 5, P. 561–568

[88] HUANG, Biao ; QI, Yutong ; MURSHED, Monjur:
Solid oxide fuel cell: Perspective of dynamic modeling and control.
In: *Journal of Process Control* 21 (2011), Nr. 10, P. 1426 – 1437

[89] HUMPHREYS, A.E.:
Some Thermophysical Properties of Components of Natural Gas and Cognate Fluids.
London : Gropue Européen de Recherches Gazières, Tech. Monograph No GERG TPC/1, 1986

[90] INUI, Y. ; ITO, N. ; NAKAJIMA, T. ; URATA, A.:
Analytical investigation on cell temperature control method of planar solid oxide fuel cell.
In: *Energy Conversion and Management* 47 (2006), Nr. 15–16, P. 2319 – 2328

[91] JAROSCH, K. ; SOLH, T. E. ; LASA, H.I. de:
Modelling the catalytic steam reforming of methane: discrimination between kinetic expressions using sequentially designed experiments.
In: *Chemical Engineering Science* 57 (2002), Nr. 16, P. 3439 – 3451

[92] JIA, Junxi ; LI, Qiang ; LUO, Ming ; WEI, Liming ; ABUDULA, Abuliti:

Effects of gas recycle on performance of solid oxide fuel cell power systems.
In: *Energy* 36 (2011), Nr. 2, P. 1068 – 1075

[93] JOOS, Franz:
Technische Verbrennung.
London : Springer, 2007

[94] KAKAÇ, Sadik ; LIU, Hongtan:
Heat exchangers: selection, rating, and thermal design.
Boca Raton, Fla. : CRC Press, 1998. –
432 S.

[95] KAKAÇ, Sadik ; PRAMUANJAROENKIJ, Anchasa ; ZHOU, Xiang Y.:
A review of numerical modeling of solid oxide fuel cells.
In: *International Journal of Hydrogen Energy* 32 (2007), Nr. 7, P. 761 – 786

[96] KANDEPU, Rambabu ; IMSLAND, Lars ; FOSS, Bjarne A. ; STILLER, Christoph ; THORUD, Bjørn ; BOLLAND, Olav:
Modeling and control of a SOFC-GT-based autonomous power system.
In: *Energy* 32 (2007), Nr. 4

[97] KANEKO, T. ; BROUWER, J. ; SAMUELSEN, G.S.:
Power and temperature control of fluctuating biomass gas fueled solid oxide fuel cell and micro gas turbine hybrid system.
In: *Journal of Power Sources* 160 (2006), Nr. 1, P. 316 – 325

[98] KARCZ, Michał:
From 0 D to 1 D modeling of tubular solid oxide fuel cell.
In: *Energy Conversion and Management* 50 (2009), Nr. 9, P. 2307 – 2315

[99] KATTKE, K.J. ; BRAUN, R.J.:
Thermal Management Modeling Into SOFC System Level Design.
In: *J. Fuel Cell Sci. Technol.* 8 (2010)

[100] KAZEMPOOR, P. ; DORER, V. ; OMMI, F.:
Evaluation of hydrogen and methane-fuelled solid oxide fuel cell systems for residential applications: System design alternative and parameter study.
In: *International Journal of hydrogen energy* 34 (2009)

[101] KIEHL, JT ; TRENBERTH, Kevin E.:
Earth's annual global mean energy budget.
In: *Bulletin of the American Meteorological Society* 78 (1997), Nr. 2, P. 197–208

[102] KIM, Jai W. ; VIRKAR, Anil V. ; FUNG, Kuan Z. ; MEHTA, Karun ; SINGHAL, Subhash C.:
Polarization Effects in Intermediate Temperature, Anode-Supported Solid Oxide Fuel Cells.
In: *Journal of The Electrochemical Society* 146 (1999), Nr. 1, P. 69–78

[103] KIRUBAKARAN, A ; NEMA, RK ; JAIN, Shailendra K.:
Distributed generation by solid oxide fuel cell: A review.
In: *Power System Technology and IEEE Power India Conference, 2008. POWERCON 2008. Joint International Conference on* IEEE, 2008, P. 1–7

[104] KOCH, Søren ; HENDRIKSEN, Peter V.:
Contact resistance at ceramic interfaces and its dependence on mechanical load.
In: *Solid State Ionics* 168 (2004), Nr. 1–2, P. 1 – 11

[105] KURZWEIL, Peter:
Brennstoffzellentechnik: Grundlagen, Komponenten, Systeme, Anwendungen.
2., überarb. u. akt. Aufl. 2013.
Wiesbaden : Springer Vieweg, 2013

[106] LARMINIE, J. ; DICKS, A.:
Fuel Cell Systems Explained.
J. Wiley, 2003

[107] LEE, HoSung:
Thermal Design. Heat Sinks, Thermoelectrics, Heat Pipes, Compact Heat Exchangers, and Solar Cells.
Hoboken, New Jersey : John Wiley & Sons, Inc., 2010

[108] LEE, Kwang H. ; STRAND, Richard K.:
SOFC cogeneration system for building applications, part 1: Development of SOFC system-level model and the parametric study.
In: *Renewable Energy* 34 (2009), Nr. 12, P. 2831 – 2838

[109] LEHNERT, W. ; MEUSINGER, J. ; THOM, F.:
Modelling of gas transport phenomena in SOFC anodes.
In: *Journal of Power Sources* 87 (2000), Nr. 1–2, P. 57 – 63

[110] LEUNG, M. ; PARK, Gunhyung ; RADISAVLJEVIC-GAJIC, V.:
Control of solid oxide fuel cells: An overview.
In: *Control Conference (ASCC), 2013 9th Asian*, 2013, P. 1–6

[111] L.G. WADE, Jr.:
Organic chemistry.
Upper Saddle River, New Jersey : Prentice Hall, 2010

[112] LI, Xianguo:
Principles of fuel cells.
New York : Taylor & Francis Group, LLC, 2006

[113] LISBONA, Pilar ; CORRADETTI, Alessandro ; BOVE, Roberto ; LUNGHI, Piero:
Analysis of a solid oxide fuel cell system for combined heat and power applications under non-nominal conditions.
In: *Electrochimica Acta* 53 (2007), Nr. 4, P. 1920 – 1930

[114] MARTINEZ, David Tomas S.:

Aportación al análisis de pilas de combustible de óxido sólido (SOFC) para integración en sistemas híbridos pila de combustible-turbina de gas, Universidad de Sevilla, Diss., 2002

[115] MATSUZAKI, Yoshio ; YASUDA, Isamu:
Electrochemical Oxidation of H_2 and CO in a H_2/H_2O/ CO/CO_2 System at the Interface of a Ni/YSZ Cermet Electrode and YSZ Electrolyte.
In: *Journal of The Electrochemical Society* 147 (2000), Nr. 5, P. 1630–1635

[116] MCBRIDE, Bonnie J. ; GORDON, Sanford. ; RENO, Martin A.:
Coefficients for calculating thermodynamic and transport properties.
National Aeronautics and Space Administration, Office of Management, Scientific and Technical Information Program ; National Technical Information Service, distributor], [Washington, DC] : [Springfield, Va. :

[117] MOGENSEN, D. ; GRUNWALDT, J.-D. ; HENDRIKSEN, P.V. ; DAM-JOHANSEN, K. ; NIELSEN, J.U.:
Internal steam reforming in solid oxide fuel cells: Status and opportunities of kinetic studies and their impact on modelling.
In: *Journal of Power Sources* 196 (2011), Nr. 1, P. 25 – 38

[118] MORRISON, R. T. ; BOYD, R. N.:
Organic Chemistry, 6th Edition.
Englewood Cliffs, New Jersey : Prentice Hall, 1992

[119] MUELLER, Fabian ; BROUWER, Jacob ; JABBARI, Faryar ; SAMUELSEN, Scott:
Dynamic simulation of an integrated solid oxide fuel cell system including current-based fuel flow control.
In: *Journal of fuel cell science and technology* 3 (2006), Nr. 2, P. 144–154

[120] NOREN, D.A. ; HOFFMAN, M.A.:
Clarifying the Butler–Volmer equation and related approximations for calculating activation losses in solid oxide fuel cell models.

In: *Journal of Power Sources* 152 (2005), Nr. 0, P. 175 – 181

[121] O'HAYRE, Ryan ; CHA, Suk-Won ; COLELLA, Whitney ; PRINZ, Fritz B.:
Fuel Cell Fundamentals.
New York : John Wiley & Sons, Inc., 2009

[122] OTA, Tomoyuki ; KOYAMA, Michihisa ; WEN, Ching ju ; YAMADA, Koichi ; TAKAHASHI, Hiroshi:
Object-based modeling of SOFC system: dynamic behavior of micro-tube SOFC.
In: *Journal of Power Sources* 118 (2003), Nr. 1–2, P. 430 – 439. –
Scientific Advances in Fuel Cell Systems

[123] PACHAURI, Rajendra K.:
Climate change 2007. Synthesis report. Contribution of Working Groups I, II and III to the fourth assessment report.
(2008)

[124] PARK, Seungdoo ; GORTE, Raymond J. ; VOHS, John M.:
Applications of heterogeneous catalysis in the direct oxidation of hydrocarbons in a solid-oxide fuel cell.
In: *Applied Catalysis A: General* 200 (2000), Nr. 1–2, P. 55 – 61

[125] PEHNT, M. ; COLIJN, M.:
Micro cogeneration: towards decentralized energy systems.
The Netherlands : Springer, 2006

[126] PEKSEN, Murat ; PETERS, Roland ; BLUM, Ludger ; STOLTEN, Detlef:
Numerical modelling and experimental validation of a planar type pre-reformer in SOFC technology.
In: *International Journal of Hydrogen Energy* 34 (2009), Nr. 15, P. 6425 – 6436

[127] PETERS, Roland ; DEJA, Robert ; BLUM, Ludger ; PENNANEN, Jari ; KIVIAHO, Jari ; HAKALA, Tuomas:

Analysis of solid oxide fuel cell system concepts with anode recycling.
In: *International Journal of Hydrogen Energy* 38 (2013), Nr. 16, P. 6809 – 6820

[128] PETERSEN, Thomas F.:
A zero-dimensional model of a 2nd generation planar sofc using calibrated parameters.
In: *International Journal of Thermodynamics* 9 (2006), Nr. 4, P. 161–169

[129] POWERS, Joseph M.:
Lecture Notes on Fundamentals of Combustion.
Department of Aerospace and Mechanical Engineering University of Notre Dame, 2012

[130] REID, Robert C. ; PRAUSNITZ, John M. ; POLING, Bruce R.:
The Properties of Gases and Liquids.
New York : McGraw-Hill, 1989

[131] RIENSCHE, Ernst ; MEUSINGER, Josefin ; STIMMING, Ulrich ; UNVERZAGT, Guido:
Optimization of a 200 kW SOFC cogeneration power plant. Part II: variation of the flowsheet.
In: *Journal of Power Sources* 71 (1998), Nr. 1–2, P. 306 – 314

[132] RYAN PATRICK HALLUM, Latham N.:
Patent number US 6455181: Fuel cell system with sensor.
2002

[133] SALOGNI, A. ; COLONNA, P.:
Modeling of solid oxide fuel cells for dynamic simulations of integrated systems.
In: *Applied Thermal Engineering* 30 (2010), P. 464–477

[134] SANANDAJI, Borhan M. ; VINCENT, Tyrone L. ; COLCLASURE, Andrew M. ; KEE, Robert J.:

Modeling and control of tubular solid-oxide fuel cell systems: II. Nonlinear model reduction and model predictive control.
In: *Journal of Power Sources* 196 (2011), Nr. 1, P. 208–217

[135] SANCHEZ, D ; CHACARTEGUI, R ; MUNOZ, A ; SANCHEZ, T:
On the effect of methane internal reforming modelling in solid oxide fuel cells.
In: *International Journal of Hydrogen Energy* 33 (2008), Nr. 7, P. 1834–1844

[136] SANGTONGKITCHAROEN, W. ; ASSABUMRUNGRAT, S. ; PAVARAJARN, V. ; LAOSIRIPOJANA, N. ; PRASERTHDAM, P.:
Comparison of carbon formation boundary in different modes of solid oxide fuel cells fueled by methane.
In: *Journal of Power Sources* 142 (2005), Nr. 1–2, P. 75 – 80

[137] SCHAEDEL, Benjamin T. ; DUISBERG, Matthias ; DEUTSCHMANN, Olaf:
Steam reforming of methane, ethane, propane, butane, and natural gas over a rhodium-based catalyst.
In: *Catalysis Today* 142 (2009), P. 42–51

[138] SEIER, Jochen ; MARKUS, Horst:
Forschungsbericht Nr. 566. Leuchtturm COORETEC, der Weg zum zukunftsfähigen Kraftwerk mit fossilen Brennstroffen.
2007. –
Forschungsbericht

[139] SHEKHAWAT, D. ; SPIVEY, J.J. ; BERRY, D.A.:
Fuel Cells: Technologies for Fuel Processing.
Oxford Amsterdam : Elsevier, 2011

[140] SINGHAL, S. ; SINGHAL, S.C. ; KENDALL, K.:
High-temperature Solid Oxide Fuel Cells: Fundamentals, Design and Applications.
Oxford Amsterdam : Elsevier Science, 2003

[141] SLIPPEY, Andrew J.:
Dynamic Modeling and Analysis of Multiple SOFC System Configurations.
2009

[142] SÁNCHEZ, D. ; CHACARTEGUI, R. ; MUÑOZ, A. ; SÁNCHEZ, T.:
Thermal and electrochemical model of internal reforming solid oxide fuel cells with tubular geometry.
In: *Journal of Power Sources* 160 (2006), Nr. 2, P. 1074 – 1087

[143] SÁNCHEZ, D. ; MUÑOZ, A. ; SÁNCHEZ, T.:
An assessment on convective and radiative heat transfer modelling in tubular solid oxide fuel cells.
In: *Journal of Power Sources* 169 (2007), Nr. 1, P. 25 – 34

[144] SORRENTINO, Marco ; PIANESE, Cesare:
Model-based development of low-level control strategies for transient operation of solid oxide fuel cell systems.
In: *Journal of Power Sources* 196 (2011), Nr. 21, P. 9036 – 9045

[145] SPIEGEL, Colleen S.:
Designing & Building Fuel Cells.
New York : McGraw-Hill Companies, 2007

[146] STILLER, Christoph:
Design, Operation and Control Modelling of SOFC/GT Hybrid Systems, Norwegian University of Science and Technology, Diss., 2006

[147] TODD, B. ; YOUNG, J.B.:
Thermodynamic and transport properties of gases for use in solid oxide fuel cell modelling.
In: *Journal of Power Sources* 110 (2002), Nr. 1, P. 186 – 200

[148] ULBIG, Peter ; HOBURG, Detlev:

Determination of the calorific value of natural gas by different methods.
In: *Thermochimica Acta* 382 (2002), P. 27–35

[149] VOLLHARDT, Peter ; SCHORE, Neil:
Organic chemistry: structure and function.
New York : Clancy Marshall, 2011

[150] WAGNER, Walter:
Wärmeübertragung, 5. Auflage.
Würzburg : Vogel Verlag, 1998

[151] WAHL, Stefanie:
Verfahrenstechnische Optimierung eines Brennstoffzellensystems auf Basis SOFC für die Kraft-Wärme-Kopplung unter Betrachtung der heißen Komponenten mit thermischer Auslegung.
2014

[152] WAHL, Stefanie ; GALLET SEGARRA, Ana ; HORSTMANN, Peter ; CARRÉ, Maxime ; BESSLER, Wolfgang G. ; LAPICQUE, François ; FRIEDRICH, K. A.:
Modeling of a thermally integrated 10 kWe planar solid oxide fuel cell system with anode offgas recycling and internal reforming by discretization in flow direction.
In: *Journal of Power Sources* 279 (2015), P. 656–666

[153] WANG, Yuzhang ; YOSHIBA, Fumihiko ; KAWASE, Makoto ; WATANABE, Takao:
Performance and effective kinetic models of methane steam reforming over Ni/YSZ anode of planar SOFC.
In: *International Journal of Hydrogen Energy* 34 (2009), Nr. 9, P. 3885 – 3893

[154] WEGENER, Eberhard:
Planung eines Waermeuebertragers. Ganzheitliche Aufgabenloesung bis zur Instandsetzung eines Rohrbuendel-Waermeuebertragers.
Weinheim : Wiley-VCH Verlag GmbH & Co. KGaA, 2013

[155] XU, Jianguo ; FROMENT, Gilbert F.:
Methane steam reforming, methanation and water-gas shift: I. Intrinsic kinetics.
In: *AIChE Journal* 35 (1989), Nr. 1, P. 88–96

[156] YANG, Jie ; LI, Xi ; MOU, Hong-Gang ; JIAN, Li:
Predictive control of solid oxide fuel cell based on an improved Takagi–Sugeno fuzzy model.
In: *Journal of Power Sources* 193 (2009), Nr. 2, P. 699 – 705

[157] ZABIHIAN, Farshid ; FUNG, Alan:
A review on modeling of hybrid solid oxide fuel cell systems.
In: *International Journal of Engineering* 3 (2009), Nr. 2, P. 85–119

[158] ZHANG, X.W. ; CHAN, S.H. ; HO, H.K. ; LI, Jun ; LI, Guojun ; FENG, Zhenping:
Nonlinear model predictive control based on the moving horizon state estimation for the solid oxide fuel cell.
In: *International Journal of Hydrogen Energy* 33 (2008), Nr. 9, P. 2355 – 2366

[159] ZHU, W.Z. ; DEEVI, S.C.:
Opportunity of metallic interconnects for solid oxide fuel cells: a status on contact resistance.
In: *Materials Research Bulletin* 38 (2003), Nr. 6, P. 957 – 972

[160] ZIMMER, Dirk:
Virtual Physics Equation-Based Modeling, Compiling Modelica.
2013

Robust Control of a Solid Oxide Fuel Cell for Combined Heat and Power Applications

The reduction of energy consumption and CO_2 emissions is one of the main environmental issues in the present day society. Distributed combined heat and power systems (CHP) are one of the most promising technologies for the achievement of this goal. Solid oxide fuel cells systems (SOFC) are specially suited for CHP applications due to their high electrical efficiency and the possibility of being operated with natural gas. However, they are highly sensitive to variations of fuel composition, which are common in natural gas provided by German grids, leading to fuel cell degradation and/or low efficiencies. The focus of this work is the investigation of this issue by analyzing the dependencies between natural gas composition and the operation of SOFCs. Therefore a complete CHP SOFC system model is developed and parameterized with experimental measurements. Additionally, solutions are provided in form of robust control strategies for preventing the degradation of CHP SOFC systems and ensuring their operation with constant efficiency .

Content:

- Fundamentals of SOFC for CHP applications
- Natural gas composition in Germany and its effects on SOFC CHP systems
- Modelling of a SOFC system
- Robust control strategies to fluctuating natural gas composition
- Evaluation of control strategies with simulation and experimental methodes